VARIABILITÄT VON FORMALDEHYD-KONZENTRATIONEN IN DER VERSCHMUTZTEN PLANETAREN GRENZSCHICHT: MESSUNGEN IM BALLUNGSRAUM VON MILANO

Zur Erlangung des akademischen Grades eines
DOKTORS DER NATURWISSENSCHAFTEN
von der Fakultät für Physik der
Universität Karlsruhe (TH)

genehmigte

DISSERTATION

von

Diplom-Meteorologin, Claudia Hak
aus Bobingen

Tag der mündlichen Prüfung: 21.07.2006
Referent: Prof. Dr. H. Fischer
Korreferent: Prof. Dr. U. Platt

VARIABILITY OF FORMALDEHYDE IN THE POLLUTED PLANETARY BOUNDARY LAYER - MEASUREMENTS IN THE MILANO METROPOLITAN AREA, ITALY (PO BASIN)

Abstract

Formaldehyde (CH_2O) plays an important role in atmospheric chemistry. As an ubiquitous intermediate product of the oxidation of hydrocarbons, it can be used as a tracer of photooxidation in the plumes of larger cities. Formaldehyde is particularly relevant as a HO_x radical source, being the second most important source of primary HO_x in the Milano area and even the most important HO_x source in Mexico City. In the scope of this thesis, comprehensive measurements of formaldehyde and other major tropospheric trace gases were performed during three major field campaigns with active long path DOAS (Differential Optical Absorption Spectroscopy) instruments at several urban and rural sites.

In an intercomparison experiment employing four different formaldehyde measurement techniques, the discrepancies between optical and wet chemical methods were studied. For this purpose, White systems (realising a long absorption path on a short base line by multiple reflections) were used for the optical techniques (DOAS and FTIR) to assure probing identical air volumes. The comparison showed that, contrary to several previous comparison studies, the optical and wet chemical techniques agreed well within 15%. The good agreement suggests that systematic errors are within 15% and that the larger differences assessed during previous intercomparisons can be attributed to the different air volumes probed.

The variability of formaldehyde was studied by means of airborne and ground-based measurements as a function of OH production and VOC reactivity. It could be understood well, both qualitatively and quantitatively, where more than 70% (in most cases more than 80%) were explained by a simple model.

Besides its secondary formation, formaldehyde has also primary sources, particularly incomplete combustion processes. These include biomass burning. From measurements in the rural vicinities of Milano, where agricultural fires were observed, formaldehyde emission factors were derived. The emissions factors found were similar to the CH_2O emission factors in the plumes of African savanna fires reported by other authors.

Table of contents

Zusammenfassung v

1 Introduction 1

2 Chemistry and Physics of the Planetary Boundary Layer 5

2.1 Sources of Atmospheric Trace Gases 5

2.1.1 Volatile Organic Compounds (VOCs) 5

2.1.2 Anthropogenic Pollutants Sources 6

2.1.3 Biogenic Trace Gas Sources 8

2.1.4 Gases Emitted from Biomass Burning 9

2.2 Photochemical Smog 12

2.2.1 Sources of HO_x Radicals 13

2.2.2 Basic Photochemical Cycle of NO_2, NO and O_3 16

2.2.3 VOC Oxidation 17

2.2.4 Atmospheric Chemistry of VOCs and NO_x 21

2.2.5 VOC- and NO_x-Limitation of Ozone Formation 24

2.2.6 Estimation of OH Concentrations 25

2.3 Formaldehyde 27

2.3.1 Typical Formaldehyde Concentrations 27

2.3.2 Role of Formaldehyde in Tropospheric Chemistry 28

2.3.2.1 Daytime Sinks 28

2.3.2.2 Nighttime Sinks 30

2.3.2.3 Lifetime of Formaldehyde 31

2.3.3 Sources of Formaldehyde 31

2.3.3.1 Oxidation of Methane and Higher Alkanes 32

2.3.3.2 Oxidation of Alkenes 32

2.3.3.3 Oxidation of Isoprene and Other Biogenic NMHCs 33

2.3.3.4 Formaldehyde from Higher Carbonyls 35

2.3.3.5 Steady State Formaldehyde Calculation 36

2.4 Processes in the Planetary Boundary Layer 37

2.4.1 Diurnal Variations of the Planetary Boundary Layer 37

2.4.2 Micrometeorology - Chemistry Relations 39

2.4.3 Radon as a Tracer for Mixing in the PBL 40

2.4.4 Deposition 42

3 Measurement Methods 45
3.1 Formaldehyde Detection Techniques in the Atmosphere 45
3.1.1 Differential Optical Absorption Spectroscopy 45
3.1.1.1 Absorption Spectroscopy 46
3.1.1.2 Basic Principle of DOAS 48
3.1.1.3 Mathematical Description of DOAS Spectra 49
3.1.1.4 Analysis Procedure 51
3.1.1.5 Error Estimation 52
3.1.1.6 Setup of an Active DOAS System 54
3.1.1.6.1 The Telescope of the LP DOAS System 54
3.1.1.6.2 The Telescope of the Multibeam LP DOAS System 55
3.1.1.6.3 The DOAS White System 57
3.1.1.6.4 The Light Source 58
3.1.1.6.5 The Quartz Fibre and Mode Mixer 59
3.1.1.6.6 The Spectrometers 59
3.1.1.6.7 The Detector Units 59
3.1.1.7 Measurement Algorithms 62
3.1.1.8 DOAS Spectral Evaluation Procedure 63
3.1.1.8.1 Comparison of Formaldehyde Reference Cross-Sections 66
3.1.1.8.2 A Lamp Structure Influencing DOAS Evaluation 69
3.1.1.8.3 Experiment on Accuracy 73
3.1.2 IR Spectroscopy (FTIR) 77
3.1.3 Hantzsch Technique (Fluorescence Detection) 78
3.1.4 DNPH Technique (Derivatisation Method) 78
3.2 Measurement Techniques for Other Trace Species 80
3.2.1 Chemiluminescence (Nitric Oxide) 80
3.2.2 Gas Chromatography (VOCs) 80
3.2.3 UV-Absorption (Ozone) 81
3.2.4 Alpha Spectroscopy (Radon) 81
3.2.5 Spectroradiometry (Actinic Flux) 82
4 Field Observations 83
4.1 The FORMAT Sites 84
4.2 The FORMAT I Campaign 85
4.2.1 Meteorological Overview of the Campaign 86
4.2.2 Measurements at Alzate (Downwind Site) 87
4.2.2.1 Trace Gas Measurements 88
4.2.2.2 Wind Sector Analysis 91
4.2.3 Measurements at Bresso (Urban Site) 93
4.2.3.1 Intercomparison Measurements 95
4.2.3.2 Trace Gas Measurements 96
4.2.3.3 Meteorological Data 96
4.2.4 3D Model Results for FORMAT I 97

4.3 The FORMAT II Campaign 98
4.3.1 Meteorological Overview of the Campaign 98
4.3.2 Measurements at Alzate (Downwind Site) 99
4.3.3 Measurements at Bresso (Urban Site) 99
4.3.3.1 Measurements of Meteorological Parameters 101
4.3.3.2 Trace Gas Measurements 102
4.3.4 Measurements at Spessa (Upwind Site) 105
4.3.5 Ozone Upwind and Downwind of Milano 107
4.4 Synopsis of Three Campaigns in the Po Basin 108
4.4.1 Radical Formation at Bresso (1998, 2002, 2003) 108
4.5 The Mexico City Campaign (MCMA-2003) 113
4.5.1 The Location 113
4.5.2 Meteorological Overview 114
4.5.3 Trace Gas Measurements 115
4.5.4 Radical Production in Mexico City 117

5 Comparison of Formaldehyde Measurements 119

5.1 Previous Intercomparisons 119
5.2 Intercomparison of CH_2O in-situ Measurement Techniques 123
5.2.1 Intercomparison of Ambient Measurements 123
5.2.1.1 Agreement Among the Hantzsch Instruments 125
5.2.1.2 Agreement Between Spectroscopic and Hantzsch Techniques 127
5.2.1.3 Agreement Among Spectroscopic Techniques 129
5.2.1.4 Agreement Between Continuous Instruments and DNPH 129
5.2.2 Fractional Differences 130
5.2.3 Comparison of Hantzsch Calibration Standards 132
5.2.4 Summary and Conclusions 133
5.3 Comparison of Long Path and in-situ Measurements 134
5.3.1 Long Path DOAS Versus in-situ Results 135
5.3.2 Nighttime Vertical Ozone Gradient 137
5.3.3 Daytime Spatial Gradient of Formaldehyde 139
5.3.4 Nighttime Vertical Formaldehyde Variation 141
5.3.5 Conclusions 143

6 Variability of Formaldehyde in the Po Basin 145

6.1 Temporal Variability of Formaldehyde 145
6.1.1 Average Diurnal Trace Gas Cycles 145
6.2 Spatial Variability of Formaldehyde 148
6.2.1 Horizontal and Vertical Variability in the Po Basin 148
6.2.2 Airborne Measurements Along the DOAS Light Beam 149

6.3 Analysis of Spatial and Temporal Variability of Formaldehyde 153
6.3.1 Measured VOC Data 153
6.3.2 Estimation of VOC Reactivities 157
6.3.3 Statistical Analysis Method 158
6.3.4 Formaldehyde Variability over the Metropolitan Area of Milano 1998 159
6.3.5 Formaldehyde Variability over the Metropolitan Area of Milano 2003 162
6.3.6 Temporal Formaldehyde Variability at Alzate 2003 165
6.3.7 Temporal Formaldehyde Variability at Bresso 2003 167
6.3.8 Discussion 169
6.4 Direct Formaldehyde Emission by Biomass Burning 171
6.4.1 Published Emission Factors 171
6.4.2 Characterisation of the Combustion Efficiency 173
6.4.3 Estimation of a CH_2O Emission Factor 176
6.4.4 Remote Sensing of CH_2O and SO_2 Distributions 180
6.4.5 Radical Budget 181
6.4.6 Regional Impact 183

7 Conclusions and Outlook 187

Abbreviations 191

Literature 193

Acknowledgements 207

Zusammenfassung

Die uns umgebende Luft ist ein Gasgemisch, das sich hauptsächlich aus Stickstoff N_2 (≈ 78.08 Vol.%), Sauerstoff O_2 (≈ 20.95 Vol.%), Argon Ar (≈ 0.93 Vol.%) und Kohlendioxid CO_2 (≈ 0.03 Vol.%) zusammensetzt. Unzählige weitere Verbindungen sind in der Luft enthalten, nehmen jedoch nur Volumenanteile einiger ppbv (engl.: parts per billion by volume, d.h. 10^{-9}) bis ppmv (10^{-6}) ein. Zumeist sind diese Spurengase sehr reaktiv und damit für die Vielzahl von chemischen Reaktionen verantwortlich, die in der Atmosphäre ablaufen. Abhängig von Ort und Zeit sind die Konzentrationen der Spurengase stark variabel, insbesondere in der unteren Troposphäre, da deren Quellen, die sich meist in Bodennähe befinden, ungleichmäßig verteilt sind.

In der planetaren Grenzschicht, welche die untersten etwa 2000 m der Troposphäre einnimmt – und daher das Luftvolumen darstellt, das uns unmittelbar umgibt – findet ein großer Teil der atmosphärenchemischen Umsätze statt. Die meisten Lebewesen sind daher den primär emittierten und sekundär gebildeten Spurenstoffen direkt ausgesetzt, die sich häufig schädlich auf deren Gesundheit auswirken. Kohlenwasserstoffe werden durch natürliche und anthropogene Quellen freigesetzt und stellen eine Stoffgruppe mit sehr großem Eintrag in die Atmosphäre dar. Ihr Abbau wird durch Reaktion mit OH-Radikalen initiiert und bildet bei starker Sonneneinstrahlung in der Gegenwart von Stickstoffoxiden (NO_x, das heißt NO und NO_2) eine Voraussetzung zur Bildung troposphärischen Ozons. Da bei der Kohlenwasserstoff-Oxidation Stickstoffoxide in einem katalytischen Kreislauf ineinander umgewandelt werden, können hohe Ozonkonzentrationen entstehen. Wegen seiner stark oxidativen Wirkung hat Ozon in der Troposphäre einen schädlichen Einfluß auf lebende Organismen. Insbesondere die von NO_x und VOC (flüchtige organische Verbindungen) Emissionen belasteten städtischen Ballungsräume (beispielsweise Los Angeles, Mexico City, Milano) sind von diesen sogenannten Photosmog-Bedingungen betroffen.

Formaldehyd (CH_2O) ist an zahlreichen Stellen der in der Atmosphäre ablaufenden photochemischen Reaktionszyklen von Bedeutung. Als Zwischenprodukt das Abbaus von Kohlenwasserstoffen stellt Formaldehyd einen Indikator für die Emissionen von VOCs und deren Photooxidation dar. Es wird dadurch in großen Mengen in der Atmosphäre gebildet. Daß das Formaldehyd Mischungsverhältnis in der Troposphäre trotzdem nur wenige ppbv beträgt, liegt an seinen wirksamen Abbaumechanismen.

Die Photolyse von Formaldehyd stellt seine wichtigste Senke dar und ist zugleich eine bedeutende Quelle für HO_2-Radikale. Zwischen den OH und HO_2 Radikalen stellt sich rasch ein chemisches Gleichgewicht ein und beide werden unter der Bezeichnung HO_x zusammengefaßt. HO_x Radikale steuern den photochemischen Abbau sehr vieler atmosphärischer Verbindungen, unter anderem den oben genannten Kohlenwasserstoffabbau. Im Zuge dieser Reaktionen

entsteht wiederum CH_2O. Dadurch nimmt Formaldehyd diese wichtige Position in der Photochemie ein. Auch um den globalen CO-Haushalt erklären zu können, ist die Formaldehyd-Chemie von großer Bedeutung. Zudem ist Formaldehyd eine wichtige Quelle für molekularen Wasserstoff (H_2) in der Atmosphäre.

Wegen seiner bedeutenden Rolle bei der Oxidation von Kohlenwasserstoffen und daher bei der Ozonproduktion ist die Messung von Formaldehyd wichtig für das Verständnis der chemischen Prozesse, sowohl in der sauberen als auch der verschmutzten Atmosphäre. Daher verabschiedete das Europäische Parlament eine Richtlinie (2002/3/EG), welche neben der Messung 30 ausgewählter Kohlenwasserstoffe auch die Messung von Formaldehyd vorgibt [*EU*, 2002]. Diese ist seit September 2003 in Kraft.

Um dem Bedarf an weiteren atmosphärischen Formaldehyd Messungen nachzukommen, wurde das Europäische FORMAT Projekt initiiert, das im Januar 2002 begann. Die Themenstellung dieser Arbeit deckt sich im Wesentlichen mit Zielsetzungen des Projekts und wird in den folgenden Abschnitten beschrieben. Im Rahmen des Projekts wurden zwei Meßkampagnen in der verschmutzten Grenzschicht an mehreren Orten im Großraum Milano (Norditalien) durchgeführt. Wegen der starken Emissionen in Milano, zusammen mit der intensiven solaren Einstrahlung und dem schwachen Luftmassenaustausch, erfährt diese Gegend im Sommer regelmäßig Episoden photochemischen Smogs. Der Datensatz wurde durch die Teilnahme an einer weiteren Meßkampagne, die in der stark verschmutzten Atmosphäre von Mexico City stattfand, erweitert.

Die vorliegende Arbeit hat im Wesentlichen zwei Schwerpunkte. Zum einen soll die Vereinbarkeit verschiedener Methoden zur Messung von Formaldehyd untersucht werden. Andererseits wird die Verteilung und Variabilität von Formaldehyd in der unteren Troposphäre untersucht.

Im Rahmen dieser Arbeit wurden aktive Langpfad DOAS Messungen in städtischer und ländlicher Luft durchgeführt und nach Formaldehyd CH_2O, Ozon O_3, Stickstoffdioxid NO_2, Schwefeldioxid SO_2 und salpetriger Säure HONO ausgewertet. Die Differentielle Optische Absorptions-Spektroskopie (DOAS) ist eine anerkannte Methode zur berührungslosen Messung von Spurengaskonzentrationen und erlaubt die Quantifizierung von Formaldehyd (und anderen Verbindungen) durch seine charakteristische Absorption im UV-A Bereich. Darüber hinaus ist durch die Kooperation mit den anderen im FORMAT Projekt teilnehmenden Gruppen eine breite Datenbasis zur Analyse zugänglich.

Formaldehyd kann mittels DOAS mit hoher Sensitivität gemessen werden. Für die absolute Kalibrierung der Messung wird lediglich eine genaue Absorptions-Wirkungsquerschnitt Referenz benötigt. Acht Formaldehyd UV Wirkungsquerschnitte, die in hoher spektraler Auflösung vorliegen, wurden miteinander verglichen, um den Bereich möglicher Differenzen bei der Formaldehyd-Auswertung zu bestimmen. Dabei wurde für die von IUPAC bzw. JPL empfohlenen Spektren ein Unterschied von 11% entdeckt.

Heutzutage kann Formaldehyd anhand etlicher Methoden, die auf unterschiedlichen Prinzipien basieren, gemessen werden. Dabei hat es in der Vergangenheit oft große Abweichungen zwischen den Ergebnissen verschiedener Methoden gegeben, insbesondere zwischen DOAS und der sogenannten Hantzsch Methode [z.B. *Cárdenas et al.*, 2000; *Grossmann et al.*, 2003]. Die Beteiligung mehrerer Gruppen mit unterschiedlichen Meßverfahren im FORMAT Projekt erforderte eine eingehende Bewertung der Unterschiede zwischen den Methoden. Um die Daten unterschiedlicher Meßmethoden zuverlässig miteinander kombinieren zu können, müssen die systematischen Unterschiede zwischen den Methoden bekannt sein. Aus diesem Grund und in Übereinstimmung mit einem grundlegenden Ziel des FORMAT Projekts wurde ein Vergleich

von vier häufig benutzten in-situ Methoden (das heißt Punktmessung) zur Formaldehyd Messung durchgeführt. Die acht beteiligten Instrumente untersuchten *dasselbe* Luftvolumen. Die Ergebnisse werden in dieser Arbeit detailliert dargelegt. Entgegen früherer Studien war die Übereinstimmung zwischen DOAS und Hantzsch gut (innerhalb 15%), was auf die Untersuchung desselben Luftvolumens zurückgeführt wurde.

Basierend auf diesem Vergleich ist es, in einem nächsten Schritt, möglich, die *unterschiedlichen* Meßmethoden miteinander zu kombinieren, jedoch untersuchen sie nun unterschiedliche Luftvolumina. Durch unterschiedliche Meßaufbauten der Bodenmeßinstrumente, die in unterschiedlichen mittleren Niveaus messen, kann die kleinskalige horizontale und/oder vertikale Variabilität untersucht werden, da die lokale Formaldehyd Verteilung relativ inhomogen ist.

Ein weiteres Hauptziel des FORMAT Projektes war es, eine bessere Kenntnis über die regionale Verteilung und Variabilität von Formaldehyd in der Abgasfahne der Stadt Milano zu erlangen. Das meiste Formaldehyd in der Troposphäre ist sekundären Ursprungs, das heißt, es wurde durch Oxidation organischer Verbindungen gebildet. Hier wird ein statistischer Ansatz verwendet, um die Variabilität von Formaldehyd auf Grundlage der Variation von OH Produktion und VOC Konzentrationen zu erklären. Die räumliche CH_2O Variabilität im Großraum Milano und in der Po-Ebene wird anhand von in-situ Flugzeugmessungen zweier Feldkampagnen untersucht. In ähnlicher Weise werden Bodenmessungen einer urbanen und einer ländlichen Station im Raum Milano verwendet, um die zeitliche Variation von Formaldehyd zu untersuchen. Bereits ein einfaches Modell konnte die gemessenen Formaldehyd Werte sowohl qualitativ, als auch quantitativ gut erklären.

Im Herbst wird die Variabilität von Formaldehyd in der Po-Ebene durch die primäre Emission von Formaldehyd bei der Verbrennung von landwirtschaftlicher Biomasse beeinflußt. Da das Abbrennen abgeernteter Stoppelfelder eine wichtige Quelle von Formaldehyd in der Po-Ebene bildet, war die Quantifizierung seiner Emission ein Ziel des FORMAT Projekts. Reis ist die vorherrschende Getreidesorte in der Po-Ebene und der Umgebung von Milano. Für die Emissionen aus der Verbrennung von Reisstroh existieren nur wenige *Labor*messungen [*Christian et al.*, 2003; *Jenkins et al.*, 1996], Emissionsfaktoren wurden jedoch noch nicht unter realen Bedingungen im *Feld* quantifiziert. In dieser Arbeit werden Flugzeug- und Bodenmessungen in Rauchfahnen landwirtschaftlicher Feuer in der Po-Ebene zur Bestimmung von Formaldehyd Emissionsfaktoren herangezogen. Für den Formaldehyd Emissionsfaktor offener Reisstrohfeuer wurde ein ähnlicher Wert gefunden, wie von anderen Autoren für Savannenfeuer in Afrika berichtet wurde. Die erhöhte CH_2O Konzentration in der Umgebung der Feuer führt zu einer größeren relativen Bedeutung von Formaldehyd im Radikalhaushalt, wodurch CH_2O zur Hauptquelle für HO_x wird. Die Feuer stellen jeweils starke Punktquellen dar, die zusammengefaßt einen bedeutenden regionalen Einfluß auf die Troposphärenchemie haben können.

Dieser Arbeit liegt folgende Gliederung zugrunde. Kapitel 2 gibt einen Überblick über die Quellen von atmosphärischen Spurengasen und die chemischen Reaktionen, die für die Bildung photochemischen Smogs relevant sind. Auf das heutige Wissen über die Formaldehyd Chemie wird dann in einem gesonderten Abschnitt eingegangen. Nach dem Chemieteil werden bedeutende physikalische Prozesse, welche die Spurengas-Variabilität beeinflussen, erläutert. Kapitel 3 beschreibt die Meßverfahren und Instrumente, die zur Messung von Formaldehyd verwendet wurden, wobei auf die hier eingesetzte Differentielle Optische Absorptions Spektroskopie besonders eingegangen wird. Weitere Meßmethoden, die von anderen Gruppen bei den Feldmeßkampagnen verwendet wurden, werden am Ende des Kapitels kurz behandelt. In Kapitel 4 werden die Messungen der drei Feldmeßkampagnen vorgestellt. Der Charakterisierung der Meßstationen und lokalen Gegebenheiten folgen die Zeitreihen der gemessenen Spurengaskonzentrationen und erste Ergebnisse der Datenanalyse. Die Bedeutung von Form-

aldehyd als Radikalquelle wird für mehrere Stationen und Kampagnen abgeschätzt. Kapitel 5 befaßt sich mit dem Vergleich der verschiedenen Meßmethoden. Die Ergebnisse des Vergleichsexperiments der in-situ Formaldehyd Messungen werden im Detail gezeigt. Anschließend werden die Ergebnisse von Messungen in verschiedenen Luftvolumina verglichen. In Kapitel 6 wird die Analyse räumlicher und zeitlicher Formaldehyd Variabilität und die Abschätzung von Formaldehyd Emissionen durch landwirtschaftliche Feuer präsentiert. Eine Zusammenfassung der gewonnen Ergebnisse mit einem kurzen Ausblick folgt in Kapitel 7.

1 Introduction

The principal constituents of the ambient air are inert or slowly reacting substances like molecular nitrogen (≈ 78.084 vol%), molecular oxygen (≈ 20.946 vol%), argon (≈ 0.930 vol%) and carbon dioxide (≈ 0.034 vol%). In addition, the gas mixture contains innumerable trace gases, which occupy volume ratios of several parts per billion up to a few parts per million. Since most of these gases are very reactive, they determine the chemical reaction cycles in the atmosphere. The concentrations of the trace gases are greatly variable, depending on time and place. In the lower troposphere, the variability is particularly large because of the non-uniform distribution of the sources. The type and amount of trace gases in ambient air largely depend on the landuse and the type of the underlying surface.

The lowermost layer of the troposphere, which is referred to as the planetary boundary layer (PBL), is an important part of the atmosphere for human life, since it is the air volume which immediately surrounds us [e.g. *Stull*, 1988]. Most air pollutants are released into the planetary boundary layer by sources located at ground level and a large part of the conversions of reactions in atmospheric chemistry take place there. Human activities are directly exposed to the primarily emitted and the secondarily formed pollutants, most of which are harmful to health. A considerable fraction of the trace gases introduced into the troposphere belongs to the group of hydrocarbons, which are released into the air from natural and anthropogenic sources. In the course of their degradation cycles, which are initiated by OH-radicals and which involve the catalytic interconversion of the odd-nitrogen compounds NO and NO_2, secondary compounds are formed from which ozone is the most abundant. Tropospheric ozone has a negative impact on the health of living organisms.

Formaldehyde (CH_2O) is an important intermediate in the degradation of hydrocarbons. Although there are manifold reaction pathways of the organic molecules, virtually all hydrocarbons generate formaldehyde in the course of their oxidation, thereby making CH_2O an indicator of photooxidation. Formaldehyde, which is a reactive and toxic gas, reaches the troposphere in large quantities by hydrocarbon oxidation and therewith represents the most important carbonyl compound in atmospheric chemistry.

Formaldehyde constitutes a major source of hydro peroxy radicals (HO_2) by its photolysis, which is its primary loss mechanism during the day. The odd hydrogen radicals HO_2 and OH (together termed HO_x) are the most important atmospheric oxidants, driving the photochemical smog formation [e.g. *Finlayson-Pitts and Pitts*, 2000]. A chemical equilibrium between them is rapidly reached. The consideration of the formaldehyde chemistry is also crucial for understanding the global budgets of OH and CO. Formaldehyde photolysis is also a major source of molecular hydrogen (H_2) in the atmosphere.

Since formaldehyde occupies a key position in tropospheric chemistry, its measurement is essential for understanding chemical processes in the clean and polluted atmosphere. Therefore, the European Parliament adopted a directive (2002/3/EC), which obliges EU member states not only to monitor ozone itself but also its photochemically reactive precursors in the air, namely nitrogen oxides and, besides a selection of 30 hydrocarbons, also formaldehyde as the only oxygenated hydrocarbon [*EU*, 2002].

In order to satisfy the need of more formaldehyde measurements in ambient air, the European project FORMAT (FORMaldehyde As a Tracer of photooxidation in the troposphere) was initiated, starting in January 2002. The aims of the project are itemised in the following paragraphs, since they provided the main motivation for this thesis. Within the scope of the project, two measurement campaigns were performed in and around Milano (Northern Italy), considered as example for a severely polluted area: Because of the large amount of emissions in Milano, together with intense solar radiation and weak interchange of air masses, the Milano metropolitan area regularly suffers from photochemical smog pollution in summer. The participation in another field campaign, taking place in the heavily polluted metropolis Mexico City, extended the data set.

In the context of this thesis, active long path DOAS measurements were performed at urban and rural sites and analysed for formaldehyde CH_2O, ozone O_3, nitrogen dioxide NO_2, sulphur dioxide SO_2 and nitrous acid HONO. Differential Optical Absorption Spectroscopy (DOAS) is a well-established method for non-destructive measurement of trace gases [*Platt*, 1994] and allows the quantification of formaldehyde (amongst others) by its absorption in the UV-A spectral range. Additionally, the cooperation with the other groups participating in the FORMAT project makes a large pool of further data accessible for analysis.

The main emphasis of this thesis is on

- the measurement of formaldehyde by DOAS
- the identification of reasons for uncertainties in formaldehyde concentrations retrieved by DOAS and other methods
- the study of the spatial distribution and variability of formaldehyde in the lower troposphere

Formaldehyde can be measured by DOAS with high sensitivity. For the absolute calibration of the measurement, merely an accurate reference absorption cross-section is required. Eight formaldehyde UV cross-sections, available in high spectral resolution, are compared to determine the range of possible differences in the formaldehyde retrieval.

Today, formaldehyde can be measured by several methods basing upon different principles. In the past, often large deviations appeared between the various methods [e.g. *Cárdenas et al.*, 2000; *Grossmann et al.*, 2003]. The participation of several institutions with different measurement techniques in FORMAT required the thorough assessment of the agreement between the techniques. In order to use the data measured by different methods, complementing one another or comparing to each other in a credible way, the systematic uncertainties between the methods have to be known. On this account and in agreement with a primary objective of the FORMAT project, an intercomparison of four frequently used in-situ (that is point measurement) methods, probing *identical* air volumes, was conducted and the results are presented in detail in this work.

Based on the intercomparison, it is, in a next step, possible to combine the different measurement techniques, however, now probing *different* air volumes. Since the local formaldehyde distribution is highly inhomogeneous, the small-scale horizontal and/or vertical variability can be studied using different measurement setups of ground-based instruments, which probed different average levels above ground.

Another main aim of the FORMAT project was to obtain a better knowledge of the regional distribution and variability of formaldehyde in the Milano urban plume. Since most formaldehyde in the troposphere is of secondary origin, i.e. generated by oxidation of organic compounds, a statistical approach is employed to explain the variability of formaldehyde on the basis of the variation of OH production and VOC concentrations. The spatial CH_2O variability in the metropolitan area of Milano and in the Po Basin is investigated using airborne in-situ measurements of two field campaigns. In a similar manner, ground-based measurements from an urban and a rural site in the Milano area are used to study the temporal variation of formaldehyde.

In autumn, the variability of formaldehyde in the Po Basin is influenced by the primary CH_2O emission from biomass burning. Since the agricultural burning of harvested stubble fields is an important source of formaldehyde, the quantification of its emission was a goal addressed by FORMAT. Rice is the predominant grain cultivated in the Po Basin and the surroundings of Milano. Since for emissions from rice straw burning only a few laboratory measurements exist [*Christian et al.*, 2003; *Jenkins et al.*, 1996], but emission factors have not been quantified under real conditions in the field yet, this is realised in this work, using airborne and ground-based measurements in smoke plumes of agricultural fires in the Po Basin. The impact of the biomass fires on the radical budget and the regional influence on tropospheric chemistry are also estimated.

The following structure underlies this thesis. *Chapter 2* gives an overview of the chemical cycles relevant to photochemical smog formation. The present knowledge of formaldehyde chemistry is specified separately. After the chemistry part, important physical processes, influencing the trace gas variability are explained. *Chapter 3* describes the instruments employed to measure formaldehyde, with the main emphasis on Differential Optical Absorption Spectroscopy. Methods for the measurement of other species are outlined shortly. *Chapter 4* comprehends the description of the field campaigns, whereby measurement sites are characterised and time series of measured trace gas concentrations are presented. The significance of formaldehyde as a radical source is estimated for several sites and campaigns. *Chapter 5* addresses the comparison of measurement techniques. The results of the intercomparison experiment of in-situ formaldehyde measurements is shown in detail. Subsequently, results from a measurement setup probing different air volumes are compared. *Chapter 6* presents the analysis of spatial and temporal formaldehyde variability and the estimation of formaldehyde emissions from agricultural fires. The main conclusions are drawn in *Chapter 7*.

2 Chemistry and Physics of the Planetary Boundary Layer

Most trace gases in the atmosphere occur naturally, but since man increasingly pollutes the atmosphere, many compounds exceed their natural levels. Air pollutants are emitted into the lowest ≈ 1000 m of the troposphere, the planetary boundary layer (PBL), and react in a multitude of reaction cycles to form secondary compounds. The trace gas concentrations in the planetary boundary layer are not only influenced by chemical reactions but also by variations of the physical conditions, e.g. the structure of the boundary layer and the presence of solar insolation. This chapter describes the chemical processes that lead to the development of photosmog conditions. The formaldehyde chemistry is a central part to this. Since the emphasis of this thesis is on formaldehyde, its formation and destruction pathways are discussed in detail. The diurnal variation of trace gas concentrations close to the ground as a function of physical conditions is discussed at the end of this chapter.

2.1 Sources of Atmospheric Trace Gases

Air pollutants can either be released directly into the ambient air (primary pollutants) or they are formed by chemical transformations in the atmosphere (secondary pollutants). Sources of primary pollutants are outlined in this section. The primary trace compounds particularly involve compounds of anthropogenic origin which are specified in *Sec. 2.1.2*, but also natural sources like volcanoes and the biosphere (see *Sec. 2.1.3*) can contribute significantly to the pool of reactive compounds. An overview of important trace gas sources, including natural and anthropogenic sources is shown in *Fig. 2.1*. Under the influence of solar radiation, these gases are converted into a mixture of secondary compounds (like O_3, H_2O_2, PANs and others), known as photochemical smog (see *Sec. 2.2*). A further significant pollutant source in several regions and on the global scale is biomass burning. The great variety of smoke constituents and methods of their quantification are presented in *Sec. 2.1.4*. Most compounds are both of anthropogenic or natural origin. This also applies to several members of the group of volatile organic compounds, introduced in the following section.

2.1.1 Volatile Organic Compounds (VOCs)

The classification of organic compounds as used in this work is outlined in this section. Organic compounds form an extremely large class of chemicals, all of which are carbon compounds. Volatile organic compounds [*] (VOCs) are organic compounds that readily and fully evaporate and remain in the air as gases when exposed to the atmosphere at standard ambient

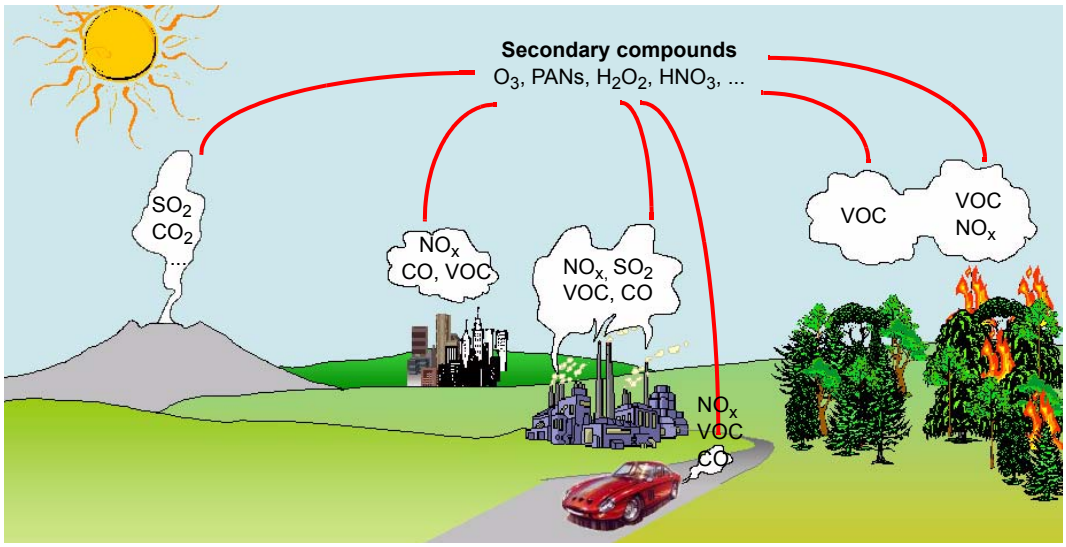

Figure 2.1: Trace gases emitted by anthropogenic and natural sources (see Sec. 2.1.2-2.1.4) react in the atmosphere under the influence of solar irradiation. The sources of most trace gases are located near the surface.

temperature and pressure. In addition to carbon and hydrogen, these compounds may contain oxygen, nitrogen and other elements, but specifically excluded are carbonic acid, metallic carbides and carbonate salts. Volatile organic compounds play an essential role in oxidant chemistry of the atmospheric boundary layer [*Chameides et al.*, 1992; *Houweling et al.*, 1998] and in the production of tropospheric ozone (see *Sec. 2.2.4*). Large numbers of groups of saturated, unsaturated and oxygenated derivatives are included within VOCs (see *Fig. 2.2*). One of the consequences of the high diversity of VOCs is the large variety of acronyms used, each defining a special class of VOCs (e.g. BVOC = biogenic VOC, OVOC = oxygenated VOC, AVOC = anthropogenic VOC). The term reactive organic gases (ROG) includes exclusively VOCs and hydrocarbons with high reactivity.

Hydrocarbons (HCs) are organic gases that contain only hydrogen and carbon. They are divided into alkanes (paraffins, C_nH_{2n+2}), alkenes (olefins, C_nH_{2n}), alkynes (C_nH_{2n-2}), aromatics (arenes) and the biochemical class of terpenoids (including isoprene and monoterpenes [*Kesselmeier and Staudt*, 1999]). Methane (CH_4) is often excluded from the sum of hydrocarbons, due to the low rate coefficient with OH. This leads to the definition of the non-methane hydrocarbons (NMHCs). Analogously, the non-isoprene hydrocarbons (NIHCs) are defined, excluding the very reactive biogenic hydrocarbon isoprene. Volatile organic compounds are NMHCs plus oxygenated hydrocarbons. Oxygenated hydrocarbons are hydrocarbons including oxygenated functional groups, such as carbonyls (aldehydes and ketones), alcohols, organic acids and organic nitrates. For an overview of the systematics of organic compounds refer to *Fig. 2.2*.

2.1.2 Anthropogenic Pollutants Sources

Anthropogenic pollutants include all compounds that are released into the atmosphere by human activities. The sources are clearly traffic and industry, but also man-made biomass burning (cf. *Sec. 2.1.4*) can be included. Several anthropogenic pollutants show a traffic-related pattern with a maximum during the day and peaks during morning and afternoon rush hour. Since

*. VOC definition: Chemical compound based on carbon chains or rings (and also containing hydrogen) with a vapour pressure > 2 mm of mercury (2.7 hPa) at 25°C, excluding methane [*NPI*, 2003].

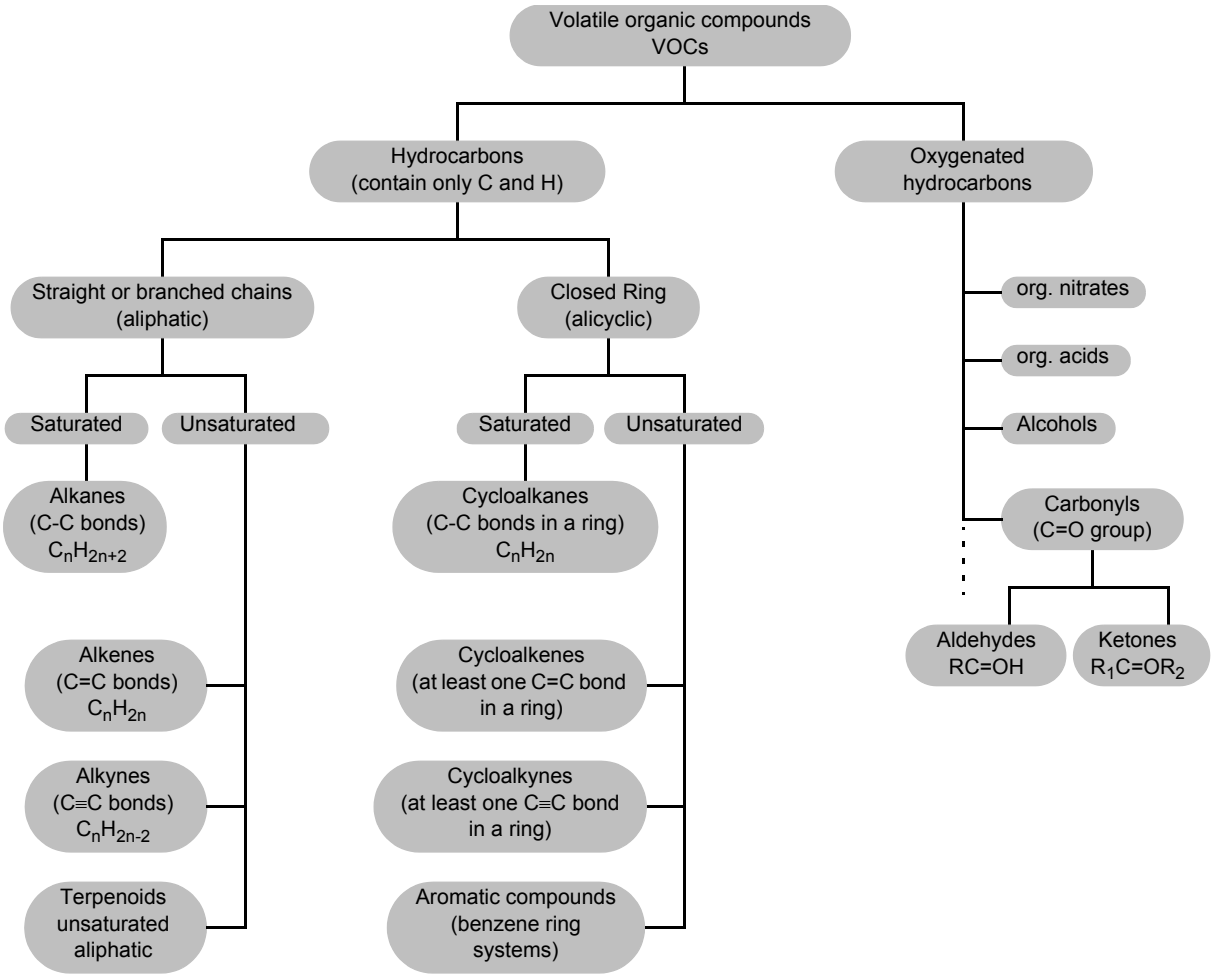

Figure 2.2: Terminology of VOCs as used in this thesis.

mobile and stationary sources account for the largest fractions, anthropogenic pollutants are important all over the year.

Transportation is an important source for a large number of compounds, especially in urban areas. Ambient nitrogen oxides (NO_x = NO + NO_2) mainly originate from motor vehicle emissions. The exhaust of combustion processes typically consists of 90% NO and 10% NO_2. The production of this *thermal* NO_x is determined by the Zeldovich mechanism which proceeds at high combustion temperatures, dissociating N_2 and O_2 molecules. The combustion of fossil fuels also releases carbon monoxide (CO) and a vast number of organic compounds (including aromatic compounds, alkanes, alkenes). Over 300 different hydrocarbons have been identified in vehicle exhaust-polluted air samples. The exact composition of the exhaust depends on the fuel type and the engine. The use of oxygenated fuels, i.e. methanol, ethanol and methyl tertiary-butyl ether (MTBE) blended fuels, was accomplished in an effort to reduce CO emissions. However, motor vehicle emissions of formaldehyde have been shown to increase with the use of oxygenated fuels [*Anderson et al.*, 1996]. The exhaust from liquefied petroleum gas (LPG) engines is rich in C_2-C_4 compounds most likely deriving from non-combusted fuel components. Two-stroke engines emit large quantities of C_2-C_7 compounds and the exhaust contains high levels of the most toxic of the VOCs, i.e. 1,3-butadiene. The composition of exhaust from four-stroke gasoline engines resembles exhaust of two-stroke engines but with a higher proportion of non-combusted aromatics. The exhaust from EURO3 diesel engines contains mainly very light hydrocarbons [*Latella et al.*, 2005]. Volatile organic compounds are also emitted from parked

vehicles, by evaporation (e.g. isopentane). Moreover, road traffic, in particular the combustion in Diesel engines, is a major source of particles in urban areas.

Industrial processes also emit a multitude of pollutants, including NO_x and volatile organic compounds. Cement works and power plants emit large amounts of NO_x. In petrochemical production and distribution (e.g. oil refineries, service stations, leaks) and natural gas processing VOCs are released. Further evaporative VOC emissions (aromatics, higher alkanes) result from solvent use, e.g. in paints. Organic solvents and their vapours also contain considerable amounts of oxygenated hydrocarbons. Gasoline evaporation is an important anthropogenic VOC source. Over 850 different hydrocarbons (alkanes, alkenes, aromatics) have been detected in the vapour over gasoline. Aromatics originate from the use of solvents and evaporative losses of fuel [*Rappenglück and Fabian*, 1999].

2.1.3 Biogenic Trace Gas Sources

The biosphere emits a large number of unsaturated organic compounds. A seasonal variability of BVOC emissions results from plant growth and phenological events. A great variability exists in the emission pattern of the diverse plant species and vegetation types and the release of VOCs by a given plant species exhibits important temporal and spatial variations. In contrast to anthropogenic compounds, biogenic VOC species cannot be reduced through emission controls.

The biogenic emissions can be an important contribution to the local and regional VOC composition. On a global scale, emissions of volatile hydrocarbons to the atmosphere by vegetation far exceed those from anthropogenic sources (see Table 2.1 or *Guenther et al.* [1995]). Plants mainly emit isoprene and monoterpenes, but also alcohols, carbonyls and alkenes [*Kesselmeier and Staudt*, 1999]. The group of biogenic carbonyls includes formaldehyde, acetaldehyde, propanal, acetone and many more as compiled by *Kesselmeier and Staudt* [1999]. Monoterpenes and isoprene are the best investigated species. Emission rates for isoprene, monoterpenes and other HCs from many different trees and shrubs are given in a detailed overview paper by *Kesselmeier and Staudt* [1999].

Table 2.1: Global emission estimates for CO, NO_x, CH_4 and VOC (in Tg yr^{-1}) from both anthropogenic and natural sources [Finlayson-Pitts and Pitts, 2000].

Source	CO	NO_x	CH_4	VOC
Anthropogenic sources	383	72	132	98
Biomass burning	730	18	54	51
Biogenic sources (cont.)	165	22	310	500
Oceans	165	0.01	10	30-300
Total	1440	122	506	750

The dominant volatile organic compound from vegetation is isoprene (2-methyl-1,3-butadiene, CH_2=CH–C(CH_3)=CH_2). Many plants synthesise isoprene enzymatically and emit large amounts. Broadleaf forests are more likely to be large sources of isoprene than are grasslands, agricultural systems, or coniferous forests [*Kesselmeier and Staudt*, 1999]. However, even among broadleaf forest stands, flux estimates vary by over an order of magnitude [*Harley et al.*, 1999]. Isoprene emission rates vary among species from near zero to over 50 nmol m^{-2} s^{-1} at 30°C. Isoprene has a large regional variability in emission [*Guenther et al.*, 1995].

The primary short-term controls over isoprene synthesis and emission are light and temperature. The emission increases exponentially between 15°C and 35°C. Above 35°C, the rate of increase slows and an optimum is reached, generally between 40 and 42°C [*Harley et al.*, 1999]. Isoprene emission further depends largely on vegetation type, vegetation density (leaf area

index, LAI) and leaf age [*Guenther et al.*, 1995]. Isoprene emissions from a given location vary from day to day in response to changes in temperature and to a lesser extent solar radiation [*Guenther et al.*, 1995]. Since isoprene emission is triggered by light, the emission rate is zero during the nighttime.

Monoterpenes are produced by a wide variety of plants, particularly conifers but also by some deciduous trees. The monoterpene flux from vegetation is generally only dependent on the temperature [*Guenther et al.*, 1995] and therefore does not decrease to zero during the night. For some plant species, however, the monoterpene emission is temperature and light triggered, similar to isoprene (see *Lenz et al.* [2001]). Some oxygenated compounds follow a similar emission regime and show a clearly light-triggered emission [*Kesselmeier and Staudt*, 1999]. *Klemp et al.* [1997] present convincing evidence of biogenic alkene emissions (ethene, propene, 1-butene) from measurements in the southern part of the Black Forest in Germany. As opposed to isoprene, these emissions continued throughout night-time periods.

Plants directly emit a large spectrum of aldehydes [*Kesselmeier and Staudt*, 1999]. Measurements by *Nondek et al.* [1992] indicate the nighttime emission of formaldehyde and acetaldehyde from forest vegetation (lodgepole pine branches), but they do not exclude artifacts due to adsorption and desorption processes within the enclosure. A study by *Kesselmeier et al.* [1997] shows evidence of a significant direct emission of formaldehyde as well as acetaldehyde from two Mediterranean tree species, *Quercus ilex* (holm oak) and *Pinus pinea* (Italian stone pine). *Martin et al.* [1991] reported diurnal fluctuations of formaldehyde concentrations above a deciduous forest with maximum values in the range of 10 ppbv around noon and assumed the photochemical decay of isoprene to be responsible for the high values.

Airborne VOC measurements in the metropolitan area of Milano revealed that isoprene contributes less than 10% to the total VOC reactivity [*Dommen et al.*, 2002]. Measurements in Northern Italy over the entire year 2000 showed that the isoprene photooxidation contributed in summer 30-60% to the ambient formaldehyde concentrations and 50-75% to the local O_3 formation [*Duane et al.*, 2002].

2.1.4 Gases Emitted from Biomass Burning

Emissions from biomass burning include a wide range of gases and particles in quantities that in some cases can be significant not only locally and regionally but also on a global scale (see Table 2.1). Biomass burning comprises the combustion of savanna, agricultural wastes, forest and wood. Global annual carbon emissions from these sources are listed in Table 2.2 and compared with carbon emissions from fossil fuel burning. What is formed during the combustion process depends on the chemical composition of the plants, hence on the plant species, the temperature of the flames and the amount of oxygen available which determine whether it is a flaming fire or a smouldering fire. These factors are described in the current section.

The analyses presented in *Sec. 6.4* focus on agricultural fires which were observed during the FORMAT II field campaign. Agricultural burning is the open burning of waste materials produced from growing and harvesting crops. It is a common procedure in Italy and many other countries that farmers burn down the fields purposely after harvesting grains such as wheat, rice or corn to remove crop residues left in the field and to control diseases. Most rice straw burning takes place in autumn or early spring, whereas corn and wheat residues are usually burned in summer.

The compounds produced by biomass burning include CO, CO_2 and NO_x and a large variety of light hydrocarbons, oxygenated hydrocarbons, polycyclic aromatic hydrocarbons (PAH), organic acids, NH_3, HCN, CH_3CN, H_2, some sulphur compounds, such as SO_2 and COS, and particles [*Finlayson-Pitts and Pitts*, 2000]. Secondary compounds like O_3, HNO_3, PAN and

Table 2.2: Types of biomass burned. Global estimates of annual amounts of biomass burning and of the resulting release of carbon into the atmosphere [Andreae, 1991].

Source of burning	Biomass burned [Tg dry matter yr^{-1}]	Carbon released [Tg carbon yr^{-1}]
Savannas	3690	1660
Agricultural waste	2020	910
Tropical forests	1260	570
Fuel wood	1430	640
Temperate and boreal forests	280	130
Charcoal	21	30
World total	**8700**	**3940**
Global carbon emissions from fossil fuel burning		6518

H_2O_2 are subsequently produced by reaction cycles shown in *Sec. 2.2.4*. The emission of SO_2 depends on the sulphur content of the plant species burned. Oxygenated organic compounds (OVOCs, e.g. formaldehyde) make up three of the top five organic compounds emitted [*Sinha et al.*, 2003]. The OVOCs originate from the thermal decomposition of cellulose [*Lemieux et al.*, 2004]. This is likely due to the high levels of elemental oxygen bound within the cellulose structures found in biomass (see below). Besides acetic acid and methanol, formaldehyde is one of the three most abundant OVOCs emitted by fires [*Yokelson et al.*, 2003].

Fuel Composition. Since each type of vegetation has a characteristic composition, the nature of the vegetative fuel plays an important role in determining the emissions from biomass fires [*Sinha et al.*, 2003]. Plant biomass consists of cellulose and hemicelluloses, which make up typically 50-70% of the dry matter. The carbon content of biogenic fuels varies only over a fairly limited range. *Yokelson et al.* [2003] indicate average carbon contents of African savanna fuels of 47.9 to 53.7%. The typical elemental composition of dry organic matter is further apportioned into oxygen ~ 42%, hydrogen ~ 6%, others (e.g. N, S, P) ~ 7%, where the sulphur content varies between 0.1-0.5%, depending on the plant type. *Jenkins et al.* [1996] report a sulphur content for rice straw of 894 mg kg^{-1} dry weight, which is comparable to the sulphur contained in barley straw and corn stover, but only half of the value for wheat straw. A similar amount of 1014 mg kg^{-1} is given by *Li et al.* [2005] for rice straw. Plants contain up to 60% water although their water content is generally lower than this before the fire season as the vegetation loses a lot of water during drought times. About 95% of the carbon exposed to fire is released into the atmosphere in the gaseous form [*Crutzen and Andreae*, 1990].

The emission factors of organic air toxics, containing carbon, oxygen and hydrogen, are predominantly a function of the combustion conditions during the burn [*Lemieux et al.*, 2004]. The emission of substances containing minor elements, such as nitrogen, sulphur and halogens, is determined both by the concentrations of those elements in the fuel (i.e. the fuel type) and by the combustion conditions [*Andreae and Merlet*, 2001].

Calculation of Emission Factors. Emission information of any combustion process is represented in two basic forms – emission ratios or emission factors. Emission ratios relate the emission of a particular species to that of a reference species, such as CO_2 or CO. Emission factors relate the emission of a particular species of interest to the amount of fuel burned. To derive emission ratios, the enhancement of trace gas concentrations due to the fire has to be known. *Excess mixing ratios* $\Delta[X]$ are obtained from eq. 2.1 by subtracting the ambient background

concentration $[X]_{background}$ of the compound X outside the plume from the value measured in the smoke plume $[X]_{smoke}$.

$$\Delta[X] = [X]_{smoke} - [X]_{background} \quad \text{(eq. 2.1)}$$

An emission ratio (ER) is obtained by dividing the excess mixing ratio of a trace species X measured in a fire plume by the excess mixing ratio of a simultaneously measured reference tracer. The most commonly used reference species are CO_2 and CO, but other compounds have also been used [*Andreae and Merlet*, 2001]. The *molar emission ratio* (ER) of X with respect to CO is defined in eq. 2.2.

$$ER_{X/CO} = \frac{\Delta[X]}{\Delta[CO]} \quad \text{(eq. 2.2)}$$

Alternatively, the slope of the regression line in a plot of the excess mixing ratio of the species X versus the excess mixing ratio of the reference tracer gives the molar emission ratio of X with respect to the reference tracer. The regression line is forced through zero [e.g. *Yokelson et al.*, 2003]. The term 'molar enhancement ratio' is preferred by some authors to the commonly used 'molar emission ratio' [e.g. *Jost et al.*, 2003], because it can be also applied to compounds that are not or not only emitted, but produced secondarily, like O_3. ERs have the advantage that they only require the simultaneous measurement of the species of interest and the reference species in and outside the smoke plume and no information is required about the fuel composition, burning rates or quantities combusted.

The *emission factor* (EF) is defined as the mass of a compound released per unit mass of dry fuel consumed, expressed in units of g kg^{-1}. The calculation of this parameter requires knowledge of the carbon content of the biomass burned and the carbon budget of the fire. Both parameters are difficult to establish in the field as opposed to laboratory experiments where they are readily determined. The total carbon released is usually estimated by adding up the measured concentrations of CO_2, CO, hydrocarbons and particulate carbon, if this information is available. The emission factor of a species X can also be calculated from ERs, using eq. 2.3 [*Andreae and Merlet*, 2001], in case that the emission factor of the reference species Y is known (*M*: molecular weight).

$$EF_X = EF_Y \cdot \frac{M_X}{M_Y} \cdot ER_{X/Y} \quad \text{(eq. 2.3)}$$

This method is used in *Sec. 6.4.3* to derive the emission factor of CH_2O from agricultural burning in the Po Basin. EFs are very useful because comparing individual EFs to each other allows sources to be compared on a purely mass basis.

Combustion Phases. Fires go through different phases of burning, with emissions of different compounds tending to be associated with each phase. During the stages of burning, different chemical processes occur that result in different emissions. Most commonly, two phases of combustion, a flaming stage followed by a smouldering stage, have been considered. After ignition, oxygen levels are sufficiently high to allow a period of open fire to occur. The hot (> 850°C), flaming stage of the fire is associated with emissions of a mixture of simple molecules, particularly CO_2, NO, N_2O, SO_2, H_2O and black/elemental carbon [*Andreae and Merlet*, 2001]. As oxygen levels fall and most volatiles have been released from the near-surface region of the fuel, the flames cease and smouldering (< 850°C) begins. Due to a lack of oxygen, incomplete oxidation occurs and CO and many partially oxygenated organic compounds, including formaldehyde, acetaldehyde, methanol, acetone and methane, are released (not efficient combustion) [*Andreae and Merlet*, 2001]. It is this mode of combustion that is responsible for the vast diversity of emission products. The amount of substances released from a given fire

(EFs) and their relative proportions are thus determined to a large extent by the ratio of flaming to smouldering combustion. Both processes occur simultaneously in a given patch.

The fire types tend to have characteristic ratios of flaming and smouldering combustion, which to a large extent determine their pattern of emission factors. In savanna fires, for example, flaming combustion dominates [*Andreae and Merlet*, 2001] and the emission factors for reduced species are fairly low. Even in a given fire type, however, the proportion of flaming combustion can vary considerably as a function of internal parameters, particularly fuel moisture and structure, and external parameters, such as the movement of the flame front relative to wind direction or terrain slope. The presence of water in the burning material reduces the flame temperature, which induces changes in the thermodynamical conditions of combustion producing higher concentrations of CO and CH_4 [*Andreae and Merlet*, 2001]. Thus, the emissions might vary as a function of season. As a result, the emission pattern from a particular fire can be quite different from the average values presented in Table 6.5.

The relative amounts of flaming and smouldering combustion can be derived from the *modified combustion efficiency* (MCE) given by eq. 2.4 [e.g. *Yokelson et al.*, 2003]. Only the excess mixing ratios of CO and CO_2 are required in the calculation.

$$MCE = \frac{\Delta[CO_2]}{\Delta[CO_2] + \Delta[CO]} \qquad \text{(eq. 2.4)}$$

In laboratory studies, *Yokelson et al.* [1996] found that pure flaming combustion has an MCE near 0.99 and pure smouldering combustion an MCE of ~ 0.8. Therefore, an MCE < 0.9 suggests > 50% smouldering combustion and an MCE > 0.9 suggests > 50% flaming combustion.

Smoke Plume Chemistry. There is a rich and varied chemistry associated with the emissions from biomass burning, which can have effects on local, regional and global scales. In addition to the compounds that are directly emitted, there are a number of compounds formed in the plume. As smoke ages, species within it are removed and others are generated by chemical and physical processes. In particular, the emissions from biomass burning have been observed to form elevated concentrations of O_3 [e.g. *Jost et al.*, 2003]. Smoke contains volatile organic compounds and oxides of nitrogen, amongst others. Together with enhanced oxygenated VOCs, especially formaldehyde, which produces HO_x radicals by photolysis (see *Sec. 2.2.1*), these compounds have a large effect on chemical reactions in a smoke plume. They react photochemically to generate ozone, hydrogen peroxide, etc., in reaction cycles described in *Sec. 2.2.4*. In young biomass burning plumes, O_3 is produced within a few hours after the emission of its precursors [*Jost et al.*, 2003]. Therefore, elevated O_3 concentrations are found downwind of fires, whereas in the immediate vicinity of the fire, a dip in O_3 concentration has been observed.

Because of its long tropospheric lifetime (several weeks), CO can be used as a tracer for combustion of biomass and fossil fuel. Species whose correlation with CO increases as the plume ages and with enhancement ratios, using CO as the reference, that also increase with plume age, are likely generated by chemical reactions in the plume. Since this is the case for ozone, the $\Delta[O_3]/\Delta[CO]$ ratio has often been used as an indicator of the degree of photochemical aging of smoke samples.

2.2 Photochemical Smog

For chemical reactions to occur, the activation energy has to be provided. Besides thermally or collisionally activated reactions, many reactions in the atmosphere proceed as *photochemical reactions*, which are initiated by interaction of molecules with electromagnetic radiation (absorption of photons). In these reactions, reactive radical compounds (see *Sec. 2.2.1*) may be produced during the day, which are key components of atmospheric chemistry.

Today in many major urban areas around the world, the anthropogenic enhancement of trace gas concentrations leads to an air pollution characterised by the formation of ozone and other oxidants far above their natural levels. Tropospheric ozone attracts attention because it is toxic to humans and plants and acts as a greenhouse gas [*IPCC*, 2001]. The WHO thresholds are frequently exceeded. In this section, the processes generating tropospheric ozone (*Sec. 2.2.2*) under the influence of solar irradiation are described. They are initiated by the reaction of radicals (see *Sec. 2.2.1*) with volatile organic compounds (see *Sec. 2.1.1*). In the presence of nitrogen oxides, the VOCs undergo a complex sequence of further photochemical reactions described in *Sec. 2.2.3*-*2.2.4*. The multitude of secondary compounds formed, of which ozone is the most abundant, is termed *photochemical smog* †.

2.2.1 Sources of HO_x Radicals

Radicals are chemical species with an unpaired electron in the valence shell, which makes them highly reactive ‡. The term HO_x combines the odd hydrogen radicals, i.e. the hydroxyl radical, OH, and the hydro peroxy radical, HO_2. Since most gaseous trace compounds in the tropospheric air are oxidised by the hydroxyl radical and thereby removed from the atmosphere, OH drives the daytime chemistry of both polluted and clean atmospheres. The mechanisms producing HO_x radicals are therefore amongst the most important processes influencing the oxidation capacity and ozone formation (see *Sec. 2.2.4*) in the atmosphere. When reacting with atmospheric trace gases, OH is regenerated in catalytic cycles, leading to sustained concentrations on the order of 10^6 molec cm^{-3} during daylight hours. Due to the short lifetime, resulting from its high chemical reactivity, the OH concentration is highly variable in space and time. Its sources and, closely associated with it, the sources of HO_2 are described in this section.

Photolysis of trace gases is the primary source of radicals in the atmosphere. The first-order rate coefficients, J, for atmospheric photolysis processes are referred to as *photolysis frequencies*. The photolysis frequency J_A of the molecule A is calculated by eq. 2.5 from the measured photon flux density $Q(\lambda)$, or solar *actinic flux* §, given the absorption cross-section $\sigma_A(\lambda)$ of the molecule and the spectral photolytic quantum yield $\Phi_{Ai}(\lambda)$ for the photolysis process of interest, all of which are wavelength dependent:

$$J_{Ai} = \int Q(\lambda) \cdot \sigma_A(\lambda, T) \cdot \Phi_{Ai}(\lambda, T) d\lambda \qquad \text{(eq. 2.5)}$$

For some molecules, for example formaldehyde, several photolysis reaction channels exist. The product yield for the respective photolytic channel i is described by the dimensionless *quantum yield* $\Phi_{Ai}(\lambda)$, which is the ratio between the number of excited A molecules proceeding by channel i to the total number of photons of wavelength λ absorbed. The absorption cross-sections and quantum yields of many compounds are reported in the literature. In this work, the spectra recommended by IUPAC [*Atkinson et al.*, 2002] were used to calculate the photolysis frequencies. Due to the absorption of light by trace gases close to the ground, the photolysis frequencies increase with altitude.

A major source of OH in both clean and polluted air is the photodissociation of ozone (R 2.1) by actinic UV radiation at wavelengths below 310 nm to produce an electronically excited oxygen atom, $O(^1D)$. The photolysis is followed by a very rapid reaction of the $O(^1D)$ atom with water vapour to give two hydroxyl radicals (R 2.2). The photodissociation of ozone has two reaction channels. For wavelengths between 310 and 850 nm a ground-state oxygen atom $O(^3P)$

†. Smog: borrowed from English condensation of the words *smoke* and *fog*, originally describing London type air pollution. Today also used for Los Angeles type photochemical pollution, although neither containing smoke nor fog.

‡. Radicals are labelled with a dot placed to the right of the molecular formula (Lewis dot notation).

§. Actinic: radiation, capable of provoking photochemical reactions.

is generated and no radicals are formed. Only at wavelengths below 310 nm, the excited oxygen atom $O(^1D)$ is generated with high yield.

$$O_3 + h\nu \rightarrow O_2 + O(^1D), (\lambda < 310 \text{ nm}), J_{O(1D)} \approx 3 \times 10^{-5} \text{ s}^{-1} \quad \text{(R 2.1)}$$

$$O(^1D) + H_2O \rightarrow 2OH^{\bullet} \quad \text{(R 2.2)}$$

$$O(^1D) + M \rightarrow O(^3P) + M \text{ (quenching)} \quad \text{(R 2.3)}$$

Reaction R 2.2 is in competition with deactivation (quenching) reactions with N_2 or O_2 molecules (R 2.3). Nitrogen and oxygen molecules have smaller rate coefficients with $O(^1D)$ than the reaction with H_2O (see Table 2.5), but, since they are the most abundant molecules in the troposphere, most $O(^1D)$ atoms formed undergo relaxation to ground-state $O(^3P)$ atoms (R 2.3). Depending on the actual water vapour content, which generally varies between 0.1 and 3%, a small fraction of $O(^1D)$ atoms, reacts with water vapour to form two hydroxyl radicals. During the measurements in Italy (see *Chapter 4*), this fraction varied between 10 and 13%. The OH production rate from ozone photolysis can be calculated as

$$P(OH) = \frac{2 \cdot J_{O(1D)} \cdot [O_3] \cdot k_{H2O} \cdot [H_2O]}{k_{O2} \cdot [O_2] + k_{N2} \cdot [N_2] + k_{H2O} \cdot [H_2O]}, \quad \text{(eq. 2.6)}$$

where k_{H2O}, k_{O2}, k_{N2} are the rate coefficients for reactions R 2.2 and R 2.3 and $J_{O(1D)}$ is the photolysis frequency of ozone to give $O(^1D)$ atoms.

HO_x radicals are also generated by the photolysis of formaldehyde and higher carbonyls. Formaldehyde is especially important in this respect because its absorption between ~ 235 and 353 nm (see *Sec. 3.1.1.8.1*) extends to longer wavelengths compared to higher aldehydes and ketones. Since the solar intensity rapidly increases with wavelength here and since CH_2O is present everywhere in the troposphere by oxidation of organic trace gases (see *Sec. 2.2.3*), the production rate of HO_2 radicals from CH_2O is much higher than for the larger carbonyls. Between 25 and 37% of formaldehyde photolysis reactions yield radicals (radical channel R 2.28). The hydrogen and formyl (HCO) radicals form hydro peroxy radicals by reaction with O_2 (R 2.29-2.30).

$$P(HO_2) = 2 \cdot J_{CH2Or} \cdot [CH_2O] \quad \text{(eq. 2.7)}$$

The HO_2 production rate from CH_2O photolysis is derived from eq. 2.7. With the tropospheric ozone photolysis, the reactions R 2.29 and R 2.30 make up the key source for HO_x radicals. Because of its significance for this thesis, the chemistry of formaldehyde is described in more detail in *Sec. 2.3.2*.

In polluted areas, OH can also be formed from the photodissociation of nitrous acid, HONO (R 2.4). The lifetime of HONO against photolysis is short (τ = 600 s, $J_{HONO} \approx 1.5 \times 10^{-3}$ s^{-1}).

$$HONO + h\nu \rightarrow NO + OH^{\bullet}, (\lambda < 390 \text{ nm}) \quad \text{(R 2.4)}$$

$$P(OH) = J_{HONO} \cdot [HONO] \quad \text{(eq. 2.8)}$$

The photolysis of hydrogen peroxide H_2O_2 at wavelengths below 290 nm is a small OH source ($J_{H2O2} \approx 7 \times 10^{-6}$ s^{-1}) at typical mixing ratios of $H_2O_2 \approx$ 1-4 ppbv [*Finlayson-Pitts and Pitts*, 2000].

$$H_2O_2 + h\nu \rightarrow 2OH^{\bullet}, (\lambda < 290 \text{ nm}) \quad \text{(R 2.5)}$$

Additionally, OH radicals are produced by the reaction of O_3 and NO_3 with a series of alkenes, dienes and monoterpenes (eq. 2.9). OH formation yields Y_{OH} for some compounds are given in Table 2.3.

$$P(OH) = k_{O3} \cdot [VOC] \cdot [O_3] \cdot Y_{OH} \quad \text{(eq. 2.9)}$$

Table 2.3: Rate constants [Atkinson, 1997] and OH formation yields [Paulson et al., 1999] from the ozonolysis of selected alkenes and dienes.

Compound	k_{O3} [cm^3 $molec^{-1}$ s^{-1}]	Y_{OH}
ethene	1.59×10^{-18}	0.18
propene	1.01×10^{-17}	0.35
1-butene	9.64×10^{-18}	0.29
i-butene	1.13×10^{-17}	0.72
1,3-butadiene	6.30×10^{-18}	0.13
isoprene	1.28×10^{-17}	0.25

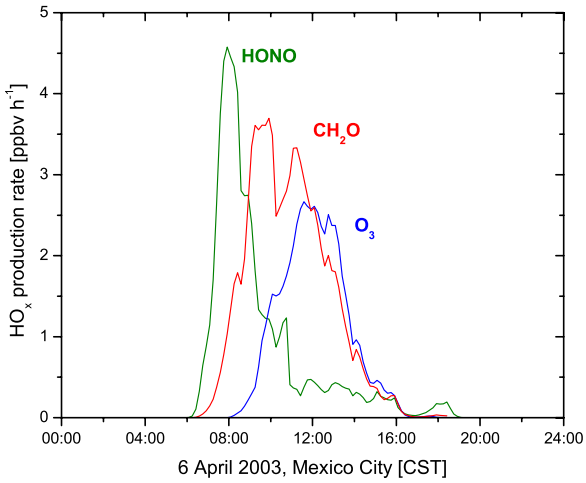

Figure 2.3: Example for the diurnal cycle of primary HO_x formation.

This is the predominant OH radical source at night, in the absence of actinic radiation.

The relative importance of these sources of OH and HO_2 radicals depends on the composition of the air mass and hence on location and time of day. *Alicke* [2000] studied the contributions of the major HO_x sources in differently strong polluted areas. The generation rates of odd hydrogen radicals in a polluted urban air mass as a function of time of day are dominated by the three most important free radical sources, i.e. HONO, CH_2O and O_3 photolysis. After sunrise, OH radicals are produced at high rates from photolysis of HONO. In mid-morning, HONO photolysis is outranged by CH_2O and by O_3 later in the day when the ozone concentration has built up significantly. An example for this sequence, derived for Mexico City conditions, is shown in *Fig. 2.3*. After noon, formaldehyde and ozone photolysis contribute at roughly equal rates to HO_x formation. There are more sources of HO_x but their contribution is on the order of a few percent. Airborne measurements over the Po Basin revealed that ozone and formaldehyde contributed almost 80% of the primary HO_x formation in the early afternoon (*Fig. 2.4*). For HONO, which was not measured on the aeroplane, a concentration of 50 pptv was assumed which is an upper limit for locations not close to the ground (see also *Dommen et al.* [2002]). This gives a maximum contribution of 12% to HO_x production by HONO photolysis. The photolysis of hydrogen peroxide, acetaldehyde and other compounds altogether account for another almost 10% of the radical formation.

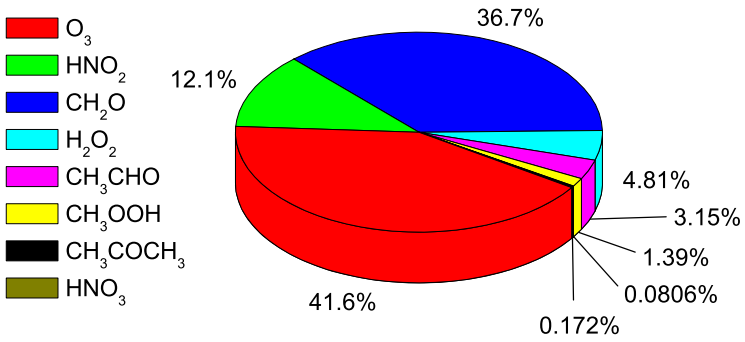

Figure 2.4: Primary HO_x radical sources in the PBL (~ 500 m a.g.l.) over the metropolitan area of Milano during the FORMAT II campaign. The fractions of photolysis and subsequent reactions were derived from airborne (MetAir Dimona) afternoon (14 h) data with the steady state model described in Sec. 2.2.6.

Once created, HO_x is partitioned within seconds into OH and HO_2 by a few fast reactions (see e.g. *Sec. 2.2.4*). The relative reaction rates of OH with CO, VOCs and O_3 to form secondary HO_2 and of HO_2 with NO and O_3 to produce secondary OH determine the partitioning of HO_x. Throughout the PBL, the production of OH and HO_2 through these interconversion reactions is much faster than the OH and HO_2 production from other sources. A steady state relative to the production and destruction of HO_x is reached rapidly. The OH and HO_2 concentrations maintain a balance with each other, which depends on the concentrations of their major sink species. The total HO_x concentration adjusts to the changing environmental conditions, such as solar radiation. Typical OH concentrations in summer are in the range $2\text{-}10 \times 10^6$ molec cm^{-3} with a maximum at local noon when photolysis peaks. Two methods for the estimation of daytime OH concentrations for field measurements are shown in *Sec. 2.2.6*. At night, OH concentrations are up to two orders of magnitude smaller than during the day [e.g. *Plass-Dülmer et al.*, 1998].

During the night, the production rate of OH becomes very small and another radical, the nitrate radical (NO_3) may become important. It is produced via the reaction R 2.6.

$$NO_2 + O_3 \rightarrow NO_3 + O_2\,,\ k = 3.5 \times 10^{-17}\ \text{cm}^3\ \text{molec}^{-1}\ \text{s}^{-1} \qquad \text{(R 2.6)}$$

During daytime, NO_3 rapidly photolyses at wavelengths below 630 nm via R 2.7, leading to a lifetime of about 5 seconds and sub-pptv mixing ratios.

$$NO_3 + h\nu \rightarrow NO_2 + O(^3P)\,,\ \lambda < 630\ \text{nm} \qquad \text{(R 2.7)}$$

At night, the absence of this strong sink allows the slow reaction of NO_2 with O_3 (R 2.6) to produce NO_3 in amounts (see below) large enough for it to act as a significant oxidant. A steady state between NO_3, NO_2 and dinitrogen pentoxide (N_2O_5) is usually reached within circa 1 minute [*Seinfeld and Pandis*, 1998] and limits the nighttime accumulation of NO_3:

$$NO_3 + NO_2 + M \leftrightarrow N_2O_5 + M \qquad \text{(R 2.8)}$$

The gas phase reactions with NO (R 2.9) and VOCs (especially alkenes, see *Sec. 2.2.4*), heterogeneous reactions and deposition are the main nighttime sinks for the nitrate radical. Also the heterogeneous loss of N_2O_5 represents a sink for NO_3.

$$NO_3 + NO \rightarrow 2NO_2\,,\ k = 2.6 \times 10^{-11}\ \text{cm}^3\ \text{molec}^{-1}\ \text{s}^{-1} \qquad \text{(R 2.9)}$$

$$NO_3 + VOC \rightarrow products\,,\ \text{see } \textit{Sec. 2.2.3} \qquad \text{(R 2.10)}$$

The NO_3 mixing ratio in the troposphere at night can vary from very small, low-pptv concentrations to several hundred pptv, depending on the particular air mass [*Finlayson-Pitts and Pitts*, 2000]. The lifetime of NO_3 at night is highly variable, but typically on the order of several minutes [*Wayne et al.*, 1991]. Due to the rapid reaction with NO (R 2.9), significant NO_3 concentrations are not found close to NO emission sources. However, in the absence of fresh emissions, NO is generally absent at night because of its reaction with O_3 (R 2.13, see *Sec. 2.2.2*).

2.2.2 Basic Photochemical Cycle of NO_2, NO and O_3

Ozone, O_3, is formed in the atmosphere exclusively via the reaction of molecular oxygen with an oxygen atom

$$O + O_2 + M \rightarrow O_3 + M\,, \qquad \text{(R 2.11)}$$

where M represents a molecule, usually N_2 or O_2, that takes up the excess vibrational energy. In the stratosphere, the oxygen atom is produced by photodissociation of O_2, a process which only occurs at wavelengths below 242 nm. However, due to the absorption by stratospheric ozone, light with wavelengths shorter than 290 nm does not reach the troposphere. The sole significant source for atomic oxygen to produce ozone in the troposphere is the photodissociation of nitrogen dioxide, NO_2, (R 2.12) at wavelengths below 410 nm.

$$NO_2 + h\nu \rightarrow NO + O(^3P)\,,\ (\lambda < 410\ \text{nm}),\ J_{NO2} \approx 7 \times 10^{-3}\ \text{s}^{-1} \qquad \text{(R 2.12)}$$

The oxygen atom is so reactive that it reacts further by R 2.11 virtually as fast as it is formed by R 2.12. Thus, the rate of ozone production is determined by the NO_2 concentration and by J_{NO2}, the photolysis frequency of NO_2. Nitrogen monoxide, NO, reacts rapidly with O_3 (R 2.13), whereby NO_2 is regenerated,

$$NO + O_3 \rightarrow NO_2 + O_2\,,\ (k, \text{see Table 2.5}) \qquad \text{(R 2.13)}$$

making the interconversion of NO and NO_2 very rapid. Because of reaction R 2.13, high concentrations of O_3 and NO cannot co-exist. As a consequence, in the absence of other processes, a photochemical steady state between ozone and NO_x is achieved, where no net ozone production takes place. This steady state is termed *photostationary state* (pss):

$$(d[O_3]/dt)_{PSS} = 0 = J_{NO2} \cdot [NO_2] - k_{R2.13} \cdot [NO] \cdot [O_3]_{PSS} \quad \text{(eq. 2.10)}$$

The steady state depends on the ratio of NO_2 to NO and on the intensity of solar radiation, i.e. it varies with the time of day, season, latitude and cloud cover. The steady state ozone concentration is given by eq. 2.11. It adjusts to changes in the $[NO_2]/[NO]$ ratio many orders of magnitude faster than the NO_2 concentration changes [*Seinfeld and Pandis*, 1998].

$$[O_3]_{PSS} = \frac{J_{NO2}}{k_{R2.13}} \cdot \frac{[NO_2]}{[NO]} \qquad \text{(eq. 2.11)}$$

However, the high ozone mixing ratios measured in the urban and regional troposphere in the afternoon are not conceivable assuming photostationary state together with the observed NO_x-concentrations. It implies that reactions additional to R 2.11-2.13 are important there. Net ozone production is only possible through chemical processes which enhance the $[NO_2]/[NO]$-ratio without consuming ozone. Thus, the rate limiting step of the reaction cycle is the oxidation of NO to NO_2. The thermal, i.e. non-photochemical, oxidation of two NO molecules by reaction with an oxygen molecule is too slow ($k = 2.0 \times 10^{-38}$ cm^6 molec^{-2} s^{-1}) to be of importance in the atmosphere and cannot explain the relatively rapid conversion of NO to NO_2. The reaction sequences responsible for the conversion of NO to NO_2 during daylight hours (see *Sec. 2.2.4*) involve HO_2, typically produced from the OH attack on organics as explained in *Sec. 2.2.3*.

2.2.3 VOC Oxidation

VOCs emitted to the atmosphere are oxidised photochemically by a succession of steps leading eventually to CO_2 and H_2O, thereby creating a mixture containing many additional oxidation products. The relative contribution of individual VOCs to the formation of specific secondary pollutants varies from one compound to another by virtue of differences in reactivity and structure, since these factors influence the rate of oxidation and the precise oxidation pathway (i.e. the degradation mechanism, see below). The atmospheric residence time of VOCs is determined by the abundance of the most important oxidants in the continental troposphere, i.e. the OH radical, O_3 and the NO_3 radical (see *Sec. 2.2.1* for their sources). The degradation schemes of saturated and unsaturated organics until reaching the first stable, non-radical products are depicted in *Fig. 2.5*. Alkanes do not react with O_3. The reaction of alkanes with OH or NO_3 proceeds by hydrogen abstraction (e.g. R 2.14).

$$OH^{\bullet} + CH_3R \rightarrow H_2O + CH_2R^{\bullet} \qquad \text{(R 2.14)}$$

The resulting alkyl radicals (R^C, here CH_2R^C) are very reactive and form peroxy radicals (RO_2^C) via a three-body addition of O_2 (see *Fig. 2.5a*). The primary step in the oxidation of alkenes, dienes and monoterpenes is the electrophilic addition of the oxidant to the double bond, e.g.

$$OH^{C} + CH_2{=}CHR + M \rightarrow HO{-}CH_2{-}CHR^C + M, \qquad \text{(R 2.15)}$$

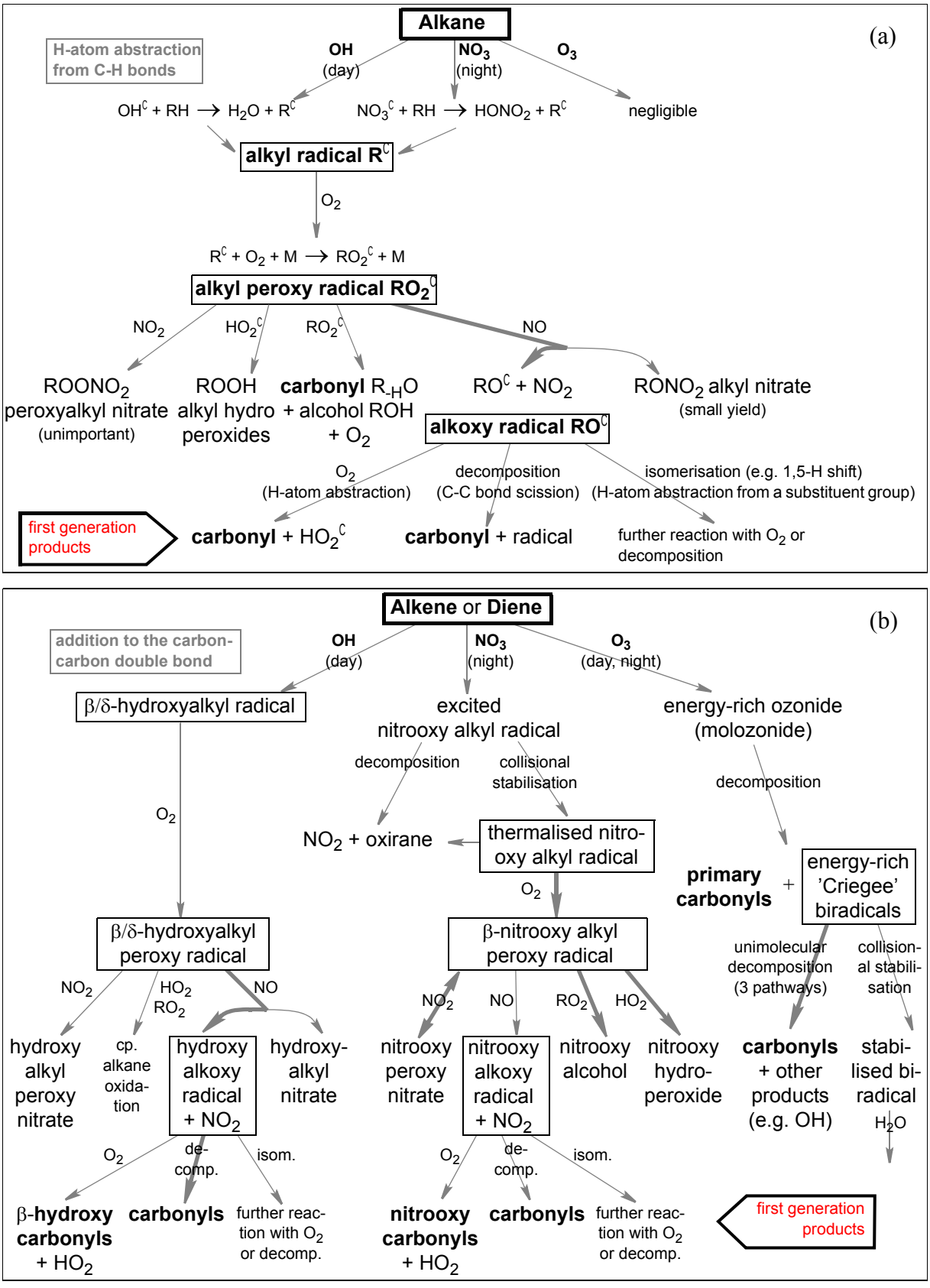

Figure 2.5: Oxidation paths of ***(a)*** *saturated and* ***(b)*** *unsaturated organics after reaction with OH, NO_3 and O_3 under tropospheric conditions as described by Atkinson [1997] and Grosjean et al. [1996]. Pathways favoured in polluted atmospheres are printed in bold. The rate constants for several VOC oxidation reactions are listed in Table 2.4.*

to form substituted alkyl radicals (also cp. $RCH_2^{\bullet}(OH)$ in *Fig. 2.6*). Via the subsequent reaction with O_2 (see *Fig. 2.5b*), organic peroxy radicals $RCH_2O_2^{\bullet}$ are formed. In both, alkane and alkene oxidation, subsequent reactions lead in the presence of NO to alkoxy radicals. This step produces an NO_2 molecule which is the key to O_3 production (see *Sec. 2.2.4*). The alkoxy radicals predominantly react with O_2 or undergo decomposition to aldehydes and/or ketones [*Atkinson*, 1997].

Table 2.4: Rate coefficients k_X of major VOCs with oxidants X = OH, O_3 and NO_3 (for 298 K) as given by Atkinson [1997] (in decreasing order of their OH-reactivity) and known CH_2O yields Y_X (per unit carbon) under high NO_x conditions (> 1 ppbv [e])

Compound	k_{OH} [cm^3 $molec^{-1}$ s^{-1}]	Lifetime τ_{OH} [a]	Y_{OH}	k_{O3} [cm^3 $molec^{-1}$ s^{-1}]	Y_{O3}	k_{NO3} [cm^3 $molec^{-1}$ s^{-1}]	Y_{NO3}
isoprene	1.00×10^{-10}	33 min	0.60	1.28×10^{-17}	0.90 [b]	6.78×10^{-13}	0.11 [c]
β-pinene	7.89×10^{-11}	42 min	0.54	1.50×10^{-17}	0.76	2.51×10^{-12}	
t-2-pentene	6.69×10^{-11}	50 min		1.60×10^{-16}		3.70×10^{-13}	
1,3-butadiene	6.65×10^{-11}	50 min		6.30×10^{-18}		1.00×10^{-13}	0.12 [c]
c-2-pentene	6.54×10^{-11}	51 min		1.60×10^{-16}		3.70×10^{-13}	
t-2-butene	6.39×10^{-11}	52 min		1.90×10^{-16}	0.168	3.90×10^{-13}	
styrene	5.80×10^{-11}	57 min		1.70×10^{-17}	0.5	1.50×10^{-12}	
1,3,5-trimeth.benz.	5.67×10^{-11}	59 min				8.80×10^{-16}	
c-2-butene	5.64×10^{-11}	59 min		1.25×10^{-16}	0.161	3.50×10^{-13}	
α-pinene	5.32×10^{-11}	1.0 h	0.23	8.66×10^{-17}	0.22	6.16×10^{-12}	
isobutene	5.14×10^{-11}	1.1 h		1.13×10^{-17}	1.03	3.32×10^{-13}	0.8
1,2,3-trimeth.benz.	3.27×10^{-11}	1.7 h				1.90×10^{-15}	
1,2,4-trimeth.benz.	3.25×10^{-11}	1.7 h		slowly		1.80×10^{-15}	
1-butene	3.14×10^{-11}	1.8 h		9.64×10^{-18}	0.63 [b]	1.35×10^{-14}	0.11
propene [d]	2.87×10^{-11}	1.9 h	0.65 [e]	1.01×10^{-17}	0.78 [b]	9.49×10^{-15}	0.10
m-xylene	2.31×10^{-11}	2.4 h				7.60×10^{-17}	
m-ethyltoluene	1.86×10^{-11}	3.0 h				4.50×10^{-16}	
p-xylene	1.43×10^{-11}	3.9 h				5.00×10^{-16}	
o-xylene	1.36×10^{-11}	4.1 h		--		4.10×10^{-16}	
o-ethyltoluene	1.19×10^{-11}	4.7 h		--		7.10×10^{-16}	
p-ethyltoluene	1.18×10^{-11}	4.7 h		--		8.60×10^{-16}	
n-decane	1.12×10^{-11}	5.0 h	0.5 [e]	--		2.80×10^{-16}	
n-nonane	9.99×10^{-12}	5.6 h	0.5 [e]	--		2.30×10^{-16}	
formaldehyde	9.37×10^{-12}	5.9 h	--	--		5.60×10^{-16}	
n-octane	8.71×10^{-12}	6.4 h	0.5 [e]	--		1.90×10^{-16}	
ethene [d]	7.95×10^{-12}	7.0 h	0.89 [e]	1.59×10^{-18}	1.06 [b]	2.05×10^{-16}	
cyclohexane	7.21×10^{-12}	7.7 h		--		1.40×10^{-16}	
3-methyl-hexane	7.15×10^{-12}	7.8 h		--			
n-heptane	7.02×10^{-12}	7.9 h	0.5 [e]	--		1.50×10^{-16}	
ethylbenzene	7.00×10^{-12}	7.9 h		--		1.20×10^{-16}	
2-methyl-hexane	6.86×10^{-12}	8.1 h		--			
cumene	6.30×10^{-12}	8.8 h				1.40×10^{-16}	

Table 2.4: Rate coefficients k_X of major VOCs with oxidants X = OH, O_3 and NO_3 (for 298 K) as given by Atkinson [1997] (in decreasing order of their OH-reactivity) and known CH_2O yields Y_X (per unit carbon) under high NO_x conditions (> 1 ppbv [e]) (Continued)

Compound	k_{OH} [cm^3 $molec^{-1}$ s^{-1}]	Lifetime τ_{OH} [a]	Y_{OH}	k_{O3} [cm^3 $molec^{-1}$ s^{-1}]	Y_{O3}	k_{NO3} [cm^3 $molec^{-1}$ s^{-1}]	Y_{NO3}
n-propylbenzene	5.80×10^{-12}	9.6 h		--		1.40×10^{-16}	
toluene	5.63×10^{-12}	9.9 h		1.50×10^{-22}		2.00×10^{-17}	
n-hexane	5.45×10^{-12}	10.2 h	0.5 [e]	--		1.10×10^{-16}	
3-methyl-pentane	5.40×10^{-12}	10.3 h		--		2.20×10^{-16}	
2-methyl-pentane	5.30×10^{-12}	10.5 h		--		1.80×10^{-16}	
n-pentane	4.00×10^{-12}	13.9 h	0.5 [e]	--		8.70×10^{-17}	
isopentane	3.70×10^{-12}	15.0 h		--		1.62×10^{-16}	
n-butane	2.44×10^{-12}	22.8 h	0.5 [e]	--		4.59×10^{-17}	
2,2-dimethylbutane	2.34×10^{-12}	23.7		--			
isobutane	2.19×10^{-12}	1.0 d		--		1.06×10^{-16}	
benzene	1.22×10^{-12}	1.9 d		7.00×10^{-23}		2.30×10^{-17}	
propane	1.12×10^{-12}	2.1 d	0.2 [e]	--		1.70×10^{-17}	
ethyne [d]	8.12×10^{-13}	2.8 d		7.80×10^{-13}			
ethane	2.54×10^{-13}	9.1 d	0.54 [e]	--		0.14×10^{-17}	
acetone	2.19×10^{-13}	10.6 d	0.67 [e]	--			
methane	6.18×10^{-15}	~1 y	1 [e]	--		$< 0.1 \times 10^{-17}$	

a. $[OH] = 5 \times 10^6$ molec cm^{-3}
b. CH_2O as primary carbonyl from alkene ozonolysis
c. *Atkinson* [1997]
d. complex rate coefficient [*Troe*, 1979] for OH reaction
e. *Palmer et al.* [2003]

The reaction with OH is the most important removal path of hydrocarbons during daytime, since most volatile organic gases are oxidised by OH and the rate constants are comparatively high (see Table 2.4). During the night, OH is not available and the reaction with NO_3 can occur in environments with low NO concentrations. Since NO_3 is much less reactive than OH (cp. Table 2.4), but can be by far more abundant than OH during the day, the nocturnal oxidation of alkenes by NO_3 can be comparable to the amount oxidised by OH during the day. However, oxidation by OH is almost the exclusive fate of alkanes since their reaction with NO_3 is much slower. Furthermore, for alkenes the ozone initiated degradation is possible during day and night. The reactions of most VOCs with NO_3 or O_3 are slow compared to the reactions with OH (cp. rate constants in Table 2.4). The results of the first photooxidation stage of almost all organic compounds are carbonyl compounds (see *Fig. 2.5*).

Carbonyls are oxygenated organic compounds, containing a carbon-oxygen double bond (C=O), the carbonyl group. In aldehydes (RCHO), the carbonyl group is bonded to H, in ketones (R_1COR_2) to another C. Carbonyls are emitted as primary pollutants (combustion, vegetation) or are produced as reaction intermediates from NO_x-mediated photooxidation of volatile organic compounds (see above). As intermediate products, carbonyls are indicators of the oxidation of the primary hydrocarbon emissions. Carbonyl compounds have received increasing attention as pollutants and as key participants in photochemical reactions influencing smog processes in the atmosphere. Due to their contribution to tropospheric ozone (see *Sec. 2.2.4*), carbonyls are important compounds in organic atmospheric chemistry. Most carbonyl

compounds, particularly aldehydes, and some of their photochemical reaction products (e.g. peroxyacyl nitrates and ozone) have well known human health and phytotoxic impacts. Carbonyl compounds are also of importance in atmospheric chemistry because their photolysis generates free radicals (see *Sec. 2.2.1*). The most abundant carbonyl in the troposphere is formaldehyde, CH_2O. Secondary formaldehyde either forms as first generation product from VOC oxidation as shown in *Fig. 2.5* or from the degradation of higher carbonyls. Because of its importance in atmospheric chemistry, it is discussed separately in *Sec. 2.3*.

2.2.4 Atmospheric Chemistry of VOCs and NO_x

The reactions that lead to net O_3 production involve the photochemical oxidation of volatile organic compounds, CH_4 and CO in the presence of nitrogen oxides and solar radiation. The numerous processes can be aggregated into two sets of reactions, the RO_x-cycle and the NO_x-cycle (see *Fig. 2.6*). The oxidation of NO to NO_2 in the latter is the key process for ozone production. Such reactions that interconvert the NO_x species are most of all processes involving hydro peroxy radicals $HO_2^{\bullet}$

$$HO_2^{\bullet} + NO \rightarrow OH^{\bullet} + NO_2 \qquad \text{(R 2.16)}$$

and organic peroxy radicals $RO_2^{\bullet}$

$$RO_2^{\bullet} + NO \rightarrow RO^{\bullet} + NO_2\,, \qquad \text{(R 2.17)}$$

where R represents an arbitrary organic rest and $RO^{\bullet}$ is an organic oxy radical. The peroxy radicals are mainly produced as intermediates in the photochemical oxidation of VOCs (see *Sec. 2.2.3*) and carbon monoxide (CO) and by photolysis of formaldehyde as outlined in the following paragraphs.

The oxidation of VOCs during the day is usually initiated by reaction with the hydroxyl radical $OH^{\bullet}$ as described in *Sec. 2.2.3*. The actual reaction mechanism depends on the structure of the VOC, but the principle is illustrated schematically in *Fig. 2.6* by the red reaction sequence. If nitrogen monoxide is present, the organic peroxy radicals, formed in the course of the VOC oxidation, react with NO in an oxygen exchange reaction to NO_2 and organic oxy radicals $RCH_2O^{\bullet}$ (R 2.17). In the reaction step most important for tropospheric chemistry, the reactive oxy radicals rapidly react with O_2 by abstraction of a hydrogen atom, producing aldehydes RCHO and hydro peroxy radicals $HO_2^{\bullet}$ ($RCH_2O^{\bullet} + O_2 \rightarrow RCHO + HO_2^{\bullet}$). Hydro peroxy radicals react again with NO and form NO_2 and OH radicals (R 2.16). Aldehydes are important intermediates during the oxidation of VOCs and have a central position within the RO_x cycle.

Formaldehyde or higher carbonyl compounds, that subsequently react to eventually yield CH_2O [*Atkinson*, 1994], react in a sequence similar to the initially described oxidation of alkanes (see R 2.14), by OH attack (R 2.18), leading to further NO oxidation (purple reaction sequence in *Fig. 2.6*):

$$RCHO + OH^{\bullet} \rightarrow RCO^{\bullet} + H_2O \qquad \text{(R 2.18)}$$

$$RCO^{\bullet} + O_2 + M \rightarrow RCOO_2^{\bullet} + M \qquad \text{(R 2.19)}$$

$$RCOO_2^{\bullet} + NO \rightarrow RCO_2^{\bullet} + NO_2 \qquad \text{(R 2.20)}$$

$$RCO_2^{\bullet} + O_2 \rightarrow RO_2^{\bullet} + CO_2 \qquad \text{(R 2.21)}$$

The reaction of the acyloxy radical $RCO_2^{\bullet}$ with O_2 (R 2.21) mostly leads to the separation of CO_2. Moreover, the photolysis of formaldehyde itself is a net source of two hydro peroxy radicals (R 2.28-2.30 in *Sec. 2.3.2.1*), which in polluted atmospheres are readily converted into hydroxyl radicals (see R 2.16).

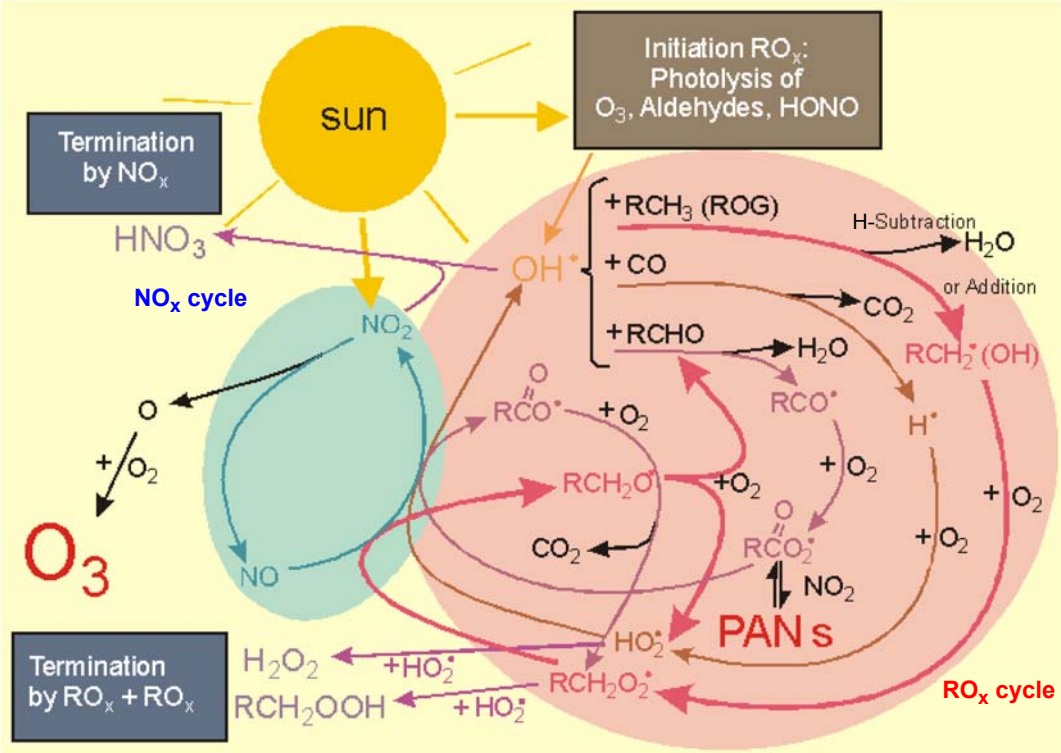

Figure 2.6: Schematic diagram of the tropospheric ozone formation by the interplay of the NO_x- and RO_x-cycles. As intermediate compounds of VOC oxidation, aldehydes, RCHO, play a central role in ozone formation. The compounds in dark grey boxes are definitive sinks and temporary reservoirs for the system. The mechanisms are described in detail in the text (figure from Staehelin et al. [2000]).

In a similar way, the oxidation of CO leads to the production of hydro peroxy radicals (R 2.22-2.23). The CO oxidation is indicated by the brown reaction sequence in *Fig. 2.6*.

$$CO + OH^{\bullet} \rightarrow H^{\bullet} + CO_2 \qquad \text{(R 2.22)}$$

$$H^{\bullet} + O_2 + M \rightarrow HO_2^{\bullet} + M \qquad \text{(R 2.23)}$$

The oxidation of alkenes by ozone (*Sec. 2.3.3.2*) contributes to the shown cycle by directly forming carbonyls and by yielding OH radicals (see *Sec. 2.2.1*).

The VOC-NO_x-cycle leads to considerably high ozone concentrations if sufficient amounts of NO_x (and VOCs) are available. In the NO-rich environment, the reaction with NO dominates as a sink for RO_x radicals, oxidising it to NO_2. Such high-NO_x conditions were given for all situations encountered during the measurements shown in this work. The aspect of VOC-NO_x-limitation is described in *Sec. 2.2.5*. Net formation of O_3 occurs because in the oxidation mechanisms shown, the conversion of NO to NO_2 is accomplished catalytically by the peroxy radicals rather than by O_3 itself. Thereby, the OH radicals are regenerated and the RO_x radical chain is closed. The rate coefficient for the reactions R 2.16 and R 2.17 is about 4000 times the rate constant for the reaction of ozone with HO_2 and also larger than the rate constant for reaction R 2.13 of ozone with NO (see Table 2.5). In the low-NO case in remote areas, the reaction of HO_2 with O_3 leads to the destruction of ozone.

The *termination reactions* R 2.24-2.26 limit or stop the conversions of the two coupled radical chains. They are depicted by dark grey boxes in *Fig. 2.6*. Under low NO_x conditions, the reaction of HO_2 or RO_2 with NO can compete with the self reactions of peroxy radicals (RO_2 and HO_2) which form organic hydro peroxides ROOH (RCH_2OOH in *Fig. 2.6*) or hydrogen

Table 2.5: Rate constants k for selected reactions [Atkinson et al., 2005].

No.	Reaction	k (298K) [cm^3 $molec^{-1}$ s^{-1}]
R 2.2	$O(^1D) + H_2O \rightarrow 2OH$	2.2×10^{-10}
R 2.3	$O(^1D) + N_2 \rightarrow O(^3P) + N_2$ $O(^1D) + O_2 \rightarrow O(^3P) + O_2$	2.6×10^{-11} 4.0×10^{-11}
R 2.11	$O + O_2 + M \rightarrow O_3 + M$	$6.0 \times 10^{-34} \times [O_2]$ $5.6 \times 10^{-34} \times [N_2]$
R 2.13	$NO + O_3 \rightarrow NO_2 + O_2$	1.8×10^{-14}
R 2.16	$HO_2 + NO \rightarrow NO_2 + OH$ [a]	8.8×10^{-12}
--	$HO_2 + O_3 \rightarrow OH + 2O_2$	2.0×10^{-15}
--	$OH + O_3 \rightarrow HO_2 + O_2$	7.3×10^{-14}
R 2.22	$CO + OH \rightarrow H + CO_2$	1.3×10^{-11} (1+0.6P/bar)
R 2.24	$HO_2 + HO_2 + M \rightarrow H_2O_2 + O_2 + M$	$5.2 \times 10^{-32} \times [N_2]$ $4.5 \times 10^{-32} \times [O_2]$
R 2.26	$OH + NO_2 + M \rightarrow HNO_3 + M$	1.2×10^{-11}

a. The rate constants of the reactions of individual peroxy radicals (including the hydro peroxy radical) with NO do not vary significantly.

peroxide H_2O_2. Reaction R 2.24 is an important source of hydrogen peroxide. During conditions with high NO_x concentrations, the reaction of hydroxyl radicals with NO_2 leads to the formation of nitric acid HNO_3 (R 2.26). This is the main termination reaction of the NO_x-cycle in the polluted boundary layer during daytime.

$$HO_2^{\bullet} + HO_2^{\bullet} + M \rightarrow H_2O_2 + O_2 + M \quad \text{(R 2.24)}$$

$$RCH_2O_2^{\bullet} + HO_2^{\bullet} + M \rightarrow RCH_2OOH + O_2 + M \quad \text{(R 2.25)}$$

$$OH^{\bullet} + NO_2 + M \rightarrow HNO_3 + M \quad \text{(R 2.26)}$$

Peroxides do not represent a permanent HO_x and RO_x loss because they can be destroyed by sunlight to produce radicals again (e.g. R 2.5). Organic peroxides either react with OH or photolyse and ultimately produce CH_2O or higher aldehydes, HO_x and H_2O. The formation of HNO_3 is an irreversible process and the most important sink for nitrogen oxides in the atmosphere. HNO_3 is removed from the troposphere either by wet and dry deposition or by adsorption on or reaction with tropospheric aerosols.

In summary, the photochemical oxidation cycle proceeding in the polluted planetary boundary layer (illustrated in *Fig. 2.6*) can be understood as two connected radical chains (NO_x and RO_x). It can generate large amounts of O_3 in an efficient mechanism which is ignited by solar radiation, providing the OH radicals (*Sec. 2.2.1*). The VOCs act as the fuel and the NO_x and HO_x/RO_x radicals as the catalysts of the ozone formation.

Typical smog weather conditions are stationary temperature inversions which favour the accumulation of pollutants in layers close to the ground, forming tropospheric ozone [*Logan*, 1985]. Especially slow moving high-pressure systems accompanied with cloudless and warm conditions and low wind speeds induce so called 'ozone episodes'. Ozone concentrations can rise within several days until these episodes are often terminated by a passing front that advects cooler and cleaner air masses and subsequently causes a drop of the O_3 concentrations. An example from the FORMAT II campaign is shown in *Fig. 4.15*.

Due to the ozone titration with NO and the ceasing photochemical production at night, O_3 levels between sunset and sunrise can be massively diminished in areas with considerable NO

sources (e.g. urban areas). Therefore, highest O_3 concentrations are usually not found close to anthropogenic sources but downwind of polluted metropolitan regions (e.g. north of Milano).

2.2.5 VOC- and NO_x-Limitation of Ozone Formation

The ozone production mechanisms are controlled by the presence of VOCs and nitrogen oxides as described above in *Sec. 2.2.4*. However, in theoretical sensitivity studies [e.g. *Sillman et al.*, 1990] it was observed that the ozone concentration depends on the initial concentrations of NO_x and hydrocarbons in a highly non-linear manner as shown in *Fig. 2.7*.

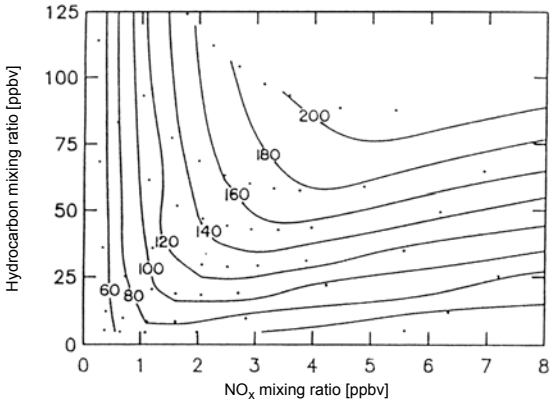

Figure 2.7: Ozone concentration isopleths (in ppbv) as a function of NO_x and VOC concentrations obtained from model runs [Sillman et al., 1990].

For a given initial hydrocarbon concentration, say 25 ppbv, the ozone mixing ratio increases with increasing NO_x concentration until it reaches a maximum of 120 ppbv O_3 at 2.5 ppbv NO_x. Further increasing NO_x concentrations lead to decreasing ozone concentrations (*NO_x-saturation*). This situation is called *VOC-limited*, as an increase of VOCs enhances the total ozone.

Different from the case discussed above, a decreasing O_3 concentration with increasing VOC concentrations at a constant NO_x level is not observed. A maximum ozone concentration is reached, exceeding a certain threshold of VOC, after which the ozone level remains constant, independent of further VOC increase. This situation is referred to as *NO_x-limited*.

For an efficient reduction of tropospheric ozone levels during summer smog episodes, it is important to know whether the respective air mass is NO_x-limited or VOC-limited. If it is VOC-limited, a reduction of NO_x will be counterproductive and the ozone concentration will further increase. This is due to the diminished degradation of O_3 by NO when reducing NO_x emissions.

Sillman et al. [1990] introduced the concept of indicators to identify VOC- and NO_x-sensitive areas. *Hammer et al.* [2002], for instance, found a transition value of 0.2 for the H_2O_2/HNO_3-indicator with model simulations. For a ratio of the chain-termination products (see *Sec. 2.2.4*) larger than this value, an air mass is NO_x-limited. The recent study by *Martin et al.* [2004] suggests using the CH_2O/NO_2 ratio as indicator for VOC-NO_x-limitation. If the ratio is below one, the system is VOC-limited, otherwise it is NO_x-limited. If the ratio is close to one, no clear conclusion is possible. Several more indicators have been presented in the literature.

The theoretical studies on the limitation of ozone production have been proved in various measurements (e.g. LOOP/PIPAPO campaign in Northern Italy). Ozone production was found to be VOC-limited within the Milano plume and NO_x-limited in the surroundings. Several studies show that the highest O_3 levels are mostly found in VOC-controlled regimes, approx. 30 km downwind of the emission sources [*Martilli et al.*, 2002; *Spirig et al.*, 2002; *Thielmann et al.*, 2002]. For the FORMAT sites, in particular, the following was found: Bresso has been identified as a site with generally VOC-limited ozone production, whereas NO_x-sensitivity prevails in Alzate [*Thielmann et al.*, 2001]. High NO_x levels and VOC-limited ozone production are typical of urban conditions. As the processing of NO_x is far more efficient than the

processing of hydrocarbons, an air mass that is VOC-sensitive in the vicinity of major emission sources will become NO_x-sensitive further downwind [*Milford et al.*, 1989].

2.2.6 Estimation of OH Concentrations

The loss of most VOCs during the day is determined by the abundance of the OH radical (see *Sec. 2.2.3*). Because of the lack of OH measurements during the FORMAT experiments, the OH concentration had to be estimated. Two methods were used to estimate the radical concentrations. Both methods are presented in this section and example results are compared.

An estimation of the current OH radical concentration is given by a steady-state model. Although the lifetimes of HO_2 and RO_2 are substantially greater than that of OH, they are still small enough that it is a reasonable assumption that they are in steady state [*Savage et al.*, 2001]. Since the hydro peroxy radical is one of the most important secondary sources of OH, the HO_2 concentration must be known or calculated simultaneously with the OH concentration.

The calculations were performed with an observation-driven zero-dimensional photochemical model based on the steady state approximations as described by *Kleinman et al.* [1997]. The steady-state model is constrained by simultaneous measurements of the major sources and sinks of HO_x radicals and environmental parameters. The model consists of the kinetic rate expressions for species, which are not constrained to their observed values, that is OH, HO_2, organic peroxy radicals and NO. The equations are integrated in an EXCEL sheet and the steady state concentrations of the radicals and NO are obtained by an iterative procedure, calculating all their source and sink terms. Thereby, three types of processes are taken into account: (1) photochemical reactions that generate the major free radicals, (2) chemical reactions that interconvert OH radicals and HO_2 or RO_2 radicals, (3) chemical reactions that remove or recombine free radicals. To determine the reactivity (R_{NIHC}) of the sum of all non-isoprene hydrocarbons, the NIHC species identified by gas chromatographs operated by other groups (see Table 6.2) were multiplied by their OH reaction rate constants and added up, $R_{NIHC} = \sum k_i \cdot [NIHC_i]$. The average rate constant $k = R_{NIHC}/[NIHC]$ for reaction of a hydrocarbon mixture with OH is applied here, so that the model treats the reaction of hydrocarbons with OH radicals as one reaction $d[HC]/dt = k \cdot [HC] \cdot [OH]$. Isoprene is considered separately.

The model yields the concentrations of free radicals and NO that are in equilibrium with the observed longer-lived compounds. The formation rate of ozone and peroxides, as well as the source and sink rates of radicals, are also obtained. The results express the situation at a particular point in time and space. The model has been described in detail by *Staffelbach et al.* [1997] and in conjunction with the ground-based LOOP measurements by *Spirig et al.* [2002].

Ehhalt and Rohrer [2000] developed a parameterisation for the OH concentration as a function of the photolysis frequencies $J_{O(1D)}$ and J_{NO2} and the atmospheric NO_2 concentrations. The highly nonlinear dependence of OH on NO_x is approximated by a Padé function:

$$[OH] = a \cdot J_{O(1D)}{}^{\alpha} \cdot J_{NO2}{}^{\beta} \cdot \frac{b \cdot [NO_2] + 1}{c \cdot [NO_2]^2 + d \cdot [NO_2] + 1} \qquad \text{(eq. 2.12)}$$

The parameters specified by *Ehhalt and Rohrer* [2000] are $\alpha = 0.83$, $\beta = 0.19$, $a = 4.1 \times 10^9$, $b = 140$, $c = 0.41$ and $d = 1.7$, indicating a strong, slightly nonlinear dependence of OH on $J_{O(1D)}$ and a small but highly nonlinear contribution from $[NO_2]$. The units used in this equation are molec cm^{-3} for [OH], s^{-1} for photolysis frequencies and ppbv for $[NO_2]$. The parameterisation is based on data obtained in a rural, relatively unpolluted area in northeastern Germany during the POPCORN campaign and is reported to accurately reproduce the measured OH values for $[NO_x] > 1$ ppbv. All quantities needed for the calculation have been measured during the field campaigns included in this thesis.

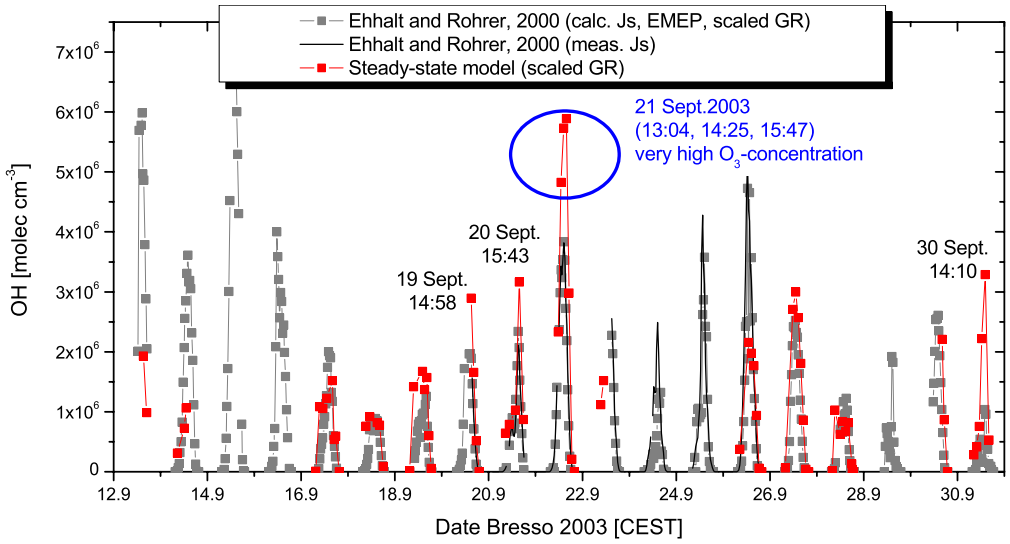

Figure 2.8: OH concentrations estimated with two different methods. The red markers represent the result from the steady-state method. OH concentrations obtained using eq. 2.12 are shown as black trace (with measured J) and grey symbols (with calculated J), respectively.

The steady-state approach of the OH estimation is compared to the method based on eq. 2.12, using data measured during the FORMAT II campaign at Bresso. The time series of estimated OH concentrations is shown in *Fig. 2.8*. Since photolysis frequencies from the spectroradiometer are not available for the entire campaign (see *Sec. 4.3.3*), they were calculated in addition using the *J*-parameterisation from EMEP ¶, scaled with measured global radiation to account for cloud cover. Here it should be noted that the full calculation with the steady-state model had a time basis depending on the irregular sample frequency of the GC system and the parameterisation by *Ehhalt and Rohrer* [2000] has a 5-minute time resolution from the NO_2 and the photolysis frequency measurements. The formula has been tested for several chemical regimes. The agreement of the results obtained with both methods is surprisingly good as can be seen in *Fig. 2.8*. Especially the day-to-day variability and the absolute values of both methods generally agree well. However, on days with exceptionally high ozone concentrations, the steady-state method provides higher OH concentrations than the formula by Ehhalt. Overall, even though eq. 2.12 was obtained in an environment (rural) rather different from the FORMAT sites (urban boundary layer), it seems to be applicable also for the urban site Bresso. The full calculation is presumably more accurate in very high and in very low NO_x conditions. In the heavily polluted metropolis of Mexico City for example, the parameterisation eq. 2.12 does not appear applicable. OH measurements were available there to compare with. There is a strongly non-linear relationship between the OH measurements by LIF and estimated OH concentrations calculated from eq. 2.12. Peak OH concentrations at noon are overestimated, whereas morning and afternoon concentrations are underestimated. The discrepancies between measurement and estimation in Mexico City might arise from not including any OH sink terms in the formula. This is particularly important in Mexico City, which is more strongly polluted with VOCs than Milano. However, due to the good agreement of the OH results of the two estimation methods, both methods are applicable to determine OH concentrations in Milano.

¶. The measured and calculated photolysis frequencies were compared and found to be in good agreement

2.3 Formaldehyde

Formaldehyde, CH_2O ¤, is an important high-yield intermediate in the oxidation mechanism of almost every VOC (see *Sec. 2.2.3*). Since in many steps which generate formaldehyde, the conversion of NO to NO_2 (R 2.16 or R 2.17) also takes place, CH_2O represents an indicator for the rate of atmospheric VOC oxidation, in the course of which tropospheric ozone is formed. The central role of formaldehyde in tropospheric photochemistry, indicated in *Sec. 2.2.4*, originates from its radical forming capability. Since the focus of this thesis is on the measurement and variability of this gaseous compound in the boundary layer, the sources and sinks which determine the formaldehyde distribution are described here in detail.

2.3.1 Typical Formaldehyde Concentrations

Formaldehyde is the most reactive and most abundant gas-phase carbonyl compound in the atmosphere. It is a ubiquitous component of both the remote atmosphere and polluted urban environments. Typical CH_2O mixing ratios in urban areas are on the order of 1-20 ppbv [e.g. *Grosjean*, 1991; *Grosjean et al.*, 1993] and can reach 10-100 ppbv in polluted air [e.g. *Harris et al.*, 1989; *Grosjean*, 1991]. Formaldehyde values as high as 150 ppbv have been reported in the 1960s in the Los Angeles area [*Stahl*, 1969]. In more remote continental locations and rural areas, mixing ratios of 1-10 ppbv have been observed due to input of additional NMHCs by vegetation [e.g. *Benning and Wahner*, 1998; *Harder et al.*, 1997; *Lee et al.*, 1998]. In clean remote air, formaldehyde mixing ratios are between 0.1 and 0.5 ppbv [e.g. *Platt et al.*, 1979; *Lowe and Schmidt*, 1983; *Ayers et al.*, 1997; *Zhou et al.*, 1996] and in the upper troposphere < 0.1 pptv [*Jacob et al.*, 1996]. These variations are due to the relatively short lifetime of formaldehyde (*Sec. 2.3.2.3*).

Table 2.6: Typical formaldehyde mixing ratios observed in different air masses.
su: summer, wi: winter, sp: spring, au: autumn

Site (characterisation)	Range [ppbv]	Method	Reference
clean Antarctic troposphere	~ 0.03-0.7 su	Hantzsch	*Riedel et al.* [1999]
Arctic air	0.1-0.7 su	Hantzsch	*de Serves* [1994]
remote marine air	0.2-0.4	DNPH	*Lowe and Schmidt* [1983]
marine air	0.3-1.9	DNPH	*Zhou and Mopper* [1993]
semi-rural (Alzate)	1-7 su 0.5-6 au	DOAS	this work (*Sec. 4.2.2*) this work (*Sec. 4.3.2*)
rural (Spessa)	1-10 au	DOAS	this work (*Sec. 4.3.4*)
urban Milano area (Bresso)	2-10.9 su 2-17 au	DOAS	this work (*Sec. 4.2.3*) this work (*Sec. 4.3.3*)
London urban area	15-20	DNPH	*Williams et al.* [1996]
downtown Rome	8-28 su 7-17 wi	DNPH	*Possanzini et al.* [2002]
urban, Budapest	d.l.-58.0 su	DNPH	*Haszpra et al.* [1991]
urban, Mexico City	1-36 sp	DOAS	this work (*Sec. 4.5.3*)
urban, Los Angeles	≤ 48	DNPH	*Grosjean* [1982]
Los Angeles area	< 70	DNPH	*Grosjean et al.* [1983]

¤. Also H_2CO or HCHO are common

Formaldehyde supports the formation of air toxics like ozone (see *Sec. 2.2.4*) and, as several other aldehydes, formaldehyde itself is harmful to human health at elevated concentration levels. It has received attention because of its carcinogenic effect and being a very toxic urban pollutant irritating the respiratory tract [*WHO*, 2000]. The major route of exposure to formaldehyde is inhalation. Indoor formaldehyde concentrations can be high due to chemical treatment of furniture, carpets etc. The indoor concentrations (25-50 ppbv, but up to 280 ppbv [*WHO*, 2000]) can be several orders of magnitude higher than levels in ambient air (see above). Owing to the extremely high concentrations of formaldehyde in tobacco smoke (50 000-100 000 ppbv [*WHO*, 2000]), smoking also constitutes a major source of formaldehyde indoors.

The lowest concentration that has been associated with nose and throat irritation in humans after short-term exposure is 0.1 mg m^{-3} (≈ 80 ppbv), although some individuals can sense the presence of formaldehyde at lower concentrations. To prevent significant sensory irritation in the general population, an air quality guideline value of 0.1 mg m^{-3} as a 30-minute average is recommended. Since this is over one order of magnitude lower than a presumed threshold for cytotoxic damage to the nasal mucosa, this guideline value represents an exposure level at which there is a negligible risk of upper respiratory tract cancer in humans [*WHO*, 2000].

2.3.2 Role of Formaldehyde in Tropospheric Chemistry

Daytime decomposition reactions of CH_2O are associated with the formation of carbon monoxide and of highly reactive odd-hydrogen radicals. In both cases CH_2O exerts an influence on the oxidising capacity of the atmosphere. On the one hand, the HO_2 radicals resulting from CH_2O photolysis drive photochemical smog formation (*Sec. 2.2.4*) and are especially important in an environment polluted with hydrocarbons. On the other hand, the chemistry of formaldehyde is important in understanding the global budget of CO which, in turn, has a large effect on the global OH mixing ratio [*Crutzen*, 1985]. The overall net change of HO_x due to hydrocarbon oxidation depends upon the NO concentration and the photolysis fractions. In the following, the daytime and nighttime loss mechanisms are described.

2.3.2.1 Daytime Sinks

In the sunlit atmosphere, formaldehyde is relatively short-lived with a minimum lifetime (see *Sec. 2.3.2.3*) of the order of few hours [*Logan et al.*, 1981]. The major daytime loss processes for CH_2O are photolysis by wavelengths less than 365 nm and reaction with the hydroxyl radical $OH^{\bullet}$. The photolytic pathway proceeds via two channels with a branching ratio dependent on the wavelength: a *molecule channel*, producing H_2 and CO, which dominates for wavelengths greater than 325 nm (R 2.27) and a *radical channel*, producing a hydrogen atom H and a formyl radical $HCO^{\bullet}$, which dominates at shorter wavelengths (R 2.28).

$$CH_2O + h\nu \rightarrow H_2 + CO\,,\ (\lambda < 365\ \text{nm}),\ J_{CH2Om} \approx 4 \times 10^{-5}\ \text{s}^{-1} \qquad \text{(R 2.27)}$$

$$CH_2O + h\nu \rightarrow H^{\bullet} + HCO^{\bullet},\ (\lambda < 337\ \text{nm}),\ J_{CH2Or} \approx 3 \times 10^{-5}\ \text{s}^{-1} \qquad \text{(R 2.28)}$$

Both reactions proceed in the troposphere with comparable speeds (see *Fig. 2.9*), although the reaction products are energy poor, stable molecules in the one case and energy rich, reactive radicals in the other case. The quantum yields for the two photolysis channels are wavelength dependent and are specified in *Atkinson et al.* [2002].

The radical products $H^{\bullet}$ and $HCO^{\bullet}$, formed by the radical channel of photolysis, are very reactive and are rapidly converted to hydro peroxy radicals $HO_2^{\bullet}$ by molecular oxygen:

$$H^{\bullet} + O_2 + M \rightarrow HO_2^{\bullet} + M\,,\ k = 9.5 \times 10^{-11}\ \text{cm}^3\ \text{molec}^{-1}\ \text{s}^{-1} \qquad \text{(R 2.29)}$$

$$HCO^{\bullet} + O_2 \rightarrow HO_2^{\bullet} + CO\,,\ k = 5.1 \times 10^{-12}\ \text{cm}^3\ \text{molec}^{-1}\ \text{s}^{-1} \qquad \text{(R 2.30)}$$

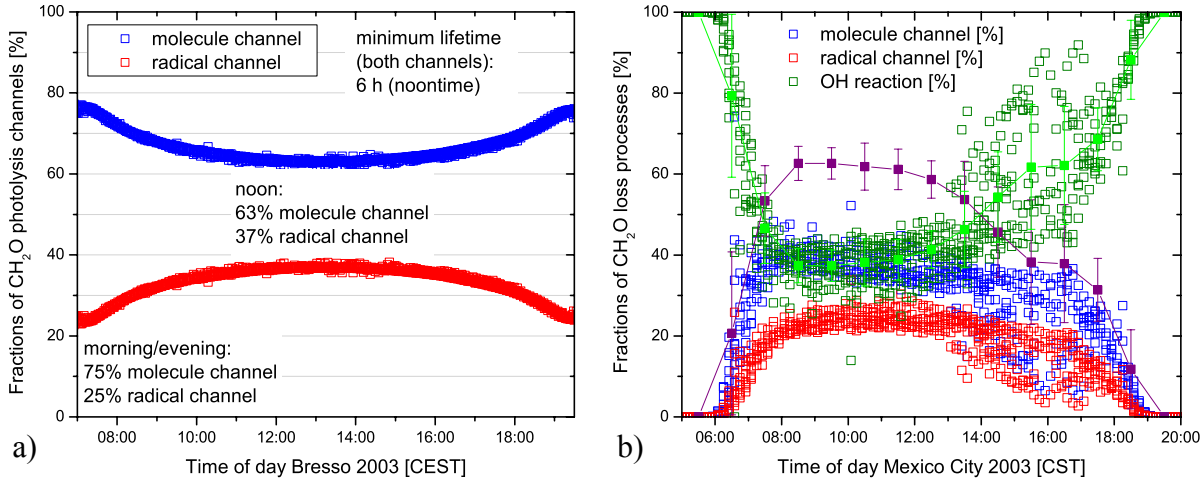

Figure 2.9: ***(a)*** *Fractions of molecule (blue) and radical channel (red) of formaldehyde photolysis for Bresso 2003 as function of the time of day.* ***(b)*** *Fractions of the three major daytime CH_2O loss pathways for Mexico 2003. The combined photolysis loss is shown as purple curve with bars representing 1 standard deviation.*

The rapid reaction with the hydroxyl radical (R 2.31) comprises the other major CH_2O loss pathway. The produced formyl radical reacts in R 2.30 to yield HO_2. In generating HO_2, the reaction with OH has no net influence on the HO_x budget, but it affects the partitioning among odd hydrogen radicals, HO_x (see *Sec. 2.2.1*).

$$CH_2O + OH^{\bullet} \rightarrow H_2O + HCO^{\bullet},\ k = 8.5 \times 10^{-12}\ \text{cm}^3\ \text{molec}^{-1}\ \text{s}^{-1} \qquad \text{(R 2.31)}$$

Both, photolysis of CH_2O and the oxidation by OH radicals, lead to the production of CO and make CH_2O an important source of atmospheric hydrogen and carbon monoxide in the non-urban troposphere. Of the three CH_2O destruction pathways shown, only the radical photolysis channel (R 2.28) results in a net change in HO_x, yielding two HO_2 radicals per CH_2O photolysed. Photolysis frequencies measured at Bresso (*Sec. 4.3.3*) showed that at noon photodissociation of CH_2O occurs with about 37% probability via the radical pathway (*Fig. 2.9a*), thus providing a major source for highly reactive HO_2 radicals. The fraction decreases to 25% at large SZAs. Similarly, in Mexico City 40% of formaldehyde photolysed, produced radicals during noontime.

The relative contributions of the reaction of OH with CH_2O and the two combined photolysis channels to the overall formaldehyde loss as a function of time of day are shown in *Fig. 2.9b* for conditions in Mexico City during the MCMA-2003 (*Sec. 4.5.3*). Measurements of OH were available from this campaign and revealed an average clear sky OH concentration of 6.4×10^6 molec cm^{-3} at noontime. The loss rates of formaldehyde towards both, photolysis and reaction with OH, peak at the same time near midday when the actinic flux is at its maximum. For time periods around midday, a maximum CH_2O loss rate of on average 1.4×10^{-3} ppbv s^{-1} is derived. Photolysis is responsible for over 63% of the CH_2O loss around noon and constitutes the major formaldehyde sink between 7 and 14 h at Mexico City. In order for the hydroxyl radical reaction with formaldehyde to be equal in importance to the photolysis process, the average hydroxyl radical concentration during the midday time periods would have to be about 9.1×10^6 $molec^{-1}$ cm^{-3} which is substantially higher than the actually measured concentration in this case. Both loss channels decrease in the afternoon. The loss by the photolysis channel, however, decreases faster than the loss by the OH channel and comprises ~ 40% of the total formaldehyde loss rate between 15 h and 17 h. At high solar zenith angles, formaldehyde loss by the reaction with OH gains importance since minor OH sources are always present (e.g. from ozonolysis of

alkenes) but solar irradiation goes to zero. Finally, a maximum net yield of HO_x radicals per CH_2O molecule destroyed is 0.5 (yield radical channel 0.25). At other sites with lower OH concentrations, photolysis was responsible for more than 70% of the formaldehyde loss [e.g. *Fried et al.*, 1997]. For measurements at Bresso (*Sec. 4.3.3*), the OH radical concentrations were estimated from the steady state model presented in *Sec. 2.2.6* and average noontime OH concentrations were found to be 4×10^6 molec cm^{-3}. The relative afternoon contributions of the loss mechanisms at Bresso are comparable to the results obtained from the Mexico data, although the OH concentrations for Bresso were modelled. Photolysis is the dominant CH_2O sink also in Bresso, accounting for 65-70% of the formaldehyde loss during the afternoon hours.

2.3.2.2 Nighttime Sinks

No photochemical processes take place during nighttime. In the absence of solar irradiation, two processes can be effective diminishing formaldehyde concentrations – reaction with the nitrate radical and deposition [*Altshuller*, 1993; *Lowe and Schmidt*, 1983].

The importance of the reaction with nitrate radicals (R 2.32) largely depends on the environment. In urban areas, this process is not expected to be of much significance, since the emissions of nitric oxide, NO, through the night suppress the concentrations of nitrate radicals (see R 2.9).

$$CH_2O + NO_3 \rightarrow HNO_3 + HCO\,,\ k = 5.6 \times 10^{-16}\ \text{cm}^3\ \text{molec}^{-1}\ \text{s}^{-1} \quad \text{(R 2.32)}$$

The typical lifetime of formaldehyde towards the reaction with the nitrate radical is 80 days, assuming a nighttime NO_3 concentration of 10 pptv (typical for the semi-rural site Alzate, see *Steinbacher et al.* [2005]).

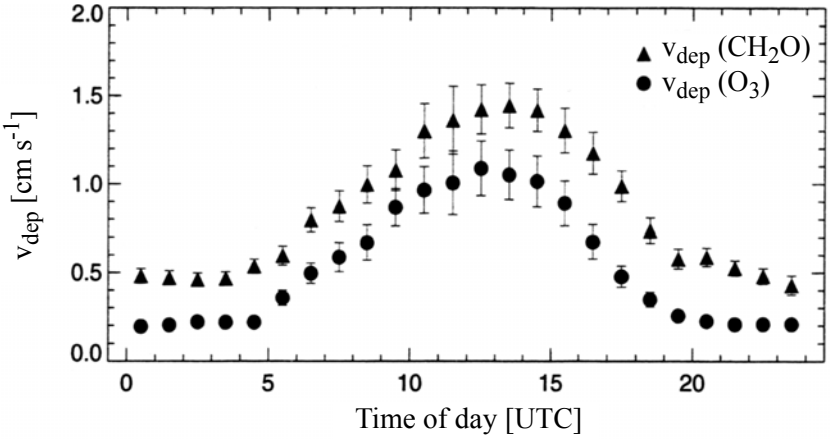

Figure 2.10: Average deposition velocities of formaldehyde (days without precipitation) and ozone over a deciduous forest as a function of time of day [Krinke, 1999].

Atmospheric CH_2O concentrations also depend on dry and wet deposition [e.g. *Lowe and Schmidt*, 1983]. Details on deposition processes are given in *Sec. 2.4.4*. The deposition flux is larger during daytime, however, due to the variable boundary layer height (see *Sec. 2.4.1*), the influence on the concentration close to the ground is greater during the night. *Krinke* [1999] measured the deposition velocity of formaldehyde over a deciduous forest and derived $v_d \approx 0.5$ cm s^{-1} during the night and maximum values of 1.4 cm s^{-1} during the day (*Fig. 2.10*). The deposition velocity for formaldehyde is considerably larger than for ozone (*Fig. 2.10*). This may be due to the high CH_2O solubility in water.

Since carbonyl compounds are polar, they can easily dissolve in rain and fog and interact with particles of condensed matter, e.g. adsorption to aerosol particles [*Carlier et al.*, 1986]. Formaldehyde can act as a precursor to organic aerosol formation in urban air [*Grosjean*, 1982]. The irreversible removal of formaldehyde by wet and dry deposition reduces the chemical activity

of the air mass and lowers the efficiency of oxidant production from hydrocarbon oxidation. The nighttime formaldehyde loss processes thus set the chemical starting conditions for the next day.

2.3.2.3 Lifetime of Formaldehyde

In the sunlit atmosphere, photolysis and reaction with OH radicals determine the atmospheric residence time of formaldehyde. At night, the removal by wet and dry deposition can be important. The lifetime τ of formaldehyde regarding photolysis, reaction with the OH radical (analogously reaction with the NO_3 radical) and deposition, respectively, is defined in eq. 2.13. Here, *h* describes the height of the boundary layer and v_{dep} is the deposition velocity (see *Sec. 2.4.4*).

$$\tau_{h\nu} = \frac{1}{J}, \qquad \tau_{OH} = \frac{1}{[OH] \cdot k_{OH}}, \qquad \tau_{dep} = \frac{h}{v_{dep}} \qquad \text{(eq. 2.13)}$$

Photolysis determines the lifetime of formaldehyde (see also *Sec. 2.3.2.1*). Typically, the lifetime of CH_2O with respect to its two major loss pathways, photolysis and reaction with the hydroxyl radical, is on the order of a 2-4 hours. The formaldehyde lifetime during the day is therefore short enough that the distribution is not affected significantly by transport, i.e. the CH_2O mixing ratio depends only on the immediate history of the observed air mass. As a consequence, virtually all of the observed CH_2O is in steady state between local production and destruction (*Sec. 2.3.3.5*). At night, the CH_2O lifetime becomes very long and thus transport can become important.

The formaldehyde lifetime towards wet and dry deposition is assumed to be in the order of a day [*Benning and Wahner*, 1998].

2.3.3 Sources of Formaldehyde

Formaldehyde is emitted directly and is produced from photooxidation of biogenic and anthropogenic volatile organic compounds (see *Sec. 2.2.3*). As a primary emission product, formaldehyde is released from incomplete combustion processes like fossil fuel combustion (e.g. motor vehicles and stationary sources) [*Anderson et al.*, 1996; *Altshuller*, 1993] and biomass burning [*Carlier et al.*, 1986], especially during smouldering combustion (see *Sec. 2.1.4*). Moreover it is released directly into the atmosphere by industrial emissions and emissions from vegetation [*Kesselmeier et al.*, 1997]. The latter is a very small source. Primary formaldehyde is locally important in urban areas, where it generally accounts for 10-20% (but up to 40% in Mexico City) of the formaldehyde present in the air mass [*Samuelsson et al.*, 2006; *García et al.*, 2005 and references therein] in summer. Vehicles are responsible for ~ 80% of the direct emissions [*Finlayson-Pitts and Pitts*, 2000]. The largest part of the formaldehyde in the atmosphere is formed as a secondary product of the VOC oxidation sequences [e.g. *Altshuller*, 1993; *Carlier et al.*, 1986], which are generally outlined in *Sec. 2.2.3*. Important formation pathways of secondary CH_2O are specified in this section.

Formaldehyde is generated by a wide range of VOCs so that the individual formation pathways cannot be delineated here in detail. Rate constants for oxidation reactions of several major organics along with their formaldehyde yields under high NO_x conditions are summarised in Table 2.4. Formaldehyde yields for C_2-C_6 VOCs are typically 0.3-1 per unit carbon [*Altshuller*, 1991a,b]. The values depend on the NO concentration, since the fate of the RO_2 radicals is controlled by the availability of NO (see *Fig. 2.5* or *Fig. 2.6*).

We confine the description of the CH_2O formation to the following mechanisms. Oxidation of methane (see *Sec. 2.3.3.1*) provides a global formaldehyde background. In continental boundary layers, oxidation of short-lived VOCs dominates over CH_4 as a source of CH_2O and results in a major enhancement of the total CH_2O concentration. Among these is the ozonolysis of 1-alkenes (*Sec. 2.3.3.2*) which directly results in the formation of CH_2O. Anthropogenic

VOCs are important formaldehyde precursors in urban environments, whereas the contribution from biogenic VOC sources can dominate in highly wooded regions, at least during the growing season. The most important biogenic VOC is isoprene, which has a lifetime of less than an hour against atmospheric oxidation and produces CH_2O with a high yield (*Sec. 2.3.3.3*). In several cases of VOC oxidation, formaldehyde is formed as a secondary product from further degradation of higher carbonyls (*Sec. 2.3.3.4*).

2.3.3.1 Oxidation of Methane and Higher Alkanes

Methane (CH_4) is the most abundant hydrocarbon in the troposphere (~1.9 ppmv). Because of its long lifetime (see Table 2.4) it is well mixed in the troposphere. Its oxidation defines the atmospheric CH_2O background concentration. In the remote troposphere, methane is the dominant formaldehyde precursor [*Lowe and Schmidt*, 1983]. The sequence of reactions initiated by reaction of CH_4 with the OH radical is shown in *Fig. 2.11*. After the initial OH attack on CH_4 and the subsequent reaction with O_2, the methyl peroxy radical $CH_3O_2^C$ is formed. This radical then reacts with NO and HO_2 to form CH_3O^C and MHP (methyl hydro peroxide), respectively. The CH_3O^C radical, which becomes the dominant product when NO concentrations exceed ~ 0.05 ppbv, is rapidly converted to CH_2O by hydrogen abstraction with molecular oxygen. As shown, the MHP breaks down slowly via a number of different pathways, all of which produce CH_2O. Photolysis forms the CH_3O^C radical and reaction with OH produces the CH_2OOH^C and $CH_3O_2^C$ radicals. The CH_2OOH^C rapidly decomposes to form CH_2O and OH. Methane oxidation has a yield of one CH_2O molecule.

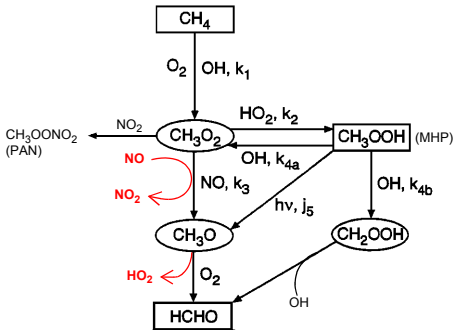

Figure 2.11: Formaldehyde production reactions initiated by OH attack on methane (CH_4). Stable species with lifetimes greater than a few hours are highlighted in boxes, while the more reactive species are indicated in ellipsoids [Fried et al., 1997]. The formaldehyde (methanal) yield is 1.

Under high NO conditions, the CH_4 oxidation mechanism indicates no net change of odd hydrogen radicals, HO_x, in the production of CH_2O. At low NO concentrations, where the MHP formation becomes important, two of the three channels involving MHP show a net loss of HO_x in producing CH_2O. At very low NO concentrations, where CH_3O_2 recombination starts to become important, there is a partial loss of HO_x in producing CH_2O [*Fried et al.*, 1997].

Higher alkanes proceed in a similar reaction sequence producing higher carbonyls (e.g. ethane forms acetaldehyde (ethanal), propane forms propionaldehyde, etc.) and ultimately lead to formaldehyde production via the carbonyl degradation mechanisms described in *Sec. 2.3.3.4*.

2.3.3.2 Oxidation of Alkenes

In addition to CH_4, other more reactive hydrocarbons are important in generating CH_2O. The simplified reaction schemes shown in *Fig. 2.5* yield carbonyls which include formaldehyde in many cases of C_2-C_6 compounds. The formaldehyde production rates from alkene reactions with OH and O_3 can be of equal magnitude during the day. The reaction with O_3 can be expressed in the following mechanism.

The reaction of ozone with terminally double-bonded olefins (1-alkenes) leads directly to the production of formaldehyde [*Atkinson et al.*, 1995; *Grosjean et al.*, 1996]. This process

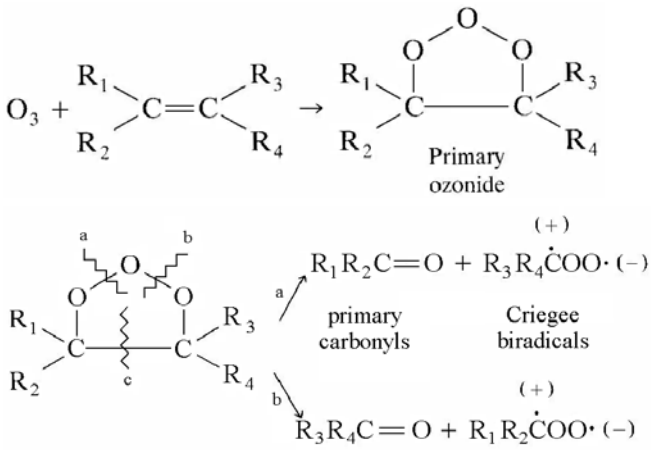

Figure 2.12: Ozone adds to the double bond of the olefin, leading initially to the formation of an energy-rich ozonide. The ozonide decomposes to form two primary carbonyls and two energy-rich Criegee biradicals. For 1-alkenes, $R_1 = H$ and $R_2 = H$, i.e. CH_2O constitutes one of the primary carbonyls.

produces CH_2O also in the absence of sunlight and may be important in polluted areas and at nighttime. The gas-phase ozone-olefin reaction (ozonolysis) is believed to proceed through the formation of a *molozonide* (a primary ozonide) and its unimolecular dissociation to two carbonyl compounds and two biradicals (so-called *Criegee intermediates*) [*Grosjean et al.*, 1996]. The reaction path is illustrated in *Fig. 2.12*. For unsymmetrical alkenes, two different primary carbonyls are formed. In the case of 1-alkenes, RCH=CH_2, formaldehyde is one of the primary carbonyls and both carbonyls, RCHO and CH_2O, are formed in essentially equal yields [*Atkinson*, 1997]. Symmetrical alkenes lead to the formation of a single primary carbonyl, which is formaldehyde in the case of ethene. The subsequent fate of the energy-rich Criegee biradicals is a subject of considerable uncertainty. They can react with water vapour and with several co-pollutants including NO, NO_2, SO_2, as well as carbonyl compounds. In the presence of water vapour, the reaction appears to be an intramolecular rearrangement to form either a carboxylic acid or an organic hydro peroxide [*Finlayson-Pitts and Pitts*, 2000], while NO_x reactions yield new carbonyls. The ozonolysis of alkenes delivers several molecules of aldehydes per molecule hydrocarbon in the case of higher NMHCs [*Carlier et al.*, 1986; *Atkinson et al.*, 1995; *Atkinson*, 1994]. Formaldehyde yields for some alkene-ozone reactions and alkene-OH reactions are given in Table 2.4.

Altshuller [1991a,b] showed that formaldehyde is produced in substantial quantities from the atmospheric photooxidation of alkenes and alkanes. The predicted yield of formaldehyde from the photooxidation of an urban mixture of alkenes is 0.39 during the summer [*Altshuller*, 1991b]. This yield is based on the complete oxidation of the atmospheric alkenes. The relative yield of formaldehyde from the photooxidation of alkanes is much smaller [*Altshuller*, 1991a]. Formaldehyde formation is dominated by reaction of olefins such as ethene and propene. An estimation of the exact yield is difficult because of the numerous reaction pathways available.

2.3.3.3 Oxidation of Isoprene and Other Biogenic NMHCs

Many organic compounds emitted by plants can be transformed to aldehydes/formaldehyde. The most significant biogenic aldehyde precursors are isoprene and some reactive terpenes which may produce high aldehyde concentrations in wooded regions [*Altshuller*, 1993; *Grosjean et al.*, 1993]. With the exception of isoprene, the production of CH_2O from the various primary VOCs emitted from vegetation is subject of uncertainty.

The principal contributor to reactive hydrocarbons during the growing season is the biogenic hydrocarbon isoprene (C_5H_8, details see *Sec. 2.1.3*). Isoprene is a highly efficient CH_2O producer. The reaction scheme for the major steps in producing CH_2O from OH-reaction with isoprene is shown in *Fig. 2.13*, where many additional and less important branching reactions have been left out for simplicity. More comprehensive details can be found in *Fehsenfeld et al.*

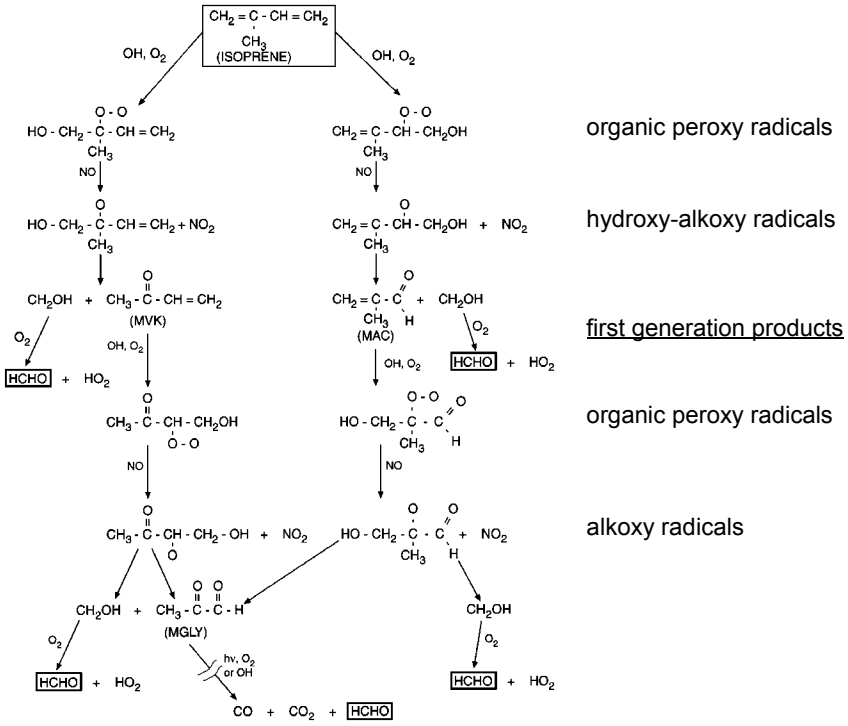

Figure 2.13: Simplified CH_2O production scheme from isoprene oxidation initiated by OH. Only the major steps are shown (adapted from Fried et al. [1997]).

[1992]. OH adds to one of four different carbon sites of isoprene. However, addition to the two terminal carbon sites is favoured. Such addition is shown on the left and right sides of *Fig. 2.13*. It is followed by rapid addition of O_2, generally to the adjacent C-atom. In high-NO_x regimes, subsequent reaction with NO produces the hydroxy-alkoxy radicals shown. The first generation products are methyl vinyl ketone (CH_2=$CHCOCH_3$) and methacrolein (CH_2=$C(CH_3)CHO$) in addition to CH_2OH fragments which further react to produce CH_2O and HO_2. Formaldehyde is also produced by further addition of OH and O_2 to the oxidation products methyl vinyl ketone (MVK) and methacrolein (MAC) as shown in *Fig. 2.13*. In both cases, reaction with NO leads to the formation of alkoxy radicals which further decompose into methylglyoxal (MGLY). As shown in *Fig. 2.13*, MGLY photolysis and reaction with OH ultimately produce additional CH_2O [*Fried et al.*, 1997]. Subsequent decomposition also produces CH_2O in many steps along the way.

The relative formaldehyde yield (per carbon) from the OH-initiated oxidation of isoprene ranges from 0.32 in the absence of NO_x to 0.67 in the presence of NO_x [*Jenkin et al.*, 1997], including the subsequent oxidation of short-lived isoprene oxidation intermediates. Rate constants and CH_2O yields from O_3 and NO_3 initiated isoprene oxidation are listed in Table 2.4. Formaldehyde can be produced within an hour from the initial oxidation by OH because the lifetime of isoprene is about 0.5 h during midday. The lifetimes of major secondary products of isoprene oxidation are about 1.5-2.5 h [*Carslaw et al.*, 2000]. The lifetime of CH_2O is a few hours (see above), so that isoprene emission is collocated with and linearly related to the resulting CH_2O enhancement.

The mechanism for the OH radical oxidation of terpenes with an endocyclic C=C double bond (α-pinene, 3-carene) or an exocyclic C=C double bond (β-pinene, sabinene) by H-abstraction and addition of OH to the C=C double bond is described in detail by *Larsen et al.* [2001]. There is a number of possible abstraction sites in the molecule and a large number of following reactions. The presence of NO_x will favour formation of carbonyl compounds while the absence of

NO_x will lead to an increase in the yields of alcohols and hydroperoxides. *Larsen et al.* [2001] give net molar yields of formaldehyde and other gas-phase products for several terpenes after 20 min reaction with OH in a smog chamber. Smog chamber determinations of CH_2O yields for α-pinene and β-pinene reactions with OH and O_3 have also been reported by *Hatakeyama et al.* [1991] (see Table 2.4).

Emissions of terpenes can exceed those of isoprene for some ecosystems, however for larger biogenic VOCs, including in particular monoterpenes, their per carbon CH_2O yields are lower than for isoprene, due to formation of organic aerosols from their low-volatile oxidation intermediates [*Hatakeyama et al.*, 1991]. Better understanding is needed of the CH_2O yields and mechanistic information regarding the oxidation of terpenes, sesquiterpenes, and other highly reactive organic compounds emitted by vegetation [*Larsen et al.*, 2001].

(Z)-3-hexene-1-ol (leaf alcohol) and (Z)-3-hexenylacetate (leaf ester), emitted by a large number of plants, can be transformed to aldehydes, such as propanal, and in presence of OH radicals and NO_x also to formaldehyde and acetaldehyde [*Atkinson*, 1994].

2.3.3.4 Formaldehyde from Higher Carbonyls

Aldehydes have shorter lifetimes than the parent alkane [*Altshuller*, 1991a] and are rapidly converted to secondary products. Depletion of higher aldehydes thereby provides a significant source of aldehydes containing less carbon atoms than the precursor. Thus, formaldehyde is generated in the course of acetaldehyde depletion, acetaldehyde in propionaldehyde depletion etc. In the presence of hydroxyl (or nitrate) radicals, a higher aldehyde is expected to be cascaded down to the shortest aldehyde, which has the longest lifetime.

The initial pathway involves H-atom abstraction from the aldehyde group producing an acyl radical ($RCO^{\bullet}$) followed by addition of O_2 to form an acyl peroxy radical, $RC(O)OO^{\bullet}$ (cp. R 2.18 and R 2.19). Acyl peroxy radicals can react with NO_2 to peroxyacyl nitrates, RCO_3NO_2 (R 2.33). As peroxyacyl nitrates (PANs) can decompose back to acyl peroxy radicals, an equilibrium is established, which strongly depends on temperature.

$$RC(O)OO^{\bullet} + NO_2 \leftrightarrow RCO_3NO_2 \qquad \text{(R 2.33)}$$

At low temperatures, the NO_2 is bound in PANs. At high temperatures, when PANs decompose, NO_2 and acyl peroxy radical are released again. Apart from their role as reservoir, the PANs also react with OH radicals (R 2.34) to yield the next shorter aldehyde ($R_{-1}CHO$).

$$RCO_3NO_2 + OH^{\bullet} \rightarrow R_{-1}CHO + \text{other products} \qquad \text{(R 2.34)}$$

However, the magnitude of the rate coefficient renders the above reaction R 2.33 with NO_2 unimportant in most cases [*Seinfeld and Pandis*, 1998]. At high temperatures, when conversion from acyl peroxy radicals to peroxyacyl nitrates is not favoured, or in the presence of NO, the acyl peroxy radicals react to alkyl peroxy radicals, $RO_2^{\bullet}$:

$$RC(O)OO^{\bullet} + NO + O_2 \rightarrow NO_2 + CO_2 + RO_2^{\bullet} \qquad \text{(R 2.35)}$$

Alkoxy radicals formed from $RO_2^{\bullet}$ (see R 2.17) either decompose or react with O_2, leading to the formation of the shorter aldehyde and other products.

Carbonyl compounds are easily photolysed from the near ultraviolet onwards. The photolysis of acetaldehyde (R 2.36) also yields CH_2O by subsequent reactions of the methyl radical $CH_3^{\bullet}$.

$$CH_3CHO + h\nu \rightarrow CH_3^{\bullet} + CHO^{\bullet} \qquad \text{(R 2.36)}$$

However, in the lower troposphere, the OH reaction of ethanal predominates over its photolysis [*Atkinson*, 1994], so that the above scheme will apply.

2.3.3.5 Steady State Formaldehyde Calculation

To calculate the formaldehyde production rate from hydrocarbon oxidation, one has to consider the OH reactivity of a single hydrocarbon or a mixture of hydrocarbons. The reactivity of a specific VOC or a group of VOCs, R_{VOC}, is determined as the product of the concentration and the corresponding second-order rate constant, k, against the oxidant (e.g. OH radical). The OH reactivity has units of per second and is given by eq. 2.14 or the sum eq. 2.15,

$$R_{VOC_i} = k_i \cdot [VOC_i], \qquad \text{(eq. 2.14)}$$

$$R_{VOC} = \sum k_i \cdot [VOC_i], \qquad \text{(eq. 2.15)}$$

where k_i [cm^3 molec^{-1} s^{-1}] is the rate constant for the reaction of OH with the i^{th} VOC. For alkenes also the oxidation with O_3 can be important producing CH_2O.

The CH_2O yield Y_{CH2O} (≤ 1) of a reaction is the percentage amount of the product formaldehyde theoretically obtained from the reaction and is a function of the NO concentration (see *Sec. 2.3.3*). Weighting the reactivities with the respective formaldehyde yields (eq. 2.16) gives the formaldehyde *production efficiencies*, i.e. the relative contributions of the measured VOCs to formaldehyde production.

$$PE_{CH2O}(VOC_i) = R_{VOC_i} \cdot Y_{CH2O}(VOC_i) \qquad \text{(eq. 2.16)}$$

The formaldehyde yields for the oxidation of several VOCs are summarised in Table 2.4. Only the yields from the first oxidation step (until reaching the first stable products) are considered. For further reaction steps it is hard to quantify the fraction of formaldehyde formed, because the branching reactions after VOC oxidation become manifold and unmanageable and depend on the composition of the air mass. However, further production of formaldehyde can occur from short-lived intermediates. The formaldehyde yields of many important species are uncertain, e.g. for aromatics. Since in the first oxidation step of aromatics no formaldehyde is formed, their formaldehyde yields were taken as zero by *Lee et al.* [1998]. However, *Volkamer* [2001] shows that formaldehyde is formed rapidly from the OH reaction of toluene with a yield of 37.2%. Not taking aromatics into account might result in an underestimation of the CH_2O formation. For FORMAT, the highest formaldehyde production efficiencies were found for alkenes (ethene and propene).

Finally, formaldehyde production rates can be calculated by multiplying the production efficiencies of the VOCs with the actual oxidant (i.e. OH or O_3) concentration (eq. 2.17).

$$PR_{CH2O}(VOC_i) = PE_{CH2O}(VOC_i) \cdot [OH] \qquad \text{(eq. 2.17)}$$

The OH concentration can be estimated with the methods given in *Sec. 2.2.6*. Typical concentrations on cloud free days in the Milano area around noon, obtained with the steady state method, were 4×10^6 molec cm^{-3} for September 2003. Though the reactivities towards ozone are very small compared to the reactivities towards the OH radical, the CH_2O production rates are comparable, since the O_3 concentration is by far larger than the OH concentration.

Assuming local steady state between CH_2O production by VOC oxidation and formaldehyde destruction, the daytime steady state formaldehyde concentration is derived from

$$[CH_2O] = \frac{\sum_i Y_i \cdot k_i \cdot [X] \cdot [VOC_i]}{k_{CH2O} \cdot [OH] + J_{CH2O}}, \qquad \text{(eq. 2.18)}$$

where k_i is the rate constant for the reaction of a VOC with the oxidant X, k_{CH2O} is the rate constant for the reaction of CH_2O with OH and J_{CH2O} is the total photolysis frequency of CH_2O. The relation assumes the maximum formaldehyde yields Y_i given in Table 2.4 which are valid for high NO_x conditions. It thus presents an upper limit for the CH_2O mixing ratio resulting

from VOC oxidation. The equilibrium concentration of formaldehyde depends on the OH concentration and J_{CH2O}. Approximate steady state conditions should be prevalent at time periods around midday, when CH_2O lifetime becomes shortest and also the photochemical destruction of VOCs is expected to peak.

The steady state calculation presented in eq. 2.18 will usually not explain the actual formaldehyde concentrations with the compounds measured since the calculation of the instantaneous formaldehyde production rate requires the knowledge of the PAN concentration and of oxygenated VOCs, which produce most CH_2O. Furthermore there is an uncertainty considering direct emissions. However, the steady state calculation (eq. 2.18) is useful to approximate the contribution of individual VOCs to the CH_2O budget and CH_2O variability.

The secondary sources of CH_2O vary seasonally, diurnally and geographically. The correlation of the CH_2O concentration distribution with the emission field of the parent VOCs depends on the VOC lifetime, on the CH_2O yield from VOC oxidation and on the CH_2O lifetime. The formaldehyde lifetime is short enough that the concentration field of formaldehyde should correlate well with the emission field of the short-lived parent VOC (see *Sec. 2.3.2.3*). The lifetimes of alkenes are generally longer than that of isoprene and those of alkanes are much longer [*Atkinson*, 1994]. Therefore, CH_2O from these VOCs is distributed over large regions. Since formaldehyde is formed in virtually all cases of VOC oxidation [*Logan et al.*, 1981] it is not source-specific.

2.4 Processes in the Planetary Boundary Layer

The planetary boundary layer (PBL) is defined as that part of the troposphere that is directly influenced by the presence of the earth's surface and responds to surface forcings with a timescale of about an hour or less [*Stull*, 1988]. These forcings include frictional drag, evaporation and transpiration, heat transfer and terrain-induced flow modification. The boundary layer thickness is quite variable in time and space. Its vertical extent varies between less than 100 m in very calm and clear nights and more than 2000 m with stormy weather or on clear and hot summer days. The remainder of the air in the troposphere is loosely called the free troposphere.

Turbulence, induced by wind, surface roughness or buoyancy, is one of the important transport processes in the boundary layer [*Stull*, 1988]. Since the emission and secondary formation of air pollutants occurs in the boundary layer, their rate of dilution depends on the degree to which turbulence propagates through the layer, i.e. on the stability conditions of the PBL. The thermal stability, which is determined by lower atmospheric temperature profiles, and the height of the boundary layer exhibit a clear diurnal course (*Sec. 2.4.1*), mainly driven by the radiation balance of the underlying surface. In the following, the processes relevant for continental conditions in mid-latitudes are outlined according to *Stull* [1988] as far as it is necessary to describe their influence on the trace gas concentrations near the surface.

2.4.1 Diurnal Variations of the Planetary Boundary Layer

Over land surfaces in high pressure regions, the boundary layer has a well defined vertical structure that evolves with a diurnal cycle which is shown in *Fig. 2.14*. The parts of the boundary layer are characterised in this section. For the identification of the layers, the knowledge of the virtual potential temperature profile (*Fig. 2.15*) is usually sufficient. The diurnal cycles of primary and secondary trace gases at ground level are governed by the meteorological processes in the boundary layer, because of their influence on transport and dilution (*Sec. 2.4.2*).

The lowermost 10 to 200 m over ground are referred to as *surface layer*. Here, turbulent fluxes and stress vary by less than 10% of their magnitude. Most primary trace gases are emitted into the surface layer and dry deposition (see *Sec. 2.4.4*) occurs in contact with the earth's surface.

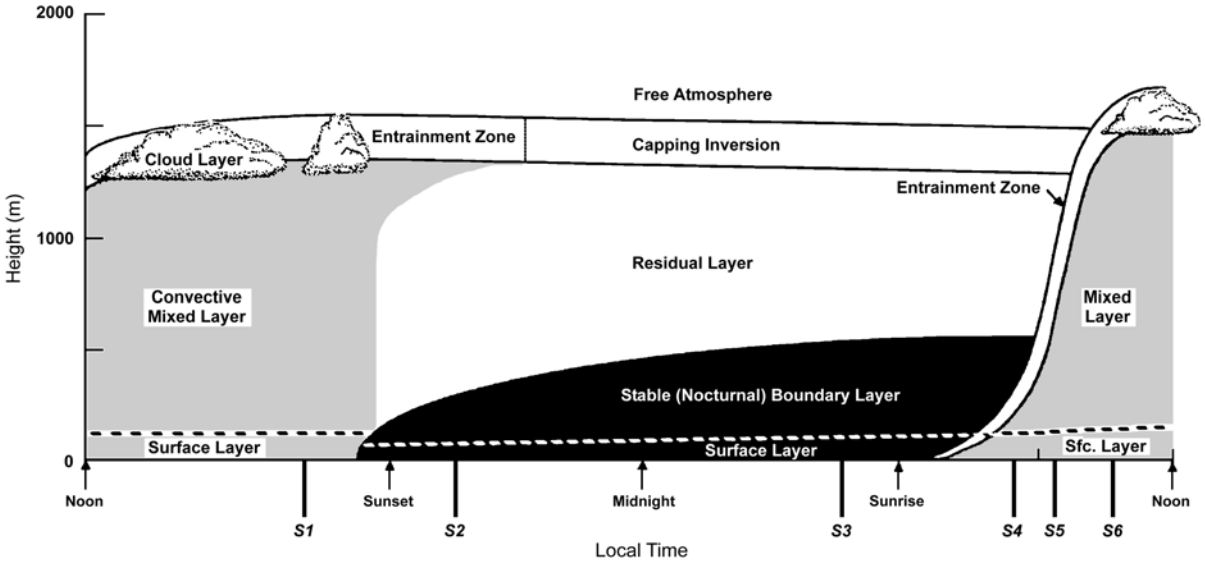

Figure 2.14: Typical development of the PBL in high-pressure regions over land during the course of the day. Three major parts can be distinguished: a very turbulent mixed layer, a less turbulent residual layer containing former mixed-layer air and a nocturnal stable boundary layer of sporadic turbulence. Vertical structures at the times marked by S1-S6 are displayed in Fig. 2.15 (figure from Stull [1988]).

During the day, the layer has only a little thickness (maximum 50 m) and an overadiabatic temperature gradient (cp. *Fig. 2.15*), whereby the emitted trace gases are in general rapidly mixed into the upper air.

In the *mixing layer* (ML), adjacent to the surface layer, the predominant part of photo-oxidant formation takes place. The turbulence in the ML is usually convectively driven, i.e. strong vertical mixing occurs due to thermals of warm air rising from the ground. The vertical extension of the mixing layer increases in the course of the day since quick thermals can ascent further due to excessive kinetic energy, whereby a mixing (entrainment) with the above air occurs. The ML reaches its maximum depth in late afternoon. In summer, the mixing height reaches altitudes of 1500-2000 m over ground in the Po Basin. Virtual potential temperature profiles are nearly adiabatic in the middle portion of the ML (S1 of *Fig. 2.15*). An inversion at the top of the ML acts as a lid to the rising thermals, thus restraining the domain of turbulence. The convection over flat terrain ceases about half an hour before sunset and turbulence decays in the formerly well-mixed layer.

The resulting layer of air is sometimes called the *residual layer* or *reservoir layer* (RL) because its initial mean state variables and concentration variables are the same as those of the recently decayed mixed layer. The trace gas concentrations in the RL stay largely constant during the night, because the photooxidation processes driven by solar irradiation and the deposition are not effective there. The RL is neutrally stratified (S2 in *Fig. 2.15*) and does not have direct contact with the ground. It often exists for a while in the mornings before being entrained into the new ML (see S4, S5 in *Fig. 2.15*). When the top of the next day's ML reaches the base of the RL, the ML growth becomes very rapid.

During clear, windless nights in the warm season, the radiative cooling of the ground overnight often causes the formation of a temperature inversion at ground level. The *stable nocturnal boundary layer* (SBL) arises as soon as the ground becomes colder than the air above (S2 in *Fig. 2.15*) and can have variable extensions, depending on the topography. Since inversions strongly limit the vertical exchange of air masses, a distinct accumulation of trace gases emitted

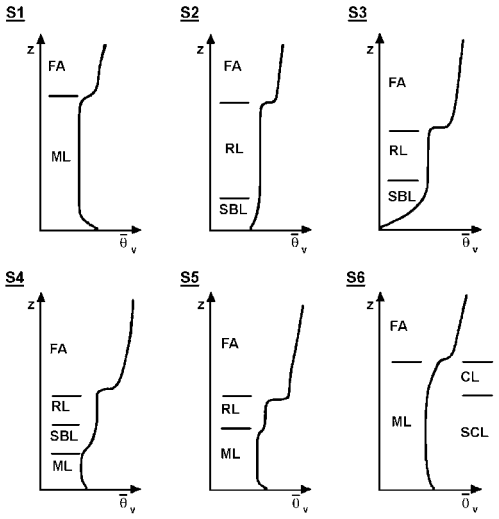

Figure 2.15: Profiles of the mean virtual potential temperature, $\bar{\theta}_v$, showing the boundary layer evolution during a diurnal cycle starting at about 16 h local time. S1-S6 identify each sounding with an associated launch time in Fig. 2.14 (figure adapted from Stull [1988]).

close to the ground occurs. The stable boundary layer is characterised by statically stable air which tends to suppress turbulence. Pollutants emitted into the stable layer disperse relatively little in the vertical. They disperse more rapidly in the horizontal. During the night, the nocturnal stable layer gradually increases in thickness (S2, S3 of *Fig. 2.15*). The height of the nocturnal boundary layer is likely to be between ~ 200 m and below 100 m. The nighttime PBL is often stably stratified over its full depth. In case of windy and cloudy weather, neutral thermal stratification prevails and there is a more smooth transition from the boundary layer to the free troposphere. These conditions are usually not connected with critical air pollution episodes.

After sunrise, solar radiation warms the ground and the negative thermal layering induces vertical mixing in increasingly higher layers. A convective mixed layer (see above) rises from the ground and the inversion is destroyed gradually (S4, S5 in *Fig. 2.15*). Since most pollutant sources are near the earth's surface, pollutant concentrations can build up in the BL. Pollutants are transported by eddies such as thermals. Cloud cover reduces the insolation at ground level and thus the intensity of thermals. Thus, the ML exhibits slower growth on cloudy days and may even become non-turbulent or neutrally stratified.

2.4.2 Micrometeorology - Chemistry Relations

The vertical mixing in the planetary boundary layer, which is linked to the vertical thermal state of the lower atmosphere, has a determining influence on the diurnal cycle of trace gas concentrations at ground level (see also *Sec. 2.4.3*), since the variations of trace gas concentrations are linked to the mixing volume. The course of nitrogen oxides and ozone concentrations, as it is typically observed on an anthropogenically polluted site during fair weather conditions in summer, is shown in *Fig. 2.16*.

After sunset, the air close to the ground is protected from vertical mixing by the nocturnal inversion (see previous section) and primary pollutants like NO, CO, also Rn (see *Sec. 2.4.3*) accumulate. The emitted NO is rapidly transformed to NO_2 by reaction with O_3 (R 2.13). This explains the simultaneous increase in NO_2 concentration and decrease in O_3 concentration in the evening. In addition, O_3 can be reduced by dry deposition (see also *Sec. 2.4.4*). Due to the persistent traffic emissions and the low mixing, these processes continue until in the early

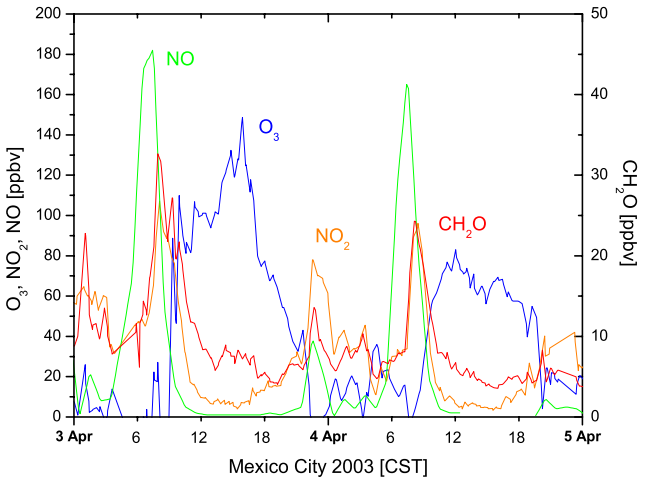

Figure 2.16: Diurnal cycle of O_3, CH_2O and NO_x concentrations as observed in a high emission rate area during the MCMA-2003 campaign at Mexico City.

morning hours usually all ozone close to the ground is removed. At less polluted sites, the ozone levels do not drop to zero ppbv during the night due to a lack of NO emissions.

The nitric oxide emissions by the morning commuter traffic in the absence of ozone lead to high NO concentrations measured during the densest traffic. Most of all, emissions and reduced vertical mixing in the shallow boundary layer determine the concentrations during this time. When the sun rises, photochemical VOC transformations generate CH_2O and also lead to the production of O_3. However, initial ozone build-up is suppressed due to the efficient titration reaction with NO, producing NO_2. This process delays peak ozone to near noon until NO has fallen to low concentrations.

In the course of the morning, the nocturnal inversion dissolves, whereby the near-surface NO and NO_2 concentrations decrease, since mixing with air of higher layers occurs, which contains much smaller NO_x concentrations. At 09:30 h the height of the mixed layer typically experiences rapid growth. At the same time, the O_3 concentration increases strongly, because of the increasing mixing height, incorporating residual layer air, with the high O_3 concentrations from the previous day, into the mixing layer. The ozone concentration subsequently continues increasing because of photochemical O_3 formation. Mixing during the day from 10:30 h to 16 h is evidently efficient in keeping concentrations of NO_x at low values.

A shallow nocturnal inversion is again established in the evening. Surface level emissions accumulate again and the decrease in O_3 at 20 h due to titration is coincident with a peak in NO_x.

2.4.3 Radon as a Tracer for Mixing in the PBL

To determine the mixing conditions in the atmosphere, one usually requires sounding data as shown in *Fig. 2.15* or micrometeorological measurements to derive the vertical eddy diffusivity *K*. However, also radon can be used as a tracer of the stability and mixing of the planetary boundary layer, as pointed out in this section.

Radon 222 is a radioactive noble gas, that is released continuously at relatively constant rates by all soil types **. Its concentration is measured as an activity in [Bq m^{-3}] as described in *Sec. 3.2.4*. Typical radon activities in continental boundary layers are between 1 and 30 Bq m^{-3}. Since the ^{226}Radium concentration is rather constant in different soil types (1 µg g^{-1} soil), the ^{222}Radon exhalation rate from continental soil surfaces is quite homogeneous. It ranges from

**. ^{238}Uranium is a trace component of all soils and the primary isotope in the main uranium-radium decay series. The noble gas ^{222}Radon is one of the decay products in this series, and, after production by ^{226}Radium decay, part of it diffuses from the soil air into the atmosphere.

30 to 100 Bq m^{-2} h^{-1}, depending mainly on the type and the texture of the soil and varying dependent on the meteorological parameters [e.g. *Levin et al.*, 2002]. The radon exhalation from ocean surfaces, in contrast, is negligible [*Wilkening and Clements*, 1975]. In the Lombard plain, radon is emitted with a typical emission rate of ≈ 70 Bq m^{-2} h^{-1} [*Facchini et al.*, 1981].

Radioactive decay can be considered as the main radon sink. With a decay constant $\lambda = 0.0076$ h^{-1}, a half-life of $T_{1/2} = 3.8$ days or a lifetime $\tau = 5.5$ days is derived. For short periods its radioactive decay can be neglected, since a strong short-term diurnal variability is overlaid. As radon is an inert trace gas, emitted only by the soil, its concentration in the troposphere is subject to turbulent diffusion, strongly representing the present atmospheric dynamics. Atmospheric radon may thus be used as a natural indicator for the build-up and break-up of ground inversions, i.e. for the efficiency of vertical mixing.

Near the ground, the radon concentration usually undergoes a typical diurnal variation with a maximum at the end of the night, caused by accumulation during conditions of nocturnal stability. A rapid decrease takes place as soon as the thermal inversion is destroyed. The dispersion of radon in the morning marks the start of vertical turbulence, which carries the radon to high height levels. Radon is diluted more and more in the extending ML and a minimum of a few Bq m^{-3} is reached in the afternoon when the mixed layer gains its maximum development. ^{222}Rn can thus be used as a quantitative tracer to parameterise diurnal changes of the inversion layer depth [*Levin et al.*, 2002]. On overcast or rainy nights, the SBL does not form and little or no accumulation of radon is observed. Low, quasi-constant values are also found in advective and turbulent situations when radon and air pollutants disperse both horizontally and vertically.

The time series of radon may thus be used as a combined tracer for atmospheric stability and the height of the PBL even without any knowledge of the vertical diffusion coefficient $K(z)$. In general, advection has to be taken into account, because the exhalation of radon depends on the soil type (see above). However, omitting the advection term in 1D models and in the discussion of vertical transport is justified by the fact that variations of the considered trace gas mixing ratios proceed on a much shorter timescale.

Since the diurnal variations of a trace gas depend both on the varying strength of the source/sink and on the intensity of transport (atmospheric dispersion), one needs knowledge of the current values of the vertical eddy diffusivity K in the atmosphere. To this end the parallel use of a tracer, namely ^{222}Rn, is helpful. After diffusion from the soil air into the atmosphere, ^{222}Rn takes part in atmospheric transport in the same way as do other soil borne gases [e.g. *Schmidt et al.*, 2001]. If compared to the mixing ratios of other gases, its activity can thus be used to parameterise the dilution of ground-level emissions in the atmospheric surface layer driven by vertical mixing. The *radon tracer method* [e.g. *Schmidt et al.*, 2001] takes advantage of this property of radon to estimate the source strength of gases exhaling out of the soil or emitted close to the ground from simultaneous measurements of Radon 222 and these gases, provided that the ^{222}Rn flux at the soil surface is known. The radon tracer method is introduced here shortly and will be used in *Sec. 5.3.4* in a modified form.

For the following paragraph, we assume a trace gas X, emitted from or close to the ground (e.g. *Schmidt et al.* [2001] used X = N_2O). From the slopes of the correlation between night-time X and ^{222}Rn concentrations, average night-time X emission rates can be estimated by using a simple one-dimensional approach: Assuming that X is released to the atmosphere at a constant rate $\overline{j_X}$ and accumulates during the night within a well-mixed ground level inversion layer of height $\overline{H}$ (assumed to be constant in time), the rate of change of a stable trace gas concentration in this ground-level atmospheric box can be described by eq. 2.19. In the case of a radioactive species, such as ^{222}Rn, radioactive decay at a rate of $\lambda c_{Rn}(t)$ has to be considered, leading to eq. 2.20.

$$\Delta c_X(t)/\Delta t = \overline{j_X}/\overline{H} \qquad \text{(eq. 2.19)}$$

$$\Delta c_{Rn}(t)/\Delta t = \overline{j_{Rn}}/\overline{H} - \lambda c_{Rn}(t) \qquad \text{(eq. 2.20)}$$

The unknown inversion layer height $\overline{H}$, which is the same for ^{222}Rn and X, is eliminated by combining eq. 2.19 and eq. 2.20,

$$\overline{j_X} = \overline{j_{Rn}} \cdot \frac{\Delta c_X/\Delta t}{\Delta c_{Rn}/\Delta t} \cdot \left(1 + \frac{\lambda_{Rn} c_{Rn}}{\Delta c_{Rn}/\Delta t}\right)^{-1}, \qquad \text{(eq. 2.21)}$$

which, for $\lambda c_{Rn} \ll \Delta c_{Rn} / \Delta t$, simplifies to

$$\overline{j_X} = \overline{j_{Rn}} \cdot \frac{\Delta c_X}{\Delta c_{Rn}} \cdot \left(1 - \frac{\lambda_{Rn} c_{Rn}}{\Delta c_{Rn}/\Delta t}\right). \qquad \text{(eq. 2.22)}$$

The flux of X into the air can thus be calculated from the X/^{222}Rn concentration rate of change ratio and the ^{222}Rn exhalation rate $\overline{j_{Rn}}$, together with a correction term (in brackets) that takes the ^{222}Rn decay into account (eq. 2.22). During a typical nighttime inversion situation, lasting 8-12 hours, the change in radon activity as a result of radioactive decay, offset by fresh emission from soil, is only 3-4% [*Schmidt et al.*, 2001]. Therefore, a mean correction factor of 0.965 is applied when estimating ^{222}Rn-based X fluxes for the regional catchment area.

2.4.4 Deposition

Physical removal at the earth's surface is important for many primary and secondary pollutants. Particles and gases can be deposited at the earth's surface in two ways, depending on the phase in which a species strikes the earth's surface and is taken up.

Pollutants may be dissolved in clouds, fog, rain or snow. When these water droplets impact surfaces like soil, grass, trees, buildings, etc., it is termed *wet deposition*. The rate of wet deposition of a pollutant is proportional to the pollutant concentration and to the precipitation intensity [*Shaw*, 1984].

Pollutants in the form of either gases or small particles can also be transported to ground level and absorbed and/or adsorbed by materials there or are adsorbed on the surfaces of airborne aerosol particles without first being dissolved in atmospheric water droplets. This is called *dry deposition*. The surface itself may be wet or dry – the term dry deposition only refers to the mechanism of transport to the surface, not to the nature of the surface itself. Dry deposition is a very important mechanism for removing pollutants from the atmosphere in the absence of precipitation. The amount of a species deposited per unit area per second in a geographical location, that is, the net flux, F, of the species to the surface, is proportional to the concentration c of that species in air (eq. 2.23). The deposition velocity, v_{dep} [cm s^{-1}], is the proportionality constant, relating flux and concentration,

$$F = -v_{dep} \cdot c, \qquad \text{(eq. 2.23)}$$

where c is the concentration at a reference height z. By convention, the deposition velocity is a positive number, but fluxes towards the surface are taken as negative; hence the negative sign in eq. 2.23. The deposition velocity is also frequently related to a resistance, r :

$$v_{dep} = 1/r \qquad \text{(eq. 2.24)}$$

$$r = r_{gas}(z) + r_{boun} + r_{surf} \qquad \text{(eq. 2.25)}$$

By analogy to electrical systems, the resistance r can be thought of as consisting of several components. Three such components are often defined (see eq. 2.25). The surface resistance (r_{surf}) depends on the detailed characteristics of the surface itself, e.g. type (leaf, building, soil, snow), wetness, etc., as well as on the nature of the pollutant being deposited (e.g. affinity of the surface for the species). The boundary layer resistance (r_{boun}) in the film of air immediately adjacent to the surface depends on the molecular diffusivity of the depositing species in air. The gas-phase resistance (r_{gas}) is determined by the vertical eddy diffusivity, K, which depends on the

evenness of the surface and the micrometeorology (wind speed, solar surface heating, etc.) that transports the gas to the surface. Since the eddy diffusivity, is a function of height, z, above the earth's surface, also the gas-phase resistance depends on the height, as does the concentration of the pollutant. As a result, the deposition velocity is also a function of height.

The relative importance of gas-phase and surface resistances depends on the nature of the depositing species and the surface as well as the meteorology [*Chameides*, 1987; *Wesely and Hicks*, 2000]. For highly reactive gases, the surface resistance may be sufficiently small so that transport to the surface becomes rate limiting; for example, the surface resistance for deposition of HNO_3 on grass during the day has been shown to be approximately zero. Similarly, *Chameides* [1987] has shown that the dynamical resistance determines essentially entirely the uptake into dew of highly soluble species such as HNO_3, whereas for less soluble compounds such as SO_2 and O_3, the surface resistance plays an important role.

Table 2.7: Deposition velocities of several gases on different surfaces.

Gas	Surface	v_{dep} [cm s^{-1}]	Reference
O_3	grass	0.5-1.8	*Graedel and Crutzen* [1994]
O_3	deciduous forest	0.2-1.1	*Krinke* [1999]
SO_2	coniferous woodland	0.1-1.0	*Graedel and Crutzen* [1994]
HNO_3	grass	1.1-3.6	*Graedel and Crutzen* [1994]
CH_2O	deciduous forest	0.5-1.4	*Krinke* [1999]

Because of the effects of physical, chemical, biological, and meteorological parameters on the resistances, the deposition velocity v_{dep} also depends on these. As a result, deposition velocities reported for various trace gases and surfaces show a wide range, from several hundredths to several cm s^{-1}, depending on the conditions during the measurement (see Table 2.7). For example, the mean value of v_{dep} for SO_2 over grass in one study was 0.56 cm s^{-1} for dry grass but 0.93 cm s^{-1} for wet grass. It is well-established that deposition velocities have a diurnal variation with daytime values being greater than those at night [e.g. *Galbally and Roy*, 1980] (see also *Fig. 2.10*). For example, peak values of O_3 deposition of up to 1 cm s^{-1} during midday but less than 0.1 cm s^{-1} in the evening have been reported. The wide ranges given for the deposition velocities reflect a combination of experimental uncertainties as well as real differences due to meteorology, nature of the surface and diurnal variations.

3 Measurement Methods

3.1 Formaldehyde Detection Techniques in the Atmosphere

The ambient formaldehyde concentration is currently measured with a number of different methods [*Vairavamurthy et al.*, 1992]. Contact-free methods, which are based on the characteristic optical absorption of the molecule in the ultraviolet or infrared region, are non-destructive and prevent reactions on the surface of a sampler. Differential Optical Absorption Spectroscopy (DOAS, *Sec. 3.1.1*) and Fourier Transform Infrared (FTIR, *Sec. 3.1.2*) spectroscopy are such direct gas-phase measurement techniques. Many techniques require the transfer of formaldehyde from the gas phase into the liquid phase. Most widely used are wet-chemical formaldehyde analysers (Hantzsch monitors, *Sec. 3.1.3*) that employ the fluorescence detection of formaldehyde-deduced species in an aqueous solution. The reaction of carbonyl compounds and hydrazone derivatives with subsequent liquid chromatographic separation is also a well-established method (DNPH, *Sec. 3.1.4*). An advantage of the optical methods, which were mainly used for the measurements shown here, is their ability to measure absolute trace gas concentrations without disturbing their chemical behaviour. For the measurement of formaldehyde, the DOAS method is well suited because of the highly structured CH_2O cross-section. The advantage of the Hantzsch technique is the ability to make simple, low cost in-situ measurements. An advantage of the DNPH method is that it allows a large number of related compounds to be collected and analysed on the same sample. Simultaneous in-situ measurements of formaldehyde by DOAS, FTIR, Hantzsch and DNPH were performed during a field campaign in Milano and the results are compared in *Sec. 5.2*. This chapter specifies several analytical techniques used to measure formaldehyde in the boundary layer. Since the active DOAS technique was used in this work, it is described in detail. At the end of this chapter measurement principles used by other groups are outlined, provided that the corresponding measurements were included in the data analysis in *Chapters 5* and *6*.

3.1.1 Differential Optical Absorption Spectroscopy

The Differential Optical Absorption Spectroscopy (DOAS) is a commonly used and powerful optical method, applied to atmospheric trace gas measurements since the late 1970's [e.g. *Platt et al.*, 1979]. The basic principle of DOAS is as follows: Light, typically in the visible and/or UV wavelength range, passes through the atmosphere where it undergoes absorption processes. It is collected by a telescope, recorded by a spectrograph-detector system and eventually spectrally analysed according to the Lambert-Beer law of light extinction. Broad-band extinction and narrow-band absorption structures appear in the measured spectra. The DOAS method uses

the narrow molecular absorption bands to identify trace gases. Their absorption strength is used to retrieve tropospheric and/or stratospheric trace gas concentrations. Several trace gases of particular importance for atmospheric chemistry have been measured using this technique. For an overview, see *Platt* [1994]. The compounds CH_2O, NO_2, O_3, HONO and SO_2, absorbing in the UV-A and UV-B, are of special interest for this thesis. Formaldehyde was detected by DOAS already in the end of the 1970's by *Platt et al.* [1979].

DOAS applications can generally be divided into passive and active DOAS systems, dependent on the light source used. The light source of *passive* DOAS systems can be the moon, stars or usually the sun. The measurement principle is to collect either direct light with an absorption pathway from the source to the telescope or using stray light which has a diffuse pathway through the atmosphere. The stray light received from one or multiple (MAX-DOAS) distinct azimuth angles has been used for several applications: long-term measurements of trace gas concentrations in the upper troposphere or measurements of direct emission plumes (e.g. of a volcano) with instruments located on the ground [*Bobrowski et al.*, 2003], measurements on board of aeroplanes [*Heue et al.*, 2005 (AMAXDOAS)], or measurements in the stratosphere with instruments attached to stratospheric balloons [*Pfeilsticker and Platt*, 1994]. With the GOME and SCIAMACHY instruments mounted on satellites also remote sensing from space is valuable [*Wagner and Platt*, 1998; *Chance et al.*, 2000]. The imaging DOAS (I-DOAS) [*Lohberger et al.*, 2004; *Louban*, 2005] is a new passive method for the spatially resolved measurement of exhaust plumes.

For measurements in the planetary boundary layer or for kinetic studies (e.g. in smog chambers) an *active* DOAS system is favourable. Thereby, a light beam emitted from an artificial light source is sent through the atmosphere on a well-defined light path. Two active setups are common: the long path DOAS (LP DOAS) to measure the integrated absorption along a light path of up to several kilometres [*Axelsson et al.*, 1990], and the White system which uses a long absorption path realised in a very confined space (e.g. 15 m) by multiple reflection [*White*, 1976]. The latter is employed for point measurements. The use of artificial light sources in active DOAS systems has the advantage that measurements can also be performed at night and at wavelengths below 300 nm, where aromatic compounds like benzene and toluene absorb. Further, due to the well-defined light paths, absolute trace gas concentrations are derived. In the following, the focus will be on active DOAS systems, which were used in this thesis.

3.1.1.1 Absorption Spectroscopy

Light passing a medium is reduced in its intensity mainly by two effects. Firstly, molecules irradiated by electromagnetic radiation absorb at distinct wavelengths directly linked to their electronic, vibrational and rotational states and therefore absorb the radiation energy yielding an excited quantum-mechanical state. The property of unique absorption structures for individual molecules is used in absorption spectroscopy to identify the molecules. Secondly, scattering processes lower the light's intensity while it is passing through the medium. Scattering can be attributed to two processes: Mie scattering, occurring on aerosol particles larger than the light's wavelength, is described by the Mie scattering coefficient ε_M. Scattering by molecules or particles smaller than the light's wavelength is described by the Rayleigh scattering coefficient ε_R. Both, Rayleigh and Mie scattering, strongly depend on the wavelength λ with different wavelength dependencies for both scattering processes ($\varepsilon_M \propto \lambda^{-1.3}$, $\varepsilon_R \propto \lambda^{-4}$).

The wavelength-dependent attenuation of light intensity from its original intensity $I_0(\lambda)$ to the received intensity $I(\lambda)$ due to the extinction processes of scattering (ε_R and ε_M) and absorption $\sigma_i(\lambda)$ by a number of trace gases along a path L is described by the Lambert-Beer law:

$$I(\lambda, L) = I_0(\lambda) \cdot \exp\left(-\int_0^L \left(\varepsilon_R(\lambda, l) + \varepsilon_M(\lambda, l) + \sum_i \sigma_i(\lambda, p, T) \cdot c_i(l) \right) dl \right) \qquad \text{(eq. 3.1)}$$

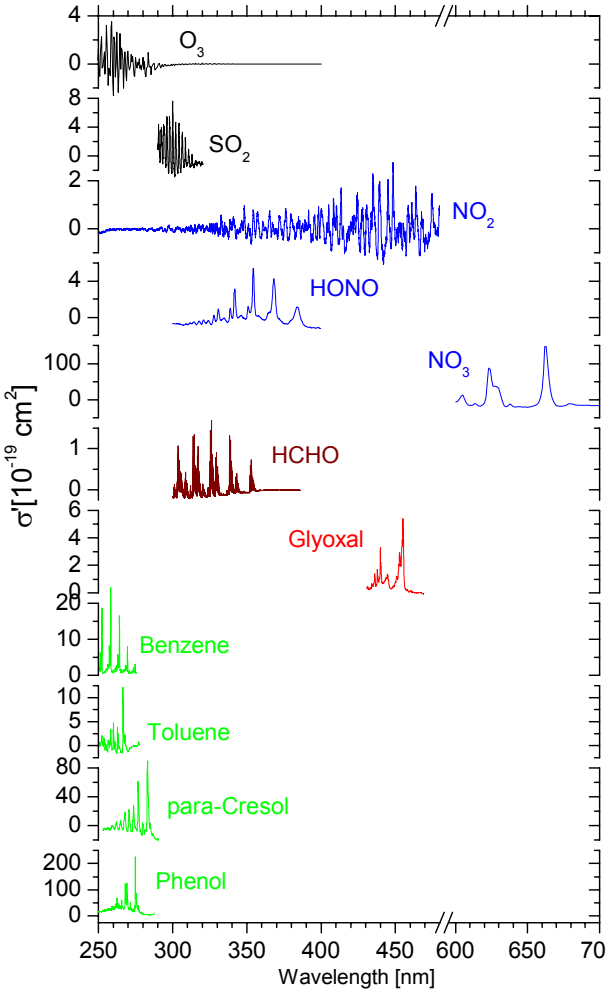

Figure 3.1: Differential absorption cross-sections $\sigma'(\lambda)$ of selected atmospheric trace gases measurable by the DOAS technique (figure from Volkamer [2001]).

The absorption of a trace gas *i* is characterised by its *absorption cross-section*, σ_i, which depends on the wavelength λ, the temperature *T* and the pressure *p*. It is quantified by the integrated concentration $c_i(L)$ of the absorber along the optical path *L* which is also referred to as the *column density*, a_i (eq. 3.2).

$$a_i = \int_0^L c_i(l)dl \approx \bar{c}_i \cdot L \qquad \text{(eq. 3.2)}$$

The absorption by all trace gases present in the light path is measured simultaneously. The compounds are identified by means of their individual absorption cross-sections (see also *Fig. 3.1*).

The Lambert-Beer law is the basis for chemical and physical studies in the laboratory, where scattering often can be neglected and the initial intensity $I_0(\lambda)$ is measurable, but the classical approach of absorption spectroscopy cannot directly be applied to atmospheric measurements for mainly four reasons. Firstly, as the absorption of trace gases mainly occurs in the near UV or VIS spectral range, special artificial light sources are needed for an active DOAS system. Xenon arc lamps, which are widely used, feature a broad-band spectral shape described by the Planck law but also show emission lines with a bandwidth similar to the trace gas absorptions. The emission lines change both in intensity and spectral shape during the lamp's lifetime and strongly depend on the part of the arc observed. The intensity $I_0(\lambda)$ as would be received from the light source in the absence of any atmospheric absorption is difficult to determine. It would involve removing the air from the absorption path. In addition, stray light (mainly from the sun)

scattered into the DOAS light path enhances the intensity detected at the spectrograph-detector-system and has to be corrected for. And finally, the broad-band extinction in the atmosphere is not only caused by scattering processes, but also by continuum absorption of trace gases. The continuum band absorptions of the different absorbers can neither be distinguished from aerosol extinction nor among each other, as these absorptions feature no structure characteristic of the individual trace gases. It is impossible to quantify all extinction processes in the solar spectral range from a spectrum measured along a light path in the real atmosphere, even if all instrument-specific spectral structures were known. A possible solution is provided by the DOAS technique which is discussed in the following sections.

3.1.1.2 Basic Principle of DOAS

The key to overcome the problem that atmospheric scattering by molecules and particles and broad-band absorption can hardly be quantified is illustrated in *Fig. 3.2*. In the DOAS technique, the measured absorption spectra are separated into different parts representing the broad-band spectral features $\sigma_B(\lambda)$ due to the light source spectrum and scattering and the narrow-band structures $\sigma'(\lambda)$ of absorption and emission.

$$\sigma(\lambda) = \sigma_B(\lambda) + \sigma'(\lambda) \qquad \text{(eq. 3.3)}$$

The definition of the threshold between 'slow' and 'rapid' variation of the absorption as a function of wavelength depends on the width of the absorption bands to be detected and the appearance of other absorption and emission structures, which should be removed from the spectrum. Commonly, high-pass filters are applied to the spectra in order to derive the differential absorption peaks of the atmospheric trace gases. Adequate low-pass filters can be applied subsequently to optimise the signal to noise ratio of the regarded trace gas absorptions, which means to minimise the statistical error of the concentrations looked for.

Usually, $\sigma'(\lambda)$ is referred to as the *differential absorption cross-section*. It describes only the characteristic narrow-band absorption structures of the different trace gases, varying rapidly with λ. The broad-band absorption structures are combined in $\sigma_B(\lambda)$. If the separation, eq. 3.3, is applied to the Lambert-Beer law, eq. 3.1, an equation suitable for atmospheric applications is obtained:

$$I(\lambda) = I_0(\lambda) \cdot \exp\left(-\int_0^L \left(\varepsilon_R(\lambda, l) + \varepsilon_M(\lambda, l) + \sum_i \sigma_{B,i}(\lambda) \cdot c_i(l) + \sum_i \sigma'_i(\lambda) \cdot c_i(l) \right) dl \right)$$

The pressure and temperature dependence can be omitted for most absorbers in the boundary layer and is no longer labelled.

The initial light intensity $I_0(\lambda)$ and the extinction varying slowly with wavelength, i.e. scattering processes and broad-band absorption, are merged to a new *differential baseline intensity* $I_0'(\lambda)$. In the further DOAS analysis only the differential part (I', σ') of the spectra is studied, which characterises the variations in transmitted intensity featuring a strong dependency on the wavelength. Removing the combined broad-band structures yields the Lambert-Beer law in its DOAS relevant form:

$$D'(\lambda) = \ln\left(\frac{I'(\lambda)}{I_0'(\lambda)} \right) = -\int_0^L \left(\sum_i \sigma_i'(\lambda) \cdot c_i(l) \right) dl, \qquad \text{(eq. 3.4)}$$

where the logarithm of the ratio of $I'(\lambda)/I_0'(\lambda)$ is defined as *differential optical density* D'. In practice, the measured spectrum is divided by the lamp spectrum to remove spectral structures from the light source. Additionally, the broad-band structures from scattering in the atmosphere can be removed by dividing the spectrum by a fitted polynomial of appropriate degree [*Stutz and Platt*, 1996]. The differential absorption cross-section references σ_i' for all trace gases that feature characteristic structures in the observed wavelength range have to be computed by

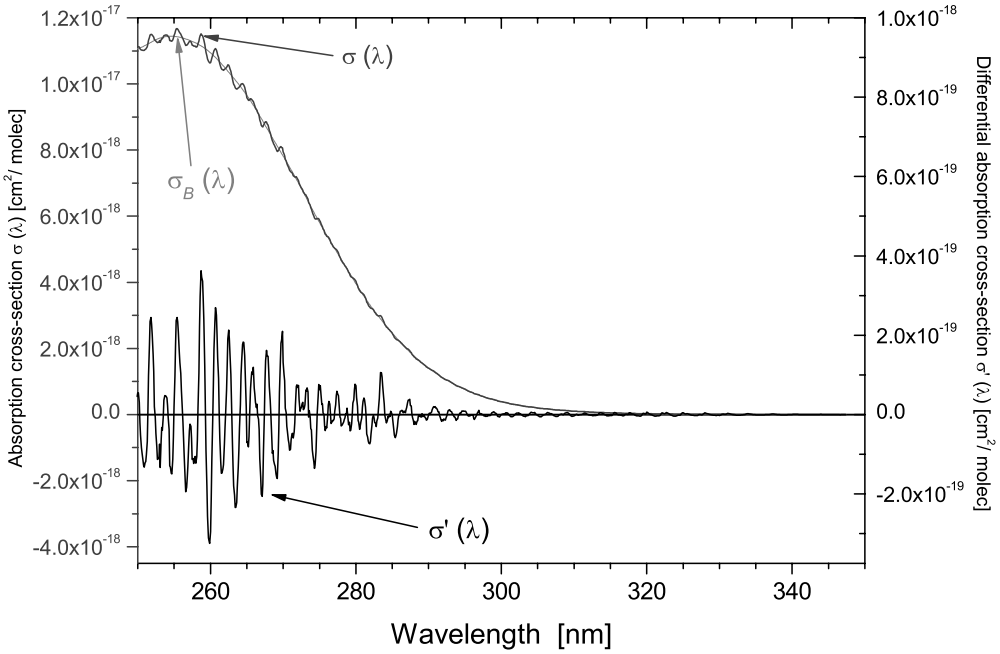

Figure 3.2: Separation of the ozone absorption cross-section according to eq. 3.3 into 'slowly' varying $\sigma_B(\lambda)$ and 'rapidly' varying $\sigma'(\lambda)$ parts by applying a numerical band-pass filter.

applying the same filter algorithm. Now, the only missing variable, apart from the desired trace gas concentrations c_i, is the total light path length L, which can be measured easily and very accurately, e.g. by a laser range finder.

3.1.1.3 Mathematical Description of DOAS Spectra

To obtain atmospheric trace gas concentrations from the measured absorption spectra, the retrieval process has to consider not only the basic atmospheric structures, but also instrument-specific spectral structures, which were not discussed in the previous section. These corrections depend on the setup of the DOAS instrument and on the characteristics of its optical components. The following sections follow the discussion by *Stutz and Platt* [1996].

The principle of an active DOAS system for the measurement of tropospheric trace gases is illustrated in *Fig. 3.3*. The light emitted by a suitable broad-band source has an initial intensity $I_0(\lambda)$ and is transmitted by optics to pass through the atmosphere along an absorption light path L. Extinction by scattering and absorption lowers the initial intensity to $I(\lambda,L)$ as expressed by eq. 3.1. The light is then collected by a telescope to be spectrally decomposed by a spectrograph-detector system. Inset (a) of *Fig. 3.3* shows the spectrum at this point, assuming an atmosphere containing only formaldehyde. As we are interested in the total signal reaching the detector, eq. 3.1 has to be supplemented by the stray light signal $M(\lambda)$ and the photon noise $N(\lambda)$, which depends on $I(\lambda,L)$:

$$I'(\lambda) = I_0'(\lambda) \cdot \exp\left(-\int_0^L \sum_i \sigma_i'(\lambda) \cdot c_i(l)dl\right) + M(\lambda) + N(\lambda) \qquad \text{(eq. 3.5)}$$

The spectrograph, as well as the detector, strongly influence the atmospheric spectrum by lowering the spectral resolution $\Delta\lambda/\lambda$ to a value characteristic for that instrument. The spectral resolution is usually in the range of a few tenths of a nanometre (here ca. 0.4 nm FWHM). The degradation of the resolution is mainly caused by the entrance slit width. Because of the limited resolution of the spectrograph the shape of spectrum $I(\lambda,L)$ changes. Thus, the natural line widths of the atmospheric absorptions are not resolved and the spectrum at the detector no

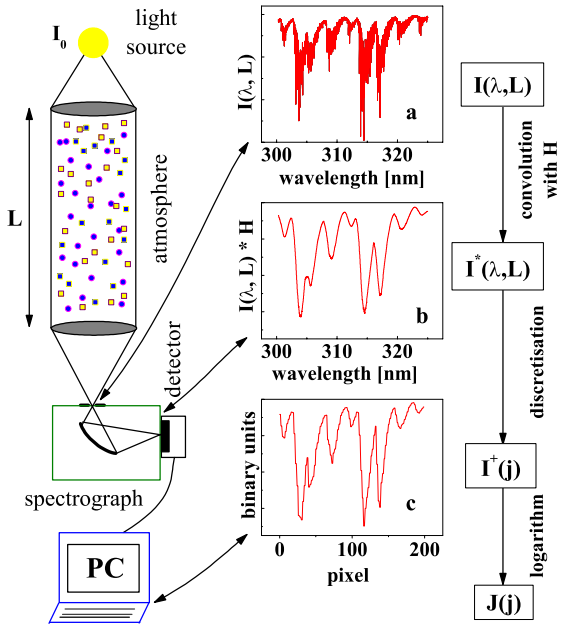

Figure 3.3: Schematic view of a simplified DOAS instrument and the spectra processing. Collimated light undergoes absorption processes on its way through the observed air mass. ***(a)*** *an example spectrum of this light entering the spectrograph is shown, assuming only formaldehyde (CH_2O) to be present in the observed air mass. The absorption spectrum shows the ro-vibronic structure of the CH_2O absorption bands.* ***(b)*** *the same spectrum convoluted by the spectrograph's instrumental function reaches the detector.* ***(c)*** *the spectrum is mapped to discrete pixels by the detector. This spectrum is then stored to the hard-disk of a PC and can be analysed numerically (adapted from Stutz and Platt [1996]).*

longer features the very fine structures of the absorption bands. This is mathematically described by convoluting the initial spectrum $I(\lambda,L)$ with the so-called *instrument function*, H, of the spectrograph to obtain $I^*(\lambda, L)$ [e.g. *Stutz*, 1996; *Stutz and Platt*, 1996]:

$$I^*(\lambda, L) = I(\lambda, L)^*H = \int I(\lambda - \lambda', L) \cdot H(\lambda')d\lambda' \qquad \text{(eq. 3.6)}$$

Inset (b) of *Fig. 3.3* presents the convoluted atmospheric spectrum $I^*(\lambda, L)$ projected on the detector after passing the spectrograph. The detector maps a continuous wavelength range with a width of typically some tens of nanometres onto the discrete number of pixels, e.g. $j = 1024$, available on the detector. Each pixel integrates the intensity in the wavelength interval from $\lambda(j_{low})$ to $\lambda(j_{high})$ *. The intensity $I^+(j)$ detected at a certain pixel j is given by eq. 3.7. The result of this discretisation, i.e. the spectrum as it is sent to the computer after being mapped on the detector and digitised by the electronics, is shown in inset (c) of *Fig. 3.3*.

$$I^+(j) = \int_{\lambda(j_{low})}^{\lambda(j_{high})} I^*(\lambda')d\lambda' \qquad \text{(eq. 3.7)}$$

The wavelength interval per pixel is defined by the wavelength-to-pixel mapping function Γ_J or *dispersion function* of the instrument. The dispersion relation between the pixel j and the corresponding wavelength $\lambda(j)$ can usually be well approximated by a polynomial of first or second order with the parameter vector γ_k [*Stutz and Platt*, 1996]. In the case of a linear dispersion this function is simply $\lambda(j) = \lambda(0) + \gamma_0 \cdot j$ with a constant spectral width γ_0 of a pixel. A spectral

*. $\lambda(j)$ denotes the centre wavelength of the diode element, $\lambda(j_{low})$ the shortest wavelength and $\lambda(j_{high})$ the longest wavelength covered by the element.

shift of the spectrum corresponds to a variation of the parameter γ_0, a linear squeeze or stretch to a change of γ_1, etc. These changes appear in DOAS measurements mainly as a consequence of varying measurement conditions since grating spectrometers are very sensitive for temperature changes. Also variations in air pressure as observed, for example, in airborne measurements, shift the spectrum on the detector due to a change in the index of refraction of air [*Pfeilsticker and Platt*, 1994]. Effects of temperature variations can partly be suppressed by thermal insulation and temperature stabilisation by heating, but must nevertheless be accounted for in the retrieval process (see below). Due to the physical properties of a spectrograph, the dispersion function Γ_J is a strictly monotonous function in the definition interval, and thus can be inverted, which is important to correct for this shift and squeeze.

Finally, the mathematical description of the logarithmised measured spectra is given by eq. 3.8. The scaling factors $a_i'(j)$ correspond to the *column density* of the absorber i (cp. eq. 3.2). They are directly linked to the average concentration and the differential optical density via eq. 3.9.

$$J(j) = \ln(I^{+}(j)) = J_0(j) + \sum_{i=1}^{m} a_i'(j) \cdot S_i'(j) + B'(j) + R'(j) + A'(j) + N'(j) \qquad \text{(eq. 3.8)}$$

$$\bar{c}_i = a_i'/L, \qquad D_i' = \sigma_i' \cdot a_i' \qquad \text{(eq. 3.9)}$$

The narrow-band absorption structures of absorber i are described by its differential cross-section $S_i'(j)$. The broad absorptions of the trace gases are represented by $B'(j)$. The extinction by Mie and Rayleigh scattering is represented by $R'(j)$. The detector is not completely homogeneous in its specifications, and has different quantum yields, dark current and electronic noise signals for the individual diodes. Any variations in the spectral sensitivity of detector or spectrograph are summarised in the term $A'(j)$, which is a function of pixel number. Noise caused by the detector noise as well as by photon statistics is impossible to discriminate and is summarised as $N'(j) = \ln(N(\lambda))$ [*Stutz and Platt*, 1996].

The sum in eq. 3.8 represents the linear combination of several different absorbers present in an atmospheric air mass. In practice, the number of absorbers, m, is limited to the trace gases with absorption structures sufficiently strong to be detectable with DOAS instruments. As the strength of the absorption structures varies with wavelength, the number of trace gases to be included in eq. 3.8 varies with the observed wavelength interval and the trace gas composition of the probed air mass. In the wavelength interval observed in the frame of this thesis, the trace gases CH_2O, O_3, NO_2, HONO and SO_2 were measured simultaneously. To retrieve the concentrations, the superimposed absorption structures of several atmospheric species have to be separated numerically from each other.

The evaluation procedure requires the retrieval of the parameters a_i' and thus the concentrations of the trace gases by taking all the atmospheric and instrumental effects into account. Further, the errors $\Delta a_i'$ of the parameters a_i', i.e. of the measured trace gas concentrations must be derived. Both tasks can be solved with linear least-squares methods if no instrumental effects are encountered. However, spectral misalignment or changes in the dispersion of the reference spectra due to a drift of the spectrograph need to be considered as discussed below.

3.1.1.4 Analysis Procedure

The band-pass filtered and logarithmised measured DOAS spectrum $J(j)$ described by eq. 3.8 is modelled by a linear combination $F(j)$ of the band-pass filtered absorption cross-sections of the trace gases absorbing in the respective spectral range represented by eq. 3.10 and a polynomial $P_r(j)$ of degree r (eq. 3.11) which acts as an additional high-pass filter:

$$F(j) = P_r(j) + \sum_{i=1}^{m} a_i' \cdot S_i'(d_{i,0}, d_{i,1}, \ldots, d_{i,k})(j) \qquad \text{(eq. 3.10)}$$

The absorption structures S_i' of the trace gases, e.g. measured in the laboratory, are input data to the procedure. The polynomial $P_r(j)$ accounts for the broad-band spectral structures caused by the characteristics of the lamp, the scattering processes and the broad-band absorption by trace gases which could not be filtered out completely. It is expressed as

$$P_r(j) = \sum_{h=0}^{r} c_h \cdot (j - j_c)^h, \qquad \text{(eq. 3.11)}$$

where the parameter j_c represents the centre pixel of the spectral region used for the evaluation.

The scaling parameters a_i' and the polynomial coefficients c_h of eq. 3.10 and eq. 3.11, respectively, are found from a linear least-squares fit of $F(j)$ to the measured $J(j)$. Subsequently, the average trace gas concentrations $\overline{c_i}$ [cm^{-3}] along the absorption path L can easily be calculated from the column densities a_i' by using eq. 3.9.

Additional to the linear fit, the analysis procedure has to align the reference spectra $S_i'(j)$ with a fixed wavelength-pixel-mapping Γ_S to the measured spectrum $J(j)$ with a wavelength-pixel-mapping Γ_J. Since the dispersion function Γ_J can vary due to environmental conditions (*Sec. 3.1.1.3*), the spectra have to be recalibrated and the dispersion function has to be adjusted. This can be achieved by shifting ($d_{i,0}$ in eq. 3.10) and stretching/squeezing ($d_{i,k}$, where k is the order of the squeeze) the reference spectra in wavelength to achieve the best match of the absorption features in the measured spectrum. Since in this case the fit procedure is no longer linear, a Levenberg-Marquardt fit is used to obtain the spectral alignment parameters $d_{i,k}$.

The analysis procedure is an iterative combination of a standard linear least-squares fit [*Albritton et al.*, 1976; *Bevington*, 1969] of the model F to the spectrum J to derive the scaling factors a_i' and the polynomial coefficients c_h, and the non-linear Levenberg-Marquardt method [e.g. *Press et al.*, 1992a] which determines the spectral shifts $d_{i,k}$ between the measured spectrum and the reference spectra. The aim of the fitting process is to minimise χ^2, i.e. the sum over the differences between the measured optical densities of the individual diode elements of the selected wavelength range and the respective values of the fitted reference spectra

$$\chi^2 = \sum_{j=0}^{n} (J(j) - F(j))^2. \qquad \text{(eq. 3.12)}$$

The procedure starts with the calculation of the linear fit with starting values $d_{i,k}$. The parameters a_i and c_h resulting from this fit are used as input data for the following non-linear Levenberg-Marquardt fit. Only one step of this non-linear iterative method is then performed, yielding the parameters $d_{i,k}$ that are used in the next call of the linear fit. The procedure continuously alternates between the two methods, always using the result of the last call of one method as starting values for the other fit method. This procedure is repeated until one of several stopping conditions for the non-linear fit is fulfilled. Normally, the fit is aborted when the relative changes of χ^2 (eq. 3.12) in the last step are smaller than a given value (usually 10^{-6}) and thus the fit has converged. The fit also stops if a number of repetitions of the iteration, determined by the user, is exceeded, or if the non-linear method becomes unstable [*Gomer et al.*, 1996; *Stutz and Platt*, 1996].

3.1.1.5 Error Estimation

A linear least-squares fit will give the best possible result and the correct errors if the following three assumptions are valid [*Albritton et al.*, 1976].

- The errors of the pixel intensity must have finite variances [*Albritton et al.*, 1976].
- The normal least-squares fit as discussed by *Albritton et al.* [1976] and *Bevington* [1969] which is used in most of the analysis procedures, assumes that the intensity errors of the individual pixels are independent.

• The systematic error of the pixel intensity is zero.

The first assumption can be verified: The error of the $J(j)$ is usually dominated by photonic noise, therefore the intensity variations are Poisson statistically distributed. However, at the high count rates encountered when using an artificial light source, this statistical function can be approximated by a Gaussian distribution. Thus, the standard deviation of the Gauss distribution is used as the error of the DOAS intensity.

The other two assumptions are not generally fulfilled and a bias can occur in the results: As the spectra are generally smoothed to minimise noise effects, the diodes of the detector show cross-dependencies to the neighbouring diodes on both sides of several per cent (see *Stutz and Platt* [1996]). To consider the interdependence of the pixel intensity errors, the least-squares method has to be extended, as described by *Stutz and Platt* [1996]. Eventually, errors of individual pixels, probably due to defective endowment of a diode, cause systematic errors of the pixel intensity (diode sensitivity structures).

The difference of the measured optical density and the result of the fitting routine is called the *residual spectrum* (or just *residual*) $R(j) = J(j) \angle F(j)$. It is an indicator for the quality of the spectral fitting results and determines the detection limit of the measurements. The residual contains all structures that are not explained by the model, for example, noise, instrumental structures and unknown absorbers. If the optical density of the residual is small compared to the trace gas absorption derived in the fitting procedure, the respective trace gas can be well detected.

A common problem with the numerical analysis of DOAS spectra is the occurrence of structures different from pure noise in the residual of the fit. Persistent residual structures cause systematic errors in the analysis which cannot be described by statistical methods. These structures may indicate an unknown absorber † (often referred to as the *X-absorber*) or are caused by the instrument itself and generally occur or disappear at random. Since DOAS is intended to observe optical densities down to less than 10^{-3}, it is necessary to correct for these structures during the analysis procedure. Since structures might change with time, correction spectra have to be taken at regular intervals during the measurement cycles. In addition, several further effects arising from scattering processes in the atmosphere, variable emission features of the light source and from the optics and electronics of the system are overlaid to the measurement spectra and can generate systematic spectral features. A precise identification and description of the residual structure is required. Systematic errors due to X-absorbers or stable residuals can be partially corrected for by fitting a typical residual or the average residual of a series of spectra to the measured DOAS spectra as an additional reference. This is justified, as residual structures due to unknown absorbers generally show strong diurnal or seasonal variations and therefore can be separated from other systematic errors [*Veitel*, 2002]. However, this method has to be applied with care, since the systematic errors discussed above, and therefore the detection limits, are diminished.

The error provided by the combined linear non-linear least-squares fitting procedure underestimates the true statistical error of a derived concentration. To account for the systematic errors of the fit, a correction factor was introduced by *Stutz and Platt* [1996]. This factor can be calculated from the random structures of the residual by Monte-Carlo methods in dependence of spectral resolution, the smoothing width, the width of the absorption structures observed and the degrees of freedom for the shifting and squeezing/stretching during the non-linear fit. It was found to be ~ 3. For a detailed description of the error calculation see *Stutz and Platt* [1996]. All errors in this work refer to this 1 σ error. The detection limit is obtained by multiplying the 1 σ error by a factor of two [*Stutz and Platt*, 1996].

†. Only those absorbers known are fitted to the measured spectrum. However, it is evident that trace gases can be present in an observed air mass which might not be known yet, but contribute to the absorption.

3.1.1.6 Setup of an Active DOAS System

Long path Differential Optical Absorption Spectroscopy (LP DOAS) systems have been employed since the mid 1970's for the measurement of tropospheric trace gases [*Platt et al.*, 1979]. Since then, the setup of the LP DOAS system went through several stages of development. Today the optical setup of a long path DOAS system consists of one Newton telescope emitting a parallel light beam from an artificial light source (usually a Xe arc lamp). The beam is folded once using retro-reflectors. The light is collected by the same telescope after having passed the absorption path of several km twice. The collected light carries absorption structures of trace gases that are present along the light path. The spectral absorptions of several trace gases are measured simultaneously (see also *Sec. 3.1.1.3*). The derived column densities correspond to trace gas concentrations averaged horizontally and vertically along the light path. Therefore, it is often difficult to compare these measurements with in-situ measurements of the same compounds (see also *Sec. 5.3*). To realise point measurements with DOAS, multi-reflection systems are advantageous (White system see *Sec. 3.1.1.6.3*). The measurements are based upon the same principle, however the absorption path is folded into an air volume with a short base length of a few metres.

Two different types of long path DOAS systems were used in this work – the classical LP DOAS and the recently developed multibeam LP DOAS. Both systems were operated with the same type of light source. The used telescopes, spectrographs and detectors, however, were different. The components of the used LP DOAS systems are described in detail in the following sections. First, we exemplify the design of the classical instrument (*Sec. 3.1.1.6.1*), the changes in the multibeam instrument are illustrated afterwards (*Sec. 3.1.1.6.2*).

3.1.1.6.1 The Telescope of the LP DOAS System

The classical long path telescope consists of two coaxial Newtonian telescopes with transmitting and receiving optic combined in one device. This design was developed by *Axelsson et al.* [1990]. A sketch of the setup of a long path DOAS instrument is given in *Fig. 3.4*.

In the optical axis of the telescope, two elliptical plane mirrors are mounted to reflect the light of both outgoing and incoming beams by 90 degrees. The main mirror is a concave spherical mirror of 300 mm diameter and a focal length of 1500 mm. The active DOAS system uses an artificial light source which is placed in the focus of the main mirror, thus the outgoing light beam should be parallel. However, since the arc of the Xe lamps used has a diameter of at least 0.3 mm (Table 3.1), the outgoing light beam is not exactly parallel but slightly diverges along its path through the atmosphere. This results in a light loss depending on the distance from the retro-reflectors. The light travels through the atmosphere where absorption by the trace gases takes place until it reaches a retro-reflector array. The array of corner cube retro-reflectors (precision of 5 arcseconds) which is positioned in a distance of up to several kilometres is used to redirect the quasi-parallel light beam exactly back into the telescope.

Due to the two plane mirrors placed in the optical axis of the telescope, only a ring-shaped area of the main mirror can be used to emit the light beam into the atmosphere. This leads to a light loss of ~ 50% compared to a fully illuminated mirror without the shading by the plane mirrors. Near the telescope, the cross section of the emitted beam resembles a ring. But after travelling a short distance its centre is illuminated as well, due to the light divergence and the atmospheric turbulence. The retro-reflector array returns the light parallel to the original light beam with a lateral offset, therefore a fraction of the returning light reaches the inner part of the telescope's main mirror. The reflected light coming from the inner part of the mirror is then redirected by the second plane mirror and focused onto an optical quartz fibre placed in the focus of the main mirror. The fibre transmits the light into the spectrograph, passing a mode mixer.

For LP DOAS measurements, a lamp reference spectrum is required, which accounts for the shape of the lamp spectrum and optical structures caused by the instrument. The reference

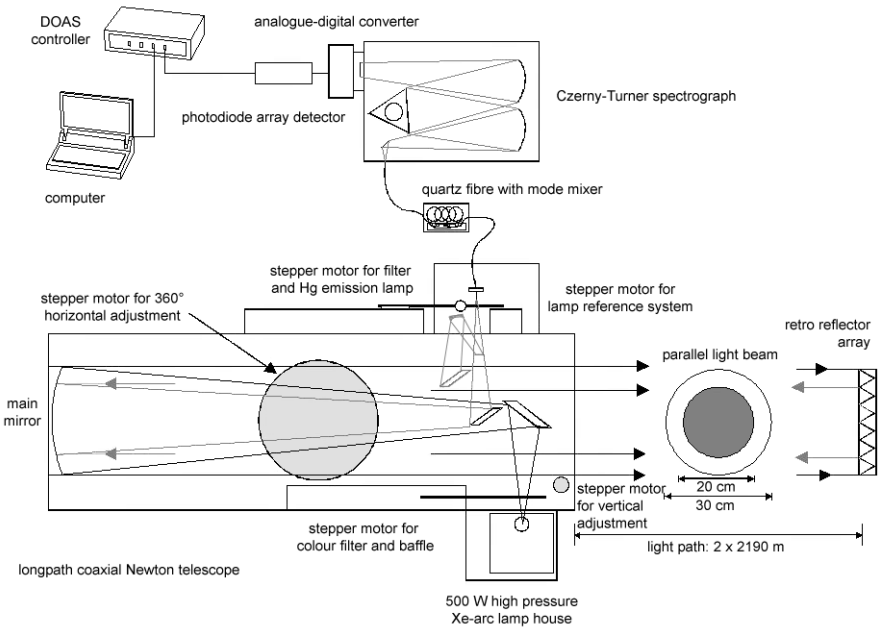

Figure 3.4: Sketch of an active DOAS long path system (top view) used for the optical detection of tropospheric trace gases (figure adapted from Hermes [1999]).

spectrum is taken using a specific *shortcut* optic, which guides the light directly (i.e. on a very short path with negligible trace gas absorption) from the lamp to the entrance of the optical fibre respecting the entrance angles of the fibre and the spectrometer. It is recommended to record shortcut spectra regularly. The shortcut optics used here is described below.

To align the emitted light beam on the retro-reflector array (and possibly at others) two motors can turn the telescope in both horizontal and vertical direction. A filter wheel which can be moved by another stepper motor is mounted close to the light source. It carries a baffle blocking the light from the lamp to record background spectra and gives the possibility to carry optical filters, e.g. UG5 (Schott, Germany), in order to remove light at certain wavelengths to reduce stray light in the spectrograph. At one motor, a mercury (Hg) lamp is mounted which can be positioned in front of the quartz fibre to record Hg emission spectra in order to determine the spectral resolution and wavelength calibration of the instrument regularly during the measurement campaign. A fifth motor carries the lamp reference system (or shortcut system) which can be moved into the outgoing light beam. The reference system consists of an elliptical plane mirror which reflects a part of the light of the outgoing light beam onto a concave mirror. After being reflected by another small plane mirror, the light is focused onto the quartz fibre (added in *Fig. 3.4* in grey colour). All stepper motors are connected with a DOAS-controller and steered by a PC using the measurement software MFC [*Gomer et al.*, 1996] which also controlled the measurement routine. This type of instrument was used for the measurements at Alzate 2002 (*Sec. 4.2.2.1*) and 2003 (*Sec. 4.3.2*), as well as at Mexico City 2003 (*Sec. 4.5.3*).

3.1.1.6.2 The Telescope of the Multibeam LP DOAS System

The multibeam long path DOAS instrument [*Pundt and Mettendorf*, 2005] is a modification of the system described above. It is an active DOAS device which emits several light beams simultaneously by only one telescope and with only one lamp as light source. This offers a high temporal resolution since measurements along several different absorption paths are performed simultaneously instead of sequentially. Currently, measurements with up to four light beams have been realised.

A sketch of the entire multibeam system, including all components needed, is shown in *Fig. 3.5*. The telescope ***A*** holds one main mirror of 1500 mm focal length and with a diameter

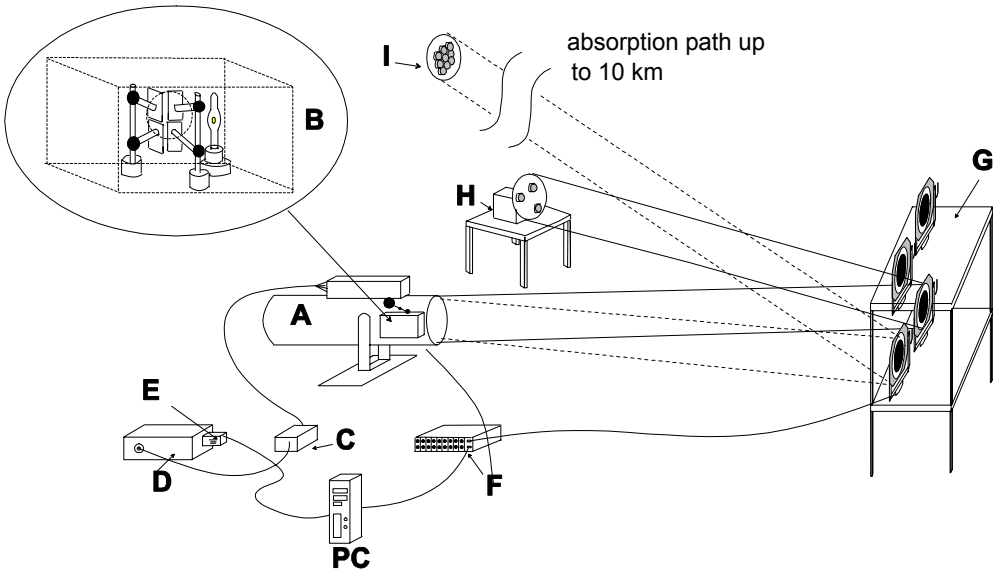

*Figure 3.5: Schematic setup of the multibeam LP DOAS system: telescope **A**, lamp house **B**, mode mixer **C**, spectrograph **D**, CCD detector **E**, stepper motor controller **F**, four plane external mirrors **G** to redirect the light beams, rotating retro-reflector disc **H** and a retro-reflector array **I** (quartz triple prisms). The distance between the telescope and the external mirrors **G** is usually 10 to 15 m. The distance between the rotating retro-reflector and the mirror rack G is 10 to 15 m as well. For a better overview, this example shows only two light beams (sketch: Kai Uwe Mettendorf, pers. comm., 2005).*

of 300 mm. The main change in comparison to the LP DOAS (previous section) is done inside the lamp house ***B***. Four additional small plane mirrors are positioned near the lamp, creating four *virtual light sources* in the focal plane of the main mirror. A detailed sketch of the optical setup of the telescope itself can be found in *Mettendorf* [2005]. Each virtual light source generates one off-axis light beam which enters the telescope with slightly differing angles towards the optical axis, depending on the position of the lamp and the corresponding lamp house mirrors and on their orientation. A rack at approx. 15 m distance in front of the telescope holds four large plane mirrors ***G*** (external mirrors) of size 360 × 320 mm^2 to redirect the light beams into the desired directions. For measuring atmospheric trace gas absorptions, they are directed onto retro-reflector arrays ***I*** distributed over the measurement area (only one array is shown in *Fig. 3.5*). After reflection at the retro-reflectors, the light is redirected via the external mirrors to the telescope. The light received from each beam is focused on different spots in the focal plane of the main mirror where the entrances of quartz fibres are mounted. The optical fibres pass a mode mixer ***C*** and further transmit the light to an imaging spectrograph ***D***, where it is spectrally decomposed. The spectrum of each beam is projected onto a separate line of a two-dimensional CCD array ***E***.

Different alternatives for the setup of the shortcut optics are currently in use for long path systems (see e.g., previous section). However, the multibeam instrument would require one specific optic for each individual quartz fibre, which is hardly to realise in practice. This problem was solved by using a retro-reflector setup ***H*** placed close to the multibeam telescope [*Mettendorf*, 2005]. To measure lamp reference spectra, I_0, the external mirrors are moved to direct the light beams towards the rotating retro-reflector disc ***H***. For these purposes, each external mirror can be justified independently ± 30° in horizontal direction and ± 15° in vertical direction using two stepper motors. In detail, the rotating retro-reflector array consists of three retro-reflectors which are arranged on a rotating disc of 300 mm diameter in order to laterally distribute the

reflecting surface in a sufficiently homogeneous way. The optics, which is used by the different light beams, is equivalent to that of the long path, thus no new structures are generated in the spectra. The absorption by trace gases along the light path of about 20 m can be neglected. For the measurements presented here, the shortcut spectra had to be prepared manually twice a day. The experiences gained from the measurements during the FORMAT II campaign, gave reason to include the regular recording of shortcut spectra in the automatic measurement routine. Measurement process and data storage are controlled by a PC. The software COS (Camera Operation Software [*Mettendorf*, 2005]) controls the amplitude of the signal by optimising the integration time per scan and regularly realigns the external mirrors to direct the light beams to the different retro-reflector arrays using an automatic routine. The telescope itself is fixed, the beams being projected onto the external mirrors once. Only the external mirrors are moved later on.

A filter wheel is located at the exit of the telescope in front of the optical fibres. It can carry optical filters in order to remove light at certain wavelengths, thus preventing stray light, and is moved by means of a stepper motor. To record scattered light (background) spectra, a baffle can be moved between the lamp and the entrance to the telescope by another motor. It blocks the lamp light being transmitted into the telescope.

Since the light beams are emitted into slightly different directions and separated later on, a net of light beams can be generated, using only few multibeam instruments. The application of these instruments is in LP DOAS-tomography [e.g. *Pundt et al.*, 2005] with several multibeam LP DOAS systems covering an area above, e.g. a town centre, with light beams to resolve the small-scale spatial distribution of trace gases in the atmosphere. Suitable measurement geometries and inversion procedures have been developed to reproduce two- or three-dimensional trace gas distributions in the monitored area (on scales of 5-10 m^2). Studies on the arrangement of a limited number of light beams to obtain optimum reconstruction results (for a Gaussian plume distribution) have been carried out by *Hartl et al.* [2006]. During the FORMAT II campaign, two multibeam LP DOAS instruments were used, measuring with three and four light beams, respectively. However, they were installed at different measurement sites (Bresso and Spessa, see *Sec. 4.3.3* and *Sec. 4.3.4*). Thus, we were not aiming at performing tomographic measurements. This would have demanded high administrative efforts to obtain permissions to place instruments and retro-reflectors and would not have been possible in the scope of the FORMAT project.

3.1.1.6.3 The DOAS White System

During the intercomparison experiment performed at Bresso during FORMAT I (*Sec. 5.2*), a modified version of the open White type multi-reflection system utilising Differential Optical Absorption Spectroscopy was operated by IUP. The performance of the White cell measurements was not part of this thesis. A detailed description of the system is given by *Trick* [2004]. The basic *White* [1976] system was improved for stability by using three quartz prisms that each also double the maximum feasible light path of the mirror system [*Ritz et al.*, 1993]. The f/100 mirror system consisted of three spherical concave mirrors of identical focal length – a field mirror and two objective mirrors, which were located at a distance of 15 m facing the field mirror. The total path length could be varied from 240 m (16 traverses) up to 2160 m (144 traverses) by adjusting the objective mirrors [e.g. *Ritz et al.*, 1993]. A xenon high-pressure lamp was used as light source. The optics of the White system were optimised for CH_2O detection, using a set of three dielectric mirrors, each with a reflectivity of > 98% around 321 ± 20 nm. The relative adjustment of the two objective mirrors to the field mirror was maintained using a new laser adjustment system (Christoph Kern, pers. comm.). Aluminium coated mirrors were used as transfer optics. A 30 cm Czerny-Turner spectrograph equipped with a 1200 grooves mm^{-1} reflective grating was used to project the spectral interval from 303 to 366 nm onto a 1024-

element diode array detector (HMT, Rauenberg) which was cooled by a Peltier element to −13°C (dispersion of 0.061 nm/pixel). The temperature of the spectrograph was stabilised to 35 ± 0.1°C in order to reduce temperature drifts. The integration time for individual scans varied between 3-30 s and several ten scans were typically binned to reduce photon noise. Lamp reference spectra were recorded twice a day at the shortest path (240 m) and residual absorptions over this reduced light path were characterised and subtracted from the measured spectra. In the spectral analysis procedure atmospheric spectra were corrected for dark current and electronic offset and divided by a lamp reference spectrum recorded the same day. The ratio spectrum was high-pass filtered by subtracting a triangular-smoothed copy of itself, thereby accounting for small changes in reflectivity near the reflectivity drop-off of the dielectric mirrors as well as Rayleigh and Mie scattering in the atmosphere.

Average trace gas concentrations of CH_2O, NO_2, O_3 and HONO were retrieved by simultaneously fitting resolution-adjusted reference spectra using the combined linear-nonlinear least-squares algorithm [e.g. *Stutz and Platt*, 1996] of the MFC software [*Gomer et al.*, 1996]. Formaldehyde was identified by four strong absorption bands in the UV between 310 and 337 nm and calibrated using the literature cross-section by *Meller and Moortgat* [2000].

The stated uncertainty of the formaldehyde UV absorption cross-section is ± 5% [*Meller and Moortgat*, 2000]. Differences between the available CH_2O cross-sections are discussed in *Sec. 3.1.1.8.1*. The systematic error of the DOAS spectrometer was determined to be < 3% as described by *Stutz* [1996]. The total systematic error of the CH_2O concentrations, determined by the DOAS is therefore < 6%. A mean detection limit of CH_2O of 0.9 ppbv was determined with an average time resolution of 137 s.

3.1.1.6.4 The Light Source

The light sources used for all DOAS measurements in this thesis were xenon (Xe) high-pressure short arc lamps. A light arc of few or less than one mm diameter between anode and cathode is created from a high voltage ignition discharge which produces a dense plasma in the xenon gas. The spectrum of a Xe arc lamp is composed of the thermal emission according to Planck's law and single Xe emission lines at several wavelengths which are broadened by pressure and temperature. The distance of the electrodes is generally small, resulting in a short arc length, thus reducing the divergence of the parallel light beam emitted from the telescope. The pressure inside the lamp is very high (up to 10^7 bar under operation conditions) yielding a high local light intensity. The colour temperature of ~ 6000 K of the used Xe lamps is similar to that of the sun. The bulb of a Xe lamp consists of a quartz glass which is extremely resistant to the pressure and temperature. The electrode material is tungsten with endowments depending on the lamp type. The cathode has an edged peak to enhance the electron emission. The anode, in contrast, is made of massive material to absorb the kinetic energy of the incoming electrons.

Two lamp types were used as broad-band light sources for the active DOAS measurements presented in this thesis: Osram XBO 500 W/RC OFR ‡ and PLI Hanovia HSA-X5002 ‡‡. Their characteristics are summarised in Table 3.1. The variability of the emission features of both lamp types caused by flaring lamp plasma was studied by *Hermes* [1999]. He found Xe emission lines at several wavelengths in the red spectral region, but none in the range used here. The emission strength and pressure broadening of the Xe-lines are variable in time and therefore the lamp structures are difficult to remove from a spectrum. It was found that lamp structures are more easily removed from a spectrum in the case of the PLI Hanovia lamp as its Xe emission bands are broader [*Hermes*, 1999].

‡. Osram GmbH, München, Germany, ‡‡. Professional Lamps Inc., USA

Table 3.1: Characteristics of the used lamp types.

Lamp type	Power	Voltage	Current	Lifetime	Light arc size	Campaign
Osram	500 W	18 V	31 A	2000 h	2.7 × 0.9 mm	FORMAT
PLI Hanovia	500 W	18 V	29 A	200 h	0.3 × 0.3 mm	MCMA

3.1.1.6.5 The Quartz Fibre and Mode Mixer

Quartz fibres were used to transmit the light from the telescope to the entrance slit of the spectrograph. The applied fibres had a diameter of 200 µm. For the multibeam DOAS measurements, a bundle consisting of twelve quartz fibres was applied. Four of the fibres, associated with the different light beams, were utilised for measurement. The quartz fibre used in the classical long path instrument was a multi mode step-index fibre with a numerical aperture of NA = 0.12. The fibres from the multibeam long path DOAS had NA = 0.108. The light leaving the fibre shows interference fringes ('modes') produced by the total reflections inside the fibre. *Stutz and Platt* [1997] found that this heterogeneous illumination of the grating and the detector leads to a high residual structures in data evaluation. Therefore, a quartz fibre *mode mixer*, according to *Stutz and Platt* [1997], is incorporated into the modern DOAS systems. The mode mixer combines a specific squeezing with a random deformation of the fibre, which leads to an equally spread illumination and therefore to a reduction of the residual structures. Nevertheless, the residual noise is generally higher compared to laboratory tests of the spectrograph-detector system with direct light transition.

3.1.1.6.6 The Spectrometers

Two different grating spectrographs were used for the trace gas measurements in this work. Their specifications are summarised in Table 3.2. Both spectrograph types are based on a setup originally developed by *Czerny and Turner* [1930]. A quartz fibre (width 200 µm) transmits the light from the telescope to the entrance slit of the spectrograph which is located in the focal plane of a convex mirror. The width of the entrance slit was adjusted to 200 µm. The spectral resolution of a spectrograph which depends on the slit width and on the reciprocal of the grating's linear dispersion was ~ 0.5 nm. In the spectrograph, the light is paralleled by the spherical mirror and reflected to a plane diffraction grating. The dispersed light is then focused by a second convex spherical mirror onto the detector unit. For the multibeam LP DOAS, the twelve fibres from the fibre bundle are arranged vertically along the entrance slit, with sufficient space between the single fibres, i.e. sufficient that spectra are processed separately in the spectrograph [*Pundt and Mettendorf*, 2005]. The wavelength region of a spectrum can be changed by a computer controlled stepper motor (tolerance 0.5 steps) by turning the grating. In order to minimise thermally caused changes of dispersion and resolution of the spectrograph, the entire spectrograph unit is thermally insulated and temperature stabilised to 30 ± 0.2°C by electrical heating.

3.1.1.6.7 The Detector Units

Two different detectors were used for the measurements with the classical long path DOAS and the multibeam long path DOAS (see Table 3.2). The features of the photo diode array (PDA) and the charge coupled device (CCD) detector are described in this section. In both cases, the detector unit is mounted in the focal plane of the spectrograph.

The main difference between a CCD array and a photodiode linear array is the readout scheme of the output signal from each element in the array. In a CCD, the signal (charge) is transferred from one element to the next one along the first row until it reaches the end of the row. The signal is such read in sequence pixel by pixel and row by row. In a PDA, the signal (current) is output at each element's unique anode and cathode, i.e. the PDA signal is read simultaneously, rather than sequentially.

Table 3.2: Specifications of the used detectors and spectrographs.

	LP DOAS	MB DOAS
detector type	PDA, S3904-1024, Hamamatsu	CCD, CCD-42, Marconi
detector size	1024 pixels	512 × 2048 pixels
spectrograph type	Acton Spectra Pro 500	Acton Spectra Pro 500i
focal length	500 mm	500 mm
aperture	1:6.9	1:6.5
reciprocal linear dispersion [a]	3.18 nm mm^{-1}	3.24 nm mm^{-1}
dispersion on detector	0.0797 nm/pixel PDA	0.0876 nm/pixel CCD

a. 600 grooves mm^{-1} plane diffraction grating

The Photo Diode Array (LP DOAS Systems)

The principal element of the detector unit of the long path system is a photo diode array consisting of 1024 silicon (Si) photo diodes (complementary metal oxide semiconductor, CMOS) of each 25 µm width and a height of 2.5 mm, arranged in a line. The capacity of each diode is 10 pF, the photoelectric well depth corresponds to 1.286×10^8 photo electrons. Every photo diode consists of an n-p semiconductor junction. Before the exposure, an inverse voltage of 2.06 V is applied to the diode inducing a depletion layer which is almost as large as the entire diode area. Then, the PDA is disconnected from the power supply. Incoming light excites a number of electrons proportional to the light intensity in the conducting layer of the semiconductor. These mobile charge carriers reduce the applied inverse voltage. After the intended integration time, the PDA is read out by reconnecting it to the power supply and measuring the current caused by recharging the PDA. The resulting signal of a single scan is amplified electronically. The signals are digitised by a 16-bit analogue-digital converter (detector saturation corresponds to $2^{16} = 65\,536$ counts) and then transferred to the computer.

The Charge Coupled Device (Multibeam LP DOAS Systems)

In order to separate the spectra from the different light paths, a two-dimensional CCD array (details see Table 3.2) is used as detector for the multibeam measurements. The signals from the individual beams, dispersed by the spectrograph in *x*-direction, are imaged to different sets of lines on the CCD-chip (*y*-direction). Hence, the spectra from the different light paths are received simultaneously and spatially separated. Each spectrum covers about 14 to 17 lines of the CCD array. To improve the signal-to-noise ratio of a measurement, it is desired to detect as many photoelectrons per time interval as possible. In the so-called *binning* mode, the signals of several pixels are additionally combined to virtually create a greater pixel size. In the measurements shown here, four pixels were binned to one (2 rows and 2 columns).

Each pixel of the CCD-chip serves as a MOS (metal oxide semiconductor) capacitor, which consists of four layers: one metal layer, one layer of silicon dioxide as isolator, one p- and one n-doped silicon layer. A voltage impressed between the n-layer and the metal layer produces a potential well for electrons in the p-layer. During exposure, incident photons generate electron-hole-pairs in the p-layer (photoelectrical effect). The charge is confined in the well associated with each pixel by the surrounding zones of higher potential. The holes are refilled by electrons from the n-doped silicon, whereas the electrons remain in the potential well until they are read out. The number of electrons released is proportional to the flux of incident photons and further depends on the quantum efficiency of the CCD-chip. The number of electrons which can be stored per pixel is referred to as full well depth.

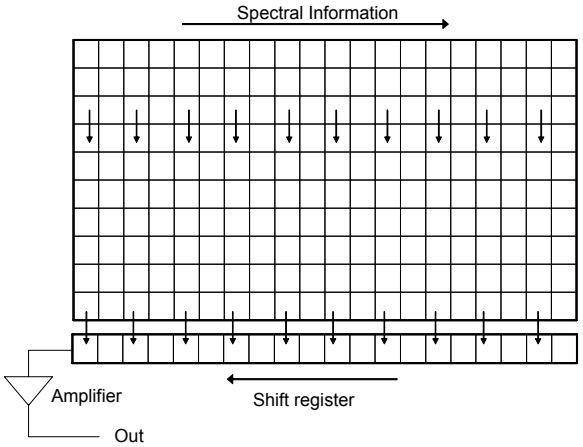

Figure 3.6: A CCD chip with 512 lines each consisting of 2048 picture elements (pixels) of 13.5 μm width was used. In the readout procedure, the lowermost line is shifted to the shift register and the others move up. The readout of the shift register occurs sequentially, pixel by pixel. The shift register is read out via an amplifier and digitised for later analysis.

As soon as the exposure is finished, the readout of the charges occurs. For this purpose, the chip has to be darkened by closing a shutter, then the polarity of the voltage impressed is reversed. Thereby, the barriers of the potential well are destroyed. The charges from the first line of the CCD are transferred into the shift register and all the lines above move down one line (see *Fig. 3.6* for illustration). The pixels in the shift register are read out one after another: As soon as the first pixel is read, the others move up one place and the next pixel is read. After the first line is read out, the second line is shifted to the shift register. This procedure is repeated until the last pixel is read. After amplification, the analogue signal is digitised and sent to a PC. For the used CCD array, the readout takes ~ 1 sec (0.5 s binned) for a digitalisation rate of 1 MHz.

Offset, Dark Current and Residual Noise

Electronic signals resulting from the detector are overlaid to each spectrum and have to be accounted for in the evaluation procedure. An *offset signal* is added to each signal to exclude negative signals under low light conditions which would reduce the resolution of the digitised values by a factor of two. The offset is proportional to the number of scans. Additional electrons in the conducting layer of a diode are created by thermal excitation. This signal is called *dark current* and is read out together with the actual signal. The dark current signal decreases exponentially with decreasing detector temperature (Stefan-Boltzmann law). In order to reduce the dark current, the detector was cooled to a temperature of – 30 ± 0.2°C by a Peltier cascade. Dark current further depends on integration time and on the signal operation of the diode array [*Stutz and Platt*, 1996].

The offset, dark current and readout noise of the different used detectors had to be determined as described below. The signals differ for the two detectors applied for the long path and the multibeam long path measurements, but remain constant over the time of the campaigns.

The offset was determined by adding 1000 scans taken at the minimum exposure time, i.e. 60 ms for the PDA (100 scans of 40 ms for the CCD), at dark conditions. This spectrum contains the signal of 1000 offsets and a dark current of 60 s (100 offsets and a dark current of 4 s). The ratio of dark current to offset is less than 10^{-3}, thus, dark current can be neglected in this spectrum. The offset level for one scan is approx. 3‰ of the measured signal. The offset signal was measured routinely several times per campaign.

The dark current was determined by recording one single scan with an integration time of 300 s at dark conditions (for the multibeam measurements 1 scan with 100 s integration time). Subsequently, the offset signal is corrected for. For typical measured intensities of 200 000 counts s^{-1} this signal plays a minor role. Several diodes possess a peak dark current signal, which probably can be attributed to endowment errors of the diodes because these peaks do not change with time.

The *dynamics* is that range in which the detector is capable of an accurate measurement of the signal and is defined as the maximum detectable signal divided by the minimum signal level. The maximum detectable signal is limited by the detector saturation, the minimum signal by the noise of the system. Due to the thermal generation of noise, the dynamics depends on the integration time. The dynamics of photodiode arrays is much higher than for CCD arrays.

Saturation exposure is that level of photon intensity where the signal of the detector is no more dependent on the incident light flux. Photodiode and CCD arrays have a linear signal response to incident photons, provided that they are modulated between zero and approximately 75% of the saturation charge. Above this value the non-linearity rises significantly.

If the fixed pattern noise is subtracted, the *residual noise* determines the lower limit of light detection or the lower limit of the system dynamic range. The residual noise of a spectrum consists of electronic noise and photon statistic noise.

The *electronic* or *readout noise* is due to the resolution of the digitalisation, the noise of the analogue-digital-converter (ADC) and other electronic components. It is determined by subtraction of two offset spectra taken in succession and calculation of the root mean square (RMS, corresponds to 1 σ noise) of this spectrum. In order to obtain the electronic noise of one scan, the RMS is divided by the total number of scans, 2N, with N being the number of scans added in one offset spectrum. If the electronic noise dominates, the amount of residual noise is similar for each scan.

Another source of noise in a spectrum is the *photon noise* which is given by the square root of the number of photons according to the Poisson statistical theory. Considering the well depth of the used detector (1 count = 1962 photo electrons for the PDA), the photon noise (1 σ) of a spectrum with 10^4 and 10^6 counts is 2.3×10^{-4} and 2.3×10^{-5}, respectively. Hence, the signal-to-noise ratio increases for an increased number of photo electrons per spectrum, e.g. by the number of scans.

Since the contribution of dark current and readout noise is very small for cooled detectors, the measurements are usually limited by the photon noise. The residual noise thus decreases with the square root of the number of counts (here, 100 scans were recorded per spectrum). The residual noise is experimentally determined by using a very stable halogen lamp, directly mounted in front of the quartz fibre, as light source. Two spectra (corrected for offset and dark current) of the same integration time scanned one immediately after the other are divided. In order to remove broad-band structures from the resulting spectrum a high-pass filter (1000 times triangular smoothing) was applied. The peak-to-peak value of the residual structure is determined from the calculated spectrum. It is generally 6-7 times higher than the RMS of the spectrum.

3.1.1.7 Measurement Algorithms

The measurements described in this thesis (*Chapter 4*) were performed using different types of long path DOAS as stated in Table 3.3. The systems are fully automated by means of a computer which controls the scanning of the spectrometer to the wavelengths of interest, the recording of spectra, the insertion of optical filters or baffle into the transmitter and the operation of an optical by-pass in order to take reference spectra of the arc lamp. The algorithm for the measurement of CH_2O in the troposphere included recording of spectra from the atmospheric light beam, background spectra, and lamp reference spectra. Depending on the spectrograph-detector system used for both instruments, the spectral window of the measurements was slightly different for different campaigns and sites (see Table 3.3) and contained the signature of the molecules of interest (CH_2O, O_3, NO_2, SO_2, HONO). In order to avoid nonlinear effects which are present close to saturation (*Sec. 3.1.1.6.7*), in the measurements presented here, the exposure time is adjusted automatically to the incoming light intensity that the diode count reaches about 70% of its saturation value before being read out. Mercury wavelength standards were recorded frequently for later spectral calibration.

Table 3.3: Overview of instruments and wavelength ranges used for measurement and evaluation at the different measurement sites.

Site	DOAS Type (Number of beams)		Instrument	Measurement range [nm]	Eval. range 'CH_2O' [nm]	Eval. range 'HONO' [nm]
Alzate 2002	long path	(1)	'GTI'	294.9-376.4	305-356	-
Mexico City 2003	long path	(1)	'Nashville'	278.5-360.1	290-350 [a]	-
				317.5-398.8	-	320-380 [a]
Alzate 2003	long path	(1)	'Nashville'	283.1-364.9	310-360	-
Bresso 2003	multibeam	(4)	'Long'	282.8-372.4	300-360	325-371
Spessa 2003	multibeam	(3)	'Hydra'	287.2-376.8	300-360	325-374

a. During the Mexico City campaign, spectra were taken in different wavelength ranges consecutively by turning the grating of the spectrograph.

The long path measurements in Alzate 2002, Mexico City 2003 and Alzate 2003 were performed using the MFC software [*Gomer et al.*, 1996]. The data acquisition was run in automatic exposure mode (γ,β,αs command), i.e. number of scans and integration time were variable and were adapted automatically according to the incoming light intensity (see above). The measurement algorithm included recording spectra from the atmospheric light beam on one fixed light path. The background spectra were recorded with one scan of 1/10 the integration time of the previous atmospheric spectrum. For the measurements at Alzate 2002 two different measurement algorithms were used. Firstly, the measurement sequence included after each atmospheric spectrum one background and one shortcut spectrum. However, to gain a better time resolution during IOPs (intensive operation periods), background and lamp spectra were taken after ten measurement spectra. Typically, one CH_2O measurement was finished every 1-2 min. For the measurements at Alzate 2003, shortcuts using the rotating retro-reflector setup were taken manually twice a day.

Because of the different design of a multibeam DOAS telescope, it was not possible to take automatic lamp spectra within the measurement algorithm at this early stage of development. For the measurements at Bresso and Spessa 2003, lamp spectra were therefore taken manually twice a day. Background spectra were recorded automatically after ten atmospheric spectra. For a background spectrum, one scan with a fixed integration time of 10 seconds was recorded. The multibeam long path DOAS measurements at Bresso and Spessa were performed with a fixed number of 100 scans for an atmospheric spectrum. The integration time was variable, according to the incoming light intensity, controlled by the COS software [*Mettendorf*, 2005]. The signal level was optimised for the beam with the highest intensity. For the other beams the detected signal might not reach the optimal level of 70% of the diodes' well depth.

3.1.1.8 DOAS Spectral Evaluation Procedure

The spectral resolution $\Delta\lambda/\lambda$ of the spectrograph and the dependence between diode number of the PDA or CCD and the wavelength (wavelength-to-pixel mapping function or dispersion relation function, Γ) were determined from emission spectra of mercury lamps. There are several methods to derive the dispersion relation. One is to plot the known wavelengths of the Hg-lines against the corresponding diode numbers of the measured line centres and to apply a polynomial fit of first or second order to the distribution of points. The regression parameters define the dispersion relation. Other methods to obtain the wavelength calibration utilise other spectra with well defined spectral features, e.g. NO_2 absorption cross-sections (cells) or Fraunhofer spectra (scattered light). These methods are tedious but very precise [§]. The spectral resolution $\Delta\lambda/\lambda$ of the detector in combination with the grating used, can be determined using the

Table 3.4: Absorption cross-sections used for the evaluation of the spectra (n.s.: not specified). Shift or squeeze applied to the references are also given.

Species	Rel. error	Resolution [nm]	Reference	Shift, Squeeze
CH_2O [a]	± 5%	0.025	*Meller and Moortgat* [2000]	--
O_3	± 3-7%	0.054 (5 cm^{-1})	*Voigt et al.* [2001]	linked to NO_2
NO_2	± 3.5%	0.011 (1 cm^{-1})	*Voigt et al.* [2002]	shift, squeeze
SO_2	± 2.4%	0.022 (2 cm^{-1})	*Vandaele et al.* [1994]	shift, squeeze
HONO	± 5%	0.08	*Stutz et al.* [2000]	linked to NO_2
O_4	n.s.	0.022 (2 cm^{-1})	*Hermans et al.* [1999]	--

a. see also *Sec. 3.1.1.8.1* for a comparison of highly resolved CH_2O cross-sections

FWHM (in nm) of the Hg emission lines as measured by the instrument. This width of a Hg single emission line (e.g. at 334 nm) yields the width of the instrument function H and therefore the minimal spectral distance between two absorption or emission lines that can be distinguished from each other with the used instrument. For the multibeam measurements, the wavelength-to-pixel mapping Γ and the instrumental function had to be determined for each beam separately, since the function Γ depends on the arrangement of the fibres along the slit.

An integral part of the spectral evaluation is represented by the trace gas references fitted to the measured spectra. Highly resolved absorption cross-sections from many compounds are published in the literature. An overview of the literature cross-sections used for the DOAS evaluation in this thesis is given in Table 3.4. To generate the trace gas references, these highly resolved absorption cross-sections are degraded to our instrument's resolution by convolution with the actual spectral line shape H of the instrument (cf. *Sec. 3.1.1.3*). This process is described by eq. 3.13 in analogy to eq. 3.6. The resulting cross-sections S_i have the same resolution as the measured spectra and can be used as input for the fitting routine.

$$S_i(\lambda) = \sigma_i(\lambda)^* H = \int \sigma_i(\lambda - \lambda', L) \cdot H(\lambda') d\lambda' \qquad \text{(eq. 3.13)}$$

For NO_2, CH_2O and SO_2, the literature reference spectra were only used to scale the corresponding reference cell spectra which were regularly recorded in the field, using cells prepared in the IUP laboratory. Since the cell spectra include the exact instrumental function and wavelength calibration of the used DOAS system, $d_{i,k} = 0$, they were preferentially fitted to the measured atmospheric spectra instead of the literature references in order to reduce systematic errors.

The spectra were preprocessed using the software MFC [*Gomer et al.*, 1996]. In this first step, solar background spectra, atmospheric spectra and lamp reference spectra were corrected for electronic offset and dark current (see *Sec. 3.1.1.6.7*). The solar background, representing atmospheric stray light, was then subtracted from the respective atmospheric spectrum. The retrieval of atmospheric trace gas concentrations was performed with the software WinDOAS [*Fayt and van Roozendael*, 2001], simulating the spectra according to the analysis model presented in *Sec. 3.1.1.4*. The corrected atmospheric spectrum was divided by a reference lamp spectrum. To remove further broad-band structures, which are caused by atmospheric scattering processes and broad-band absorption, a high-pass filter was applied to the atmospheric spectrum by dividing by a smoothed (2000 times 'triangular' smoothing) copy of the spectrum. The spectrum which contains only the narrow-band absorption structures of the trace gases is

§. For the Bresso measurements 2003, not enough Hg spectra between changes of the spectrograph settings were available, thus, these methods had to be used to derive the wavelength-to-pixel mapping.

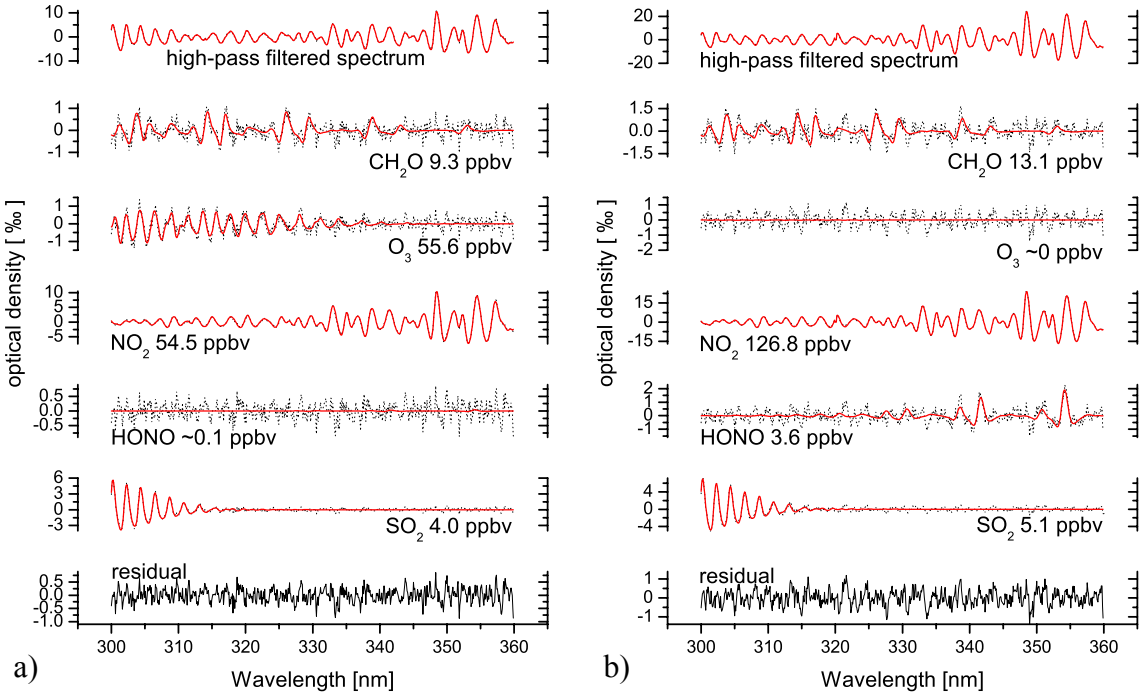

*Figure 3.7: Examples of the DOAS evaluation for **(a)** an afternoon spectrum from 17 September 2003, 13:47 h, **(b)** a nighttime spectrum from 18 September 2003, 21:30 h measured at Bresso during the FORMAT II campaign. Red traces show trace gas fits, black dotted traces denote fit + residual.*

logarithmised to provide a differential optical density. High-frequency noise can be eliminated by applying a triangular smoothing algorithm (low-pass filter). The parameters for the high-pass filter and the low-pass filter were derived by minimising the statistical error of the evaluated concentrations.

The first few pixels, which are often afflicted with instrumental errors, were neglected for analysis and the remaining wavelength interval was separated into two ranges depending on the species examined. In the wavelength range chosen for the identification of CH_2O, O_3 and SO_2, also NO_2 and HONO have distinct differential absorption structures (*Fig. 3.1*). NO_2 and HONO concentrations were retrieved in the second interval containing the three major HONO absorption bands; CH_2O, O_3 and O_4 (O_2-O_2 collision complex) were also fitted here. The respective limits of the CH_2O and HONO fitting ranges are specified in Table 3.3.

Finally, the combined linear/non-linear least squares fit (*Sec. 3.1.1.4*) was performed, using the set of trace gas reference spectra, two lamp emission spectra and a 5^{th} order polynomial high-pass filter. The two lamp reference spectra and the reference cross-sections were subject to the same sequence of filters as described for the atmospheric spectra. Due to variations of the ambient conditions, linear shift and first-order squeeze (cf. *Sec. 3.1.1.4*) were admitted for several reference spectra as specified in Table 3.4. Finally, the concentrations of the respective trace gases were determined from the scaling parameters of the reference spectra and the light path length. The length of the atmospheric light path was determined (within an uncertainty of < 1%) with a laser range finder.

Two examples of the LP DOAS data evaluation from Milano are provided by *Fig. 3.7*. A typical afternoon spectrum (*Fig. 3.7a*) shows strong absorption structures from all trace gases except HONO, whereas a typical nighttime spectrum (*Fig. 3.7b*) features absorptions by all measured trace gases except O_3. The respective concentrations are given in the graph. Average concentration levels and detection limits (2 σ) of the trace gases measured for this thesis are given in Table 4.1 and Table 4.4. The average size of the residual structure over the period of

observations was 1-2 ‰ (peak-to-peak). During FORMAT, a mean true statistical error (see *Sec. 3.1.1.5*) of the CH_2O concentration of 300-400 pptv was observed with variations due to changes in lamp parameters.

3.1.1.8.1 Comparison of Formaldehyde Reference Cross-Sections

In the DOAS method, the complex vibrational-rotational absorption structure between 240 and 360 nm (see *Fig. 3.8*) is used for identification of CH_2O. With its highly structured spectrum, formaldehyde stands out from the higher aldehydes and ketones, since it already allows the measurement of low CH_2O concentrations in the atmosphere by UV-absorption with high sensitivity. A major advantage of DOAS (as well as FTIR in the IR) over wet chemical techniques is its independent absolute calibration, based on absorption cross-section data measured in the laboratory. The accuracy of a DOAS measurement is thus influenced mostly by the accuracy of the used reference cross-sections of the investigated species. The accuracy of the formaldehyde cross-section further translates in the quantification of HO_2 radical production from CH_2O photolysis in two ways – the accuracy of the concentration measurement and of the photolysis frequency (cf. eq. 2.5). Therefore, several highly resolved UV absorption cross-sections of formaldehyde are compared in the following.

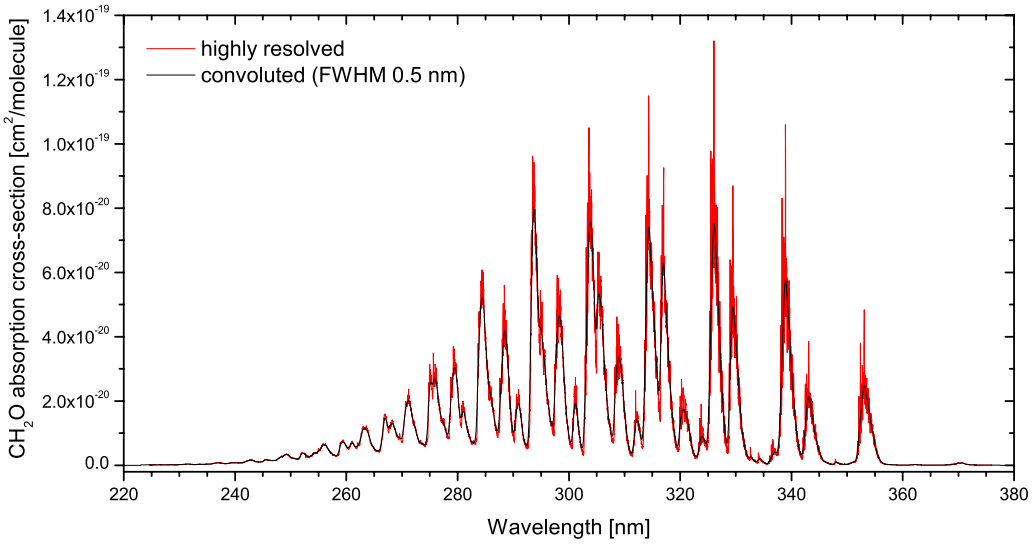

Figure 3.8: Absorption spectrum of CH_2O at 298 K [Meller and Moortgat, 2000]: highly resolved (red) and convoluted with a Gauss function of FWHM 0.5 nm (black), which is the typical spectral resolution of the used spectrometers.

Various studies of the wavelength and temperature dependence of the CH_2O absorption cross-section have been performed in past years (see Table 3.5). Hence, a variety of high-resolution absorption cross-sections of formaldehyde in the UV spectral range are available. While most of the studies report similar shapes of the spectrum, there are discrepancies concerning the absolute value of $\sigma_{CH2O}(\lambda)$. The value of the cross-section at 314.3 nm (296 K) published by different authors over the past 30 years varies from 4.16×10^{-20} cm^2 [*Bass et al.*, 1980] to 7.47×10^{-20} cm^2 [*Pope et al.*, 2005]. The studies of *Bass et al.* [1980], *Cantrell et al.* [1990] and *Meller and Moortgat* [2000] report measurements at different temperatures. The absorption bands are shifted to longer wavelengths with increasing temperature and become broader. This effect originates in the distribution of the S_1 state at higher temperature onto higher rotational and vibrational states of the molecule. The temperature dependence of the CH_2O absorption cross-section is given in a table by *Meller and Moortgat* [2000] with an uncertainty of ± 8%.

Since 2002, the International Union of Pure and Applied Chemistry (IUPAC) Subcommittee on Gas Kinetic Data Evaluation for Atmospheric Chemistry [*Atkinson et al.*, 2002] recommends

Table 3.5: Highly resolved formaldehyde absorption cross-sections and their spectral specifications (n.s.: value not specified in the paper).

Authors	Uncer-tainty	Wavelength range [nm]	Spectral resolution [nm]	Disper-sion [nm]	Temp. [K]
Bass et al. [1980]	n.s.	258.7-359.5 (at 100 Torr)	0.05	0.025	296 [a]
Moortgat et al. [1980]	± 5%	215.7-370.2 (in air)	0.5	0.08	284.7
Cantrell et al. [1990]	± 5%	300.3-385.8 (in vacuum)	0.011 at 330 nm 1.00 cm^{-1}	0.04-0.07	296.16 [a]
Rogers [1990]	± 1-2%	240.0-367.3 (in vacuum)	0.011-0.044	0.016	296 ± 2
Meller [1992]	± 5%	224.7-375.9 (in air)	0.021-0.028	0.01	297
Meller and Moortgat [2000]	± 5%	224.6-356.6 (in air)	0.025 (avg.) [b] 2.73 cm^{-1}	0.01	298 [a]
Bogumil et al. [2003]	± 1.1%	247.3-400.0 (in vacuum)	0.21-0.22	0.11	293
Pope et al. [2005]	n.s.	313.1-320.0 (in air)	0.001 0.10 cm^{-1}	0.001	294

a. also other temperatures available
b. 0.021-0.028 nm

the use of the *Meller and Moortgat* [2000] data over the entire spectral range, yet the measured cross-sections are reported 5-10% higher than the spectrum previously recommended. However, the NASA Evaluation of 2003 [*Sander et al.*, 2003], recommends the absorption cross-section by *Cantrell et al.* [1990], which only covers a limited wavelength range (λ = 300-375.5 nm). Other cross-sections reported in literature were not recommended due to various issues. Problems with the strong absorptions bands between 320 and 350 nm are reported for the cross-section by *Bass et al.* [1980]. The spectrum by *Rogers* [1990] reportedly contains discrepancies at wavelengths shorter than 280 nm [*Meller and Moortgat*, 2000]. A very highly resolved cross-section including two absorption bands between 313 and 320 nm was recently published by *Pope et al.* [2005].

The seven available CH_2O absorption cross-sections are compared in the spectral range 300-360 nm, with the exception of the cross-section by *Pope et al.* [2005], for which a smaller range was used (312-320 nm). All spectra were obtained at a temperature of 296 ± 3 K (see Table 3.5). Since the spectra were recorded with different instruments at different spectral resolutions R_i, they had to be adapted to a common spectral resolution. As the spectral resolution of the spectrographs used in this work is approximately 0.5 nm FWHM, the spectra were convoluted with Gaussian functions of appropriate FWHM G_i (with $G_i^2 = (0.5\ \text{nm})^2 - R_i^2$) to result in 0.5 nm spectral resolution (see also *Fig. 3.8*). Vacuum wavelengths were converted to air wavelengths using the formula for the refractive index by *Edlen* [1966]. For comparison of the cross-sections the spectrum by *Meller and Moortgat* [2000] was fitted to the other cross-sections applying a non-linear least-squares fit with five fitting parameters: A quadratic polynomial (three parameters) accounting for small baseline differences, a scaling coefficient accounting for differences in the absolute magnitude of the cross-sections (one parameter) and a linear wavelength shift coefficient (one parameter) accounting for differences in the wavelength calibration. During non-linear fitting, a linear shift and a polynomial high-pass filter were

Table 3.6: Results of the comparison of formaldehyde cross-sections with respect to Meller and Moortgat [2000] in the wavelength range 300-360 nm. The rightmost column shows the relative deviation in magnitude. All spectra were degraded to a resolution of 0.5 nm.

Cross-section	Shift [nm]	Scaling factor	Deviation [%]
Bass et al. [1980]	−0.06879	0.5806	−41.9
Moortgat et al. [1980]	+0.03570	0.9213	− 7.9
Cantrell et al. [1990]	+0.01935	0.8854	−11.4
Rogers [1990]	−0.07476	0.8304	−17.0
Meller [1992]	+0.00013	0.9981	− 0.2
Meller and Moortgat [2000]	+0.00000	1.0000	+ 0.0
Bogumil et al. [2003]	−0.01602	1.0270	+ 2.7
Pope et al. [2005]	−0.00694	1.0470	+ 4.7 [a]

a. only in range between 311 and 320 nm

employed to minimise the influence of wavelength shifts and of baseline drifts and stray light. The observed differences in magnitude and wavelength shifts relative to the cross-section by *Meller and Moortgat* [2000] are summarised in *Fig. 3.9* and Table 3.6. The relative deviation of the evaluation output for various cross-sections from the result obtained using the reference by *Meller and Moortgat* [2000] is also given in Table 3.6.

The recommended CH_2O cross-sections [*Meller and Moortgat*, 2000; *Cantrell et al.*, 1990, see above] differ by 11.4% in the spectral range between 300 and 360 nm. There is a small wavelength shift of about 0.02 nm between both cross-sections. The differences in the absorption cross-sections imply a potential 11% difference in the concentration determined by DOAS depending on the cross-section used by the particular authors, with higher concentrations derived using the cross-section by *Cantrell et al.* [1990]. The four most recent publications on the CH_2O cross-section [*Meller*, 1992; *Meller and Moortgat*, 2000; *Bogumil et al.* 2003; *Pope et al.* 2005] have the highest values. In the range between 300 and 360 nm they differ at most by 3% from each other. However, one should point out that the cross-section by *Bogumil et al.* [2003] was scaled to the absolute absorption cross-section by *Meller and Moortgat* [2000]. The good agreement between the mentioned cross-sections implies that they might represent the reality rather than the deviating and older spectrum by *Cantrell et al.* [1990], recommended by JPL. The cross-section best suited for DOAS evaluation and calculation of photolysis frequencies appears to be the one by *Meller and Moortgat* [2000], since it covers the widest wavelength range. In previous comparisons of measurement methods, the cross-section employed in the DOAS retrieval process was often not specified by the authors (see overview of previous intercomparisons in *Hak et al.* [2005]). In this work, the cross-section by *Meller and Moortgat* [2000] at 298 K, which is recommended by IUPAC [*Atkinson et al.*, 2002], was used for the CH_2O evaluation.

An extension of the study on cross-sections includes IR spectra (Rainer Volkamer, unpublished manuscript, 2005). The measurements by *Rodenas García et al.* [2003] in the UV and IR spectral ranges act as link between the UV and the IR spectra. This study suggests to rescale the cross-sections according to relative scaling factors found in the comparison of UV and IR spectra. In a new study, *Gratien et al.* [2006] compared UV and IR formaldehyde absorption cross-sections and performed White cell measurements in both wavelength ranges in a chamber containing CH_2O. They found very good agreement both, between the IR spectra and between the cross-section by *Meller and Moortgat* [2000] and the IR cross-sections, using their

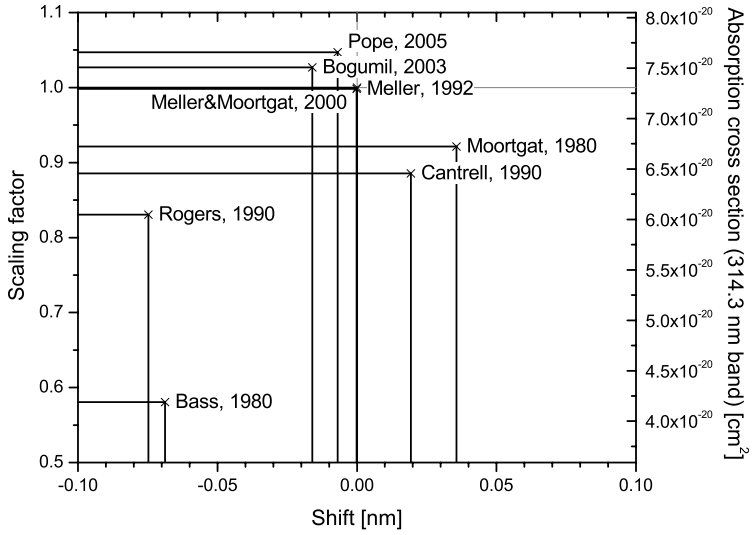

Figure 3.9: Overview on the differences in magnitude and wavelength calibration of the available highly-resolved absorption cross-sections of formaldehyde with respect to the spectrum by Meller and Moortgat [2000]. The cross-sections (at 296 ± 3 K) were compared in the spectral range 300-360 nm using a non-linear least-squares fit approach (figure from Hak et al. [2005]).

measurements as a link between both wavelength ranges. This result should be sufficient to recommend the spectrum by *Meller and Moortgat* [2000] as the most accurate CH_2O cross-section currently available for a wide wavelength range.

3.1.1.8.2 A Lamp Structure Influencing DOAS Evaluation

A persistent structure has been found regularly in the residuals of the DOAS evaluation. To look into the origin of the structure, lamp references and atmospheric spectra were scrutinised. In this section, the structure is introduced, its effect on spectra evaluation results is quantified and its probable origin is proposed.

Two different shortcut setups for recording lamp reference spectra were used during the measurements in FORMAT II. For long path DOAS instruments a built-in mirror system has been used for several years. For the multibeam system, a new rotating retro-reflector setup had to be developed. Both constructions are described shortly in *Sec. 3.1.1.6.1* and *Sec. 3.1.1.6.2*, respectively. The long path DOAS systems offer the chance to compare the built-in mirror system with the rotating retro-reflector setup. The rotating disc is fixed to a tripod which was placed few metres in front of the telescope to take the reference spectra and removed afterwards. A comparison of both shortcut setups was done during the measurements at Alzate 2003 with the 'Nashville' LP DOAS system to find out which of both setups is better suitable for evaluation of the measured atmospheric spectra.

On 1, 2, 6 and 7 October 2003, shortcut spectra were first recorded with the built-in mirror system and directly afterwards with the rotating disc setup. The shortcut spectra were taken twice a day in blocks of three to five spectra per shortcut setup type. The lamp spectra were compared here by dividing each two and high-pass filtering the resulting spectrum. (1) The spectra within one block of the same type (i.e. 'built-in Nashville' or 'rotating retro'), taken consecutively, are compared to check the random short-term variability (peak-to-peak noise). (2) Spectra of the same type but recorded on consecutive days are compared to test whether there is a variability on the time scale of a day which might be due to temporally varying components, e.g. the characteristics of the lamp. (3) Finally, spectra from the two different shortcut setup types taken in succession are compared to each other.

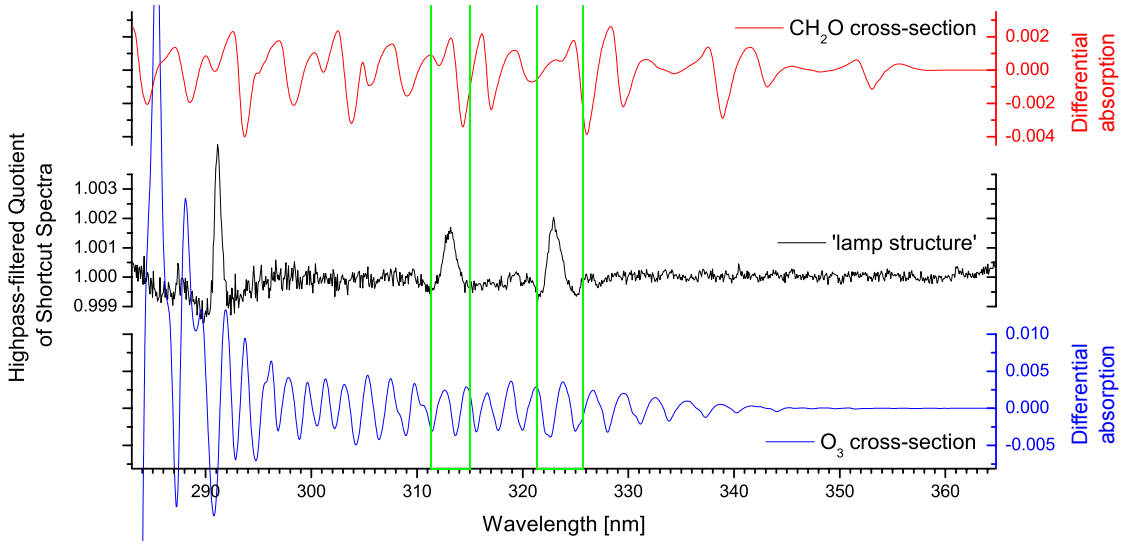

Figure 3.10: The middle panel shows the 'lamp structure' resulting from the high-pass filtered ratio of a Nashville shortcut and a rotating retro-reflector shortcut from 2 October 2003 (21:30 h). The differential absorption spectra of formaldehyde and ozone are displayed in red and blue. Two peaks (in green frames) are located in the spectral window used for formaldehyde evaluation (see Table 3.3).

Lamp spectra from all available days were compared in this way. The results can be summarised as follows: (1) For spectra from the same series, one recorded immediately after the other with the same shortcut setup type, uniform random noise spectra result from the comparison procedure. The size of the noise structure varies between less than 1 and around 2‰ for both shortcut types. (2) For shortcut spectra both taken with the built-in Nashville setup but on successive days, a weak structure becomes apparent, consisting of three peaks with a fixed position superimposed to the random noise. Similarly, for shortcut spectra recorded with the rotating retro-reflector setup with the time-lag of one day, the same structure is observed. The three peaks are equally located as observed before and more distinct. (3) However, the mentioned structure is most pronounced comparing a spectrum taken with the built-in shortcut and one taken with the rotating retro-reflector shortcut, even if one is recorded shortly after the other. The high-pass filtered ratio spectrum of the Nashville shortcut and the rotating retro-reflector shortcut recorded few minutes later, shown as black curve in *Fig. 3.10*, includes three distinct peaks in the measured wavelength range (~ 283-365 nm) which have the same fixed locations at 291.0, 313.0 and 322.8 nm as the weaker structures mentioned above. The shown spectrum results from shortcuts taken on 2 October, but the same structure of similar character was also found in the shortcut ratios of the other days.

The shown structure has not only been found in the Alzate 2003 evaluation. Peaks at the same locations have also been observed occasionally in the spectra of several other field campaigns, independent of the long path DOAS setup used and almost independent of the lamp type used (i.e. MCMA-2003 with LP DOAS 'Nashville' and PLI lamps; FORMAT II with multibeam LP DOAS and Osram lamps). The peaks of the structure have also been observed in atmospheric spectra, where the data revealed that sudden changes from one spectrum to the next can appear. Before the change, there is a long series of spectra which do not contain this structure, after the change, the spectra show the structure, or vice versa. The changes are thus easily discernible by a step in the temporal evolution of peak-to-peak residuals. Several examples for this behaviour were observed in the measurements at Bresso 2003 and Spessa 2003. It was not observed in all four beams but preferentially in one or in some cases two beams, where the structure occurred from time to time. The structure does not become obviously apparent in individual shortcut or

atmospheric spectra, but after forming ratios of two spectra as it is done in spectra evaluation. The origin of the structure is therefore supposed to be a non-random change of the lamp as explained below.

The described reproducible structure is inherent to both shortcut types and it is found in atmospheric spectra, but its extent varies with time. If the structure was caused by the optical elements, it would permanently persist, however its markedness varies spontaneously from time to time. All in all, the observations indicate that the variability of the lamp emission characteristics is responsible for the detected structure. Therefore, we assume that the three peaks represent a lamp structure. Since in the DOAS evaluation, the ratio of atmospheric spectrum and lamp reference is formed, the small changes in the emission features of the lamp are reflected here significantly. The Xe lamps proved to be instable in the spatial location of the hot spot [e.g. *Veitel*, 2002], i.e. the Xe lamp spectrum shows structures that depend on time and on the observed area of the arc. The appearance or disappearance of the structure might have to do with these changes of the location of the lamp arc. This could also explain the differences between the shortcut spectra recorded with different shortcut systems.

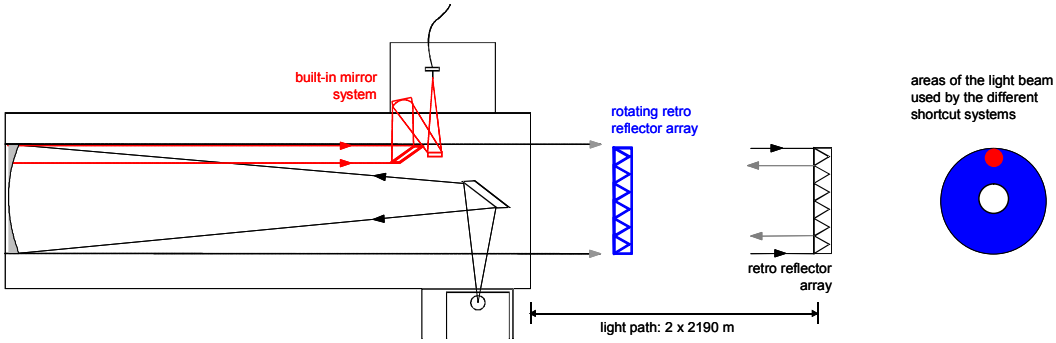

Figure 3.11: Telescope including only elements necessary to record lamp references. In the built-in shortcut system (red) additional mirrors are moved into the light beam. The rotating retro-reflector array (blue) is placed in front of the telescope. A cross section of the light beam comparing the areas used by both systems is shown on the right.

For the shortcut spectra, the origin of this structure can be circumscribed to differences in the optical course of the light beam measured. In the built-in shortcut systems only a small part of the light, which is used for the atmospheric measurement, is extracted from the entire beam for the measurement of a lamp spectrum (see *Fig. 3.11*). As the built-in shortcut systems generally 'look' at a lamp arc area that differs from the area used for the atmospheric measurements, the lamp structures can differ in the lamp shortcut and atmospheric spectra. However, the homogeneity of the outgoing beam has always been assumed. The new method involves a rotating retro-reflector array, placed in front of the telescope to reflect the outgoing light beam back to the main mirror and further onto the quartz fibre (see *Fig. 3.11*). The rotating shortcut averages over the outgoing ring of light and promises a more homogeneous image of the light source spectrum. The advantage of the rotating setup is that the used optical components are identical to those of the atmospheric spectra and the light paths only differ in the length. The markedness of the structure originates from the different areas of the lamp arc extracted by the respective optics.

Two of the lamp structure peaks are located inside of the wavelength range used for CH_2O evaluation (*Fig. 3.10*). Their positions coincide with absorption bands of the formaldehyde and ozone cross-section (see *Fig. 3.10*) and can be shown to influence the column-densities of these trace gases resulting from the fit if the structure is not corrected for (see *Sec. 3.1.1.8.3*). The

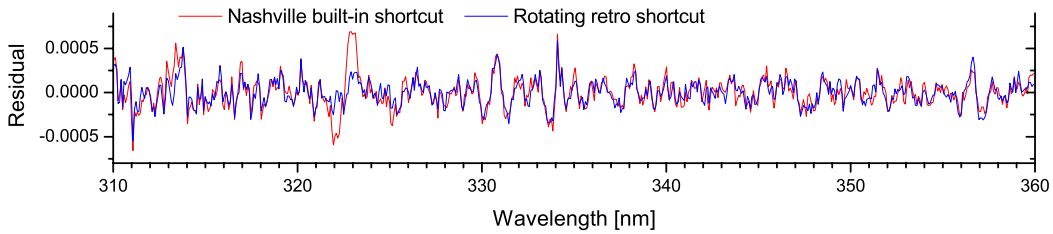

Figure 3.12: Residual structures of a spectrum taken on 2 October 2003 at Alzate (13:47 h) evaluated with the rotating retro-reflector shortcut (blue) and the Nashville shortcut (red). The residual of the latter is dominated by the lamp structure.

feature at 323 nm was found in some cases to have a size of more than 4‰ (e.g. 4.5‰ on 14 September, 18:36 h, beam 2, Bresso). This is comparable to or larger than the optical densities of ozone, formaldehyde or nitrous acid in this wavelength range. To test the effect of both shortcut setups on the spectra analysis, the fitting results from an analysis run with the Nashville shortcut spectrum as lamp reference were compared to those from an analysis run with the rotating retro-reflector setup. A typical example is shown in *Fig. 3.12* for a spectrum recorded on 2 October 2003 at Alzate. Using the built-in Nashville shortcut, peaks in the residual structure became apparent, situated at the fixed locations mentioned earlier. When using the rotating retro-reflector shortcut, the structure is hardly discernible in the residual. In this case, the structure is introduced to the analysis by the used shortcut spectrum. In these tests performed at Alzate, the fit results usually showed a larger residual structure when using the built-in shortcut system. The described observations are valid for all days for which shortcut spectra of both systems are available. The experiments between 1 and 7 October at Alzate showed that the rotating retro-reflector shortcut is well suitable for long path DOAS since it is less sensitive to the lamp structure.

For previous measurements only the built-in shortcut system, which supports the occurrence of lamp structures in the residuals, was available. *Veitel* [2002] encountered unwanted structures and he fitted an average residual as an additional reference. Also *Mettendorf* [2005] observed a structure which lead to problems with the ozone analysis. He fitted a simulated 323 nm structure to the spectra which was generated as a polynomial of 4th degree.

As mentioned above, the optical densities of formaldehyde and ozone are of the same order of magnitude as the lamp structure size. The derived concentrations of these compounds can vary depending on the lamp reference type used for the evaluation. For the studied days,

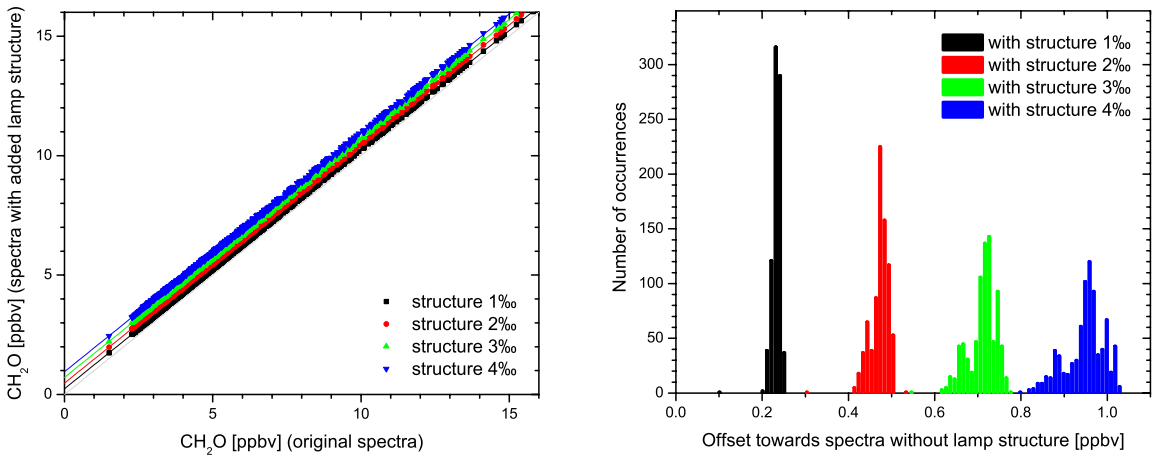

Figure 3.13: For spectra which are subject to the lamp structure, the evaluation procedure yields a formaldehyde concentration offset, dependent on the structure size. This is depicted in the left hand and the right hand plot for four structure sizes.

concentration differences of 5% for ozone (average concentration 37 ppbv) and up to 20% for formaldehyde (average concentration 3.0 ppbv) were found between the fitting results of both used shortcut systems (for a detailed study see below). The optical densities of the NO_2 and SO_2 absorptions are an order of magnitude larger than the structure size. The NO_2 and SO_2 column densities are uninfluenced by the choice of shortcut type and therefore of the structure. For the HONO evaluation an effect of the structure is usually avoided since the wavelength window for HONO evaluation starts at wavelengths larger than 325 nm. For ozone and formaldehyde, however, a limitation of the wavelength range is not favourable.

The structure can affect the retrieval of CH_2O and O_3 concentrations. To quantify the effect of the lamp structure, real atmospheric spectra, measured at Alzate 2003 and using the Osram lamp (see *Sec. 3.1.1.6.4*), were subjected artificially to the lamp structure of different peak sizes and spectra evaluation was performed. The concentration results obtained with peak sizes of 1, 2, 3 and 4‰ were compared to the original result without the structure. Analysis of the spectra yielded offset concentrations for O_3 and CH_2O. No effect was found for SO_2 concentrations. The offset obtained for formaldehyde is shown in *Fig. 3.13* and has a value of 0.95 ppbv for a structure size of 4‰. Ozone concentrations were influenced weakly with a maximum offset of 2.4 ppbv for structure size 4‰.

It can be concluded that additional structures can appear in the spectra, which are not caused by trace gas absorptions. Since the structure is most probably caused by lamp features, we cannot prevent it with the currently used telescope design. The structure can appear or disappear suddenly from one spectrum to the next. This might be assigned to sudden changes of the brightest spot of the lamp which have been reported previously. The state is constant before and after the change. As it disturbs the spectra analysis and gives rise to significant concentration offsets, it causes a systematic error and has to be reduced. To obtain credible O_3 and CH_2O results, we suggest to fit the lamp-structure as an additional reference (see also *Sec. 3.1.1.5*). That this is justifiable is shown in the following section.

3.1.1.8.3 Experiment on Accuracy

It is interesting to test whether one obtains the same results from four DOAS light beams, all using identical absorption paths. For this purpose, a multibeam long path DOAS system was operated, directing all four light beams along a common absorption path of 1625 m (single way) onto the same retro-reflector array. The multibeam telescope emits and receives up to four light beams simultaneously (*Sec. 3.1.1.6.2*). The beams are generated by the same lamp, but pass different optical elements afterwards: the light leaves the lamp in different exit angles, aiming at separate lamp house mirrors. After passing different external mirrors, the beams are reflected then by the same retro-reflector array, reach the telescope, where they are transferred to the spectrograph by different quartz fibres and are finally imaged to different lines of the CCD chip. Different structures could thus arise from the different mirrors, by getting light from different parts of the lamp or by CCD structures. The amount of possible effects of this ensemble of differences is studied in this section.

The 20 h experiment was carried out on 7 October 2003 at Bresso during the FORMAT II campaign. In order to compare the results, the spectra processing procedure was identical for the four beams. The spectra were analysed in the spectral range 300 to 350 nm, applying the procedure described in *Sec. 3.1.1.8*. Reference cross-sections of CH_2O, O_3, NO_2, SO_2 and HONO and one lamp reference were fitted to the spectra ¶. The formaldehyde concentration (average of the four beams) varied between 2.4 and 8.4 ppbv during the observed day. The variation of the formaldehyde concentration with time as measured with the four light beams is

¶. Only one lamp reference since before the experiment no lamp reference spectrum was taken – at least not with the used spectrograph grid.

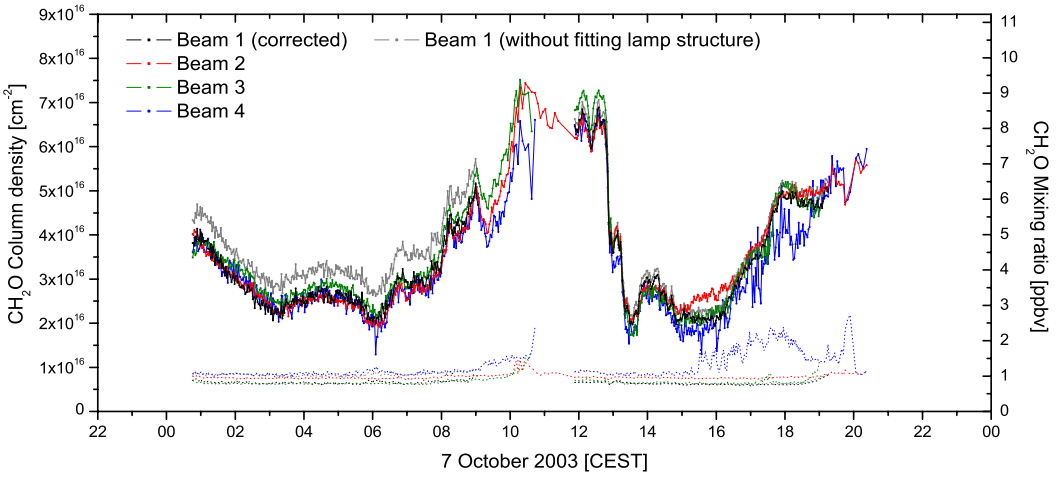

Figure 3.14: Time series of formaldehyde measured by four light beams, all pointing to the same retro-reflector array, with a single path length of 1625 m (FORMAT II, Bresso, 7 October 2003). The grey curve reflects the results for beam 1 initially obtained for beam 1. The black curve shows the result after correcting the lamp structure. The detection limits are shown as dotted lines.

shown in *Fig. 3.14*. The agreement between the results was very good in the morning (between 0 h and 9 h), but note the offset in the concentration measured by beam 1 (grey trace), which is discussed below. For the second half of the experiment (12-20 h) the conditions were less favourable. It started with high concentrations around 9 ppbv. While beam 1 and 4 agreed very well during the first hour (12-13 h) of high concentrations, beam 3 showed substantially (10%) higher concentrations and beam 2 had slightly lower concentrations. Beam 4 had the lowest signal intensity of all beams (see Table 3.7) for that day and over the entire duration of its operation and therefore the lowest signal-to-noise ratio. In the afternoon, the alignment of beam 4 is further degrading and its results should not be further considered.

In the morning spectra (00:45-09:03 h) of beam 1, the lamp structure, introduced in the previous section, was very pronounced. The feature at 322.9 nm had a size of ~ 4‰, the feature at 313.0 nm was slightly less pronounced (see *Fig. 3.15*). The structure was only observed in

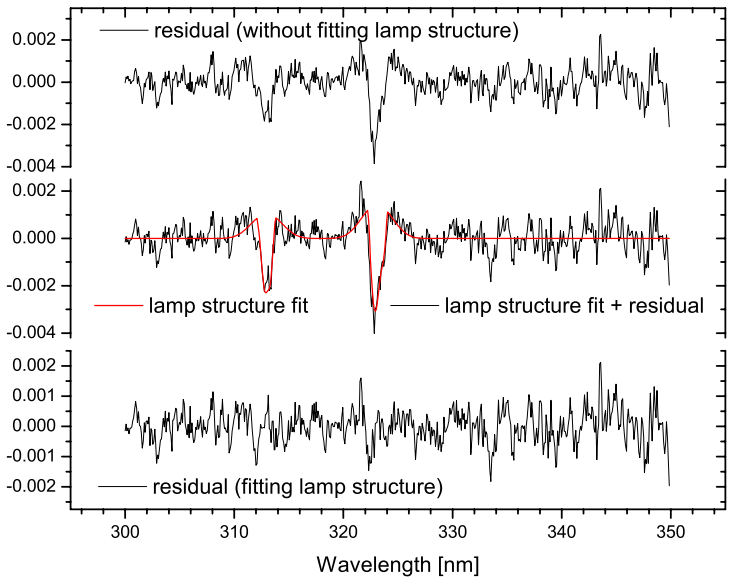

*Figure 3.15: **(Top)** Residual without fitting the 'lamp structure'. **(Middle)** 'lamp structure' fit. **(Bottom)** Residual after fitting the lamp structure reference. The spectrum was recorded on 7 October 2003 at 06:48 h in Bresso.*

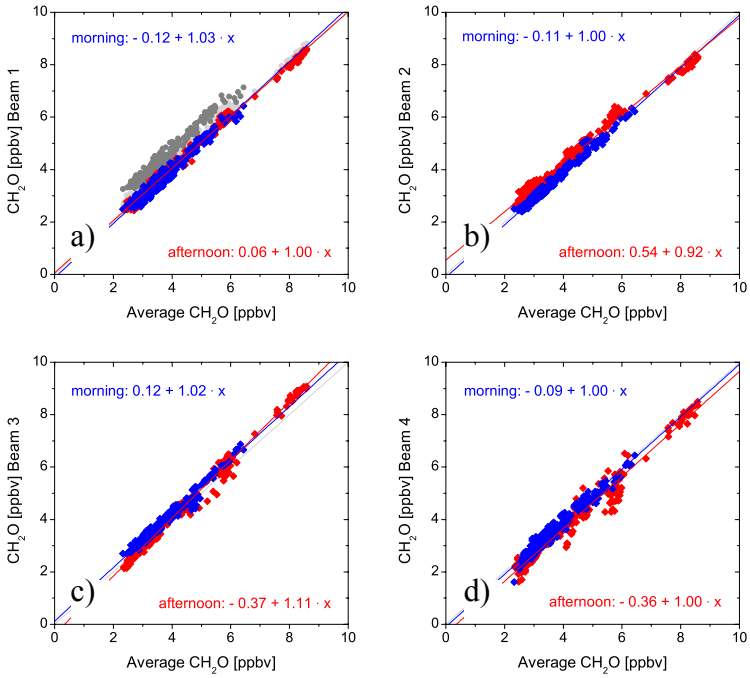

*Figure 3.16: Scatter plots of the CH_2O results of **(a)** beam 1 to **(d)** beam 4 versus the average of the four beams. The regression statistics, separately for morning (blue) and afternoon (red), are given for each plot. The grey line represents the one-to-one correspondence line. Uncorrected results from beam 1 are shown in (a) as grey (morning) and light grey (afternoon) markers.*

one of four beams. We found in *Sec. 3.1.1.8.2* that the CH_2O evaluation reacts very sensitively towards this structure, resulting in a significant concentration offset and higher residuals. The substantial offset observed in *Fig. 3.14* for beam 1 results (grey trace) towards the results of the other beams is thus effected by the lamp structure. In the afternoon spectra (11:53-18:56 h), the structure was weak. The day will thus be subdivided into these two parts. The first phase contained nighttime hours with high concentrations of CH_2O, NO_2 and HONO. Since only one lamp reference was used here for spectra evaluation, the change of the structure is clear to have occurred in the atmospheric spectra as a consequence of a change in the lamp emission. Before the change, the structure could not be handled with the available lamp reference which was recorded at the end of the experiment. The structure size observed in beam 1 exceeds the optical densities of CH_2O, O_3 and HONO absorptions usually detected in Bresso by far. In the example spectrum shown in *Fig. 3.15*, the lamp structure had a size of 0.004, the optical densities of formaldehyde and nitrous acid were 0.0015 and 0.003, respectively (ozone was below the detection limit at night). A correction spectrum containing the features at 313 and 323 nm is included as an additional reference (*Fig. 3.15*, middle panel) in the DOAS evaluation. The black trace in *Fig. 3.14* is the result for beam 1 if this reference-structure is fitted to the absorption spectra. It is in perfect agreement with the other three beams apart from random differences and deviations due to degrading alignment.

For further comparison of the results from four beams, the mixing ratio of each beam is displayed in *Fig. 3.16a-d* versus the average mixing ratio of the four light beams. Due to the degraded alignment in the afternoon and the varying extent of the lamp structure, morning and afternoon results are compared separately. The line fit parameters for morning and afternoon data are included in the plots of *Fig. 3.16*. Beam 1 results corrected for the lamp-structure (blue and red markers) and uncorrected results, displayed with grey markers, are shown in *Fig. 3.16a*. The structure leads to a systematic offset (here ~ 0.7 ppbv) in CH_2O concentration. By fitting

Table 3.7: Measurement uncertainty and measured intensity of the four beams during the experiment on 7 October 2003 at Bresso.

	Beam 1	Beam 2	Beam 3	Beam 4
avg. 1σ uncertainty	0.31 ppbv	0.32 ppbv	0.27 ppbv	0.41 ppbv
avg. intensity [counts/channel]	4.68×10^6	7.75×10^6	4.97×10^6	8.54×10^5

the lamp structure to the atmospheric spectra, the offset can be corrected. The offset of beam 1 without fitting the structure, compared to the averaged result of the other beams was quantified to be 0.68 ppbv in the morning ($b = 1.02$, $a = 0.68$) with a structure size of 0.004 and 0.28 ppbv in the afternoon ($b = 1.00$, $a = 0.28$) with a structure size of ~ 0.001. After correcting for the lamp structure, the four beams are in very good agreement. The regression slopes, b, generally differ by less than 4%. The y-axis intercepts, a, are smaller than the detection limits. The deviations from the one-to-one line for beams 2 and 3 derive mainly from the discrepancies observed between 11:53 and 12:55 h (*Fig. 3.14*). During this period, the average intensities of both beams are reduced compared to later. Excluding these data points from the regression yields $b = 1.00$, $a = 0.28$ for beam 2. The agreement of beam 3 results with the average only slightly improves ($b = 1.08$, $a = -0.31$). The possible reason for the deviation of beam 2 and 3 around 12 h is a slight misalignment of the external mirrors, since the incoming light intensity of these beams was reduced to about 75% compared to later. These data points at the highest concentrations measured influence the slope of the regression line in *Fig. 3.16*. Beam 4 spectra are noisy, especially during the afternoon and are not expected to yield reliable results.

The average measurement uncertainty during that day is summarised in Table 3.7 for beam 1 (without fitting the structure), 2, 3 and 4, respectively. If the structure is fitted to beam 1, the uncertainty is 0.27 ppbv. The average 1 σ value of the residual structure and the corresponding 2 σ detection limit are listed for each light beam.

Since the photons from the four beams are detected simultaneously on the same CCD-chip, the integration time for one spectrum is the same for all beams (*Sec. 3.1.1.6.7*). The measurement routine adapts the exposure time only to the beam with the highest intensity, so that a certain saturation degree is reached for that particular beam (*Sec. 3.1.1.7*). In the ideal case, the detector is exposed until 70% of diode saturation is reached for all beams. However, this is not generally the case. In the measurements at Bresso at this particular day, beam 2 was the beam with the highest intensity. Beams 1 and 3 had 60% of this on average (i.e. 40% of diode well depth). Beam 4 only had 10% of the intensity of beam 2 (only 7% of well depth). Since the integration time is optimised for the beam with the highest intensity, the remaining beams can have large noise-to-signal ratios. This is especially the case for beam 4 which should not be considered. According to *Mettendorf* [2005], the fraction of stray light from adjacent beams can be 11-26%. For beam 4 it is lower, since the used fibres are not directly adjacent on the CCD. Since the multibeam DOAS was developed to derive spatially resolved information by tomographic means, the quality of the overall evaluation is determined by the weakest beam. This can be seen as a major problem since large differences in received intensities have been observed in the experiment presented here. There should be a similar illumination of the detector for all beams. The achievement of comparable intensities for all beams could be assured by using more than one detector.

For the tomographic application it has to be verified that all beams provide the same results when they are treated identically. Each individual path measurement provides a result which is regarded to be reliable. However, when there is only one measurement, no statement on its accuracy can be made. The sensitivity of the evaluation results towards additional spectral

structures cannot be tested since usually there is no reference measurement to compare with. Spectral structures as the one introduced in the previous section can influence the analysis and give rise to deviations from the true result. For tomographic long path DOAS measurements, accurate measurements along all light beams are absolutely necessary. That this requirement is not always fulfilled, has been shown by the presented experiment. This represents a limitation for the application of tomography for formaldehyde. A solution was found by fitting the lamp structure. Alternatively, a new telescope design is currently being developed at the IUP, using a fibre construction to introduce the light into the telescope (Jens Tschritter, pers. comm., 2006). In this system, the problem of the varying lamp structures discussed above will not arise, since the same optical components will be used for atmospheric and shortcut spectra. Regular measurements of all beams to the same retro-reflector are also recommended for the multibeam measurements to identify and reduce the errors of the different light beams.

3.1.2 IR Spectroscopy (FTIR)

Since almost all molecules absorb infrared light, the infrared spectroscopy is a further method to quantify formaldehyde by its absorption structures. Similar to UV absorption spectroscopy (*Sec. 3.1.1*), IR spectroscopy uses the absorption of certain frequencies of radiation by molecules which is a result of vibrational and rotational transitions within the molecule. The difference of the Fourier Transform Infrared (FTIR) method towards the DOAS method is in the detection. Instead of using dispersive spectrophotometers, the main component in the FTIR spectrometer is a Michelson interferometer [*Griffiths and de Haseth*, 1986]. The interferometer splits and recombines a light beam. It uses a stationary and a moving mirror to create an interference pattern (interferogram). As the moving mirror scans back and forth, the detector observes light and dark bands corresponding to partial and total constructive and destructive interference in the detected output beam. Since the infrared source emits light over a broad range of frequencies, the resulting interferogram represents the sum of all cosine waves generated by each individual infrared frequency. Complete constructive interference occurs only at the point where both mirrors are at equal distances from the beam splitter (for all frequencies). The interferogram (measured intensity versus mirror displacement) is a function of time domain and the spectrum (intensity versus wavenumber) is a function of frequency domain. The interferogram contains all the spectral information collected by the instrument and is converted into a spectrum by applying the cosine Fourier transform. Formaldehyde is identified in the spectra by a characteristic doublet at 2779 and 2781.5 cm^{-1} [*Tuazon et al.*, 1978].

This technique has high spectral resolution (i.e. 0.06-1.0 cm^{-1}) and good time-resolution [*Tuazon et al.*, 1978]. It can be applied in two modes of operation: In passive operation, the thermal emission from the trace gases under consideration is used. A particular example for a passive system is the Michelson Interferometer for Passive Atmospheric Sounding (MIPAS) [*Fischer and Oelhaf*, 1996]. In active operation, an artificial light source is used. Long path or White type setups are usually chosen for the detection of tropospheric trace gases [*Tuazon et al.*, 1978]. In the latter, an infrared beam is passed through a sample cell of up to 2 km in a multiple-reflection optical path. This method was part of an intercomparison of formaldehyde point measurement techniques (see *Sec. 5.2*). The open path FTIR White system was set up by CTH and ran semi-continuously over 28 days, between 22 July and 18 August. The system consisted of an infrared spectrometer coupled to an open path multi-reflection system (White system) with a base path of 25 m and a total path length of 1 km. The White system was based on the retro-reflector design outlined by *Ritz et al.* [1993] with minor modifications. An FTIR (BOMEM MB 100) computer-controlled spectrometer with a resolution of 1 cm^{-1} was employed. A 24 h dewar InSb detector was used covering the spectral region from 1800 to 3500 cm^{-1}. The spectra were analysed using the non-linear fitting software NLM (D. Griffith, pers. comm.), which is a further development of the MALT code [*Griffith*, 1996]. In NLM, line

parameters from the HITRAN compilation [*Rothman et al.*, 1987] are convolved with appropriate instrument parameters and subsequently least-squares fitted to the measured spectra to derive the average concentration of various molecules along the measurement path. During most of the campaign, 64 consecutively recorded spectra were binned, thus yielding a measurement time resolution of 5 min. The measurement precision as obtained from the standard deviation of the CH_2O measurements is around 0.2 ppbv. The overall accuracy, as determined from the uncertainty of 5% in the spectroscopic data [*Rothman et al.*, 1987], an offset which depends on the CH_2O concentration and the precision, is specified to vary from 27% for a measured mixing ratio of 2 ppbv to 6% for 15 ppbv.

3.1.3 Hantzsch Technique (Fluorescence Detection)

A widely used method for the measurement of formaldehyde concentrations is based on the so-called *Hantzsch* reaction, which is sensitive to CH_2O in aqueous solutions. The method described by *Kelly and Fortune* [1994] was initially used by *Nash* [1953]. Gaseous formaldehyde from ambient air is transferred quantitatively into the liquid phase using a stripping coil with a well defined exchange time between gas and liquid phase. The coil is kept at 10°C to ensure a quantitative sampling (> 98%) of CH_2O even at pressures as low as 600 hPa. The reaction of CH_2O with the Hantzsch solution containing acetylacetone, acetic acid and ammonium acetate in a heated reaction coil generates the fluorescent dye 3,5-diacetyl-1,4-dihydrolutidine (DDL). Formaldehyde is quantified fluorimetrically by exciting the DDL at 253 or 412 nm (Hg lamp or now LEDs) and detecting the fluorescence signal at 510 nm, which is specific to CH_2O. The gas flow is controlled by a mass flow controller with a precision of 1.5%, and a constant liquid flow is provided by a peristaltic pump. Studies of interferences showed that the technique is very selective for formaldehyde, with the response for other molecules found in typically polluted air masses being several orders of magnitude lower.

Commercial ¤ Hantzsch instruments were operated by three groups in the FORMAT campaigns to continuously measure the CH_2O mixing ratio. In the intercomparison experiment (*Sec. 5.2*) during FORMAT I, the results of five Hantzsch monitors were compared with other formaldehyde point measurement results. The BUW used an Aero-Laser HCHO analyser, model AL4001. The PSI monitor and the three IFU instruments were new versions of the AL4001, the AL4021, which is identical in the chemistry components, but with slight modifications mainly concerning the temperature stabilisation of the fluorimeter and the layout of the gas flow. All Hantzsch instruments were equipped with the same optical filters. For the sake of brevity, the five instruments used in the intercomparison will be referred to as IFU1, IFU2, IFU3, PSI, and BUW. The time resolution of the instruments (0-90% of the final value after a change in concentration) is ~ 90 s with a delay time of approx. 260 s (depending on the flow rate settings) caused by the stripping and reaction coils. The systems were calibrated once per day using liquid standards, which were prepared independently by each group. Zero adjustment was performed once per day (IFU), every six hours (PSI) and about six times per day (BUW), respectively using Hopcalite® cartridges. The ozone cross sensitivity is stated to be a positive linear signal of 200 pptv CH_2O per 100 ppbv of ozone. Refer to Table 4.2 for detection limit, accuracy and precision of the instruments in the field.

3.1.4 DNPH Technique (Derivatisation Method)

There are a number of methods, in which derivatives of carbonyl compounds are formed that can be easily separated and measured [*Vairavamurthy et al.*, 1992]. The most common of these is the use of silica gel or octadecylsilica (C18) cartridges coated with acidified 2,4-dinitro-

¤. AL4001 and later models, Aero-Laser GmbH, Garmisch-Partenkirchen, Germany

phenylhydrazine (DNPH), which reacts with carbonyls to form stable hydrazones. Some care must be taken during sampling to avoid artifacts due to reactions of O_3, which has been shown to give positive interferences for C18 cartridges but negative interferences when silica gel is used as the sorbent [*Gilpin et al.*, 1997]. The cartridges are analysed in the laboratory by first eluting the DNPH-carbonyl hydrazone from the solid sorbent (e.g. silica gel) with a suitable organic solvent (e.g. acetonitrile). In the liquid phase, the mixture of hydrazones, formed from the reactions of the set of carbonyl compounds commonly found in air, can then be separated using HPLC (high-performance liquid chromatography) and quantified using UV absorption detection near 360 nm [e.g. *Duane et al.*, 2002]. For a homologous series, hydrazones corresponding to the higher molecular weight carbonyl compounds elute later during the chromatographic separation. The formaldehyde concentration is obtained from the given volume of air passed through the cartridge and the mass of the eluant. Derivatisation of CH_2O using DNPH allows quantitation of low levels of CH_2O. Since the hydrazones are highly stable, the samples need not be analysed at the collection site. Derivatisation techniques are limited by the required time integration (e.g. 2 h) of sample collection which does not describe the rapid fluctuations in the CH_2O concentrations.

During the FORMAT campaigns, JRC used the DNPH technique at all three sites to collect carbonyl samples in two-hour periods during the day. The results at Bresso were compared with other in-situ formaldehyde measurements (see *Sec. 5.2*). Sampling was done according to the standard of the European Monitoring network, EMEP [*Rembges et al.*, 1999]. The air sample (flow 0.9-1.0 l min^{-1}) was drawn through an ozone scrubber (Waters Sep-Pak® KI-cartridges) before passing into the DNPH-coated C18 cartridges (Waters Sep-Pak® DNPH-cartridges). Airborne carbonyls are hereby collected as their non-volatile 2,4-dinitrophenylhydrazone derivatives.

The cartridges were eluted with 2.5 ml of acetonitrile in the laboratory, diluted with 2.5 ml of H_2O and stored at 5°C until analysis. The samples were analysed by HPLC-UV (high performance liquid chromatography) with a temperature stabilised (20°C) 30 cm × 3.9 mm C18-coated silica gel (4 µm) column (NOVO-PAK) run in the gradient mode (0.9 ml min^{-1}). Detection and quantification were carried out at 360 nm. The employed eluents were H_2O (A-eluent) and acetonitrile (B-eluent). The gradient was programmed from 50% B to 90% B in 42 min. The detection limit for this method was in the range of 5-20 ng formaldehyde (S/N = 3).

A possible interference may be caused by the coelution of hydrazones of target compounds with hydrazones of other aldehydes and ketones. However, for the formaldehyde-hydrazone no interference has been reported to date. Due to high humidity clogging the sample cartridges during the night and early morning, the automatic sampling system was not used during night time and both the first and the last samples were taken without ozone scrubber. Positive interference in the form of a number of extraneous peaks in the HPLC-UV chromatograms has been reported for C18 DNPH-cartridges, when used at high atmospheric ozone concentrations without ozone scrubber [*Vairavamurthy et al.*, 1992]. In the present study, sampling without ozone scrubber was only carried out at low ozone concentrations. Thus, positive interference is unlikely. Moreover, no extraneous peaks were monitored. However, as in all kinds of chromatographic analysis, coelution of unknowns with the target analytes cannot be excluded. In previous studies of ambient air from this area, JRC used the DNPH technique at low ozone concentrations without ozone scrubber and have been able to rule out interference from potential co-eluents by analysis of the DNPH extracts not only by HPLC-UV but also with HPLC coupled to atmospheric pressure mass spectrometry [*Duane et al.*, 2002].

Blank samples were taken on a daily basis by exposing DNPH cartridges to open air without sample flow. The formaldehyde blank levels were all below 2 nmol/cartridge. For an air volume of 120 l this leads to a detection limit of 0.5 ppbv. Accuracy and precision are indicated in Table 4.2.

3.2 Measurement Techniques for Other Trace Species

3.2.1 Chemiluminescence (Nitric Oxide)

The chemiluminescence method for gas analysis of nitric oxide is based on the detection of photons emitted by electronically excited NO_2 molecules during a relaxation process (chemiluminescence). The excited NO_2* molecules are produced by the reaction of the ambient NO with ozone generated in the device. The chemiluminescence signal is proportional to the NO concentration in the sampled air. It is detected photo-electrically, e.g. by a photomultiplier tube. Only about 20% of the NO_2 that is formed by R 2.13 is in the excited state. The largest portion of the NO_2* returns to the ground state without radiation emission due to collisions with other molecules (quenching). To enhance the photon yield, the pressure in the reaction chamber is reduced. Nitrogen dioxide can be measured analogously by first converting NO_2 to NO photolytically using a broad-band arc lamp. The photolysis system is followed by chemiluminescence detection of the product NO as described above. Refer to the review on the application of chemiluminescence to atmospheric measurements by *Navas et al.* [1997] for more details.

During the FORMAT campaigns, measurements of NO and NO_2 were performed at Alzate by Paul Scherrer Institut (PSI), Switzerland, with a commercial chemiluminescence device (CLD 770 AL ppt, Eco Physics, Duernten, Switzerland). For the measurement of NO_2, the molecules are first transformed to NO by a photolytic converter (PLC 770). The same type of instrument was used by IUP at Bresso 2002, but without photolytic converter.

3.2.2 Gas Chromatography (VOCs)

Gas chromatography is the technique usually used for the separation and identification of individual VOCs. Separations in chromatography are based on multiple partition of the analyte between two phases, a stationary and a mobile phase. A gas chromatograph (GC) uses a thin capillary fibre for separation, known as the column. The mobile phase is a chemically inert carrier gas (e.g. helium) flowing through the column. The stationary phase is solid (e.g. Al_2O_3) and lines the inside of the column. The gaseous sample is injected into the entrance of the column and is further transported by the carrier gas. In the column, the analyte is adsorbed onto the stationary phase. Gas chromatographic separation occurs because of differences in the positions of adsorption equilibria between the gaseous components of the sample and the stationary phase. The rate at which the individual components of the sample progress along the column depends on the strength of adsorption (affinity for the stationary phase), which in turn depends on the type of molecule, the column material and the temperature. The separation column usually has a length of 25-60 m and is wound into a small coil which is built into an oven. By continuously increasing the temperature, a rapid and complete separation of the mixture is achieved. Since each type of molecule has a different rate of progression, the various components of the analyte mixture are separated as they progress along the column and reach the column at different times.

As the chemicals exit the column, they enter the detector. The flame ionisation detector (FID) is the most common detector due to its excellent sensitivity for organic compounds. The analyte molecules are transported by the carrier gas into a hydrogen-air flame where they are ionised thermally. The produced ions can be measured if there is a potential difference between the flame jet and a collector electrode. The detector signal is linearly proportional to the amount of the analyte over a large concentration range. The magnitude of the signal is plotted versus the time and a chromatogram is generated. The substances are identified by the residence time of the analyte in the column (retention time).

During the FORMAT II campaign, GC-FID instruments were applied by EMPA in

Alzate 2003, by JRC in Bresso 2003 and by MetAir/PSI on board the Dimona 2003 (and 1998). The individual hydrocarbons can be quantified with a detection limit of 5-20 ppbv [*Dommen et al.*, 2002].

3.2.3 UV-Absorption (Ozone)

UV-absorption provides an accurate means to measure ozone. Several commercially available instruments use this method which is based on the ultraviolet absorption of O_3 at 254 nm. The instruments apply the 254 nm emission line emitted from a low pressure mercury discharge lamp as the UV light source. The gas sample flows into a sample cell, passing a valve that alternately guides the flow directly to the cell or via a selective ozone scrubber. The two ways alternate every ten seconds. The UV light transmitted through the sample cell is detected by evacuated photo-tubes. The difference in light transmission between the ambient sample and the ozone scrubbed reference sample is directly related to the O_3 concentration through the optical path length and the absorption coefficient of O_3 at 254 nm according to the Beer Lambert law (eq. 3.1). UV-absorption could be an absolute measurement, like DOAS, if the absorption path in the tube was perfectly known. Since the absorption path can be lengthened due to reflexion at the tube walls – and thus the instrument has to be calibrated regularly – the method does not tap the full potential of absorption quantification of ozone by means of the Lambert Beer law. Conversion of the measured O_3 concentration to mixing ratio units requires the accurate measurement of temperature and pressure in the absorption cell.

Ozone was measured by IUP at Bresso with a commercial short path UV-absorption instrument (Horiba APOA 360) with a time resolution of 1 min and a detection limit of 1 ppbv. Ozone measurements by PSI at Alzate, by MetAir and by IFU were also performed by UV-absorption.

3.2.4 Alpha Spectroscopy (Radon)

In conjunction with meteorological data, atmospheric radon activity measurements provide a useful source of information on stability and mixing of the lower boundary layer (see *Sec. 2.4.3*). A ^{222}Rn monitor for continuous observations of the atmospheric ^{222}Rn daughter activity was used at Alzate. The atmospheric ^{222}Rn concentration is measured indirectly via its short-lived decay products with the so-called static filter method [*Levin*, 2000]. The short-lived ^{222}Rn daughters (^{218}Po, ^{214}Pb, ^{214}Bi, and ^{214}Po), being isotopes of heavy metals, immediately after generation become attached to submicron aerosol particles [*Jacobi and André*, 1963], which are collected on a quartz fibre aerosol filter. The α-activity accumulated on the filter is assayed online by α-spectroscopy. Ambient air is continuously pumped through a quartz fibre filter, where the ^{222}Rn daughters are quantitatively collected. The flow rate (of about 1-2 m^3 h^{-1}, depending on the pump) is monitored with a flow sensor (MKS) [*Levin*, 2000]. The α-decay of the ^{222}Rn daughters ^{218}Po (E_α = 6.0 MeV) and ^{214}Po (E_α = 7.7 MeV) is measured in-situ with a surface barrier detector, and the net atmospheric ^{214}Po activity concentration is then calculated from the ^{214}Po activity on the filter. The mean α-activity of the ^{222}Radon daughter ^{214}Po measured during a certain time interval (e.g. one hour) on the filter is almost directly proportional to the atmospheric ^{222}Radon daughter activity approximately one hour before. This 'time delay' is due to the pure β-emitters ^{214}Pb and ^{214}Bi having a life time of 39 min resp. 29 min and thus leading to a mean effective time lag of the measured α-activity on the filter of about 50 minutes.

One shortcoming to determine the atmospheric ^{222}Radon activity accurately with the filter technique is the interference of the α-activity of the ^{220}Radon daughters (coming from the ^{232}Thorium series), namely ^{212}Po (E_α = 8.8 MeV) and ^{212}Bi (E_α = 6.1 MeV) which are also collected on the filter. However, it is possible to assay the composite spectrum of the α-activity on the filter with sufficiently high energy resolution.

Under most meteorological conditions, the radon daughters are in secular radioactive equilibrium with atmospheric ^{222}Radon, hence, the atmospheric ^{222}Rn (gas) activity can be determined via its short lived aerosol-attached daughter activity. The monitor is suitable to measure ^{222}Rn activities at hourly resolution down to 0.5 Bq m^{-3} with an uncertainty well below ± 20% [*Levin et al.*, 2002].

3.2.5 Spectroradiometry (Actinic Flux)

The spectral actinic flux quantifies the in-situ radiation available to a molecule from all directions for the initiation of a photodissociation process. It can be measured in-situ quantitatively and spectrally resolved with a spectroradiometer or calculated by means of atmospheric radiation transfer models.

The actinic flux spectroradiometer (Bentham DMc150FC) used for the FORMAT and Mexico campaigns consists of a double monochromator (DM) spectrograph equipped with tunable gratings (2400 grooves mm^{-1}) and a photomultiplier for photon detection. It was characterised in detail by *von Friedeburg* [2003]. The instrument measures the spectrally resolved absolute intensity of the actinic flux. The radiation from the upper hemisphere is collected by a Teflon® diffusor optic which is particularised below in more detail. The wavelength ranges relevant for the photolysis frequencies of different molecules are scanned during successive time segments. Thus, recording an actinic flux spectrum takes about 5 min with the instrument. Absolute actinic flux calibration was performed before and after the campaigns at the Forschungszentrum Jülich, Germany, using certified irradiance standards as described by *Kraus et al.* [2000].

During the FORMAT campaigns in Bresso, the fibre bundle with the detector-head was sited on the roof of the container. Measurements were performed in the wavelength interval of 280 to 425 nm, suitable for J_{NO2}, J_{HONO}, $J_{O(1D)}$ and J_{CH2O}. The step width was set to 1 nm, yielding a temporal resolution of approx. 5 min (see above). Only one type of a filter, moved by a filter wheel in the DM, was used additionally during the measurement by the spectroradiometer: an UG5 UV-pass filter was introduced to keep out VIS when looking at UV. The filter wheel also contains a black disc for dark current recording after each solar spectrum. At Mexico City, the spectroradiometer measured solar actinic flux spectra from 280 nm to 450 nm with a step width of 1 nm.

The instrument has been compared to other spectroradiometers and filterradiometers in an intercomparison campaign that was conducted in Jülich in June 2005 ($SZA_{min} = 27°$). The results agreed within 10% and better: J_{NO2} + 4%, $J_{O(1D)}$ + 10%, J_{CH2Or} + 7%, J_{CH2Om} + 6% [*Bohn et al.*, 2005]. Since the Heidelberg and Jülich spectroradiometers were not identical in construction, additional experiments with our instrument were performed in the laboratory utilising a tungsten lamp. It was found that the detector head was no 2π-head with almost uniform sensitivity for all angles of incidence within a solid angle of 2πsr, as had been assumed so far, but that the sensitivity showed a cosine dependence, decreasing with increasing solar zenith angle. Surprisingly, the agreement of the photolysis frequencies determined from the actinic fluxes measured outdoor by both spectroradiometers was nevertheless quite good (see above). This indicates that multiple scattering, taking place in the atmosphere, causes the solar radiation to fall onto the detector head relatively uniform from all directions. Consequently, the angle-dependent sensitivity is hardly of importance at most polluted continental sites. For the measurements presented in *Chapter 4*, the instrument has only been employed in heavily polluted urban areas, where aerosols are abundant and the near-isotropy of the incident light is assumed to be fulfilled.

4 Field Observations

To assess the distribution and variability of formaldehyde, the results from three field measurement campaigns in polluted urban areas are analysed in this thesis. Two campaigns were part of the FORMAT (FORMAldehyde as a Tracer of photooxidation in the troposphere) project, which was supported by the European Union [*]. Another campaign was MCMA-2003 to investigate the atmospheric chemistry of the Mexico City Metropolitan Area (MCMA):

- July / August 2002 in Lombardia (Italy) referred to as the FORMAT I campaign
- April / May 2003 in Mexico City (Mexico) referred to as the MCMA-2003 campaign
- September / October 2003 in Lombardia (Italy) referred to as the FORMAT II campaign

The main aim of the FORMAT project was to obtain a better knowledge of the regional distribution and variability of formaldehyde in the Milano urban plume and in the Po Basin. Another objective was to intercompare various measurement techniques for formaldehyde in order to understand and reduce discrepancies between various measurement methods. Further goals were to gain a better understanding of the role of formaldehyde in the oxidation processes of organics, to compare measured and modelled formaldehyde and use the improved knowledge to strengthen the capability of atmospheric chemistry models to calculate formaldehyde and thereby predict smog episodes in Europe. Additional information is also given in the final report of the project. To address these objectives two field campaigns were conducted in Northern Italy. The first campaign was the 'summer campaign', the second was planned as a 'winter campaign' but was held in autumn. Altogether eight research groups [†] were involved in the FORMAT project.

In Mexico City, the variability of formaldehyde in a strongly polluted environment was investigated. The general goals of the field campaign were to develop improved emission inventories for volatile organic compounds and nitrogen oxides, to develop a better understanding of formaldehyde sources and atmospheric chemistry, to investigate fine particulate components and sources and to develop improved understanding of odd nitrogen levels and partitioning.

This chapter gives an overview of the conditions experienced during the field campaigns in the greater Milano area and in Mexico City. The locations of each campaign are introduced and the meteorological conditions and time series of measured trace gas data are presented. All times in this thesis are given as Central European Summer Time (CEST = UTC + 2), except for Mexico City, where Central Standard Time (CST = UTC – 6) is used.

---

*. project number EVK2-2001-00120

†. [1] NILU, [2] IUP, [3] IFU, [4] IUP-HB, [5] PSI, [6] UIO, [7] CTH, [8] JRC, for full names of the institutes refer to list of abbreviations at the end of the thesis.

4.1 The FORMAT Sites

The Po Basin is a mostly flat area in northern Italy extending 500 km from east to west. It is bordered by the Alps in the north and west and the Apennines in the south as shown in the inset of *Fig. 4.1*. The Po Basin is the most important industrial and agricultural region of Italy. The southern part is an agricultural area, with fields extending along the river Po and irrigated plains.

Milano is located in the western part of the basin and is the capital of the region of Lombardia. Milano is the largest city and the most important industrial and economic centre in the basin. It is characterised by a high density of residential and commercial premises and a very high volume of vehicular traffic with 1-2 million vehicles per day in Milano and surroundings. Surrounding the city, mainly in the north, the suburbs make up a high-emission-rate region, marking the metropolitan area [*Dommen et al.*, 2002]. The metropolitan area, *Grande Milano*, has a population of ~ 7 million inhabitants.

The experimental region extended from the Po south of Milano to the Alpine foothills 40 km north of Milano. An overview of this region, showing the locations referred to in this thesis, can be obtained from *Fig. 4.1*. The densely populated Milano metropolitan area was chosen as one of the largest urban and industrial regions of Europe. Several campaigns had been conducted in the surroundings of Milano in the past, e.g. POLLUMET 1992/93, PIPAPO 1998 [*Neftel et al.*, 2002], so the local conditions were already well-known. Since both, pollutant emission and solar insolation are high on this area, the public health is strongly affected by episodes with high photo-oxidant levels [e.g. *Prévôt et al.*, 1997; *Thielmann et al.*, 2001]. This can be attributed to frequent anticyclonic conditions with intense solar radiation and calm winds, fostering ground-based radiative inversions during the night and subsidence inversions at low heights during daytime. Due to the shelter offered by the mountains, stagnant conditions characterised by a low air replacement over the Po Basin are very frequent and the accumulation of emissions and photo-oxidants is favoured. Due to the vicinity of the Alps in the north and the Apennines in the south,

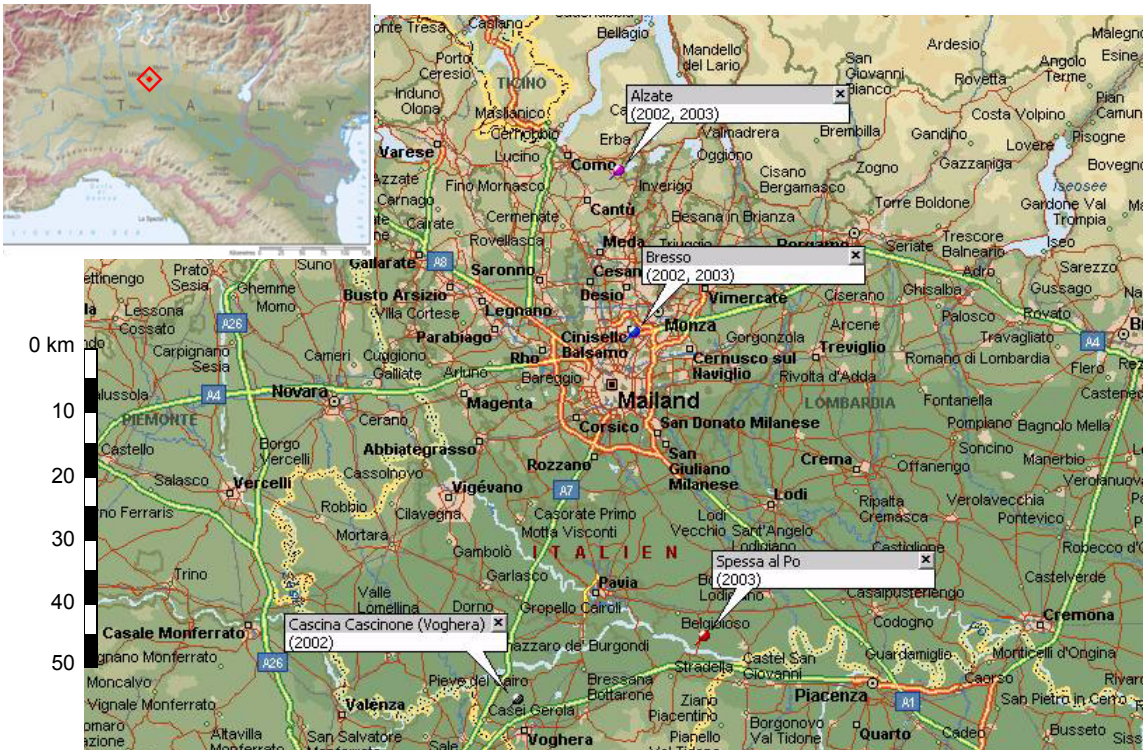

Figure 4.1: The metropolitan area of Milano including the measurement sites: the background stations Voghera (2002) and Spessa (2003), respectively, the urban station Bresso at the northern edge of Milano and the downwind site Alzate (Verzago).

leading to orographically and thermally induced mountain-valley circulations in summer, the flow in the plain is clearly separated into two parts (more or less half way across the Po Basin), one moving toward the Alps and the other moving south [*Dosio et al.*, 2002]. This weak mesoscale flow establishes in the Po Basin in high pressure conditions and weak synoptic circulation. Consequently, southerly winds between Milano and the Alpine foothills prevail during daytime, the dominating winds are northerly during nighttime. As a consequence, Po Basin air is advected towards the Alps and ozone peaks are often found north of Milano in the afternoon [*Prévôt et al.*, 1997; *Thielmann et al.*, 2002] (see also *Sec. 2.2.4*). Three highly instrumented monitoring sites, situated along the prevailing daytime wind direction, were established: south of Milano (Voghera, Spessa), in Milano (Bresso) and north of Milano (Alzate). In addition to the three ground-based sites as well three research aeroplanes were involved. Due to a crash of the MetAir Dimona in summer 2002 it was not available during FORMAT I.

The site south of Milano, i.e. upwind of the city, should provide information on the background trace gas concentrations. The location of the upwind site had to be changed from one campaign to the next. The two other sites Alzate and Bresso were identical to the ground stations during the LOOP/PIPAPO experiment in 1998. This provides the opportunity to expand the data sets to three campaigns in the Po Basin. We therefore frequently make use of the PIPAPO data in this thesis. The intent of the observations at Bresso was to characterise the chemical composition of the urban air mixture before extensive processing had occurred. The air from the urban centre, as it is advected downwind from Milano, is subject to dilution and chemical reactions leading to the decrease of primary pollutants and the formation of formaldehyde, ozone and other secondary pollutants. Airborne observations and measurements at Alzate, which is often located in the plume downwind of Milano, were used to determine the composition of the urban plume in later stages of its evolution. The downtown measurements provide the initial conditions for that process.

North foehn events occur with a frequency of ~ 4-6% during summer months [*Weber and Prévôt*, 2002]. They are characterised by strong northerly wind and low relative humidity. The north foehn advects cleaner air masses from the free troposphere above the Alpine crest to the boundary layer of the highly polluted Po Basin, inducing a strong decrease of pollutant levels there. An almost complete replacement of air over a large part of the Po Basin occurs and the air quality south of the Alps is clearly improved compared to other days.

4.2 The FORMAT I Campaign

The first FORMAT field campaign took place from 22 July to 20 August 2002 at three sites in the surroundings of Milano. IUP measured at two sites (Alzate and Bresso) and operated an aeroplane (e.g. *Heue* [2005]; *Wang et al.* [2006]). The campaign was subdivided into two periods. The first one (until 31 July) addressed the comparison of different formaldehyde measurement techniques. The second phase concentrated on air chemistry measurements. The intercomparison of in-situ techniques, which was performed at Bresso, is described in detail in *Sec. 5.2*. FORMAT I is considered as the summer campaign and included the 'ferragosto', the Italian major holiday time. The measurements carried out in August should be examined on the premise that in this period almost all industrial and commercial activities in Milano stop and also the local traffic is greatly reduced. Data from vehicle count stations in Milano (operated by ARPA) show 65% lower traffic on usual weekends than on working days. During weekdays in August the traffic is reduced to 55% compared to the rest of the year. It reaches a minimum on 15 August, which is an important holiday (*ferragosto*, Assumption Day). On that day, the traffic in Milano is actually reduced to ~ 35% compared to a usual working day. The traffic data (André Prévôt, pers. comm.) was from the year 2000 but it is assumed that the situation is similar in other years. The reduced traffic implies likewise diminished emissions in August.

4.2.1 Meteorological Overview of the Campaign

The meteorological conditions during the 2002 campaign were characterised by more unstable weather than usual. Temperatures were lower and there was more precipitation than in an average year. There were no long periods that allowed for build-up of high concentrations of CH_2O and other photo-oxidants. The standard meteorological parameters, measured by PSI at Alzate, are shown in *Fig. 4.2*. The temperatures reached 29°C during the day, dropping during the night to values of 16°C.

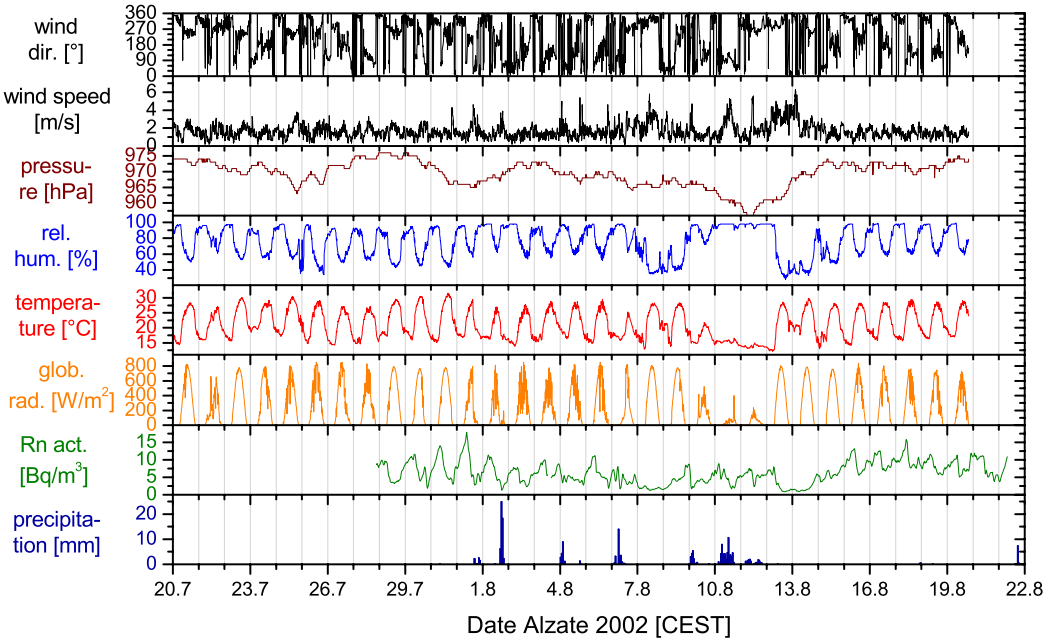

Figure 4.2: Meteorological parameters measured by PSI and atmospheric radon activity measured by IUP at Alzate during FORMAT I. The precipitation data is from an ARPA (Agenzia Regionale per la Protezione dell'Ambiente) monitoring station at Erba, a village located 6 km NE of Alzate.

Three fair weather periods were observed during FORMAT I. The intercomparison week for in-situ measurements took place within the first period, which lasted from 22 to 31 July. An upper-tropospheric ridge which developed after 27 July and an associated surface high pressure area, extending over southern and central Europe, prevailed during the intercomparison week, leading to fair weather conditions. One day (30 July) had temperatures above 30°C. The temperature during the intercomparison week varied between 17°C and 32°C. The global radiation reached 800 W m^{-2} every day. The relative humidity ranged from 75 to 100% during several nights and was typically 50-60% during the day, with an average of 62% over the complete week. There were no rain events in the greater Milano area during the intercomparison week. The impact of the high was superseded by a trough evolving over Ireland which introduced a low-pressure episode after 31 July. A cyclonic flow pattern developed, steering low pressure systems on a track passing over Northern Italy. After a few unstable days with short shower events, 7 and 8 August showed fair weather conditions with high radiation and temperatures. During the period from 9 to 12 August, a low pressure system with precipitation passed the area and there were three days with rainfall. The last days of the campaign period, from 12 to 22 August, were again dominated by a high pressure system, leading to stable weather and favourable conditions for photochemical reactions. An intensive observation period (IOP) was held during this period. Three north foehn days (7, 12 and 13 August) were identified during the campaign period according to the criteria described by *Forrer et al.* [2000]. Maximum wind speeds > 7 m s^{-1} were registered during the foehn events.

During the 2002 campaign, the airflow pattern at Alzate and Bresso was dominated by a weak alternate north-south flow as described above. The influence of the mountain breeze system is most pronounced at Alzate, compared to Bresso and the site south of Milano, strongly affecting the pollutant levels there. At Alzate, the wind blew from the north during the night and early morning with low speed (< 1 m s^{-1}), gradually turned to southerly before noon and abruptly changed to northerly in the evening again. The turning time of the wind direction is important for the transport of the Milano plume. The evening wind shift occurred almost coincident with sunset which varied from 21:04 at the beginning to 20:25 h at the end of the campaign. Sunrise was between 5:55 and 6:28 h. The wind speed at Alzate is low in the early morning and late evening hours, suggesting a reduced mixing when the mixing layer and the stable nocturnal boundary layer, respectively, start to develop during the day. The wind speed was usually weak at 1-3 m s^{-1}. Higher wind speeds were only observed before and after the rainy period on 7 August 2002.

4.2.2 Measurements at Alzate (Downwind Site)

Alzate is a village in the province of Como, situated in a semi-rural area close to the pre-Alpine foothills and approximately 35 km north of Milano. The measurement site (45°46' N, 9°10' E, 404 m above sea level (a.s.l.)) was situated outside the small village of Verzago (part of Alzate) on a small hill, elevated above the surroundings. An overview of the area is given in *Fig. 4.3*. Three measurement containers were placed at the border of a corn field. Local anthropogenic emissions originated only from a small blind alley passing the measurement containers and a few houses nearby. There are no major emission sources to the south within a few kilometres. The closest major emission source is a quite busy road, connecting Como and Bergamo, about 1 km northeast of the site. During daytime, rather low influence from this street is

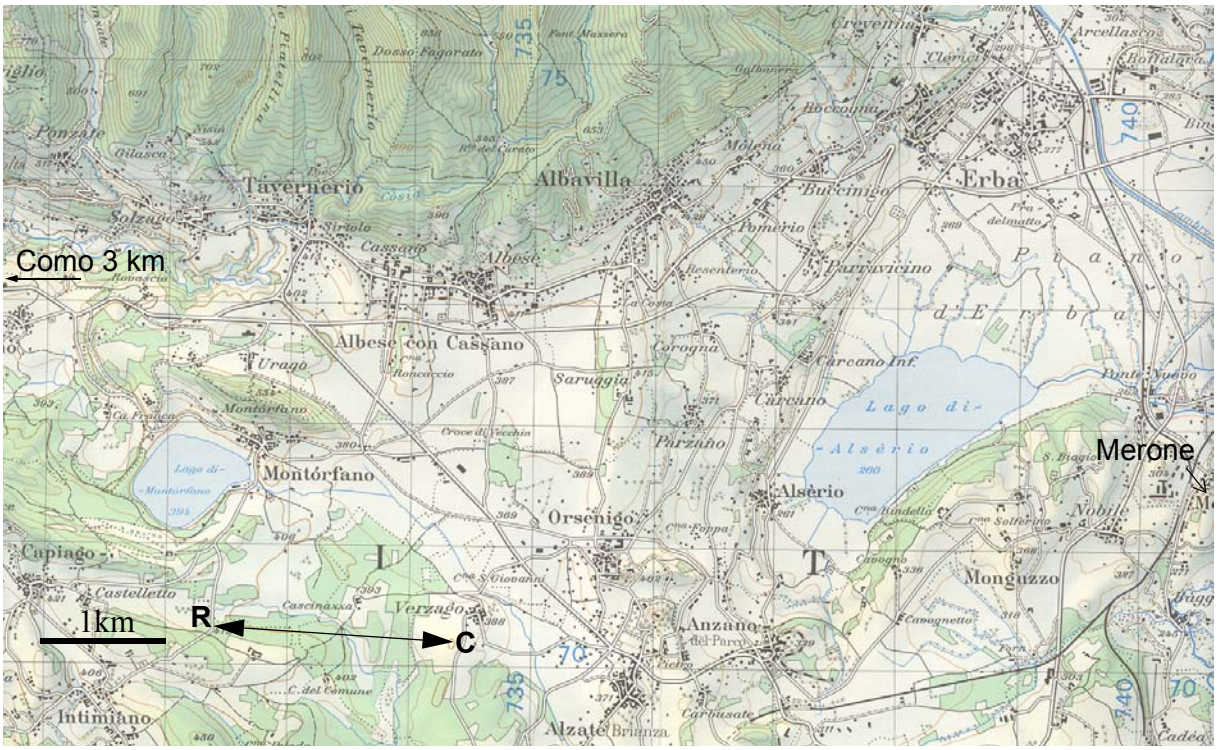

*Figure 4.3: Map of the surroundings of Alzate. The measurement site was located elevated on a small hill outside of Verzago which is a part of Alzate. There are several deciduous forests in the vicinity of the station, mostly to the west and south. The DOAS light path extends 2190 m (single way), pointing from the telescope **C** into westerly direction onto an array of 80 retro-reflectors **R**.*

expected due to the prevailing southerly wind direction. A cement works is located at Merone, 6 km ENE of the measurement site, representing a strong source for NO_x. The closest forest to be considered as an isoprene source was located 300 to 400 m in southerly and westerly direction. The surrounding area was patchy with fields, meadows, forests and small villages. Thus, the local environment was not homogeneous with respect to biogenic and anthropogenic emissions. Alzate is considered as representative for the semi-rural surrounding of Milano. Measurements at this site had already been conducted in the LOOP/PIPAPO experiment in 1998 [e.g. *Thielmann et al.*, 2002].

Air from the south brings significantly polluted air from the Milano metropolitan area to the site. Peak wind speeds of 2.5 m s^{-1} at Alzate imply a minimum transit time of 3 h from downtown Milano to the measurement site. This transit time is comparable to the typical CH_2O lifetime (see *Sec. 2.3.2.1*), which rules out that significant amounts of CH_2O emitted at downtown Milano could reach the Alzate receptor site. With the average wind speeds of ~1.5 m s^{-1} during the day, air masses from the Milano metropolitan area need 3-4 h to reach Alzate. Formaldehyde at Alzate is thus assumed to be predominantly of secondary origin, thereby representing a tracer of oxidation of organics.

During the first FORMAT campaign, the site was instrumented with a long path DOAS ('GTI') and a radon monitor from IUP and several in-situ instruments operated by the other groups (IFU, PSI, JRC). These included a Hantzsch monitor (*Sec. 3.1.3*) from IFU to measure formaldehyde. Ozone and nitrogen dioxide were measured by PSI applying UV-absorption (*Sec. 3.2.3*) and chemiluminescence in combination with a photolytic converter (*Sec. 3.2.1*), respectively. The inlets of these instruments were installed at 2 m above ground. Differences between path-integrating DOAS measurements and in-situ measurements are discussed in *Sec. 5.3*. Standard meteorological parameters were measured at Alzate by PSI (see *Fig. 4.2*). The wind measurements occurred at 10 m height, all other parameters were taken at 2 m height. The mast was placed a few metres from the containers in the corn field. The DOAS light beam passed over a topographically varying terrain (see *Fig. 6.5* for illustration), first above a corn field, then traversed a dip in the terrain with a gliding airfield and afterwards mostly passed over densely forested areas of deciduous trees (green areas in *Fig. 4.3*). The retro-reflector array was fastened onto an antenna mast at a height of 35 m above ground level. The location of the mast base is close to Capiago Intimiano in 443 m above mean sea level. There is about 70 m of elevation gain over the light path with an average height of the beam of 30 m above ground level. Over the forest with trees of ~ 20 m height, the beam passed around 10 m above the canopy. The forest underneath the beam consisted of *Quercus pubescens* (downy oak) and *Castanea sativa* (sweet chestnut) [*Lenz et al.*, 2001]. *Quercus pubescens* is a strong isoprene emitter, whereas *Castanea sativa* emits highly reactive monoterpenes. No direct anthropogenic sources are present along the light beam.

4.2.2.1 Trace Gas Measurements

DOAS spectra were recorded continuously over a time span of four weeks from 24 July to 20 August 2002. The long path DOAS system and its components and specifications are described in detail in *Sec. 3.1.1.6.1*. The measurement algorithm is explained in *Sec. 3.1.1.7*. Trace gas concentrations measured at Alzate, spatially averaged over the DOAS light path, are shown in *Fig. 4.4*. The average concentrations and detection limits of the measured compounds are listed in Table 4.1 for the entire period.

In addition to the DOAS, a radon monitor was operated by IUP at Alzate to measure the α-activity of ^{222}Rn decay products (see *Sec. 3.2.4*). This information helps characterising the diurnally varying mixing conditions within the probed air mass (see *Sec. 2.4.3*). The inlet of the radon monitor was set up 1.5 m above ground level outside the container which housed the

Hantzsch monitor from IFU and our LP DOAS telescope. The time series of Rn activity measured at Alzate, is shown in *Fig. 4.2* along with the meteorological data measured by PSI at the site and the ARPA (regional monitoring network) precipitation measurements at Erba.

Formaldehyde. A strong diurnal variation of CH_2O, typical of a photochemical pollutant, could be observed for the sunny clear-sky days. For the maximum in the early afternoon, peak mixing ratios of 4-5 ppbv on average and up to 8 ppbv were found. Formaldehyde displays a less clear diurnal variation during periods of lower photochemical activity due to lower solar radiation, particularly in the middle of the campaign. During nighttime, the CH_2O mixing ratio declined to a minimum of 1 ppbv. Under stable conditions, the minimum value during night was higher. Probably the loss processes were less efficient in the observation level of the DOAS than closer to the ground (see also *Sec. 5.3.4*). Formaldehyde is quite strongly correlated with ozone. This indicates that photochemical sources control CH_2O levels at Alzate. Very low formaldehyde concentrations occurred during the foehn episodes when strong winds aided the dispersal of trace gases. Mixing ratios of formaldehyde for the lower PBL have been derived by *Heckel et al.* [2005] from MAX-DOAS measurements at Alzate. The authors stated excellent agreement with simultaneous measurements by the Hantzsch monitor and the long path DOAS.

Ozone. Ozone mixing ratios usually stayed below 95 ppbv with daytime peak mixing ratios of ~ 70 ppbv on average, reflecting a generally slightly polluted boundary layer during FORMAT I. In a few cases, when afternoon temperatures reached 30°C, up to 100 ppbv have been measured. There is a broad maximum in O_3 mixing ratio between 15 and 18 h, peaking around 16-17 h. Minimum ozone levels at night are around 45 ppbv along the DOAS light path. The in-situ monitor close to the ground measured lower nighttime concentrations reaching around 30 ppbv in the morning (see *Sec. 5.3.2*). Daily variations in O_3 concentrations were largely driven by meso-scale meteorology and by the variations of mixing in the PBL. There is also a low-frequency component associated with the passage of synoptic weather patterns, which resulted in build-up periods of a few days. A gradual increase in O_3 concentrations occurred, for example, in concomitance with stable anticyclonic meteorological conditions and strong atmospheric stability during the IOP starting from 13 August.

Nitrogen dioxide. Nitrogen dioxide shows a diurnal variation peaking usually in the morning and the evening with values as high as 20 ppbv during the last week of July, but strongly reduced peak mixing ratios (~ 13 ppbv) during August, when traffic intensity and emissions dropped due to the holiday effect. The low boundary layer height during these periods allows the accumulation of NO_2. During the day, NO_2 is rapidly photolysed, leading to daytime mixing ratios of ~ 2 ppbv. The highest levels were measured in end-July, i.e. before traffic intensity and emissions dropped due to the holiday effect.

Sulphur dioxide. Mixing ratios of SO_2 are generally below 2 ppbv and no pronounced diurnal variation is discernible. During the first days of measurements in July, peak mixing ratios up to 4 ppbv were observed during daytime. The SO_2 peaks in the morning were often coincident with NO_2 peaks, pointing to rush hour traffic as a source of both pollutants. However, SO_2 peaks later in the day, e.g. on 31 July, are usually not correlated with NO_2. Under the conditions of reduced emissions because of holidays, no distinct SO_2 peaks were measured during the month of August with mixing ratios usually below 1 ppbv.

Radon. Pronounced diurnal cycles of the ^{222}Rn daughter activity were observed in Alzate (*Fig. 4.2*), since the vertical mixing conditions in the atmospheric surface layer vary strongly between day and night (especially in summer). The diurnal variation of radon activity and its dependence on atmospheric stability is explained in detail in *Sec. 2.4.3*. On 12-13 August, the north foehn advects air masses without appreciable radon content. The strong wind cleans the

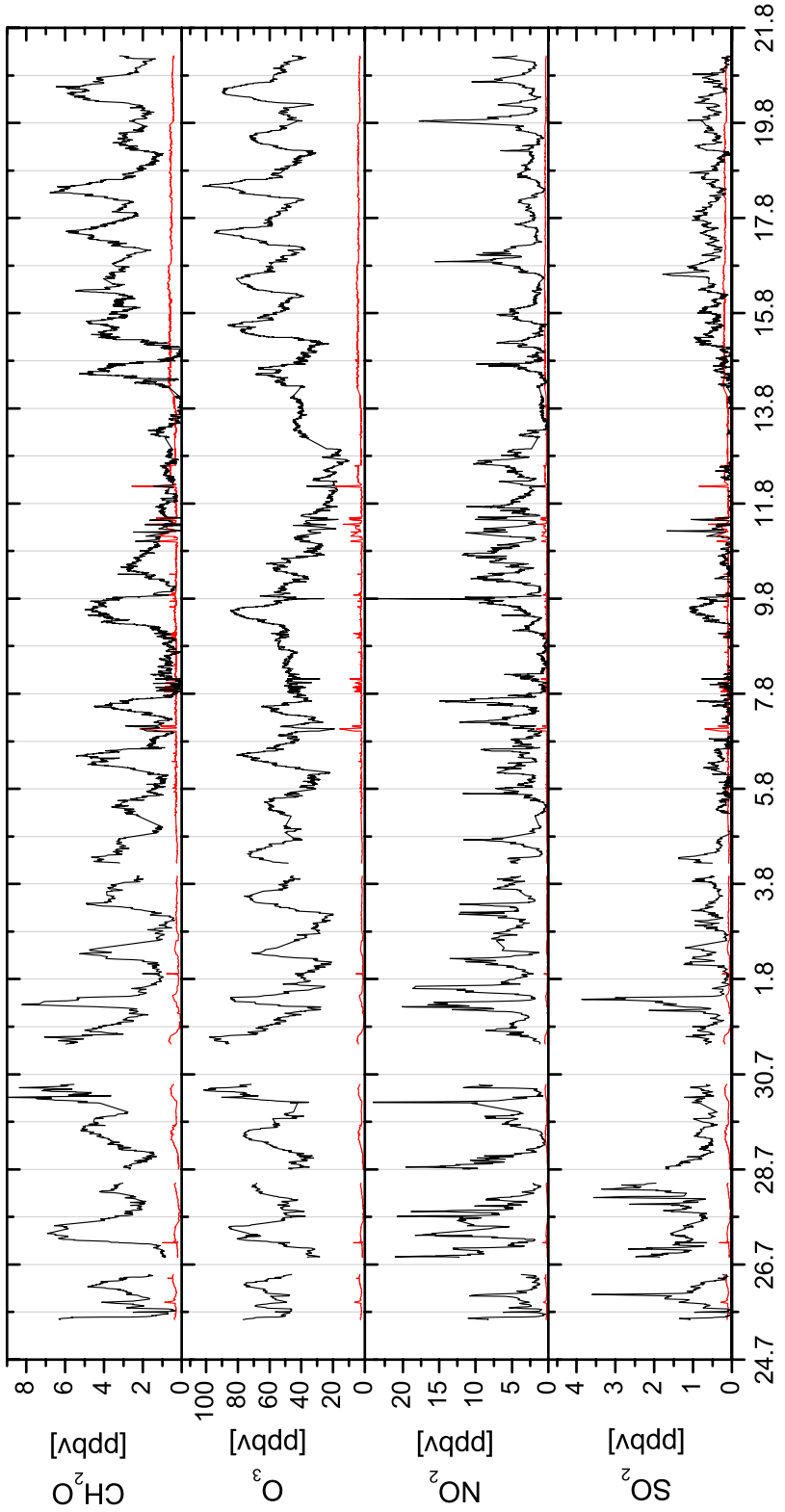

Figure 4.4: Trace gas mixing ratios measured by the long path DOAS system at Alzate during the FORMAT I campaign. Detection limits of the trace gases are indicated as red lines (also refer to Table 4.1).

Table 4.1: Overview of average and maximum (30-minute averages) mixing ratios of selected species measured at Alzate and Bresso during FORMAT I.

Species	Instrument	Location	Avg. det. limit [ppbv]	Avg. 4-8 h [ppbv]	Avg. 13-17 h [ppbv]	Max. mix. rat. [ppbv]
CH_2O	LP DOAS	Alzate	0.64	1.43	3.52	8.0
O_3	LP DOAS	Alzate	4.67	43.88	68.54	100.7
NO_2	LP DOAS	Alzate	0.49	3.04	1.62	20.3
SO_2	LP DOAS	Alzate	0.21	0.31	0.40	3.9
Radon	Rn-Monitor	Alzate	0.5 Bq m^{-3}	8.01 Bq m^{-3}	4.56 Bq m^{-3}	17.93 Bq m^{-3}
CH_2O	DOAS White [a]	Bresso	0.86	2.43	3.94	10.9 [b]
O_3	DOAS White [a]	Bresso	9.54	16.39	51.64	106.9
NO_2	DOAS White [a]	Bresso	0.69	20.42	5.58	50.7
SO_2	DOAS White [a]	Bresso	0.19	0.82	0.50	1.7
HONO	DOAS White [a]	Bresso	0.34	1.37	0.31	3.2

a. operated and evaluated by S. Trick (see *Trick* [2004])
b. The highest CH_2O concentration 13.7 ppbv (30-min avg.) was measured during the lorry experiment.

atmosphere and radon concentration as well as the concentrations of most other trace gases fall to very low values. During the IOP from 14 to 20 August, the wind varied between northerly and southerly with moderate and low wind speeds, leading to a distinct variation of the radon activity and of other trace gases. The nighttime variation of radon and formaldehyde is further studied in *Sec. 5.3.4*. Strong diurnal variations were observed with large concentration decreases during the morning hours, marking the start of convection.

4.2.2.2 Wind Sector Analysis

The dependency of trace gas concentrations measured at Alzate on the wind direction was studied using the PSI wind data obtained at the site (*Fig. 4.2*). The trace gas concentrations from the in-situ and long path instruments generally followed the airflow patterns described above. The percental apportionment of wind directions encountered at Alzate, separated into eight sectors, is shown in *Fig. 4.5* for four different periods of the day. The time periods have unequal length and were chosen according to the diurnal wind pattern, covering two phases of the fully developed mountain-valley breeze system and two transition phases (morning and evening). The length of the bars in *Fig. 4.5* indicates the frequency (in percent) that the wind comes from the respective direction sector. The trace gas concentrations of formaldehyde (upper panels), ozone (middle panels) and nitrogen dioxide (lower panels) were subdivided into bins of low, moderate and high concentrations. The transitions between these concentration ranges were chosen as appropriate for the respective trace gas. This concentration information is given as segments of different shades of grey within the wind sector bars. The length of the segments represents the relative fraction of the respective concentration range. The wind sector analysis mainly shows the typical diurnal patterns of the trace gas concentrations and the wind direction, but one can also obtain further information from it. During the day, 65% of the time southerly (SE, S, SW) wind directions were observed and only 10% from the north. The air masses sampled at Alzate during the day were thus usually impacted by emissions from the metropolitan area of Milano and their secondary products. During night, the situation was reversed with nearly 70% wind from the north (NW, N, NE) and 15% from the south. In the transition periods no clear pattern is recognisable. Wind from the eastern sectors is often encountered in the morning transition period.

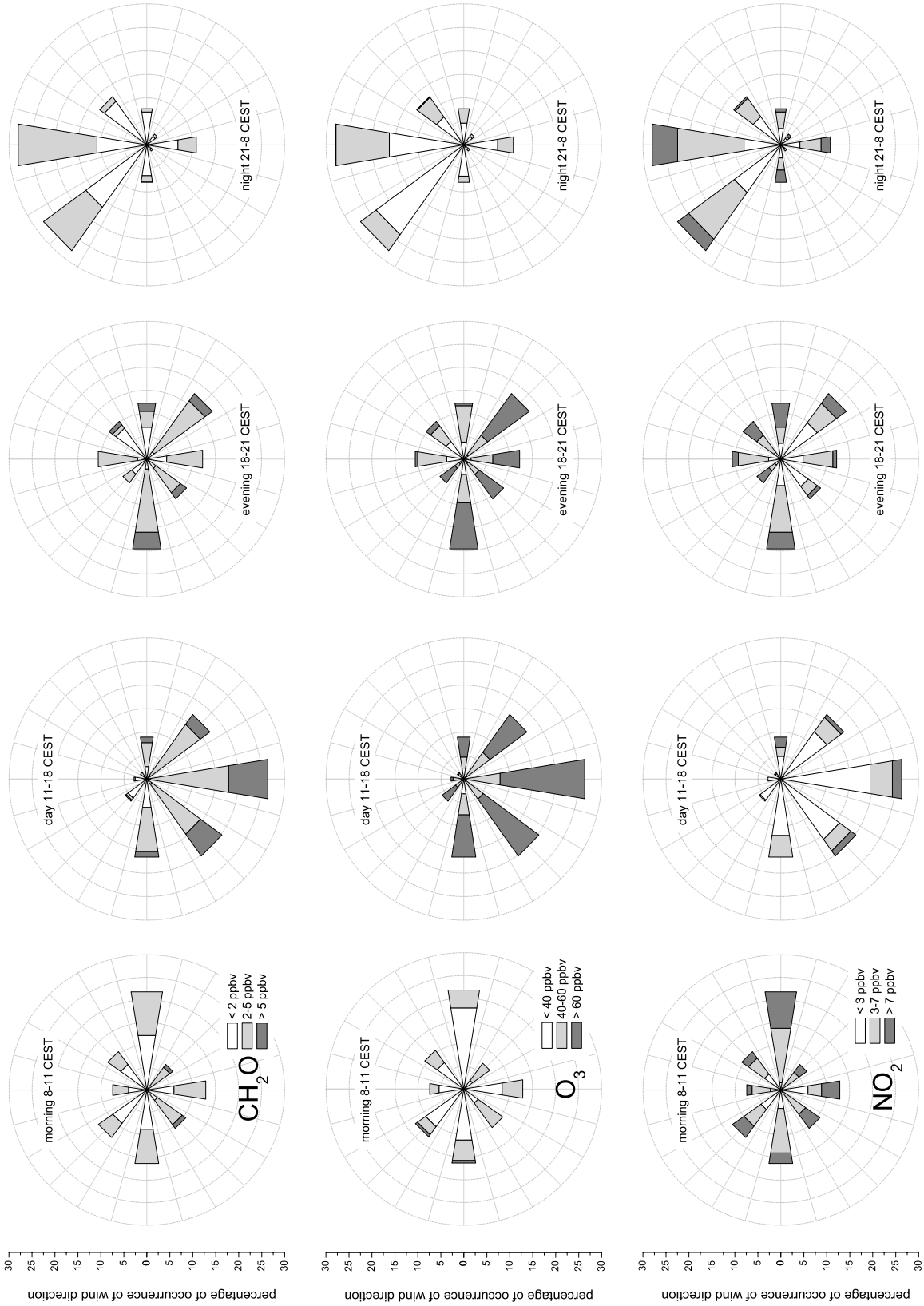

Figure 4.5: Wind roses for Alzate, weighted for the frequency of occurrence of the wind direction in eight sectors. The length of the bars corresponds to the frequency of wind directions. Relative portions of low, medium and high concentration bins as a function of wind direction are included as white, light grey and grey segments for formaldehyde (top), ozone (middle) and nitrogen dioxide (bottom).

Formaldehyde (upper row of *Fig. 4.5*) exhibits changing concentrations coincident with the changes in air flow. High formaldehyde concentrations were encountered primarily during daytime under southerly wind conditions. During the day, 26.5% of the air masses from the south have formaldehyde mixing ratios > 5 ppbv and 68.5% between 2 and 5 ppbv. For northerly wind, the concentrations are generally low, independent of the time of day. In the morning, the CH_2O content does not differ for different wind directions. Photochemical formation has not started to a great extent or processed air has not reached Alzate yet. In the evening, lower concentrations are measured if the wind comes from the pre-Alpine hills and lakes in the NE (valley flow). The predominantly low CH_2O concentrations that are measured under N and NW wind conditions during the day can be identified to be due to foehn events. The measurements of secondary compounds and anthropogenic hydrocarbons (by PSI) indicate low anthropogenic pollution during strong northerly flow.

In the short morning period, the mixing layer (see *Sec. 2.4.1*) has not developed to its full extension yet and ozone mixing ratios are below 40 ppbv (middle row of *Fig. 4.5*). The high ozone concentrations during the day are mainly due to the mixing with the residual layer from the previous night, where high ozone concentrations are conserved and additional ozone, formed from VOCs and nitrogen dioxides emitted in Milano and the metropolitan area and transported to Alzate under southerly wind conditions. During nighttime, in contrast, ozone concentrations measured in the stable nocturnal boundary layer decrease to low levels due to deposition and (less important at Alzate) chemical reactions. Comparatively low ozone concentrations are measured in east wind situations, especially during morning and evening hours. This is attributed to the NO_x emissions from the cement works at Merone and subsequent titration reaction of ozone with NO. The evening hours 18-20 h are a transition period when southerly wind is still often encountered and carries high ozone concentrations. For westerly directions, high ozone concentrations are measured as well. The Milano plume has often been detected in the west [e.g. *Dosio et al.*, 2002], explaining the high O_3 concentrations from the west. For northerly and northeasterly wind, mixing ratios below 60 ppbv outweigh. In this direction there are no source regions of secondary pollutants. The rare occasions of northerly wind during the day are due to foehn situations. On days with northerly wind, O_3 concentrations are below 60 ppbv.

The nitrogen dioxide concentrations (lower row of *Fig. 4.5*) are highest in the morning due to the low boundary layer height and morning traffic emissions. At any time of the day, NO_2 mixing ratios above 7 ppbv are primarily found for easterly wind direction. At night, the frequency of high NO_2 levels from northerly directions exceeds the occurrence of high NO_2 levels in air advected from the east. The thermal NO (see *Sec. 2.1.2*) originating from the clinker production in the cement works influences the composition of trace gases coming from the eastern sector. There are no occasions with NO_2 concentrations below 3 ppbv in the morning when the wind is coming from the east. During the day, NO_2 concentrations are generally low. Due to the short photolytic lifetime of only a few minutes, mixing ratios below 3 ppbv are measured predominantly. High daytime NO_2 concentrations are only measured in southerly and easterly wind situations when air masses from the metropolitan area are advected to the measurement site. No elevated NO_2 concentrations are observed for northerly and westerly wind. The accumulation of NO_2 emitted close to the ground in the stable nocturnal layer leads to high NO_2 concentrations measured during nighttime.

4.2.3 Measurements at Bresso (Urban Site)

Bresso (45°32’ N, 9°12’ E, 146 m a.s.l., 27 000 inhabitants) is a densely populated suburb of Milano at a distance of approximately 5 km north of the city centre. Bresso was the FORMAT site representative for urban conditions. It is located inside the motorway belt around Milano and has some light industry. The area surrounding the Bresso site is primarily residential and

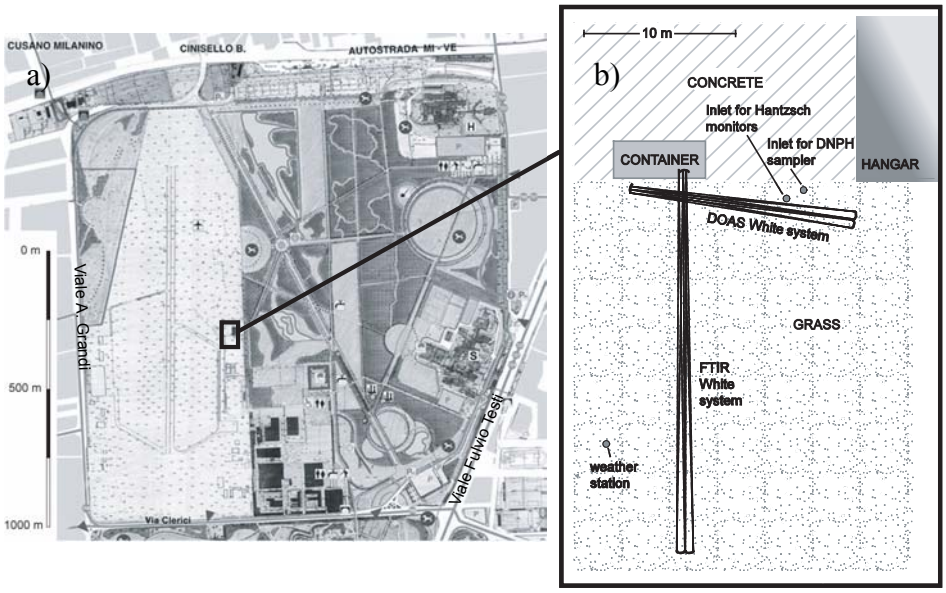

Figure 4.6: ***(a)*** *Surrounding area of the site at Bresso (MI), including the Red Cross base to the right of the small airfield and Parco Nord, a local recreation area (picture: Parco Nord Milano [2004]).* ***(b)*** *The setup of the instruments during the intercomparison experiment. The site was used for both FORMAT campaigns (figure from Hak et al. [2005]).*

commercial. During the day, Bresso is downwind of the city centre and strongly influenced by primary and secondary pollutants from the city. The measurement site was located on the premises of an Italian Red Cross division adjacent to the small airfield of Aeroporto Civile G. Clerici (see *Fig. 4.6a*). The adjoining ~1.2 km^2 in the west were grass-covered. The airfield was only used for takeoffs and landings during the day and primarily on the weekend. The closest sources for road traffic emissions were a busy street 550 m west of the site (Viale A. Grandi, with an adjacent residential area) and a major motorway (A4, connecting Torino and Bergamo) at a distance of 1000 m which passes at the northern end of the airfield. The motorway showed generally low traffic in August, compared to other months, with a peak traffic density in the morning and afternoon rush hours. The Parco Nord, a ~ 2.2 km^2 green recreation area with trees borders upon the east and represents a possible source for biogenic hydrocarbons. Several hundred metres farther to the east, the Viale Fulvio Testi, a main road with high traffic density, leads to downtown Milano. There are no known emission sources for CH_2O in the direct surroundings of the site ‡. Vehicular and industrial emissions of CH_2O can mix with photochemically produced formaldehyde from anthropogenic and biogenic hydrocarbon emissions, so that both primary and secondary sources of CH_2O are of importance at Bresso. Measurements of photooxidants at this site had already been conducted in the LOOP/PIPAPO field experiment in 1998 [e.g. *Neftel et al.*, 2002]. The wind at Bresso was predominantly from northeast at night and southeast during the day providing air from downtown Milano.

The first week of the campaign was used to intercompare both similar instruments and different in-situ techniques for the measurement of formaldehyde (*Sec. 4.2.3.1*), before the instruments were distributed to the other sites within the Po Basin for the remainder of the campaign. After the intercomparison week, an experiment to study the vertical distribution of formaldehyde was carried out over the period of roughly one day. It included three Hantzsch monitors, which had also been involved in the intercomparison, and the DOAS White system to sample

‡. Twice during the campaign, lorries with running engines were operated immediately next to the measurement instruments.

at four height levels between 0.8 m and 9.6 m over ground. The height level of the DOAS beam was 1.5 m. Due to the uncertainties and the different instruments used for this experiment, no final result could be obtained from the vertical experiment. To derive vertical profiles and deposition fluxes of CH_2O it is suggested to apply one instrument which is moved vertically and to use greater vertical distances of the sampling heights.

4.2.3.1 Intercomparison Measurements

The intercomparison of in-situ formaldehyde measurements continued from 23 to 31 July under conditions which were appropriate for moderate photo-oxidant production (see *Sec. 4.2.1*). Daytime ozone mixing ratios of up to 85 ppbv were measured at the site. Measurements of the standard meteorological parameters were performed continuously at the intercomparison site. Four different techniques were involved in the intercomparison experiment. A DOAS White system was operated by colleagues from IUP who also performed the evaluation of the spectra. These measurements were described by *Trick* [2004]. An FTIR White system was operated by CTH, five Hantzsch monitors from three different groups (IFU, PSI, BUW) were involved and time-integrated cartridge samples were taken by JRC (see page 191 for specification of institute acronyms). The principles of the measurement methods and specifications of their operation are outlined in *Sec. 3.1.1.6.3* and *Sec. 3.1.2*-*Sec. 3.1.4*. The detection limit, accuracy and precision of the individual instruments are presented in Table 4.2. The physical arrangement of the instruments is sketched in *Fig. 4.6b*. A shipping container, which was located on the forecourt of a hangar building (~ 10 m high), housed the field mirror of the FTIR and the spectrographs of both White systems. The DOAS field mirror was placed in front of the container. The objective mirrors of the FTIR White system were located on a tripod, 25 m away from the field mirror. The light paths of the two White systems were set up approximately 1.5 m above the ground with a crossing alignment. For the comparison with the spectroscopic techniques, the sampling ports of the Hantzsch monitors and the DNPH-sampler were both mounted close to the intersecting pathways of the two multi-reflection systems at a height of about 1.2 m above ground and at a distance of a few metres from each other. Thus, sampling of the same air mass by all instruments can be implied. The Hantzsch monitors were sampling from a 10 m common PFA inlet line with 4 mm inner diameter, which lead to a hangar where the Hantzsch instruments were operated. The inlet line was protected from ambient aerosols by a Nuclepore® inline filter (47 mm diameter, 0.5 µm pore size), which was replaced once per day. The results of the intercomparison are discussed in *Sec. 5.2*.

Table 4.2: Detection limit, accuracy, precision of all the instruments for the field measurements during the intercomparison campaign as stated by the groups.

Instrument/Type	Institute	Time period of operation	Det. lim. [ppbv]	Accuracy	Precision	Time res. [min]
DOAS White system	IUP	24/07-19/08	0.9	± 6%	0.45 ppbv	1-2
FTIR White system	CTH	22/07-18/08	0.4	6-27% [a]	0.2 ppbv	5
Hantzsch AL4021	PSI	23/07-26/07	0.15	± 15% [b]	± 10% [b]	~1.5
Hantzsch AL4001	BUW	24/07-31/07	0.15	± 15% [b]	± 10% [b]	~1.5
Hantzsch AL4021	IFU [c]	24/07-17/08 [d]	0.15	± 15% [b]	± 10% [b]	~1.5
DNPH	JRC	23/07-18/08	0.5	± 10%	0.1 ppbv	120

a. depends on present formaldehyde concentration (6% for 15 ppbv and 27% for 2 ppbv)
b. or 150 pptv (whatever is larger)
c. three instruments
d. except IFU3: 25-29 July

4.2.3.2 Trace Gas Measurements

The largely reduced emissions from mobile and stationary sources in August lead to the 'holiday effect', inhibiting the development of pronounced ozone episodes which are typical for the Milano area in the remaining summer months. However, July/August was the only time period in summer 2002 when all participating groups were available. Further, with its unsettled weather situation, the FORMAT I campaign provided unfavourable conditions for the build-up of high pollutant concentrations. The average and maximum mixing ratios of selected trace gases measured at Bresso during the FORMAT I campaign are listed in Table 4.1.

Considering the data of the entire campaign at Bresso, comparatively low urban formaldehyde concentrations were measured. Afternoon maxima were well below 10 ppbv, apart from a few exceptions. Levels of the order of 2 ppbv were found during the night.

Depending on the photochemical activity, daytime ozone values reached a maximum of 90 ppbv between 15 and 17 h. Ozone levels below 5 ppbv are observed during the nights in July, as the titration reaction with NO from local emissions destroys most of the ozone, which is not reproduced in the absence of photolysis. In August, nighttime concentrations were higher, most probably due to the lower emissions.

Nitrogen dioxide mixing ratios up to 50 ppbv were measured at night when it is not photolysed and can accumulate in a shallow surface layer. The daytime minimum value of 5-6 ppbv is reached between 15 and 17 h. Nitrous acid followed a diurnal variation similar to that of nitrogen dioxide with maximum mixing ratio up to 3 ppbv during the night and minimum mixing ratios of ~ 0.3 ppbv during the day. Sulphur dioxide mixing ratios had a maximum below 1 ppbv during the morning hours and never exceeded 2 ppbv.

4.2.3.3 Meteorological Data

A weather station [§] measuring the standard meteorological parameters was operated by IUP in Bresso. The 2 m high mast was located approximately 30 m away from the DOAS container. The time resolution of this data was 5 minutes.

The spectral actinic flux was measured by IUP at Bresso during the FORMAT I campaign with a scanning spectroradiometer (see *Sec. 3.2.5*). Photolysis frequencies for NO_2, HONO, $O(^1D)$ and CH_2O were calculated according to eq. 2.5 using the measured actinic flux data and the IUPAC recommendations [*Atkinson et al.*, 2002] for the cross-sections and quantum yields of the respective compounds. The determined photolysis frequencies are shown in *Fig. 4.7*. At night they are zero, increasing during daytime with solar irradiation and depending on the cloud coverage. On the rainy days (9-11 August), lower values are observed compared to sunny cloudless days (12-14 August). The minimum solar zenith angle (SZA) with peak photolysis frequencies was reached at ~ 13:30 CEST, increasing from 27° at the beginning of the campaign to 33° at the end. The average peak values of the photolysis frequencies and the average lifetimes with respect to photolysis, given in brackets, were $J_{NO2} = 6.2 \times 10^{-3}\ s^{-1}$ ($\tau = 2.5$ min), $J_{O(1D)} = 2.8 \times 10^{-5}\ s^{-1}$ ($\tau = 10$ h), $J_{CH2Or} = 3.0 \times 10^{-5}\ s^{-1}$, $J_{CH2Om} = 4.8 \times 10^{-5}\ s^{-1}$ (both channels together $\tau = 3.5$ h), $J_{HONO} = 1.5 \times 10^{-3}\ s^{-1}$ ($\tau = 12$ min). The radical channel of formaldehyde photolysis comprises 38% at noon and 30% for large solar zenith angles in the morning and evening. The contributions of the major primary sources to HO_x production at Bresso are studied in *Sec. 4.4.1* for three campaigns performed at this site.

§. Hoffmann Meßtechnik, Rauenberg, Germany

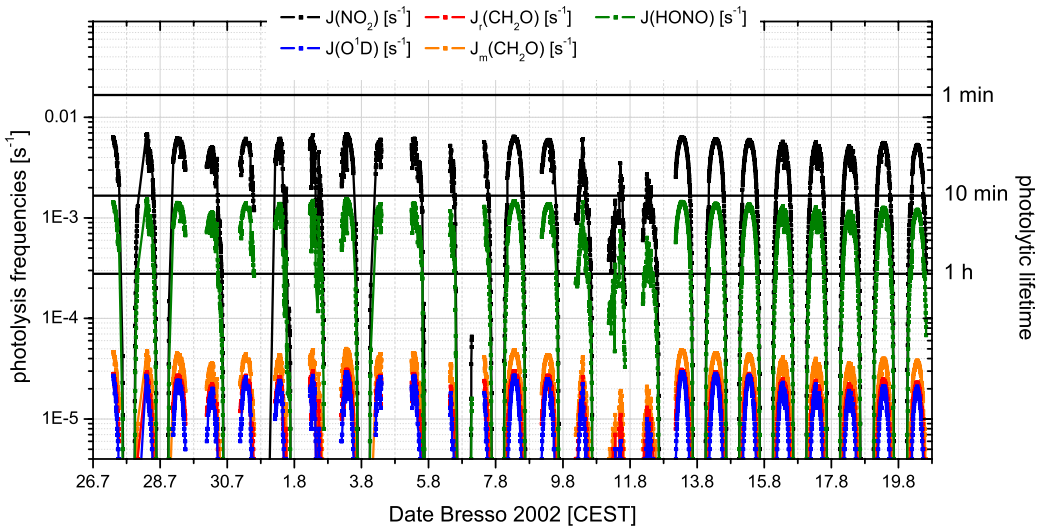

Figure 4.7: Photolysis frequencies J_{NO2}, $J_{O(1D)}$, J_{HONO}, J_{CH2Or} and J_{CH2Om} as measured during the FORMAT I campaign at Bresso 2002. On the right hand axis, the corresponding photolytic lifetime of the trace gases is indicated.

4.2.4 3D Model Results for FORMAT I

The measurement and modelling of CH_2O is important for understanding the processes that control the formation of ozone and other photo-oxidants in the troposphere in heavily polluted areas like the metropolitan area of Milano. A 3-D regional chemical transport model (NILU RCTM) was applied by NILU/UIO to interpret the observations.

Liu et al. [2006] assessed the performance of the model by comparing model results with ground-based and airborne measurements from the FORMAT I campaign. The model was found to be able to reproduce the photochemical episodes during fair weather days. The comparison of different CH_2O observations with model results revealed the importance of representativity of the measurements by different instruments. For the ground-based formaldehyde measurements at Alzate, the best agreement with the model was achieved with the point measurements. The path integrating DOAS measured by far higher values as illustrated in the lower right panel of *Fig. 4.8*. We assume that the long path measurement over the forest is strongly influenced by rapid formaldehyde formation from isoprene and is therefore not representative for the entire model grid cell. This is further discussed in *Sec. 5.3*. The model was also evaluated with aircraft data along the flight track. It was found that the model was able to capture the Milano city plume and the modelled concentrations agreed generally well with the

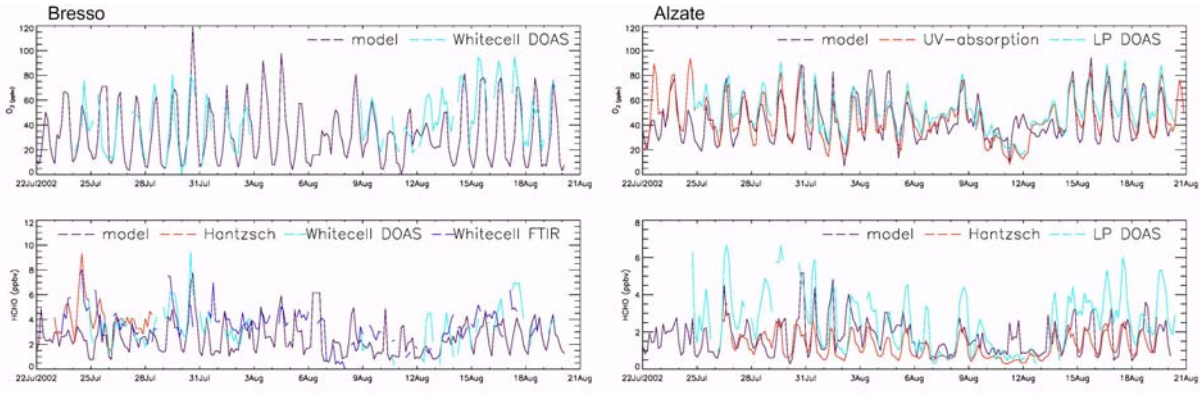

Figure 4.8: Modelled and measured mixing ratios of ozone and formaldehyde (every three hours) at Bresso and Alzate (figure from Liu et al. [2006]).

measurements. *Liu et al.* [2006] infer that the discrepancies between model results and airborne measurements are mainly caused by the meteorological data driving the model, as the location of the simulated plume is strongly controlled by the wind field used in the model.

The NILU regional chemical transport model is driven by meteorological data from a numerical weather prediction (NWP) model, which is based on the NORLAM model from the Norwegian Meteorological Institute. Global meteorological analyses and forecasts from ECMWF (European Centre for Medium Range Weather Forecasts) are used as initial and boundary conditions. The model uses sigma coordinates and stereographic map projection. Horizontal resolutions of the model can be defined from 150 to 15 km at 60°N. The model uses one way nesting and provides the coarse scale chemistry output as boundary conditions for the fine scale model. A detailed description of the NWP model can be found in *Flatøy et al.* [1995]. A comprehensive description of the gas phase chemistry of photochemical oxidants is given in the model. As described by *Flatøy et al.* [1995], the chemistry scheme is quite similar to the EMEP Lagrangian photooxidant model. Surface emissions are specified in the model for NO_x, CO, VOC and SO_2.

4.3 The FORMAT II Campaign

The second FORMAT campaign was held in autumn 2003. Ground-based trace gas measurements were made between 10 September and 7 October at three sites. At all three locations, IUP operated DOAS instruments. For the FORMAT II campaign, basically the same stations as for the FORMAT I campaign were used (see overview in *Fig. 4.1*). Thus, the setups and instrumentations at Alzate and Bresso were more or less identical compared to the previous campaign. For the southern (upwind) station another site, Spessa (20 km to the east of the 2002 location), had to be found since Cascina Cascinone (Voghera) was not available. Moreover, the airfield of Spessa offered better logistical possibilities. Apart from higher biomass burning activity that leads to occasional spikes in the data, the change in the location does not affect the results. This is supported by the extensive aircraft flights in the area south of Milano. The aircraft operation period covered nine days, starting on 15 September and ending on 27 September, involving three aeroplanes.

4.3.1 Meteorological Overview of the Campaign

The weather was more stable during the 2003 campaign than in the 2002 campaign. Because of the stable fair weather and the non-holiday conditions, higher ozone and formaldehyde levels were encountered in 2003. The summer of 2003 was one of the hottest and driest summers on record. The synop station at Milano Linate reported only seven days over the period June to August 2003 when the maximum temperature was below 30°C [*ECMWF*, 2004]. Until mid-September 2003 the dry and warm weather continued.

The FORMAT II campaign started with a foehn event on 12 September, followed by stable anticyclonic conditions associated with a ridge stretching from Eastern Europe towards North Africa at high and mid levels. The temperatures reached 29°C during the day, dropping during the night to values of 12°C (see *Fig. 4.9*). Meteorologically stable conditions prevailed until 22 September when a trough passed the Po Basin, which resulted in a drop of the afternoon maximum temperature from 29.2°C on 21 September to 23.2°C on 23 September at Bresso. After 24 September, conditions were unsettled with lower daily maximum temperatures, a less pronounced diurnal wind variation and higher wind speeds. Several days in this period were cloudy to overcast.

The same diurnal pattern of wind shifts as described for FORMAT I (see *Sec. 4.2.1*) is observed at Alzate and Bresso during FORMAT II, but due to seasonal reasons, time-shifted. Sunset occurred during the FORMAT II campaign between 19:36 and 18:57 h, sunrise occurred

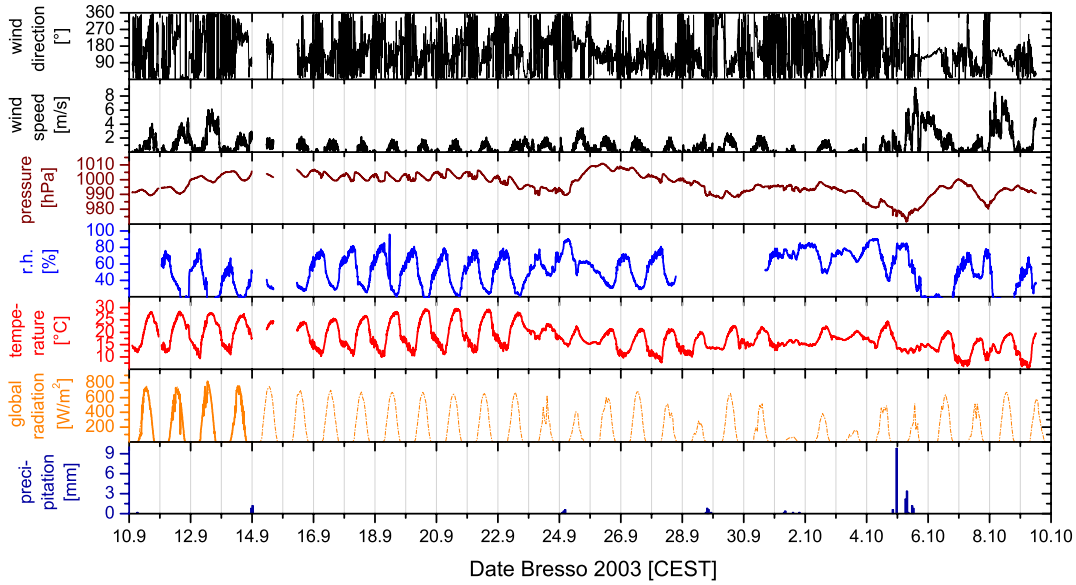

Figure 4.9: Meteorological parameters measured by IUP at Bresso 2003. The precipitation data and the radiation data after 14 September are from an ARPA (Agenzia Regionale per la Protezione dell'Ambiente) monitoring station at Cinisello Balsamo, the suburb where the DOAS retro-reflectors were installed.

between 07:01 and 07:26 h (first values for beginning of the campaign, latter ones for end of the campaign). The southern site at Spessa is neither influenced by the Alpine circulation nor by the local circulation due to the Apennines. A weak east-west flow is observed there. The wind speed was generally weak at 0-2 m s^{-1}. By the end of the campaign, strong wind was experienced, diluting the trace gases to very low concentrations.

4.3.2 Measurements at Alzate (Downwind Site)

For the second FORMAT campaign, IUP was measuring at Alzate again with a long path DOAS ('Nashville') and a radon monitor. Other groups at the same site were equipped with O_3, CH_2O, NO, NO_2 monitors and a GC, performing point measurements. The DOAS light path was the same as during the first campaign (see *Sec. 4.2.2*). Since the delivery of the measurement container was highly delayed, DOAS measurements could not start before 23 September. Unfortunately, this was the end of the fair weather period and of a distinct ozone event (see *Fig. 4.15*). Since there were instrumental problems, only few data is available, starting 23 September until 8 October. This data is in very good agreement with other data taken at the site. The radon monitor was installed inside the measurement container. The inlet tube was mounted at a height of 3 m above ground at the measurement mast of PSI to sample the ambient air. The air inlet was co-located on the mast with those for nitrogen oxides, ozone, hydrocarbons. In the night 28-29 September there was a power failure affecting the entire country, which stopped all kinds of trace gas measurements for half a day.

4.3.3 Measurements at Bresso (Urban Site)

The same site as in the previous year (see *Fig. 4.6a*) was offered by Croce Rossa Italiana (CRI) again to set up the instruments at Bresso. During FORMAT II, a multibeam long path DOAS (see *Sec. 3.1.1.6.2*) was operated on the forecourt of the hangar instead of the White system. DOAS measurements at Bresso were made simultaneously along three different light paths which were arranged as illustrated in *Fig. 4.10*. The choice of light paths had to comply with a number of requirements: To attain adequate sensitivity for the DOAS measurement,

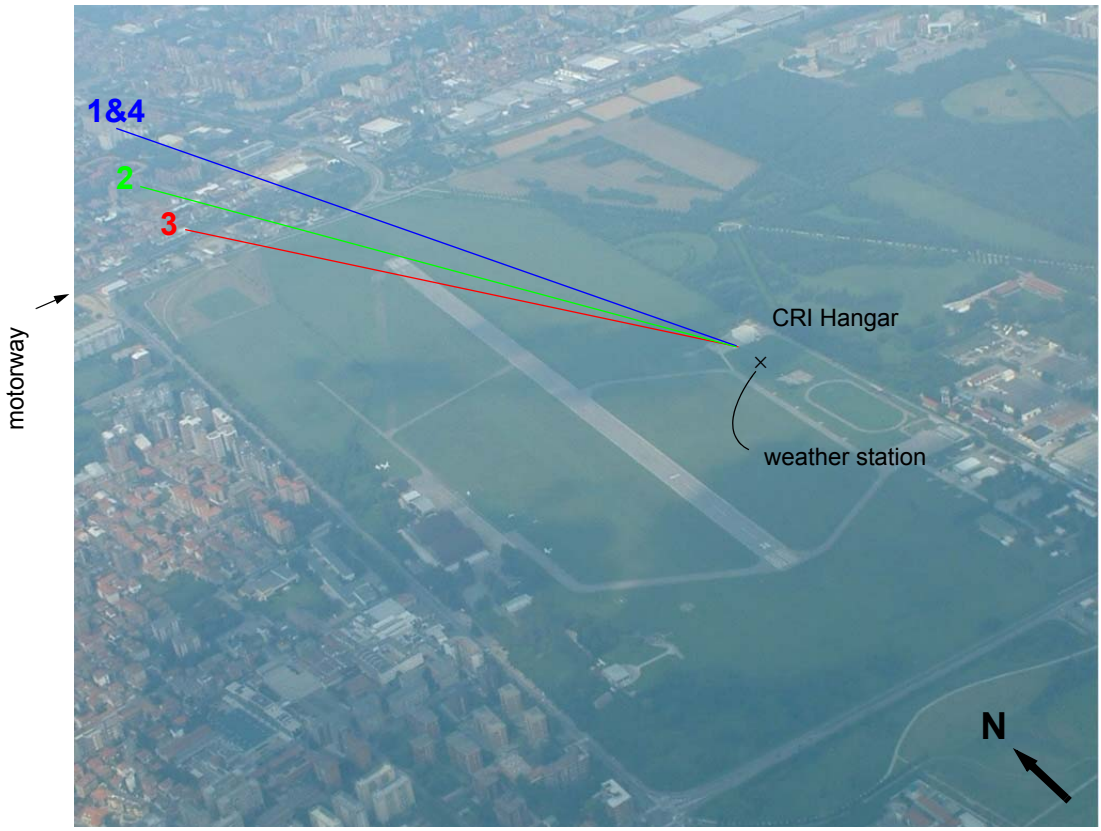

Figure 4.10: Aerial photograph of the airfield at Bresso to give a geographical overview of the DOAS light paths starting from the CRI area to an apartment house (beam 1, blue), a church (beam 2, green) and a building of an industrial company (beam 3, red) located in the neighbouring suburb Cinisello Balsamo (photo courtesy of Klaus-Peter Heue).

the light path lengths had to exceed 1000 m (single way). For this reason, only targets in the north were eligible. Further, we need a suitable, static building (e.g. house, lattice mast) with the possibility and, above all, the permission to attach a case with retro-reflectors being externally illuminated day and night by a 500 W lamp. For beam 4, we waited three weeks for a permission to fix an array on a residential house and finally decided to aim it to the same reflector array as beam 1. On these accounts, the four light beams at Bresso were very close together in the end. However, this was no drawback, since it was not an aim here to gain supplementary information on the spatial trace gas distribution through the utilisation of several individual light beams, but primarily to obtain simple concentration information and to fundamentally test the field capability and the long-run application of the new multibeam instrument in the field, as well as to further develop the measurement software. As described in *Sec. 3.1.1.6.2*, the light beams emitted by the multibeam telescope are separated by external mirrors. The rack holding the external mirrors was placed 20 m from the telescope and was anchored in the ground with wire cables and tent pegs. All light beams traversed above a highly frequented motorway. Contrary to the previous one, during the second campaign, the motorway showed high traffic density, particularly early in the morning and in the late afternoon. Time series of trace gas mixing ratios measured by the DOAS are shown in *Fig. 4.12*, where the same colours as in *Fig. 4.10* were used for the beams 1-3. Details on the four light beams are summarised in Table 4.3. The longest beam (beam 1) extended from the CRI hangar to an apartment house in Cinisello Balsamo. Beam 4 aimed at the same retro-reflector as beam 1 but since it provides no further information, it is not included in *Fig. 4.12*. A mast serving as campanile of the church S. Pio X in Cinisello Balsamo was used to attach retro 2. Beam 3 pointed to a building of an industrial company (Elfes S.r.l.).

Table 4.3: Characteristics of the four light beams at Bresso. The reflector locations are listed as height above ground. The path lengths are given as twice the distances to the reflector which is the actual absorption path.

Light path name	Reflector height	Light path length	Time period [a]
(1) House	~ 30 m	2 × 1603 m	18/09-09/10/2003
(2) S. Pio X	~ 20 m	2 × 1330 m	09/09-09/10/2003
(3) Elfes S.r.l.	~ 8 m	2 × 1086 m	06/09-09/10/2003
(4) House	~ 30 m	2 × 1603 m	25/09-09/10/2003

a. The operation time of beams 1-4 differed because we had to wait for final permissions to install the individual retro-reflector arrays.

During the campaign, the multibeam system at Bresso was operated by colleagues from IUP, however, the analysis of the spectra from the four light beams was part of this thesis. The other groups operated an FTIR White system (CTH), a GC and a DNPH sampler (JRC) and a Hantzsch monitor (IFU) at Bresso. The Partenavia aeroplane, operated by IUP (see *Heue* [2005]), was also based at Bresso. The additional instrumentation from IUP at Bresso comprised a weather station and a spectroradiometer.

4.3.3.1 Measurements of Meteorological Parameters

The standard meteorological parameters were measured by IUP with the same weather station as during the previous campaign. The 2 m high mast was located approx. 30 m away from the DOAS container. The time resolution of the data, which is shown in *Fig. 4.9*, was 5 min. Due to a defect of the pyranometer after a few days of measurements, presumably caused by a lightning strike in conjunction with a thunderstorm (on 14 September), radiation data from an ARPA station in Milano are shown additionally as a dotted orange line.

The spectral actinic flux was measured at Bresso with a spectroradiometer (see *Sec. 3.2.5*). The photolysis frequencies of NO_2, $O(^1D)$, CH_2O (both channels) and HONO, derived with eq. 2.5, are shown in *Fig. 4.11*. Only a few days of radiance data are available since the control of the grating motors broke down after 25 September. The minimum SZA during the time of

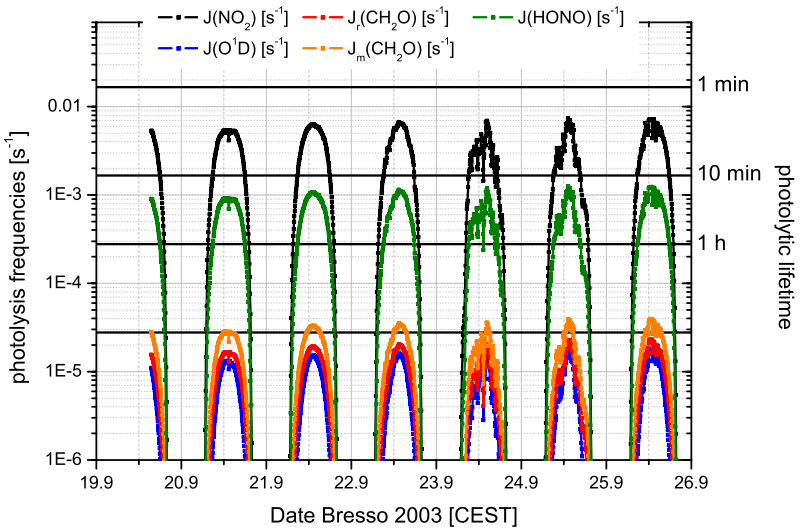

Figure 4.11: Photolysis frequencies measured with a spectroradiometer at Bresso 2003 during the FORMAT II campaign. The corresponding photolytic lifetime is indicated on the right hand axis.

operation varied between 45° and 47° and occurred around 13:15 CEST with the following average peak values of the photolysis frequencies:
$J_{NO2} = 6.0 \times 10^{-3}$ s^{-1} (τ = 3 min), $J_{O(1D)} = 1.5 \times 10^{-5}$ s^{-1} (τ = 18.5 h), $J_{CH2Or} = 2.0 \times 10^{-5}$ s^{-1} (τ = 13.9 h), $J_{CH2Om} = 2.9 \times 10^{-5}$ s^{-1} (τ = 9.6 h) and $J_{HONO} = 1.0 \times 10^{-3}$ s^{-1} (τ = 17 min). This results in a combined photolysis frequency of $J_{CH2O} = 4.9 \times 10^{-5}$ s^{-1} (photolytic lifetime = 5.7 hours) at noon. The measurements of the actinic flux in Bresso 2003 indicate that the molecular and radical channels comprise ~ 63% and 37%, respectively, of the photolytic CH_2O loss at noon. In the morning and evening only 25% of the CH_2O photodissociations proceed via the radical channel. The combined lifetime with respect to photolysis and OH reaction was τ = 3.3 h applying measured photolysis frequencies and [OH] = 4×10^6 molec cm^{-3}, calculated with the steady state model (*Sec. 2.2.6*).

4.3.3.2 Trace Gas Measurements

Since all light paths were very close together, it is not surprising that the agreement of the results of three DOAS beams is generally very good (see *Fig. 4.12*). Frequently the three time series coincide on even short timescales. Usually, the concentrations of the different trace gases obtained by the three beams agreed within the error limits given in Table 4.4. On a few occasions there are indications of disagreement. This is rather attributed to the lower signal to noise ratio in the shortest light beam (beam 3) than to spatial differences. The spectra from beam 4 were only analysed partly due to their very low light signal (see also *Sec. 3.1.1.8.3*). At the beginning of October, strong wind gusts hampered the measurements. The external mirror racks were exposed to wind gusts which caused alignment problems at the end of the campaign. Therefore the routine measurements were interrupted after 2 October and instrumental tests were performed. Another measuring day followed on 7 October pointing with all four light beams onto the same retro-reflector array. The results of this experiment are discussed in *Sec. 3.1.1.8.3*. Although taking place in autumn, higher concentrations of all trace gases were measured during FORMAT II than during the previous campaign (cp. Table 4.1 and Table 4.4). The large traffic volume typical for Milano and the weather conditions favourable for the build-up of high pollutant concentrations are responsible for that.

Formaldehyde. Formaldehyde mixing ratios up to 25 ppbv at noon were found during this campaign (see *Fig. 4.12*). The diurnal variation of formaldehyde is similar to the NO_2 variation with maximum concentrations between 10 and 12 h and a second peak is observed at ~ 21 h during the fair weather period in September. In cloudy conditions, the two peaks appear earlier and the morning peak is less pronounced. The short-term diurnal formaldehyde variation is superposed by a slow buildup variation during the high pressure conditions in mid-September. Minimum night time mixing ratios around 5 ppbv were registered in this period, increasing from night to night. The first peak presumably arises from the photooxidation of HCs emitted south of Bresso earlier in the day and transported to the site during the transformation process. The first peak is of photochemical origin. This indicates that photochemical sources control CH_2O levels at Bresso. Some correlation is observed also for CH_2O with NO_x and SO_2.

Nighttime formaldehyde peaks coincided with NO_2 peaks and are thus attributed to direct emission of CH_2O in Bresso. The contribution of the reaction of alkenes with ozone was found to be very small. Considering the ozonolysis of ethene, propene, 1-butene, isobutene, 1,3-butadiene and isoprene (measured by JRC), maximum production rates of altogether 0.3 ppbv h^{-1} were derived, where ethene, propene and isobutene accounted for the largest fractions. Refer to Table 2.4 for the rate constants and yields. The high CH_2O values further indicate high primary VOC reactivity.

Ozone. At Bresso, ozone was only detected during the day when the boundary layer is mixed and O_3 is formed photochemically. The ozone maxima occurred between 15 and 18 h along with

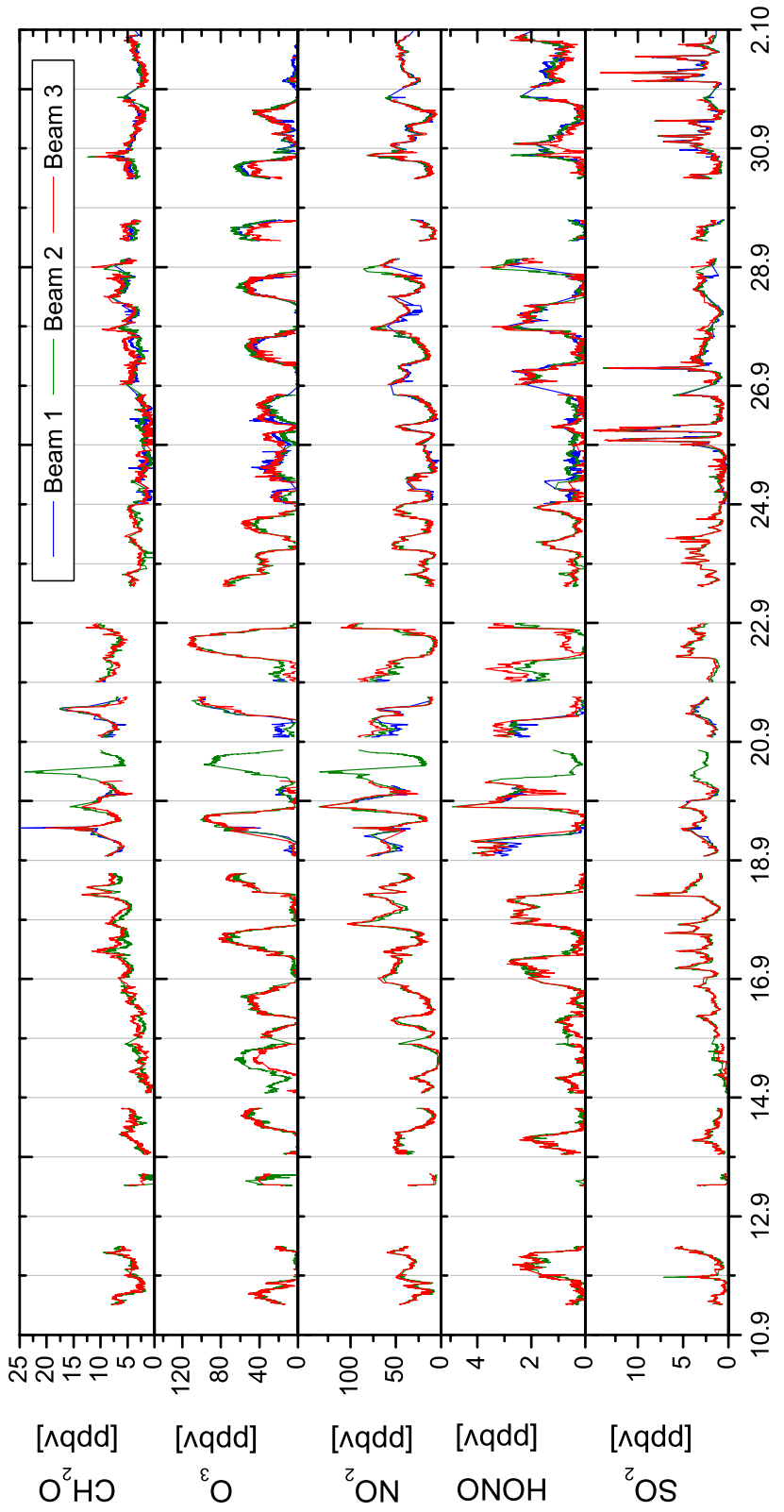

Figure 4.12: Trace gas mixing ratios measured by DOAS at Bresso during the FORMAT II campaign along the three light beams. The error bars of the measurements (refer to Table 4.4) were omitted for a clearer illustration. Ticks mark midnight.

minimum NO_2 concentrations (see *Fig. 4.12*). Average daytime maxima and nighttime minima are given in Table 4.4 for the fair weather and the instable period. Due to the lack of ozone formation mechanisms at night and its short lifetime due to reaction with NO (for 100 ppbv NO, the O_3 lifetime is approx. 20 sec) the nighttime ozone levels (after 21:30 h) were very low, often below the detection limit of a few ppbv (see Table 4.4). The lack of ozone during the night implies that the radical levels at night are also very low since NO_3 is not formed and the production of OH by ozone and alkene reactions is insignificant (*Sec. 4.4.1*). The long stable period favoured a net ozone buildup of the order of 7.3 ppbv d^{-1} between 16 and 21 September. The highest ozone mixing ratios at Bresso were observed on 21 September with up to 114 ppbv. With the passage of the trough between 21 and 23 September, afternoon maximum ozone mixing ratios dropped from 114 ppbv to 55 ppbv.

Nitrogen dioxide. During night, NO_2 levels at Bresso range between 45 and 100 ppbv, indicating large sources and a shallow boundary layer. Peak levels occur in the morning when vertical mixing is still limited and emissions are high due to rush hour traffic. The primary pollutants have an early night maximum between 21 and 23 h. Between 14 and 16 h, NO_2 is minimal (~15-20 ppbv). There is an anticorrelation between O_3 and NO_2, which is expected in an air mass which has been in contact with NO_x emissions just a short time before.

Nitrous acid. Mixing ratios of nitrous acid are more or less linked to the NO_2 variation and show a typical pronounced diurnal cycle. HONO values at Bresso increased during the night with increasing atmospheric stabilisation and increasing NO_2 levels and reached 3.5 ppbv in the middle of the night. After sunrise, i.e. after the initial onset of photolytic reactions, and a destabilisation of the nighttime boundary layer, the HONO levels rapidly decreased and stabilised at ~ 200 pptv during the day.

Table 4.4: Overview of average and maximum (30-min average) mixing ratios for several species measured during two periods of FORMAT II: 17-22 Sept. / 24-30 Sept. The detection limits are the average values for the entire campaign.

Site	Species	Method	Avg. det. limit [a]	Avg. mix. rat. 4-8 h [a]	Avg. mix. rat. 13-17 h [a]	Maximum mix. rat. [a]
Alzate	CH_2O	Hantzsch [b]	0.15	3.77 / 1.36	5.44 / 2.55	7.7 / 4.5
Alzate	O_3	UV-absorption [b]	1.0	70.93 / 13.94	114.67 / 42.92	137.9 / 73.6
Alzate	NO_2	chemiluminescence [b]	0.5	4.26 / --	4.88 / --	20.7 / --
Bresso	CH_2O	MB LP DOAS	0.78-0.90 [c]	6.92 / 3.10	6.72 / 3.16	17.4 / 8.6
Bresso	O_3	MB LP DOAS	4.20-6.06 [c]	9.20 / 6.77	83.51 / 37.73	107.2 / 58.3
Bresso	NO_2	MB LP DOAS	0.46-0.66 [c]	57.39 / 33.37	25.75 / 19.45	113.4 / 81.8
Bresso	SO_2	MB LP DOAS	0.10-0.14 [c]	1.73 / 3.33	3.04 / 1.78	7.3 / 10.2
Bresso	HONO	MB LP DOAS	0.26-0.36 [c]	2.52 / 1.21	0.16 / 0.31	3.4 / 3.2
Spessa	CH_2O	MB LP DOAS	1.00	1.17 / 0.60	2.31 / 2.56	8.6 / 9.4
Spessa	O_3	MB LP DOAS	7.20	15.37 / 15.51	98.17 / 48.93	115.9 / 87.7
Spessa	NO_2	MB LP DOAS	0.70	21.30 / 9.31	4.45 / 7.98	38.5 / 39.8
Spessa	SO_2	MB LP DOAS	0.18	1.17 / 1.04	2.31 / 0.94	4.9 / 4.3
Spessa	HONO	MB LP DOAS	0.30	0.84 / 0.02	below d.l.	1.4 / 1.4

a. in [ppbv]
b. not sufficient DOAS data available in Alzate for regarded time period 17-22 September
c. range between longest and shortest beam

Sulphur dioxide. A distinct weekly pattern of sulphur dioxide with no peaks during the weekends had been observed at the same site during the PIPAPO campaign. SO_2 peaks of up to 9 ppbv have been measured in 1998 [*Alicke*, 2000]. Due to the strongly changing meteorological conditions during FORMAT II, the weekly cycle is less pronounced here. Occasionally, very sharp peaks with SO_2 differences up to 15 ppbv occurred temporally staggered in the three beams (e.g. on 25 and 26 September, see *Fig. 4.12*). The peaks did not come along with increased concentrations of other trace gases like NO_2. Traffic can therefore be ruled out as the strong SO_2 source. The rapid increase and decrease of concentrations points to the short term release from a source very close by. Indeed, an industrial company, dealing with gases is located very nearby in the southern part of Parco Nord (Andrea Cortella, CRI, pers. comm., 2004).

4.3.4 Measurements at Spessa (Upwind Site)

Spessa al Po (45°08' N, 9°21' E, 64 m a.s.l., province of Pavia) is located 40 km south of the centre of Milano (see *Fig. 4.1*) in an agriculturally used area. The flat environment is typical for the region south of Milano. In the surroundings, predominantly rice is cultivated in dry field culture. There is no industry and no major traffic in the surrounding area. A weakly frequented motorway (A21 Alessandria – Piacenza) is running south of the river Po at a distance of approximately 5 km. The instruments were installed on the ground of a farmstead which also houses a gliding field (see lower right corner of *Fig. 4.13*). The Po runs 3 km south of the farm. IUP operated a multibeam long path DOAS at Spessa. There were also a Hantzsch monitor, a DNPH sampler and a MAX-DOAS at the site, operated by other groups. A meteorological station by NILU mounted on the roof of a hangar provided the meteorological data at this site. Also a small open research aircraft ('microlight'), operated by IFU, was based at Spessa.

Three light paths, passing over rice fields, were realised with the multibeam long path DOAS system at this site. The long path extended over 2140 m (single path) and went to a silo (43 m over ground). Two other light paths were very short (725 m one way) and the retro-reflectors

Figure 4.13: Agricultural surroundings of the farm 'Speziana' at Spessa including the DOAS light paths and their path lengths (one way).

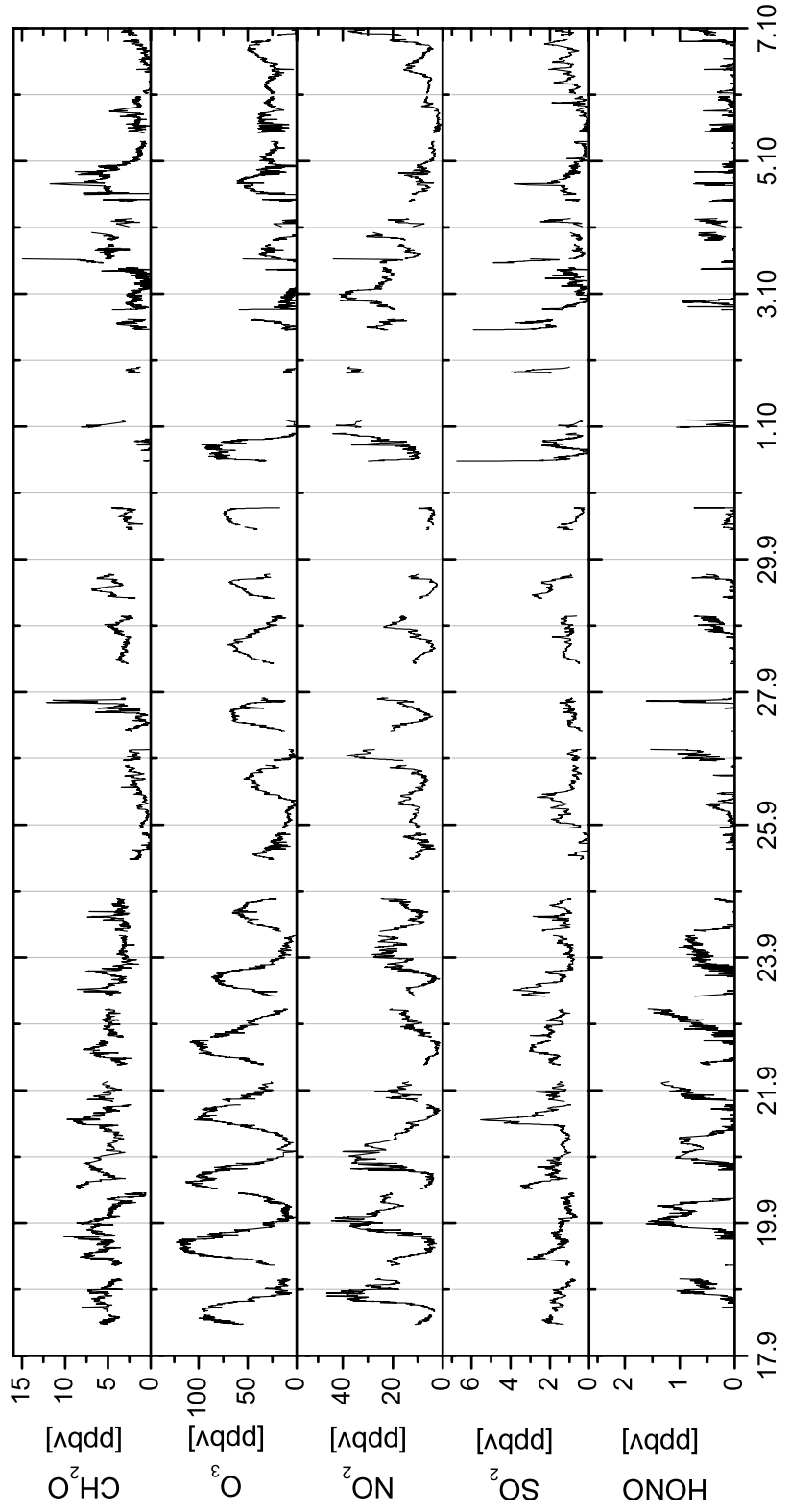

Figure 4.14: Time series of DOAS trace gas measurements at Spessa during the FORMAT II campaign. Only data from the long light path is shown. Detection limits of the trace gases are shown in Table 4.4.

were attached in two heights (29 m and 52 m) of another agricultural building in order to derive profile information. The setup of light paths is shown in *Fig. 4.13*. It turned out that the two short light paths were too short to derive vertical profiles. Therefore, the time series of concentrations in *Fig. 4.14* only show data from the long light beam. Spectra were recorded at Spessa between 17 September and 7 October 2003. The multibeam system at Spessa was operated by colleagues from IUP, however, the spectral analysis of the three light beams was part of this thesis. The spectra were analysed for CH_2O, O_3, NO_2, SO_2 and HONO. The measurements were sometimes interrupted by low visibility, occasional power failures and instrumental problems. Nighttime measurements are often missing in the time after 23 September. This is due to the vicinity of the river Po and the development of fog during the night. Usually, the fog did not dissolve until 10 h in the morning.

Formaldehyde. In the absence of local pollution sources, the CH_2O diurnal variation at Spessa observed by the DOAS was weak. The fair weather conditions during the first week of measurements should provide the opportunities for the secondary formation of formaldehyde. But there seem to be no high concentrations of hydrocarbons. The direct anthropogenic emission of formaldehyde is supposed to be negligible in this area. Formaldehyde peaks were observed when nearby rice fields were burnt. The time of these peaks coincided with peaks of SO_2. Since it is usual in the rural areas in the Po Basin south of Milano that peasants burn down the stubble fields after the harvest, such agricultural fires were observed at the site day-to-day. The trace gas emission from the agricultural fires and the quantification of CH_2O emission is discussed in detail in *Sec. 6.4*. An in-situ Hantzsch monitor at Spessa observed a diurnal variation more pronounced than in the urban atmosphere. This might be attributed to the stronger influence of deposition within a lower NBL in the country than in the city.

Ozone. Daytime maxima of 100 ppbv are comparable to the concentrations measured at Bresso (see also *Sec. 4.3.5*). In the late evening, ozone mixing ratios dropped to values between 10 and 15 ppbv. This background value was roughly constant throughout the night because no considerable sources of ozone sink species, like NO, are present at Spessa. The day-to-day variability of ozone concentrations was associated with the varying meteorological conditions. Days with high O_3 levels occur in groups, most notably between 17 and 23 September.

Nitrogen dioxide. The NO_2 mixing ratio reached 20-40 ppbv at night with the highest values during the high-pressure phase. Daytime minimum values were 2-3 ppbv.

Nitrous acid. During daytime, HONO concentrations at Spessa were usually below the detection limit. Nighttime peak values usually ranged between 1 and 1.5 ppbv.

Sulphur dioxide. Since there are no anthropogenic SO_2 sources in the vicinity of the site, like vehicular traffic or industry, no variability is discernible in the diurnal course of sulphur dioxide. Mixing ratios between 1 and 2 ppbv are usually observed. However, in the plumes of agricultural fires, pronounced peaks up to 5 ppbv occur, since SO_2 is produced in the combustion of the sulphur contained in the plant (see *Sec. 2.1.4*) and is released to ambient air. In *Sec. 6.4*, the co-emission of CH_2O and SO_2 is used to determine a formaldehyde emission factor from the agricultural fires.

4.3.5 Ozone Upwind and Downwind of Milano

As mentioned in *Sec. 2.2.4*, ozone concentrations are usually highest downwind of larger cities. The three FORMAT measurement sites which are arranged upwind, within and downwind of the city of Milano (see *Fig. 4.1*) confirm this observation. The ozone concentrations measured at Spessa, Bresso and Alzate between 14 and 24 September 2003 are shown in *Fig. 4.15a*. The development of a distinct ozone event can be observed in this period with up to

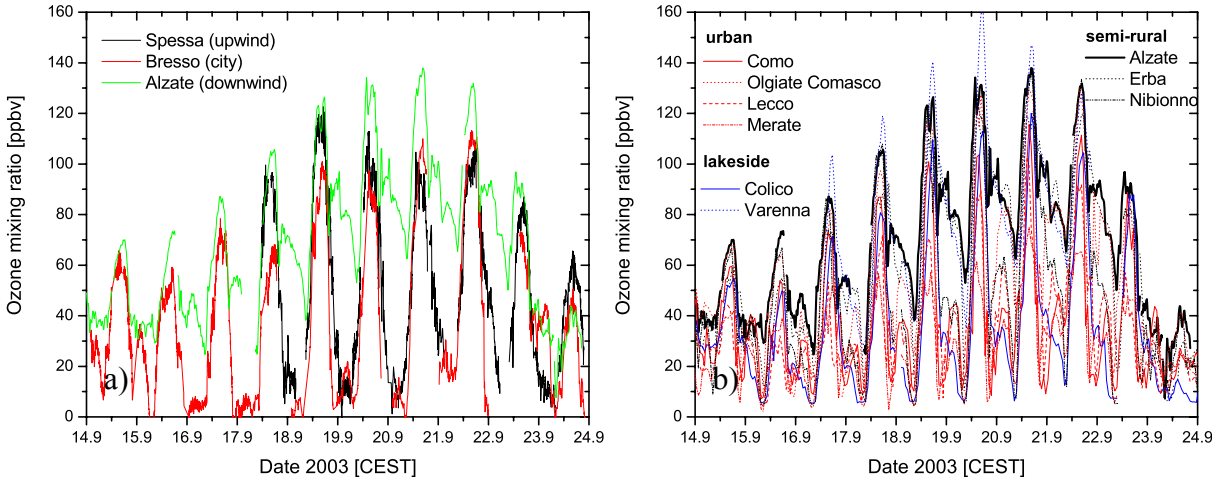

Figure 4.15: ***(a)*** *Ozone mixing ratios upwind, within and downwind of Milano during a buildup period in FORMAT II.* ***(b)*** *Ozone data from ARPA measurement stations close to and surrounded by the Alpine foothills.*

30 ppbv higher ozone values than further upwind measured at Alzate on 20 September. The ozone event was terminated on 23 September by the passage of a front.

It is also interesting to compare the diurnal variations of the ozone concentration at the different sites. Bresso, which is most strongly influenced by anthropogenic emissions, usually shows the most rapid drop of ozone concentrations in the evening. Values close to the detection limit are measured there throughout the night due to the reaction with NO. The behaviour of the nighttime ozone concentration at Alzate points to a strong dynamical influence. After sunset, the concentrations initially drop due to local NO_x emissions, but then increase again in steps. Since there are no ozone sources at night, this indicates the advection of a different air mass. A similar development of ozone concentrations is observed at several stations of the regional monitoring network ARPA which are located in the vicinity of Alzate (*Fig. 4.15b*). Urban stations like Como, Olgiate Comasco (east of Como), Lecco and Merate (south of Lecco) experience a strong ozone decrease to low levels in the evening followed by a significant secondary ozone peak at night between 3 and 5 h. Another minimum is found there during the morning rush hour at 8:30 h. The semi-rural stations Alzate (FORMAT station), Erba and Nibionno do not show a strong ozone decrease in the evening. Due to a lack of emissions in these areas, the concentrations keep at high levels and a weak increase between 4 and 5 h is discernible before the morning minimum. In contrast, no nighttime ozone peaks are found at the stations on the shore of Lago di Como (Colico and Varenna) where the values dropped after sunset and stayed low throughout the night. Overall, the advection of ozone-rich air masses at night can be observed at many stations close to the Alpine foothills with varying distinctiveness. It indicates complex dynamic mechanisms in the pre-Alpine region.

4.4 Synopsis of Three Campaigns in the Po Basin

4.4.1 Radical Formation at Bresso (1998, 2002, 2003)

As pointed out in *Sec. 2.2.1*, formaldehyde is an important radical source. The fraction of HO_x radicals from CH_2O photolysis is deduced in this section. For the three field campaigns conducted at Bresso, i.e. the PIPAPO campaign and the two FORMAT campaigns, the HO_x radical production rates were derived. For this purpose, the LP DOAS data measured by *Alicke* [2000] at the same site during the PIPAPO campaign in May/June 1998 are included besides our own data.

The major radical producing compounds are ozone, formaldehyde and nitrous acid (see *Sec. 2.2.1*). VOC oxidation by ozone contributes to OH production as well, but VOC data are only available for 1998 [*Grüebler*, 1999] and 2003 [*Latella et al.*, 2005]. According to eq. 2.7 and eq. 2.8, the HO_x production rates from formaldehyde and nitrous acid depend only on the photolysis frequencies and concentrations of CH_2O and HONO. For the OH production from ozone photolysis, the water vapour content of the air is an additional important factor (see eq. 2.6). The HO_x production rates were calculated from the relevant concentrations and photolysis frequencies measured at Bresso, involving meteorological data. The average HO_x production rates from the three campaigns as a function of the time of the day are shown in *Fig. 4.16a-c*. The contributions of HONO, CH_2O, O_3 and VOCs change over the course of a day. The contribution from the ozonolysis of VOCs, given for PIPAPO and FORMAT II, represents a lower limit for OH production, since during both campaigns only a restricted number of alkenes and dienes was measured ¶. The VOC oxidation contributes predominantly in the evening hours since high ozone concentrations are available and at the same time the evening rush hour provides high concentrations of VOCs. The average absolute production from VOCs reaches 2×10^6 molec cm^{-3} s^{-1} at ~19 h. During night, VOC ozonolysis is the only HO_x source. As HONO accumulates during the night and readily photolyses under solar radiation, it is the most important OH source in the early morning hours. The absolute OH production rate by HONO after sunrise is of comparable magnitude for all three campaigns. From the later morning hours on, the HO_x production is dominated by formaldehyde and ozone photolysis, whereby their absolute and relative contributions vary between the three campaigns as described in the following.

During PIPAPO, ozone and formaldehyde had similar average HO_x production rates (*Fig. 4.16a*). Owing to the high concentrations of these trace gases in May/June 1998 and at the same time the seasonally highest photolysis frequencies, the absolute radical production by formaldehyde and ozone frequently reached more than 1.2×10^7 molec cm^{-3} s^{-1} at noon.

Relatively large daytime HONO concentrations derived for FORMAT I (see Table 4.1) made HONO an important HO_x producer also during the afternoon hours (*Fig. 4.16b*). The HO_x production rates from ozone and formaldehyde both peak between 13 and 14 h when the actinic flux is at its maximum, but ozone accounts for a larger amount of HO_x than formaldehyde during FORMAT I. The contribution of formaldehyde photolysis to HO_x production at noon (13:30 h) is around 32%, whereas ozone accounts for 47%. The disagreement of 10-15% between the in-situ formaldehyde measurement methods found in *Sec. 5.2* contributes on average less than 4% to the uncertainty in the total HO_x production rate calculated from the measured data.

For the FORMAT II trace gas data, the average concentration of the three light beams was taken and due to the change in weather conditions (see *Sec. 4.3.1*), two time periods were distinguished (*Fig. 4.16c*). During the fair weather period until 22 September, trace gas concentrations were enhanced and at the same time the solar irradiation was highest (no clouds). Formaldehyde was found to be the most important primary HO_x radical producer after 10 h at Bresso during the smog conditions of the FORMAT II campaign. Maximum noontime HO_x formation rates from CH_2O of more than 1×10^7 molec cm^{-3} s^{-1} were derived. Only in the early morning hours, HONO was more effective producing OH. The maximum of the production rates by formaldehyde is one hour before the maximum by ozone. The subsequent cloudy period with lower pollutant levels showed significantly lower radical production rates. Under these conditions, HONO even dominated HO_x production during the entire day. Since the spectro-

¶. PIPAPO: i/1-butene, 1,3-butadiene, isoprene, cis-2-pentene, trans-2-pentene, 2-methyl-2-butene and styrene; FORMAT II: ethene, propene, 1-butene, i-butene, 1,3-butadiene and isoprene.

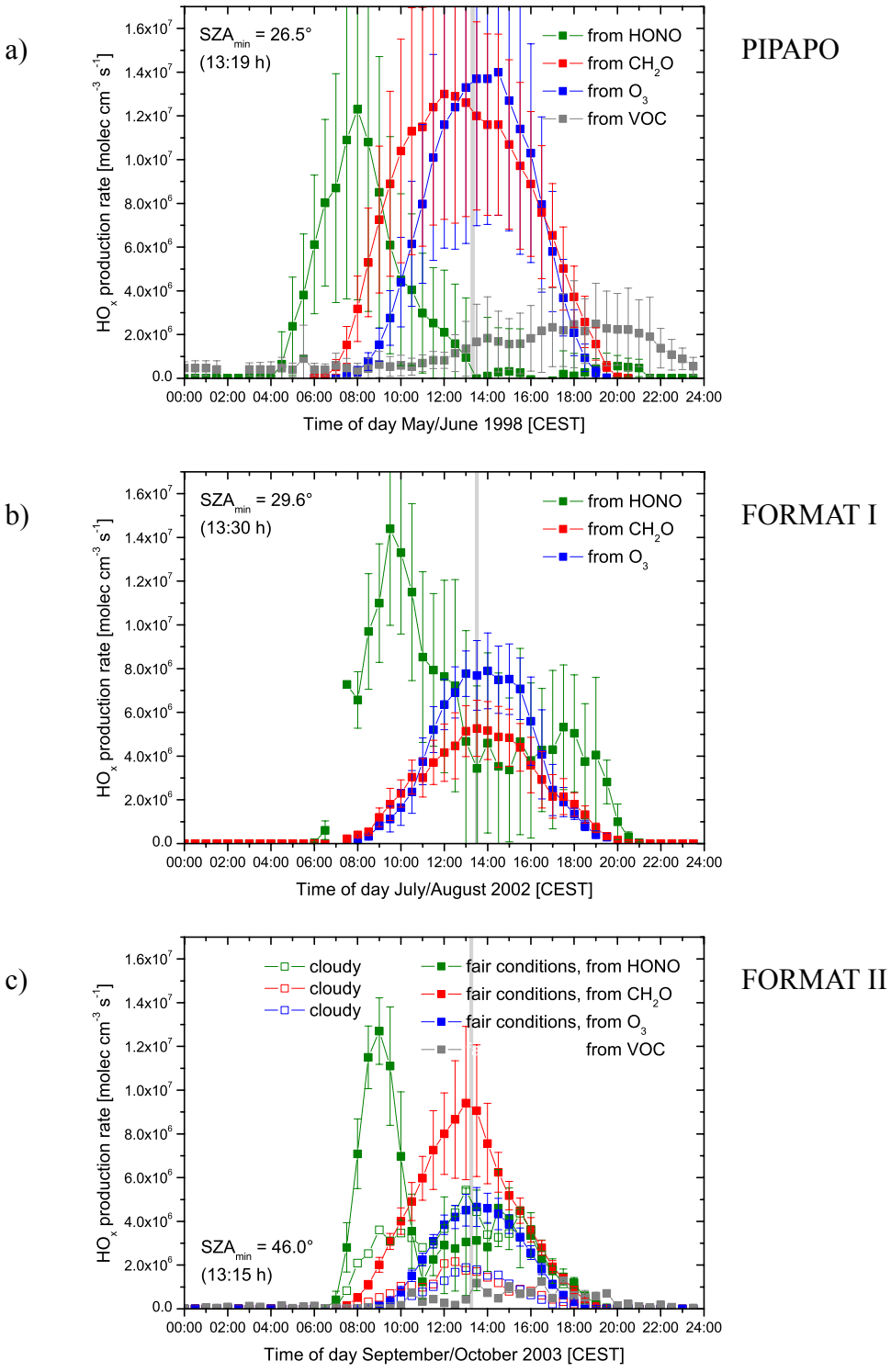

*Figure 4.16: Average production rates of HO_x radicals by photolysis of HONO, CH_2O and O_3 and by VOC oxidation during the **(a)** LOOP / PIPAPO campaign, **(b)** FORMAT I campaign, **(c)** FORMAT II campaign at Bresso (averages over entire campaigns, except rainy days). The FORMAT II data are separated into the fair weather days and the cloudy days.*

radiometer was operative only during some days of the FORMAT II campaign (see *Sec. 4.3.3*), the study was restricted to the time period between 19 and 26 September 2003. For the fair weather conditions, the days 20-21 September were used, for the autumn conditions the days 24-25 September.

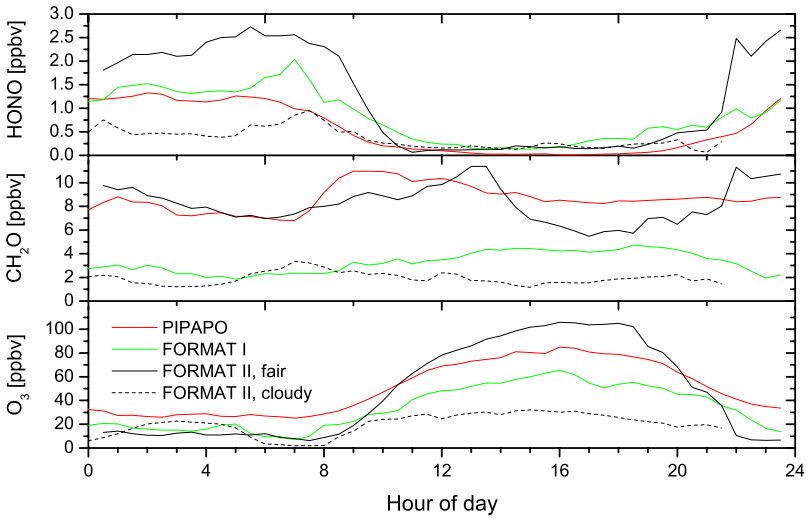

Figure 4.17: Average mixing ratios of HONO, CH_2O and O_3 at Bresso during the three campaigns as a function of the time of the day.

The differences between the absolute production rates and relative contributions of the major sources for three campaigns at the same site can be explained by the combination of various parameters. Due to the seasonal variation of the noonday minimum SZA, which is indicated in the plots of *Fig. 4.16*, the highest photolysis frequencies were met during the PIPAPO measurements in May/June. Moreover, the trace gas concentrations were high during PIPAPO, compared to the FORMAT campaigns (see *Fig. 4.17*), collectively giving rise to the highest absolute HO_x production rates observed at Bresso during PIPAPO.

During FORMAT I in July/August, the photolysis frequencies for the cloudless case were almost as high as during PIPAPO, but two effects coincide, resulting in comparatively low photo-oxidant concentrations and low radical production. Firstly, the measurements occurred for the most part in August. During this month, the emission of air pollutants is considerably reduced (holiday effect, see *Sec. 4.2*). Secondly, due to the adverse meteorological conditions during FORMAT I, the photochemical activity of the air was greatly diminished, so that formaldehyde and ozone concentrations were low (cp. *Fig. 4.17*).

The relative importance of formaldehyde as a radical producer is increased in FORMAT II towards the FORMAT I campaign and exceeds the ozone contribution to the radical budget both during noon and in the afternoon (see *Fig. 4.16b,c*). Although both formaldehyde and ozone concentrations were higher under the non-holiday conditions in FORMAT II than in the previous summer, the variation of the relative importance of CH_2O and O_3 for HO_x production is mainly ascribed to the lower water vapour content of the air during the FORMAT II campaign. This is reflected in a smaller fraction of $O(^1D)$ atoms reacting with H_2O to generate OH. As shown in Table 4.5, this fraction varied about 12 ± 3% for the campaigns in 1998 and 2002 and was significantly lower (7 ± 2%) during the 2003 campaign.

Surveying the results from previous measurements at urban sites by other authors, one finds large differences concerning the relative contributions of the major radical sources. These differences are due to a different composition of the air at the reported sites, but also meteorological conditions play a role. *Ren et al.* [2003] derived an integrated HO_x production rate of 34.7 ppbv day^{-1} in New York City in July 2001 (during PMTACS-NY2001). During that campaign, the HO_x production was dominated by the photolysis of HONO, accounting for 56% of the HO_x production on average, due to relatively high HONO mixing ratios (1.4 ppbv in the morning, 0.4-0.5 ppbv in the afternoon). Their study further revealed a contribution of 13% by ozone photolysis, 10% by VOC ozonolysis and only 8% of the daily HO_x production is

Table 4.5: HO_x production at Bresso during three campaigns. There was a varying fraction of $O(^1D)$ atoms taking the OH yielding reaction channel, F_{OH}. The average 24 hours integrated values of radical production from the four major HO_x sources are shown below.

	PIPAPO 1998 [a]	FORMAT 2002	FORMAT 2003
average F_{OH}	12.0%	11.1%	7.2%
minimum F_{OH}	8.2%	6.9%	4.7%
maximum F_{OH}	17.7%	14.5%	9.9%
OH from HONO (24 h)	8.8 ppbv d^{-1} (20.1%)	10.5 ppbv d^{-1} (53.8%)	7.0 ppbv d^{-1} (39.5%)
HO_2 from CH_2O (24 h)	15.5 ppbv d^{-1} (37.1%)	4.0 ppbv d^{-1} (20.2%)	7.3 ppbv d^{-1} (40.5%)
OH from O_3 (24 h)	13.5 ppbv d^{-1} (33.8%)	5.0 ppbv d^{-1} (25.9%)	3.6 ppbv d^{-1} (20.0%)
OH from VOCs (24 h)	3.7 ppbv d^{-1} (9.1%)	not available	irregular samples
total HO_x (24 h)	41.5 ppbv d^{-1}	19.6 ppbv d^{-1}	17.9 ppbv d^{-1}

a. measurements performed by B. Alicke (see *Alicke* [2000])

explained by formaldehyde, due to the low average CH_2O concentration of 1.9 ppbv during daytime. In airborne measurements during the Nashville/Middle Tennessee Ozone Study in July 1995, *Lee et al.* [1998] found that formaldehyde as an important free radical precursor contributed 25-30% of the total radical production during midday and even more during morning and late afternoon periods. However, they only considered formaldehyde and ozone as HO_x radical sources. Another study by *Possanzini et al.* [2002] considered the contributions of formaldehyde, acetaldehyde and ozone to HO_x production. Their measurements in the city centre of Rome indicated that formaldehyde photolysis was by far the most important source of OH radicals in Rome during all sunlight hours in the summers of 1994-1997. The OH production rate of formaldehyde exceeded those of ozone and acetaldehyde by one order of magnitude.

In comparison, the average total daily HO_x production at Bresso was between 20 and 40 ppbv day^{-1} (see *Fig. 4.18*), depending on the season. These values are similar to the result by *Ren et al.* [2003]. The photolysis of HONO, CH_2O, O_3 and ozone reactions with alkenes accounted for campaign-averaged fractions as specified in Table 4.5. Depending on the

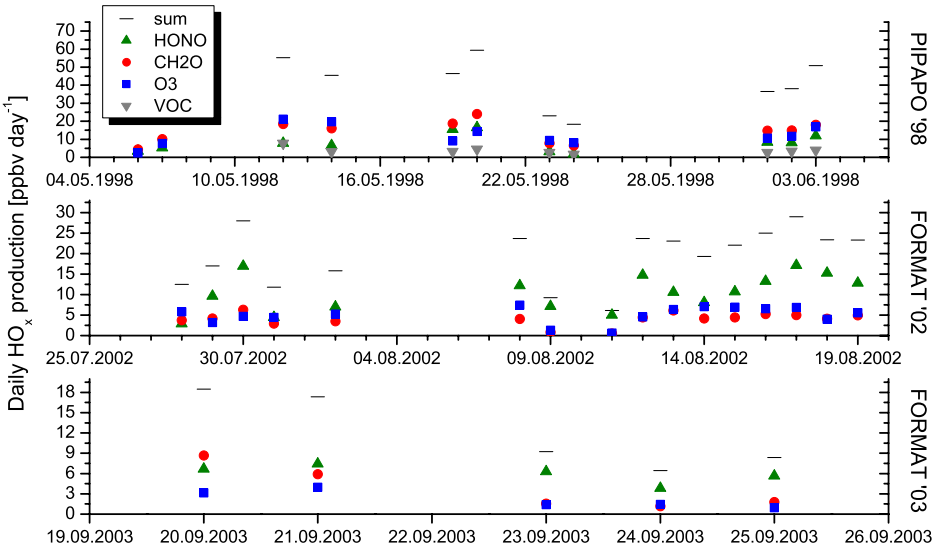

Figure 4.18: Total HO_x production per day for the three campaigns at Bresso and individual contributions from CH_2O, HONO, O_3 and VOCs. Only data from non-rainy days is shown.

atmospheric composition and meteorological conditions during the three campaigns, varying absolute radical production rates and varying relative precursor contributions are observed at one and the same site. The role of formaldehyde as a radical source is important though with a contribution of at least 20-40%. The daytime HONO concentration at Bresso during PIPAPO as stated by *Alicke* [2000] was very low compared to both FORMAT campaigns. However in all three cases, the derived daytime HONO concentrations were usually below the detection limit during the afternoon (cp. Table 4.1 and Table 4.4). The absolute daily HO_x production by HONO photolysis and the relative importance given in Table 4.5 and *Fig. 4.18* therefore represent upper limits, the actual contribution being lower. Because of its high photolysis frequency, an uncertainty of the HONO concentration strongly influences the determination of HO_x production. Formaldehyde and ozone are always above the detection limit and are of approximately equal importance if integrated over an entire day.

4.5 The Mexico City Campaign (MCMA-2003)

MCMA-2003 was a major field campaign investigating the atmospheric chemistry of the Mexico City Metropolitan Area (MCMA). The campaign was held between end of March and 4 May 2003 at several sites in Mexico City. Thus, it was designed to be towards the end of the dry season when solar radiation is intense but daily convective rainfall has not yet begun. In addition, it included school vacations as well as the Holy Week and Easter when traffic is greatly reduced in the entire city, providing a natural experiment for the impact of emissions reductions. The time zone in the MCMA was Central Standard Time (CST = UTC – 6). Solar noon during the campaign was within 5 minutes of 13:35 h.

4.5.1 The Location

The Mexico City Metropolitan Area is situated inside a basin at 2240 m altitude and 19°N latitude. The basin is surrounded by high mountains on three sides. The MCMA-2003 field campaign was based at the National Centre for Environmental Research and Training (Centro Nacional de Investigación y Capacitación Ambiental, CENICA). The CENICA supersite (19°21.53' N, 99°04.41' W) is housed on the campus of UAM (Universidad Autónoma Metropolitana) in the delegación Iztapalapa (see *Fig. 4.19*) in the south-east of the city. The area features commercial, residential and industrial buildings as well as the conservation area Cerro de la Estrella.

The long path DOAS measurements by IUP together with MIT and most other measurements by other groups were conducted on the roof top of the CENICA building. Two LP DOAS instruments were installed in a temperature-controlled enclosure. The DOAS-1 ('HMT') instrument measured in three different wavelength ranges (aromatic compounds, HONO and NO_2) by turning the grid of the spectrometer. The single path length to a telephone mast was 540 m. The results are not further discussed here ¤. Only data from DOAS-2 is described and used here. The DOAS-2 ('Nashville') system switched between four different wavelength ranges (see below) in order to measure formaldehyde, nitrous acid, glyoxal and NO_3 (only at night). An array of retro-reflectors was placed at 'Museo El Fuego Nuevo' (19°20.90' N, 99°05.47' W) on the slope of the local hill 'Cerro de la Estrella', resulting in a total atmospheric light path of 4420 m, on average 70 m above ground.

¤. see forthcoming paper by Volkamer, R., M. Zavala, L. T. Molina, M. J. Molina, et al., Open-path emission factors derived from DOAS and FTIR measurements in the Mexico City Metropolitan area, Atmos. Chem. Phys. Discuss., in preparation, 2006.

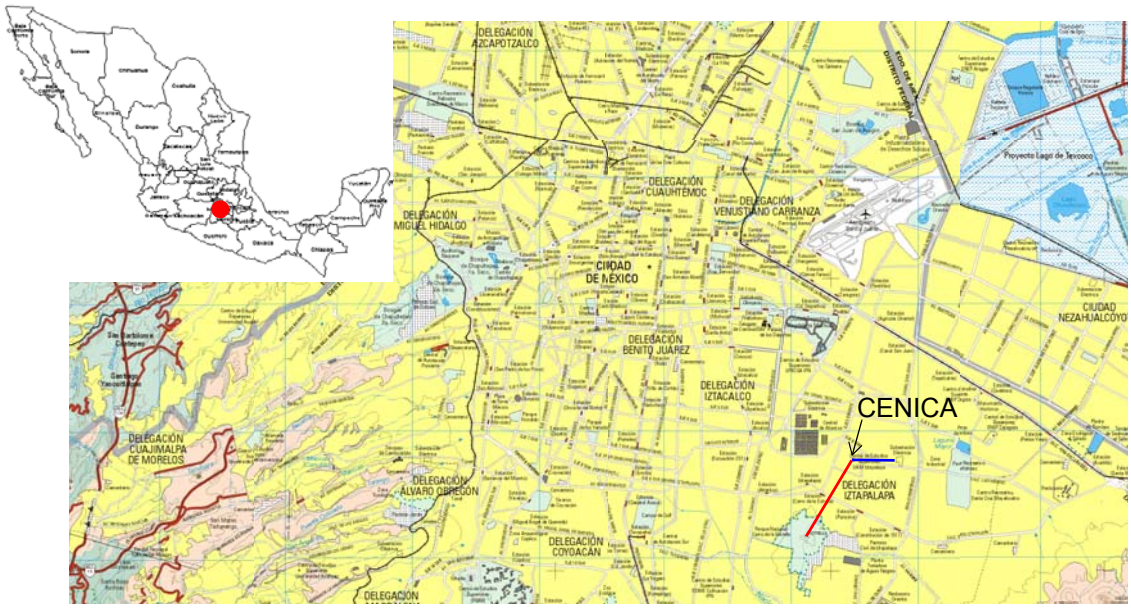

Figure 4.19: Map of the centre of Mexico City including the light paths of DOAS-1 (blue) and DOAS-2 (red). The DOAS measurements were performed 10 km south-east of downtown Mexico City (map from Maps-of-Mexico [2003]).

4.5.2 Meteorological Overview

April is a transition month between the hot dry season and the wet season. Therefore weather events from both kinds of seasons are occurring in brief succession. Typically, the mean April synoptic flow is dominated by a low level anticyclonic circulation over central southern Mexico and westerly winds aloft north of 20°N. This leads to subsidence over the Mexico basin with weak surface winds, favourable to the development of thermally driven circulations [*de Foy et al.*, 2005]. This pattern was observed for two episodes during MCMA-2003: 14-17 April and 1-3 May. Under these conditions, ozone levels are highest in the south of the city. Occasionally, strong surface northerlies bring cold moist air and rain to Mexico City. This occurred twice during the campaign, on 8-10 and 20-22 April, and once before the beginning of the campaign, on 29-31 March [*de Foy et al.*, 2005]. The remaining days of the campaign had unperturbed westerlies with very weak anticyclonic conditions to the south and a strong subtropical jet just to the north of the MCMA. This results in high ozone levels in the north of the city [*de Foy et al.*, 2005]. Meteorological parameters were measured during MCMA-2003 by MIT. The temperature ranged from 10 to 32°C and the relative humidity from 5 to 98%. The measurement period was characterised by clear to partially clouded skies during the morning and afternoon hours, with some evenings featuring mild convective rainfalls. The predominant wind directions are from the north-east and south, but there is no clear pattern in the winds. For wind speed, there is a clear pattern that differs little between the episodes. Winds are below 2 m s^{-1} in the early morning, increase steadily from sunrise to speeds of 4 to 6 m s^{-1} at sunset and then decrease until about midnight. The wind direction is southerly in the early morning, shifting to northerly during the day and back to southerly at night.

The spectral actinic flux was measured by spectroradiometry (see *Sec. 3.2.5*). The photolysis frequencies for NO_2, $O(^1D)$, CH_2O and HONO were calculated using absorption cross-sections and quantum yields, as described in eq. 2.5. The time series are shown in *Fig. 4.20*, indicating the photolytic lifetimes on the right-hand axis. Data are available between 2 and 22 April. Afterwards, the instrument was shipped back to Germany. The minimum solar zenith angle

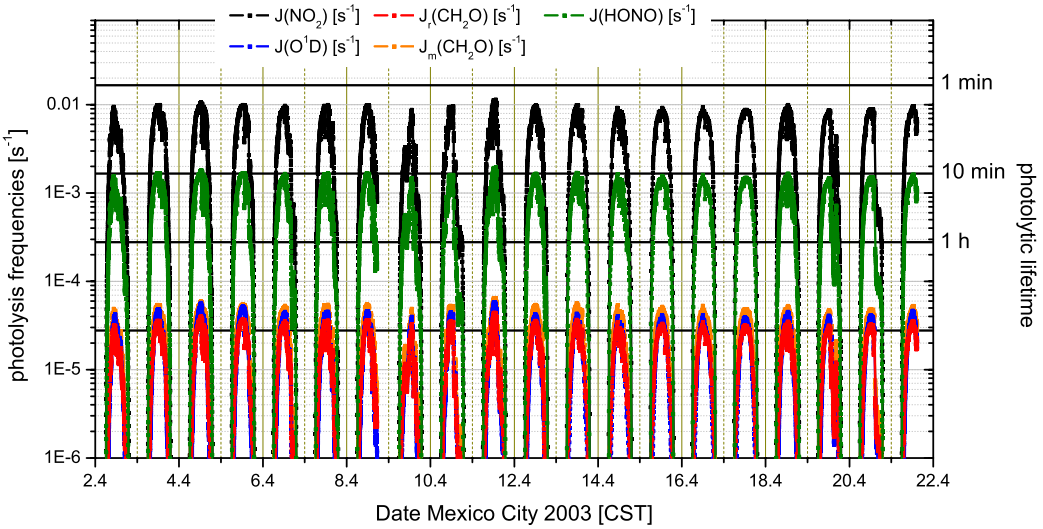

Figure 4.20: Photolysis frequencies J_{NO2}, $J_{O(1D)}$, J_{CH2O} (both channels) and J_{HONO} measured with a spectroradiometer at CENICA in Mexico City during the MCMA-2003 campaign. The time is given as Central Standard Time.

occurred at ~13:35 CST and decreased from 14° to 7° during the time period of the campaign. Average peak values of the photolysis frequencies were $J_{NO2} = 8.7 \times 10^{-3}$ s^{-1} ($\tau = 2$ min), $J_{O(1D)} = 4.1 \times 10^{-5}$ s^{-1} ($\tau = 6.8$ h), $J_{CH2Or} = 3.2 \times 10^{-5}$ s^{-1} ($\tau = 8.6$ h), $J_{CH2Om} = 4.8 \times 10^{-5}$ s^{-1} ($\tau = 5.7$ h), $J_{HONO} = 1.5 \times 10^{-3}$ s^{-1} ($\tau = 11$ min). The photolysis frequencies derived from the actinic flux measurements in Mexico City 2003 indicate that ~ 60% of the photolytic loss of CH_2O at noon occurs via the molecular channel. The remaining 40% of the photolysis reactions of formaldehyde yield radicals. The combined photolysis frequency is 7.6×10^{-5} s^{-1} (photolytic lifetime $\tau = 3.9$ hours) at noon. In the morning and evening only 23% of the CH_2O photodissociations proceed via the radical channel. A minimum formaldehyde lifetime of ~ 2 h with respect to photolysis and reaction with OH (measured, see below) was derived at noon.

4.5.3 Trace Gas Measurements

Atmospheric spectra were recorded with DOAS-2 by sequentially projecting 81 nm wide wavelength intervals onto the 1024-element PDA. The centre wavelengths 318, 357, 427 and 642 nm were tuned in successively. Formaldehyde was retrieved every 2-15 min from evaluating the spectral range between 290 and 350 nm. Time-resolved mixing ratios of CH_2O, O_3, NO_2, SO_2 and HONO are shown in *Fig. 4.21*. Continuous measurements were made over a 10 day and a 16 day period in April and May 2003.

OH radical concentration was measured by Penn State University with laser-induced fluorescence (LIF) in detection chambers at low pressure, a technique commonly referred to as FAGE (Fluorescence Assay by Gas Expansion). The technique and instrument is described by *Faloona et al.* [2004]. During MCMA-2003, the OH detection chamber was mounted on a tower 6 m above the roof of the CENICA building. The laser and electronics were housed in the rooftop laboratory with the DOAS instruments.

Formaldehyde. Formaldehyde mixing ratios ranged from 1 to 36 ppbv. Formaldehyde has a marked diurnal variation, well correlated with the NO_2 variation. Minimum values occurred at night, increasing with the rush hour. The peaks occur during the morning between 8 and 10 h. Formaldehyde mixing ratios up to 30 ppbv were observed frequently at the site. The daytime atmospheric residence time under MCMA conditions was 2 h and more.

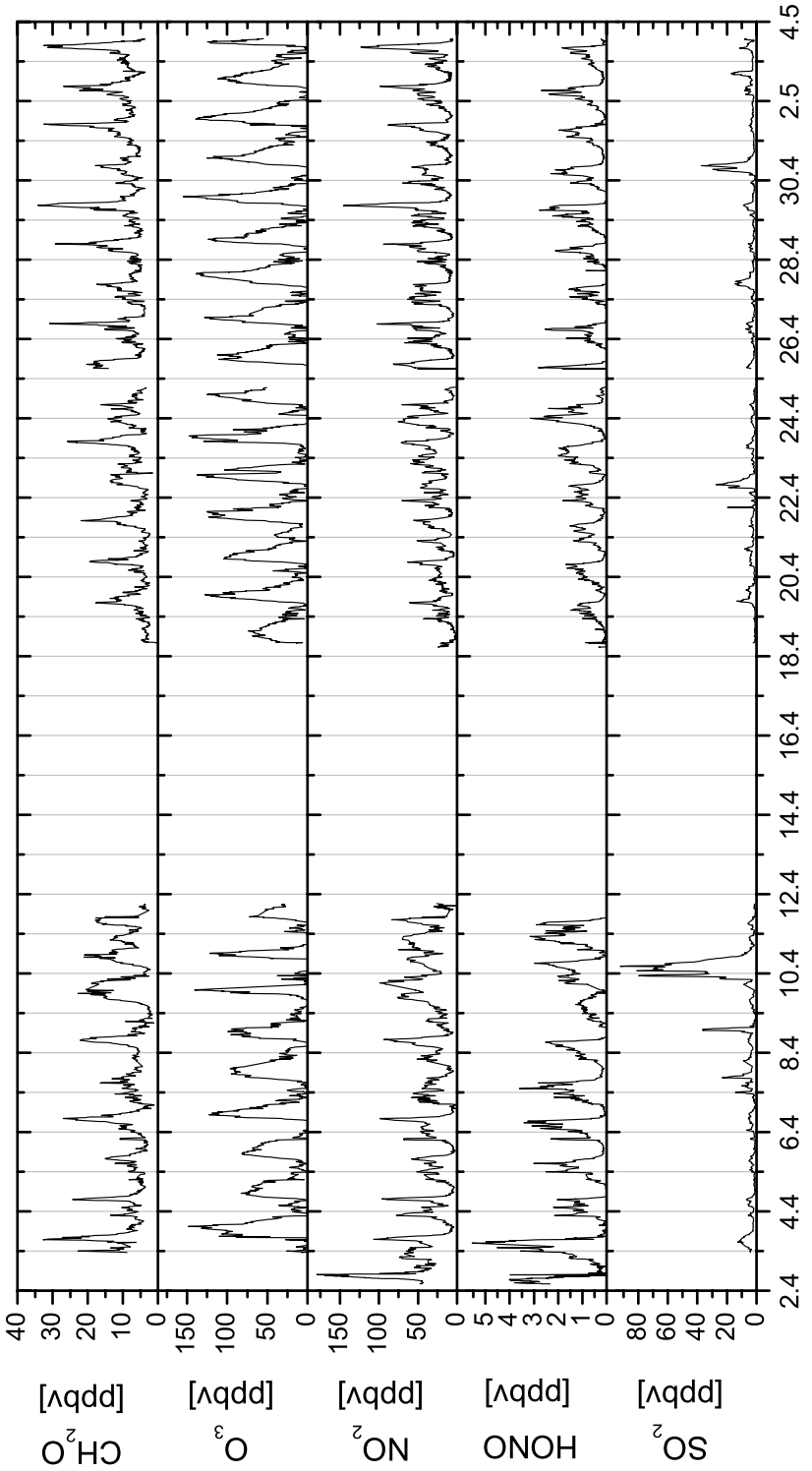

Figure 4.21: Trace gas mixing ratios measured with DOAS-2 at the CENICA roof in Mexico City between 2 April to 4 May 2003. The time is given as Central Standard Time (= UTC – 6). In the time between 12 April and 18 April, the measurements were interrupted since the lamp power supply was broken.

Ozone. Ozone has a prominent cyclical behaviour. It is a diurnal variation between a nighttime minimum and a daytime maximum. Maximum ozone concentrations occur around 14-15 h. Mixing ratios of 120 ppbv were frequently exceeded. At night, low ozone levels close to the detection limit of a few ppbv were observed with occasional increases, probably featuring a dynamical component as discussed in *Sec. 4.3.5* for conditions in Italy.

Nitrogen dioxide. The NO_2 mixing ratio in the probing height of ~ 70 m a.g.l. at Mexico City generally varied between 10 ppbv in the early afternoon and maximum levels of more than 100 ppbv in the morning. At night, concentrations between 30 and 40 ppbv were measured. During the day, NO_2 and O_3 were clearly anti-correlated. Ozone was only detected when NO_2 was low.

Nitrous acid. HONO shows a pronounced diurnal cycle with maxima of 3 ppbv in the probing height at night and concentrations below the detection limit in the afternoon.

Sulphur dioxide. SO_2 shows the highest concentrations during daytime with no typical pattern being discernible. The concentrations typically ranged between 1 and 30 ppbv. The distinct SO_2 plume on 10 April is of unknown origin.

4.5.4 Radical Production in Mexico City

The production rates of odd hydrogen radicals, HO_x, from HONO, CH_2O and O_3 were calculated from the concentrations measured by DOAS and the photolysis frequencies measured with the spectroradiometer. The result for the data between 2 and 22 April is shown in *Fig. 4.22*. HONO is the most important primary OH radical source in the early morning as long as considerable HONO concentrations are available. The HONO concentrations soon (≈ 3 h after sunrise) drop to very low values due to photolysis. Formaldehyde is the most important HO_x source in Mexico City over most of the day, with a maximum HO_2 production in the later morning hours. The maximum OH production due to ozone occurs around 12 h with a production rate comparable to that of formaldehyde at the same time.

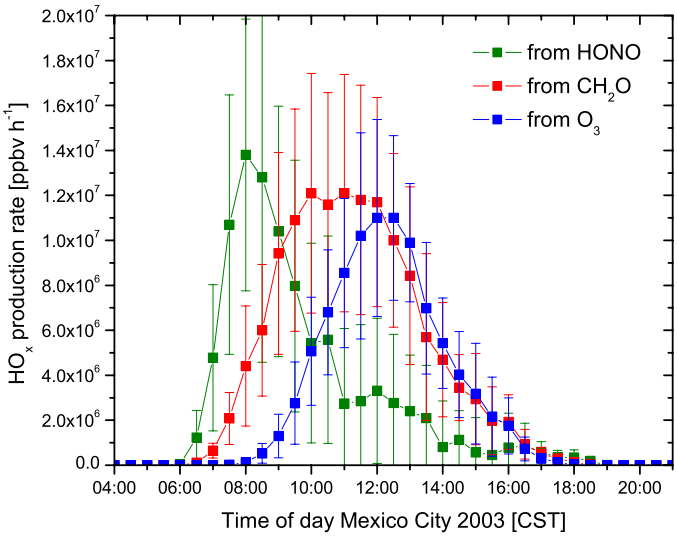

Figure 4.22: HO_x radical production rates from HONO, CH_2O and O_3 during MCMA-2003 as a function of the time of the day. Formaldehyde is the most important HO_x source over most of the day.

The radical production rates by formaldehyde and ozone are roughly equal in the afternoon. In the MCMA, CH_2O photolysis is the dominant radical source, starting in the late morning and sustaining photochemical smog formation throughout the day. The maxima of the three major

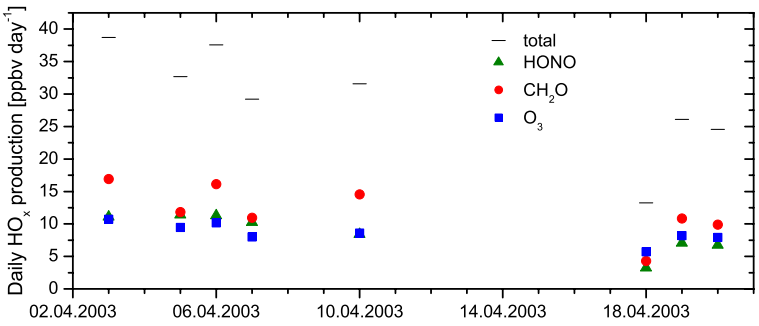

Figure 4.23: Daily total HO_x produced by photolysis of HONO, CH_2O and O_3 during the MCMA-2003 campaign.

radical sources are clearly separated, corresponding to the times of their concentration maxima. The absolute HO_x production from HONO, CH_2O and O_3, integrated over 24 h, was calculated for those days without interruption in the data series and is shown in *Fig. 4.22*. On average, 29 ppbv HO_x are produced per day by CH_2O, O_3 and HONO photolysis. During most days of the MCMA campaign, formaldehyde was the most important source of primary HO_x radicals accounting for 40.1 ± 4.5%.

5 Comparison of Formaldehyde Measurements

Accurate formaldehyde measurements are crucial for our understanding of the overall tropospheric chemistry (see *Sec. 2.3*). Several independent techniques for the quantification of formaldehyde with different time resolutions and detection limits have become available over the last two decades (see *Sec. 3.1.1-3.1.4*). Despite its importance and the relatively large number of different measurement techniques employed, there is still considerable uncertainty in ambient measurements of formaldehyde. A number of direct intercomparison experiments have been performed and CH_2O measurements have been included into air chemistry related field campaigns like BERLIOZ (BERLIn OZone experiment) in 1998 [*Volz-Thomas et al.*, 2003], LOOP/PIPAPO (PIanura PAdana Produzione di Ozono) in 1998 [*Neftel et al.*, 2002], SOS (Southern Oxidants Study) in 1995 [*Lee et al.*, 1998]. A summary of previous formaldehyde intercomparisons between various combinations of the techniques applied in the present study is given in *Sec. 5.1* (see also Table 5.1). The data from these campaigns and intercomparisons indicate that there is still significant disagreement between the individual techniques.

Since it is necessary to obtain a better understanding of the reasons for differences between the various measurement techniques in order to reduce the disagreement, an intercomparison study was performed in the scope of the FORMAT project, which included both wet chemical and optical techniques. For active remote sensing methods different optical setups are in use (see *Sec. 3.1.1.6*), probing different air volumes, which certainly can cause disagreement.

For in-situ measurements, a folded light path arrangement (e.g. White system) had been developed [*White*, 1976]. It combines the advantage of a long optical absorption path to attain adequate sensitivity with a small measurement volume to allow for comparison with other in-situ measurements. The intercomparison study, presented in *Sec. 5.2*, involves such White systems.

Results obtained with the long path setup (see *Sec. 3.1.1.6*) are averages over a light path extending a distance of several km. The comparison to in-situ measurements provides insight into local meteorological dynamics and chemistry, as shown in *Sec. 5.3*.

5.1 Previous Intercomparisons

- *Kleindienst et al.* [1988] compared five techniques to analyse CH_2O mixtures in zero air, photochemical mixtures inside a smog chamber and ambient air in a semi-rural area. In the zero air experiment, the average of all the techniques was used as a reference. The values obtained by the Hantzsch as well as the DNPH were systematically higher than the overall average by 21% and 6%, respectively. For the measurements in ambient air, a comparison between the DNPH with an enzymatic CH_2O monitor and a TDLAS (Tuneable Diode Laser Absorption Spectroscopy) instrument yielded a correlation of $r = 0.91$, but only 6 and 10 data points were

taken, respectively. The Hantzsch was in a preliminary state of development and therefore not included. The disagreement between the techniques was attributed to calibration differences.

- An intercomparison performed by *Lawson et al.* [1990] in urban ambient air included DOAS and FTIR White systems, Hantzsch, DNPH, TDLAS and an enzymatic fluorimetric technique. The average of the spectroscopic techniques was used as the reference. The Hantzsch system produced values 25% lower than the spectroscopic average, the DNPH values were 15-20% lower. The slopes of the regression lines were 0.74 and 0.75, respectively (correlation $r = 0.7$-0.9). The main conclusions were that good agreement was observed between the spectroscopic techniques and that differences with the Hantzsch technique were caused by a decrease in the efficiency of the scrubber.
- A study carried out at low formaldehyde concentrations of below 2 ppbv is reported by *Trapp and de Serves* [1995], who compared results from Hantzsch and DNPH-cartridges technique taken in the tropics. The slope of the regression line was close to unity ($b = 1.02$) and the coefficient of determination between the two techniques was $r^2 = 0.8$ ($r = 0.89$).
- *Gilpin et al.* [1997] conducted an intercomparison experiment with four continuous methods and two cartridge methods. The experiment employed spiked mixtures and ambient air. In ambient air, the Hantzsch results were 36% higher than those from TDLAS, which was used as a reference. Absolute gas standards were used in this study. The differences observed between TDLAS and the other techniques were attributed to calibration differences and collection efficiencies of the coils and diffusion scrubbers used by some of the participants. They recommended carrying out in-situ calibrations with gas-phase standards introduced at the instruments' air inlets.
- *Jiménez et al.* [2000] report on measurements taken in the Milan metropolitan area during the LOOP/PIPAPO field experiment. Results obtained with a commercial long path DOAS (DOAS 2000) and a DNPH-sampler were compared. For the seven days of concurrent measurements, the slope and intercept of the DOAS versus the DNPH results were 0.78 and 1.96 ppbv ($r = 0.32$). Due to a total optical path of only 425.2 m, the detection limit of the DOAS was high (around 3.75 ppbv). DOAS results were also compared to predictions by a 3D Eulerian photochemical model. The absorption cross-section used for the DOAS evaluation is not specified.
- *Cárdenas et al.* [2000] compared long path (LP) DOAS, Hantzsch and TDLAS results at a clean maritime site (Mace Head, Ireland) and a semi-polluted site (Weybourne, United Kingdom). They report correlation coefficients of $r = 0.67$ ($r^2 = 0.45$) between LP DOAS and Hantzsch data at Mace Head (CH_2O levels below 1 ppbv) after eliminating outliers, with the Hantzsch measuring higher values (slope $b = 0.62$). At levels of up to 4 ppbv measured at Weybourne, the agreement between two different LP DOAS instruments and a Hantzsch monitor was improved, with $r^2 = 0.76$ and 0.82, respectively. The Hantzsch measured higher values than both LP DOAS instruments ($b = 0.44$ and 0.13). The coefficient of determination for both DOAS instruments was $r^2 = 0.50$. One DOAS instrument measured significantly higher values than the other, with a slope of 0.36. There was good agreement ($b = 0.85$, $r^2 = 0.94$) between TDLAS and Hantzsch for indoor measurements in the range between 1 and 11 ppbv. The authors did not indicate which cross-section was used for the DOAS evaluation.
- *Pätz et al.* [2000] measured formaldehyde with TDLAS and Hantzsch during a field campaign at Schauinsland mountain (Germany). The concentrations measured by both instruments were very close to the theoretical concentration of the employed reference gas. The comparison in ambient air was carried out on a cloudy day with little photochemical activity. The average difference between the two instruments was 0.22 ppbv at an average mixing ratio of 2 ppbv.

- *Volkamer et al.* [2002] show results of a CH_2O comparison of a Hantzsch monitor and a DOAS White cell at formaldehyde levels between 25 and 100 ppbv. The experiment was conducted in April 2002 in the EUPHORE smog chamber under well controlled experimental conditions during a toluene oxidation experiment. The agreement was within 10% (slope of regression line = 0.89), with the Hantzsch measuring the higher values. The standard from IFU was employed for calibration of the Hantzsch. The DOAS calibration was based on the cross-section by *Cantrell et al.* [1990] (see *Sec. 3.1.1.8.1* for a discussion on CH_2O cross-sections). The agreement in the presence of photooxidation products from toluene oxidation indicates that cross-interferences are unlikely to be a major error source in either technique.
- *Klemp et al.* [2003] report on a comparison of a commercial Hantzsch system and a TDLAS. The measurements were performed in the framework of the EVA experiment at a site located in the city plume of Augsburg, Germany. Good agreement within 5% between both methods was observed during photochemically inactive conditions ($b = 1.05$, $r^2 = 0.83$). For heavily polluted events with ongoing photochemistry, the Hantzsch measurements exceeded those of the TDLAS by a factor of up to two ($b = 1.81$, $r^2 = 0.71$). Calibration errors and negative interferences of the TDLAS were ruled out as reasons for the observed deviations. Positive interferences of the Hantzsch remained among the possibilities.
- During the BERLIOZ field campaign, formaldehyde was measured by an LP DOAS and a Hantzsch monitor (AL4001) at a rural site in Pabstthum, Germany [*Grossmann et al.*, 2003]. The mixing ratios measured by the LP DOAS were systematically larger. The regression analysis of the two data sets yielded a slope of 1.23 on average ($r^2 = 0.66$). During days with high photochemical activity, however, the difference was a factor of 1.7. Differences of even higher magnitude were observed at the BERLIOZ sites Eichstädt and Blossin [*Volz-Thomas et al.*, 2003] during an intensive operation period. The discrepancies could not be resolved. The cross-section by *Meller and Moortgat* [2000] was used for the DOAS calibration.
- Measurements utilising FTIR and DOAS White systems, Hantzsch and DNPH-cartridge methods were carried out in the EUPHORE smog chamber in Valencia as part of the European project DIFUSO. The experiments were conducted at different concentration levels of formaldehyde and under very different experimental conditions, e.g., with diesel exhaust in the dark or with mixtures of diesel exhaust and different hydrocarbons under irradiation with sunlight. For concentrations below 5 ppbv, i.e. close to the detection limit of the DOAS in EUPHORE, the DOAS method yielded systematically higher values than the Hantzsch monitor, whereas the FTIR had values comparable to the Hantzsch. For concentrations between 10 ppbv and 100 ppbv, the agreement between all methods was very good (Jörg Kleffmann, pers. comm.).
- A more recent comparison of formaldehyde measurements has been carried out by groups involved in the OVOC campaign (within the ACCENT frame work) in the SAPHIR smog chamber of the research centre Jülich in January 2005. It involved a DNPH-sampler, a DOAS White system, a PTRMS and two Hantzsch monitors. The formaldehyde concentration in the chamber was calculated gravimetrically. The comparison measurements covered three days with in each case different conditions. The DOAS only participated at the third day. For formaldehyde in dry synthetic air, PTRMS and Hantzsch agreed perfectly, DNPH results were very low. In synthetic air with water vapour, the agreement of PTRMS, Hantzsch and DNPH was very good. In synthetic air with water vapour and ozone, PTRMS and DOAS agreed very well, the Hantzsch measured lower values. The results will be discussed in detail in forthcoming papers by R. Steinbrecher and A. Wisthaler (Jens Boßmeyer; Armin Wisthaler, pers. comm., 2006).

Table 5.1: Overview of previous formaldehyde intercomparisons including this study. Techniques which are also included in the present study are marked bold and their principles are described in Sec. 3.1.1-3.1.4.

Authors	Methods	Site / Project	Conc. [ppbv]	Time span
Kleindienst et al. [1988]	TDLAS Si-Gel DNPH cartridges DNPH solution **Hantzsch** Enzyme fluorimetry	semi-rural (North Carolina, USA)	1-10	16/06-26/06/1986
Lawson et al. [1990]	TDLAS **FTIR White system** **DOAS White system** **C18-DNPH cartridges** **Hantzsch** Enzyme fluorimetry	urban (Glendora, Los Angeles metropolitan area, USA)	4-20	13/08-21/08/1986
Trapp and de Serves [1995]	**Hantzsch** **C18-DNPH cartridges**	tropical continental BL (Venezuela) / ASTROS	< 0.05-2	10/09-23/09/1993
Gilpin et al. [1997]	TDLAS coil/DNPH **Hantzsch** Enzyme fluorimetry Si-Gel DNPH cartridges **C18-DNPH cartridges**	urban (Denver/Boulder metropolitan area, USA)	1-6	19/05-03/06/1995
Jiménez et al. [2000]	LP DOAS Si-Gel DNPH cartridges	suburban (Milan metropolitan area, Italy) / LOOP	0-10	02/06-09/06/1998
Cárdenas et al. [2000]	LP DOAS (two) TDLAS **Hantzsch**	clean maritime (Mace Head, Ireland) semi-polluted (Weybourne, UK)	< 0.05-0.8 ca. 0.2-4	28/07-07/08/1996 14/10-31/10/1996
Pätz et al. [2000]	TDLAS **Hantzsch**	continental background (Schauinsland, Germany) / SLOPE	1-3	22/05/1996
Volkamer et al. [2002]	**Hantzsch** **DOAS White system**	smog chamber (EUPHORE, Spain)	25-100	April 2002
Grossmann et al. [2003]	LP DOAS **Hantzsch**	rural (Pabstthum, Germany) / BERLIOZ	0-7	13/07-06/08/1998
Klemp et al. [2003]	**Hantzsch** TDLAS	urban (downwind of Augsburg, Germany) / EVA	0-4	02/03-31/03/1998
Kleffmann, pers. comm., 2004	**FTIR White system** **DOAS White system** **Hantzsch** **DNPH cartridges**	smog chamber (EUPHORE, Spain) / DIFUSO	< 0.1-100	May/June 2000
Hak et al. [2005] (this study)	**FTIR White system** **DOAS White system** **Hantzsch** (five) **C18-DNPH cartridges**	urban (Milan, Italy) / FORMAT	1.5-13 (30 min. avg.)	23/07-31/07/2002

In summary, during past intercomparison campaigns, the level of agreement varied from good to quite poor, with no obvious pattern being discernible. To effectively compare in-situ techniques with long path methods, one must keep in mind that spatial gradients of CH_2O may occur. Although this problem of probing different air volumes can be avoided by using multi-reflection systems (e.g. White system), only one such comparison study has been published to date (*Lawson et al.*, 1990; see above). The significant differences (± 25%) in that study were attributed to instrumental problems. The inconsistencies and uncertainties found in the studies

listed above, emphasised the need for an intercomparison of CH_2O measurement techniques involving exclusively in-situ techniques. The above overview further indicates that the FTIR method has been rarely used in the past for CH_2O measurements in ambient air.

An intercomparison of several commonly used techniques for the measurement of formaldehyde is presented in *Sec. 5.2*. The study was carried out to evaluate differences *between the various techniques* and *among similar instruments*. The assembly involved eight instruments working with four independent techniques, including two spectroscopic techniques – Differential Optical Absorption Spectroscopy (DOAS) (see *Sec. 3.1.1.6.3* for the particular instrument and *Sec. 3.1.1* for DOAS in general) and Fourier Transform Infra Red (FTIR) interferometry (see *Sec. 3.1.2*) –, Hantzsch fluorimetry (see *Sec. 3.1.3*) and DNPH cartridge sampling (see *Sec. 3.1.4*). Multi-pass systems were employed for the spectroscopic techniques to ensure probing of the same air volume by all instruments. In this intercomparison, the Hantzsch technique was represented by five similar Hantzsch instruments. The setup of the intercomparison experiment is described in *Sec. 4.2.3.1*. The results of this intercomparison are also published by *Hak et al.* [2005].

5.2 Intercomparison of CH_2O in-situ Measurement Techniques

5.2.1 Intercomparison of Ambient Measurements

After the campaign, the final formaldehyde data of the individual groups was openly collected and compared. The temporal resolution of the data ranged from two to five minutes for the optical instruments and the Hantzsch monitors (these methods will hence be referred to as 'continuous methods'), whereas the DNPH method required two hours for each sample. Due to the different measurement intervals of the various instruments, each of the continuous instruments' data sets was integrated and 30 min averages were calculated on a common time scale. When compared to the DNPH results, the data were integrated over two hours.

Figure 5.1 presents the formaldehyde mixing ratio time series as measured (*a*) by the Hantzsch instruments and (*b*) by the optical methods. Because large differences between DOAS and Hantzsch results were found previously (e.g. *Grossmann et al.* [2003]), (*c*) shows a direct comparison between DOAS and BUW Hantzsch results. This Hantzsch monitor was operating almost continuously. The time series of two-hour integrated values for each instrument is shown in (*d*), where the horizontal bars denote the CH_2O levels and the duration of the DNPH measurement periods.

Ambient mixing ratios between 1 and 13 ppbv (for the 30 min averages) were detected by all instruments and the temporal variation was generally in good agreement (see *Fig. 5.1*). However, the observations obtained from the IFU1 instrument are systematically higher than those from all other instruments until 28 July. After that date, IFU1 measured considerably lower concentrations than the other instruments. On 25 and 26 July, a diverging temporal behaviour of IFU2 was observed when compared to all other instruments (*Fig. 5.1a*). After 26 July, IFU2 levels are in good agreement with the other Hantzsch levels. The accordance between the Hantzsch monitors IFU3, PSI and BUW was notably good. However, a slight offset between the results of IFU3 and PSI compared to those of BUW is discernible. The overall agreement between the DOAS measurements and the BUW Hantzsch is good (*Fig. 5.1c*). Particularly large offsets between the two methods, as reported in previous comparisons (see overview in *Sec. 5.1*), were not detected. Occasionally occurring differences are likely due to local inhomogeneities caused by cars or lorries. For the six days of DNPH measurements during the intercomparison week, the rough temporal variation of the formaldehyde concentration during the day was well described by the two-hour integrated measurements (*Fig. 5.1d*). The observed

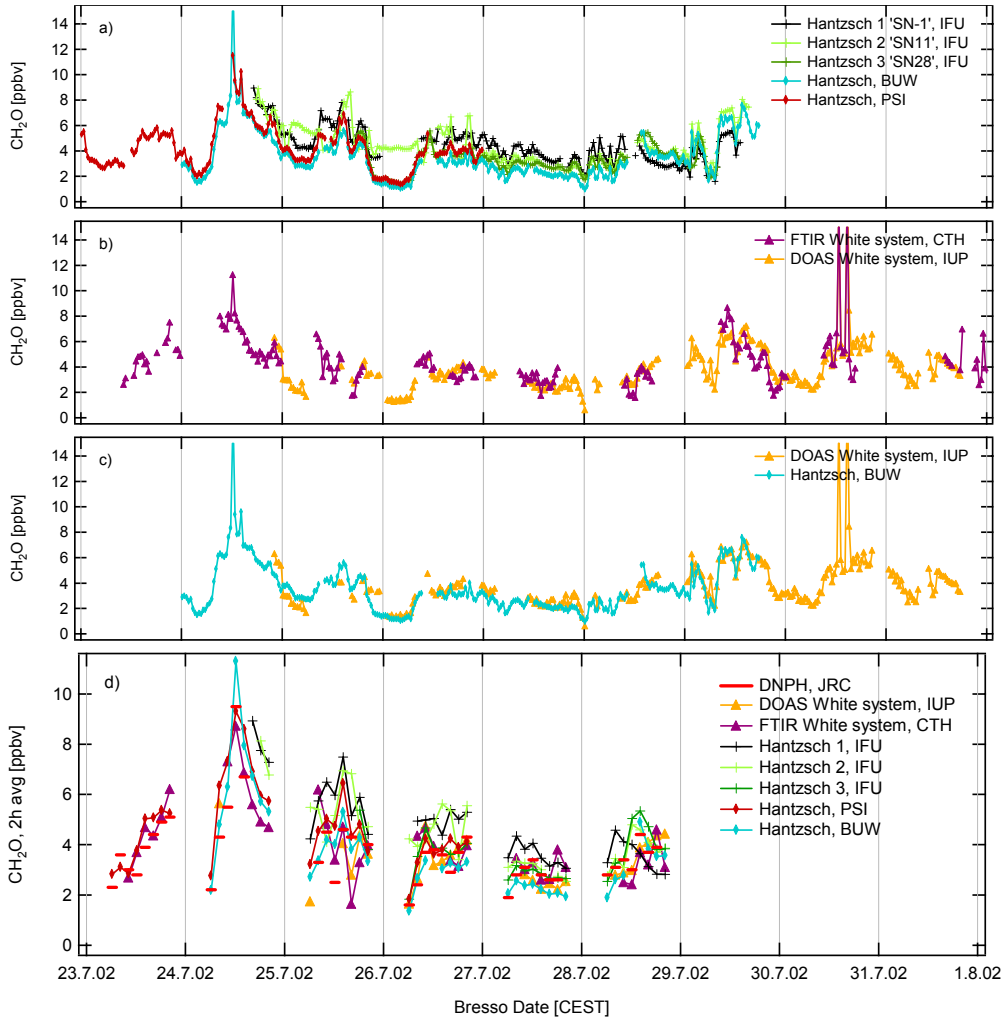

Figure 5.1: ***(a-c)*** *Formaldehyde time series as half hourly averages (ticks at 00:00 Central European Summer Time) at Bresso during the intercomparison week as measured* ***(a)*** *by the five Hantzsch monitors and* ***(b)*** *by the optical techniques FTIR and DOAS.* ***(c)*** *Direct comparison of the DOAS (yellow triangles) and BUW Hantzsch monitor (blue rhombs) results. Note that the two peaks occurring on 30 July can be attributed to a local lorry emission source initiated by the experimentalists. Those points were omitted for the intercomparison.* ***(d)*** *Formaldehyde measurements by the continuous instruments DOAS, FTIR and Hantzsch (as two hour averages) and DNPH (samples of two hours). The length of the horizontal lines corresponds to the duration of the DNPH measurement periods (figure from Hak et al. [2005]).*

concentration levels agree with those of most of the continuous instruments. The discrepancies mentioned for IFU1 and IFU2 are recognisable here as well.

During the intercomparison week, the formaldehyde mixing ratios were comparatively low for an urban site, varying between 1 and 6 ppbv most of the time. Typical CH_2O mixing ratios around 10 ppbv were reported for the LOOP/PIPAPO campaign 1998 at the same site in Bresso [e.g. *Alicke et al.*, 2002]. Five days of the present study exhibit a diurnal pattern with minimum values during night and higher levels during daytime, whereas three consecutive days feature no pronounced diurnal variation and CH_2O levels of around 4 ppbv. Two events of particularly high formaldehyde concentration occurred on 24 July and 30 July. The first event was caused by lorries usually stored in the hangar nearby. During this event, however, they were parked within 100 m of the measurement site with their engines running idle. This incident gave rise to

an experiment conducted on 30 July, when the lorries were placed close to the instruments with the diesel engines running. The rapid increase of CH_2O, CO and HONO within a few minutes indicates a distinct exhaust-gas plume and most probably an inhomogeneous formaldehyde distribution within the probed air mass. Thus, the time series used for the intercomparison do not contain the data points from these two incidents. In the evening of 29 July, a change in the sampling line setup was performed. The inlets of the Hantzsch instruments IFU1, BUW and IFU2 were mounted at different height levels to measure possible vertical differences in the formaldehyde distribution (see *Sec. 4.2.3*). Therefore, the Hantzsch instruments were no longer sampling identical air masses and these data points are not included in the intercomparison either.

The data for the ambient measurements was compared by pairing sets of data for all combinations of instruments for which simultaneous measurements were taken. Linear regressions were calculated for each pair of instruments in order to compare slopes, intercepts and correlation coefficients. Since both data sets in the regression are subject to error, an ordinary least squares regression is inappropriate. Because only the vertical distances of the data points to the regression line (only y direction) are minimised, the true slope of the regression line is underestimated [*Riggs et al.*, 1978]. Thus, the regressions were calculated using a method which is often called *orthogonal regression*. This method minimises the distance in both directions (both y and x direction). Individual errors of the data points are accounted for by a weighted line fit described in *Press et al.* [1992b]. Scatter plots for almost all pairs of continuous instruments are shown in *Fig. 5.2a-r*. The statistical data for all combinations are depicted in the plots and summarised in Table 5.2. After a modification in the instrument on 28 July, IFU1 measured lower values. The two time periods before and after this modification are considered separately in the following regression analysis and the markers for the second period are displayed as stars in *Fig. 5.2*. After a change in the system on 26 July, the agreement between IFU2 and the other instruments is good. Only the measurements taken after 26 July are considered reliable. Thus, the regression results of IFU2 shown in Table 5.2 exclude the first two days of operation.

5.2.1.1 Agreement Among the Hantzsch Instruments

Scatter plots for most combinations of Hantzsch results are shown in *Fig. 5.2a-i*. The Hantzsch measurements from PSI, BUW, IFU1 and IFU3 correlate very well. The correlation coefficients exceed $r = 0.9$ for most combinations (*Fig. 5.2a-g*, Table 5.2). The highest degree of correlation was found between the two Hantzsch instruments PSI and BUW with a correlation coefficient of $r = 0.99$ for the three days of simultaneous measurements. The slope of the regression line is near unity ($b = 1.04$), but there is a positive offset of 0.46 ppbv for PSI, significant at the 95% level. A similar result was found for IFU3 with a slope of $b = 0.98$ and an offset of 0.55 ppbv when compared to BUW. IFU3 and PSI agree with a high degree of correlation ($r = 0.98$). The linear regression reveals a slope not significantly different from unity and no offset. However, IFU1 measured systematically higher values for the first period, when compared to IFU3, PSI and BUW, which is evident in the slopes of the regression lines: They are significantly steeper than one and show non-zero intercepts. For the second period, IFU1 measured distinctly lower concentrations than all other instruments. This becomes apparent by the second regression line.

The correlation and regression analysis including IFU2 results shows little agreement with correlation coefficients between 0.45 and 0.75 if one considers the complete IFU2 data set (grey markers in *Fig. 5.2*). The data points are highly scattered around the regression lines (not all figures shown here). The scattering for IFU2 can partly be attributed to the diverging results as a consequence of malfunction of the system on 25 and 26 July (*Fig. 5.1a*). If one considers only the reliable IFU2 data points after 26 July, there are no mutual points with PSI, but the comparison with BUW yields $r = 0.97$, $b = 0.95$, $a = 0.81$ (*Fig. 5.2d*). IFU1 and IFU2 results agreed

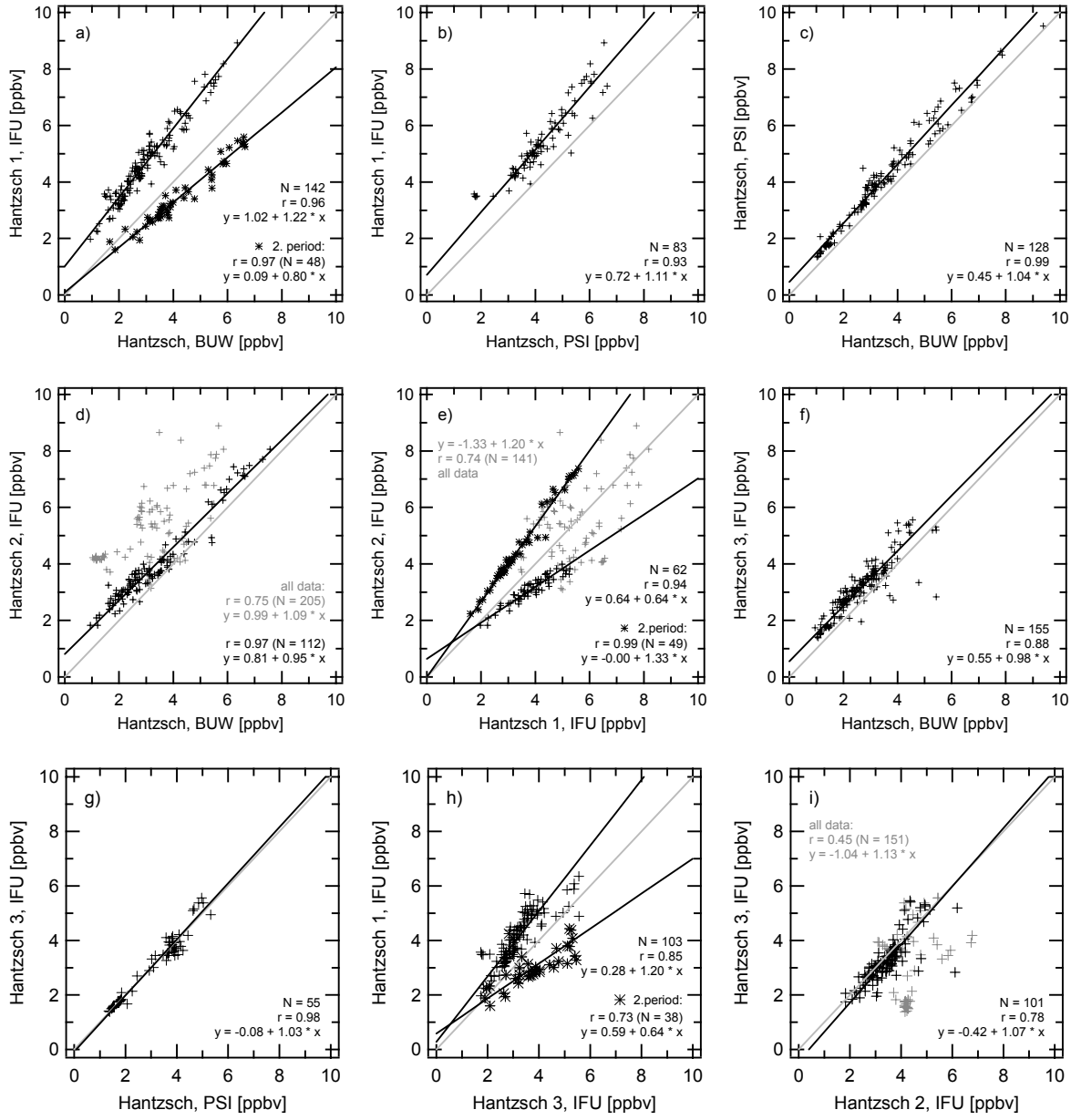

Figure 5.2: ***(a)-(r)*** *Scatter plots for most pairs of the seven continuously measuring instruments taking part in the intercomparison. The CH_2O mixing ratios are plotted versus one another for matched times of measurements and linear regressions were calculated. The solid lines drawn through the data correspond to the weighted orthogonal least squares fit [York, 1966] to the data (black) and the one to one correspondence line (grey), respectively. For the two periods of IFU1 measurements (before and after 28 July 12:00 CEST) individual regressions were calculated. Additional grey markers indicate questionable IFU2 data points before 26 July. Regression parameters for the overall data sets and subsets are given in the plots (figure from Hak et al. [2005]).*

considerably better after 26 July ($r = 0.94$) than for the entire data set, but with a slope of only $b = 0.64$ ($a = 0.64$), which to some degree matches the previously observed positive bias of IFU1. Possible reasons for the disagreement among these five nearly identical instruments are discussed in *Sec. 5.2.3*.

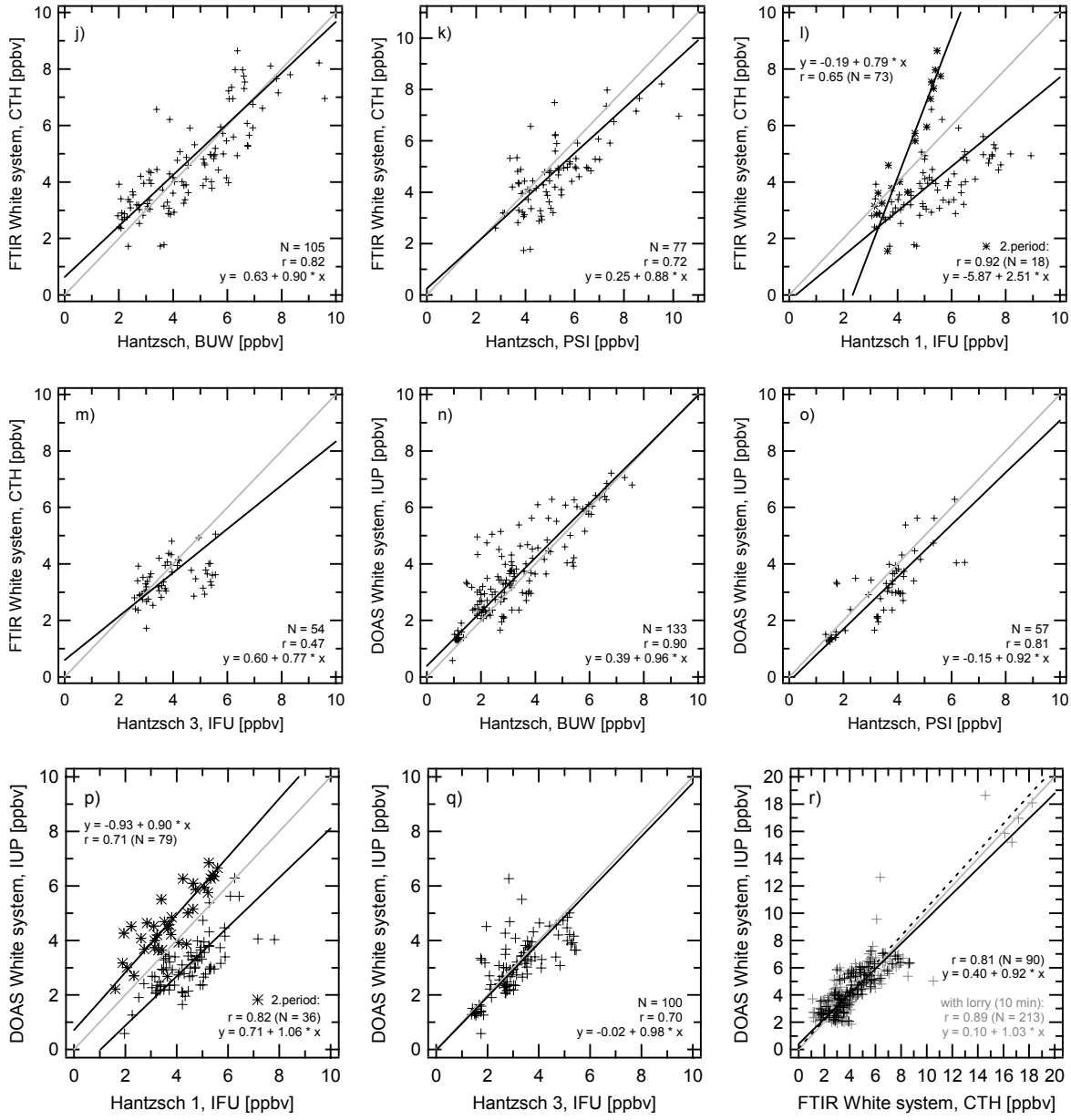

Figure 5.2 (continued)

5.2.1.2 Agreement Between Spectroscopic and Hantzsch Techniques

Comparisons between the results from the spectroscopic techniques (DOAS, FTIR) and Hantzsch data are shown in *Fig. 5.2j-q*.

The FTIR measurements compare quite well with the BUW Hantzsch data (*Fig. 5.2j*), with a slope close to unity ($b = 0.90$, $a = 0.63$). Similarly, a regression line with no significant deviation from the one-to-one line was found for FTIR versus PSI. As a smaller number of data points was available, the degree of correlation is somewhat lower (*Fig. 5.2k*). The correlation coefficient between FTIR and IFU1 data for the time span until 28 July is lower ($r = 0.65$). There is a significant deviation from the 1:1 line ($b = 0.79$), with IFU1 showing the larger values. After 28 July IFU1 measures significantly lower concentrations than the FTIR (*Fig. 5.2l*). A good agreement was found between FTIR and IFU2 (values after 26 July) with a slope of $b = 0.97$ ($r = 0.90$), whereas the employment of the complete data set shows strong scattering. No coherence is recognisable between FTIR and IFU3 (*Fig. 5.2m*), where only 54 mutual data points are available. The observed concentration range is very small here.

Table 5.2: Results of the orthogonal regression analysis [York, 1966] between the continuous instruments (see also Fig. 5.2). $[CH_2O]_y = a + b\,[CH_2O]_x$, where y and x are the corresponding instruments and a and b are the intercept and slope of the regression line, respectively, with 95% confidence intervals. N is the number of data points included in the regression and r is Pearson's correlation coefficient. The first column indicates the corresponding plot in Fig. 5.2 (for some regressions no plot is shown).

Fig.	y	x	a [ppbv]	b	r	N
a)	IFU1 [a]	BUW	1.02 ± 0.17	1.22 ± 0.05	0.96	142
b)	IFU1	PSI	0.72 ± 0.40	1.11 ± 0.09	0.93	83
c)	PSI	BUW	0.46 ± 0.12	1.04 ± 0.03	0.99	128
d)	IFU2 [a]	BUW	0.81 ± 0.15	0.95 ± 0.04	0.97	112
-)	IFU2	PSI	1.49 ± 0.65	0.96 ± 0.16	0.58	100
e)	IFU2 [a]	IFU1	0.64 ± 0.22	0.64 ± 0.06	0.94	62
f)	IFU3	BUW	0.55 ± 0.21	0.98 ± 0.07	0.88	155
g)	IFU3	PSI	–0.08 ± 0.21	1.03 ± 0.06	0.98	55
h)	IFU1 [a]	IFU3	0.28 ± 0.39	1.20 ± 0.12	0.85	103
i)	IFU3	IFU2 [a]	–0.42 ± 0.47	1.07 ± 0.13	0.78	101
j)	FTIR	BUW	0.63 ± 0.40	0.90 ± 0.09	0.82	105
k)	FTIR	PSI	0.25 ± 0.74	0.88 ± 0.14	0.72	77
l)	FTIR	IFU1 [a]	–0.19 ± 0.73	0.79 ± 0.14	0.64	73
-)	FTIR	IFU2 [a]	–0.22 ± 0.71	0.97 ± 0.15	0.90	35
m)	FTIR	IFU3	0.60 ± 0.62	0.77 ± 0.16	0.47	54
n)	DOAS	BUW	0.39 ± 0.27	0.96 ± 0.08	0.90	132
o)	DOAS	PSI	–0.15 ± 0.56	0.92 ± 0.15	0.81	57
p)	DOAS	IFU1 [a]	–0.93 ± 0.84	0.90 ± 0.18	0.71	79
-)	DOAS	IFU2 [a]	–0.07 ± 0.49	0.93 ± 0.11	0.93	69
q)	DOAS	IFU3	–0.02 ± 0.48	0.98 ± 0.15	0.70	100
r)	DOAS	FTIR	0.40 ± 0.39	0.92 ± 0.09	0.81	90

a. Note that, for reasons stated in the text, the regression results given for the IFU2 instrument were calculated omitting the data of 25 and 26 July and the regression results for IFU1 exclude data after 28 July, 09:15 CEST.

A large amount of mutual data points was obtained for the pair DOAS and BUW (*Fig. 5.2n*), where a good correlation ($r = 0.90$) is found. The slope of the regression line is not significantly different from unity ($b = 0.96$). There was also fairly good agreement between DOAS and PSI ($r = 0.81$, $b = 0.92$). The 1:1 line is enclosed within the 95% confidence interval of the regression slope and there is no significant offset (*Fig. 5.2o*). IFU1 first measured considerably higher values than the DOAS ($b = 0.90$, $a = -0.93$). The result for the second period is shown by the second regression line in *Fig. 5.2p*. For values after 26 July, the agreement between DOAS and IFU2 is good ($r = 0.93$, $b = 0.93$, no significant offset). However, including the complete IFU2 data set reveals less agreement. The regression between DOAS and IFU3 displays a slope not significantly different from unity and no significant offset (*Fig. 5.2q*).

5.2.1.3 Agreement Among Spectroscopic Techniques

The FTIR measured predominantly during daylight hours, whereas the DOAS system was generally also operated at night (see time series in *Fig. 5.1b*). Altogether, there are 90 mutual points between the two White systems (30 min averages) during the intercomparison week. The correlation is fairly good with $r = 0.81$ (*Fig. 5.2r*). At the 95% confidence level the regression slope ($b = 0.92$) is not significantly different from unity.

Both instruments detect the average concentrations along the respective folded light paths. During the intensive lorry experiment, the lorries were located upwind of the air volume surveyed by both White systems. A comparison was performed using 10 minute averages, due to the temporal limitation of the experiment to two events of 30 minutes each. Maximum values around 19 ppbv (10 minute average) were measured by both instruments during the lorry experiment and a correlation of $r = 0.89$ and a slope of $b = 1.03$ were found, thus nearly yielding a one-to-one correspondence. The dashed line in *Fig. 5.2r* is the regression line to the ten minute data including the lorry experiment (grey markers).

5.2.1.4 Agreement Between Continuous Instruments and DNPH

The DNPH samples were taken every two hours during daytime. Therefore, two-hour averages of the continuous instruments were compared to the integrated results obtained from the cartridges. As mentioned before, the data containing the lorry plumes was omitted in the calculations. The results are presented in scatter plots in *Fig. 5.3a-f*. The statistical parameters are summarised in Table 5.3. For all cases, the regression slopes are below unity, however for IFU2, IFU3 and DOAS unity is included within the 95% confidence interval. The regression analysis for DNPH versus Hantzsch BUW and PSI revealed slopes of $b = 0.76$ and correlation coefficients of around $r = 0.90$. The instruments IFU1, IFU2, IFU3 attained correlation coefficients of $r = 0.40, 0.59, 0.74$ (note the different measurement intervals; IFU2 values after 26 July) with systematically higher values for IFU1 than for the DNPH. The slopes of IFU1, IFU2, IFU3 are $b = 0.64, 0.97, 0.83$. Plotting the DNPH data versus the FTIR data also reveals a regression slope lower than unity ($b = 0.74$) and an intercept not significantly different from zero (correlation coefficient $r = 0.66$).

The mixing ratios measured by DNPH, Hantzsch, DOAS and FTIR techniques correspond moderately well to each other on the two hour time scale. However, short term variations cannot be resolved. In summary, the DNPH results are slightly lower than those measured by the continuous instruments for up to 30 common data points in the concentration range from 1 to 8 ppbv.

Table 5.3: Linear orthogonal regressions [York, 1966] for the correlations between DNPH and the continuous methods (see also Fig. 5.3). The definition of parameters is specified in Table 5.2.

Fig.	y	x	a [ppbv]	b	r	N
a)	DNPH	BUW	0.92 ± 0.45	0.76 ± 0.12	0.90	30
b)	DNPH	PSI	0.37 ± 0.75	0.76 ± 0.16	0.86	26
c)	DNPH	FTIR	0.76 ± 0.87	0.74 ± 0.20	0.66	31
d)	DNPH	IFU1	0.51 ± 1.08	0.64 ± 0.23	0.40	27
-)	DNPH	IFU2 [a]	–0.23 ± 1.71	0.97 ± 0.48	0.59	13
e)	DNPH	IFU3	0.28 ± 0.88	0.83 ± 0.24	0.74	23
f)	DNPH	DOAS	0.77 ± 0.81	0.80 ± 0.23	0.75	23

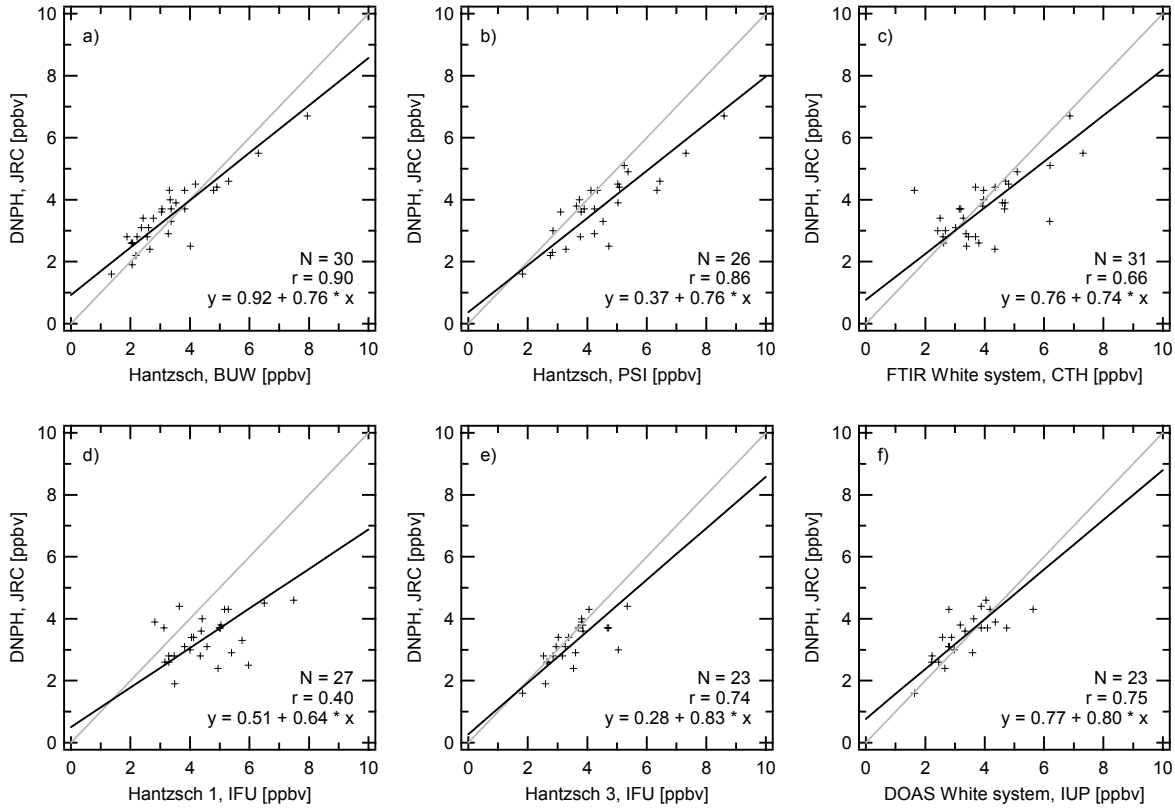

Figure 5.3: Regressions of the DNPH cartridge results from the intercomparison week plotted versus those from continuous techniques for concordant two hour time spans. The solid black line drawn through the data is the orthogonal least squares fit to the data [York, 1966]. The grey line represents the one-to-one correspondence (figure from Hak et al. [2005]).

5.2.2 Fractional Differences

The agreement between measurements of the continuous instruments and a reference instrument is summarised in histograms of the fractional differences δ (see eq. 5.1 for definition).

$$\delta = ([CH_2O]_{instr} - [CH_2O]_{ref})/[CH_2O]_{ref} \qquad \text{(eq. 5.1)}$$

For the comparison among the continuous instruments, the BUW Hantzsch was chosen as the reference because it was almost continuously operating over the entire intercomparison period. The results are depicted in *Fig. 5.4a* for the overall data sets. *Figure 5.4b* illustrates the resulting fractional differences for the two-hour integrated measurements of all instruments, using the DNPH data as reference.

The plots show the histograms of the data (shaded bars) and fitted Gaussian functions (black curve). The respective statistical information is given in the legend of each plot. The fact that the average, median and mode (i.e., the most probable fractional difference) of the PSI, IFU1 and IFU3 distributions are similarly positioned, suggests symmetry in the distributions and therefore mostly random differences. The PSI histogram has a narrow distribution with a standard deviation of σ = 0.12. The DOAS, FTIR, IFU1, IFU2 and IFU3 histograms show σ of 0.27, 0.27, 0.21, 0.66 and 0.18, respectively. The IFU2 histogram has a slightly skew distribution which is due to the erroneous results from 25 and 26 July. After eliminating those outliers, the IFU2 histogram shows an almost symmetrical δ-distribution. In this case, the average, median and mode are nearly collocated (average = 0.23, median = 0.19, mode = 0.21) and the standard deviation is decreased to 0.24. The distributions for the spectroscopic techniques DOAS and

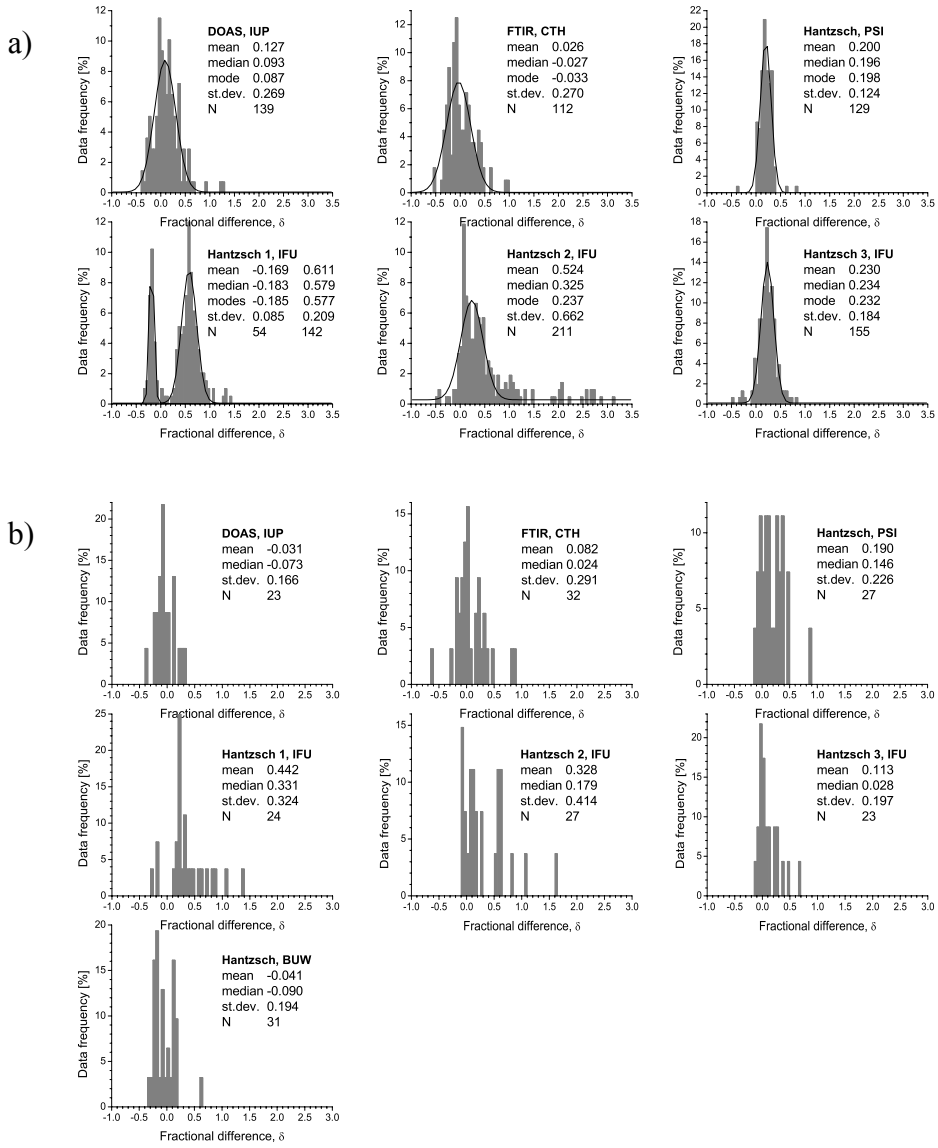

*Figure 5.4: Fractional difference histograms for each of the formaldehyde instruments calculated relative to a reference instrument. For the comparison of **(a)** the continuously measuring techniques, the reference instrument is the BUW Hantzsch monitor. In plot **(b)** the reference instrument is the DNPH sampler. Each panel shows the frequency for the data falling into 0.05 fractional difference bins (normalised to the number of coincident data pairs). The legends show the statistics for the complete data sets (figure from Hak et al. [2005]).*

FTIR are wider than those for most of the Hantzsch instruments. Most instruments show a positive bias with respect to the reference BUW Hantzsch instrument (Table 5.4, upper row). The relative difference between the DOAS and the BUW Hantzsch is + 9%. On average, 3% lower values were found for the FTIR than for the BUW. The PSI, IFU1, IFU2 and IFU3 values were approximately 20, 58, 21 and 23% higher than the BUW results, respectively. After the instrumental modification of IFU1, the results were 19% smaller than those from BUW. In order to verify the relative differences between the results of the seven instruments, fractional differences were also calculated using DOAS as a reference (Table 5.4, lower row). The previous result was confirmed, with the Hantzsch measurements (except IFU1) being within the ± 11% range of the DOAS. DOAS and FTIR agree within 5%. This is also consistent with the

Table 5.4: Relative differences of the measurement results determined with reference to the BUW Hantzsch (see also Fig. 5.4a) and to DOAS, respectively.

	DOAS	FTIR	PSI	IFU1	IFU2	IFU3	BUW
Relative to BUW Hantzsch	+8.8%	−3.3%	+19.8%	+57.7% −18.5%	+21.0%	+23.2%	--
Relative to DOAS White system	--	−5.1%	+11.1%	+41.3% −19.2%	+10.6%	+7.2%	−10.3%

uncertainty of the used cross-sections (see *Sec. 3.1.1.8.1*). The relative deviations obtained with the fractional differences are in line with the uncertainties expected from Table 5.2.

As the sample size is small for the fractional differences relative to DNPH (N = 23-31, see Table 5.3), it was refrained from fitting Gaussians to the histograms in *Fig. 5.4b*. The distributions for DOAS, FTIR, PSI and IFU3 are almost symmetrical. The histogram for IFU2 is less symmetrical because of several higher fractional differences caused by the instrumental problems during the first days of the intercomparison measurements. If these days are omitted, only two days of common data points are remaining. The data sets of DOAS, FTIR, PSI, IFU3 and BUW agreed with the DNPH results within ~ 15%. For IFU1 and IFU2, the differences were larger. Mean and median coincide only in a few cases. Due to the small sample sizes of only 20-30 data points, the statistical information should be regarded carefully in this part of the study.

5.2.3 Comparison of Hantzsch Calibration Standards

Although the three groups working with the Hantzsch technique used instruments basically identical in construction (see *Sec. 3.1.3*), differences among their results were found (see *Sec. 5.2.1.1*) which were significant on the 95% level. Therefore, also the standard solutions, that is, formaldehyde solutions with a known concentration, required for the calibration of the Hantzsch instruments, were compared to each other. These solutions are produced by diluting a commercially available 37% CH_2O-solution to a stock-solution of about 10^{-1} to 10^{-2} mol l^{-1}, which is titrated regularly and is then further diluted to about 10^{-6} mol l^{-1} for calibration (see also Aero-Laser AL4001 HCHO analyser manual).

Formaldehyde solutions with high concentrations contain a significant fraction of para-formaldehyde which interferes with the titration. Although the para-formaldehyde concentration is negligible in diluted solutions, a waiting time of at least 24 h between dilution and titration is recommended to ensure the conversion of all para-formaldehyde. The IFU 0.01 mol l^{-1} and PSI 0.05 mol l^{-1} diluted (working) standards were shown to be stable over several years with less than 0.2 percent deviation over one year. The field standards were taken from these working standards, stored in cooled boxes and further diluted to concentrations of ~10^{-6} mol l^{-1} in the field for calibration. At this level of dilution, the solution is no longer stable for more than one hour, even when stored in a refrigerator.

The liquid formaldehyde standards, which were used by IFU, PSI and BUW for the calibration of their Hantzsch instruments, were independently prepared by each group. At the beginning of the campaign (on 24 July), the standard solutions (levels about 10^{-6} mol l^{-1}) of the three groups were compared using one of the IFU instruments (SN28, in this study called 'IFU3'). Each group prepared a solution of ~10^{-6} mol l^{-1} from the individual standards. The standards by BUW and PSI agreed within 5% (PSI/BUW = 1.05). However, the results indicated a ~ + 30% deviation of the calibration standards of IFU when compared to the other groups. A 6% difference between the standard solutions of BUW and PSI was found on the same day using the PSI instrument (PSI/BUW = 1.06).

After the first discrepancies were observed in the data, the working standards of IFU and PSI were again analysed in the PSI- and IFU-laboratories. The analyses again yielded a 30% higher concentration for the IFU standard than for the PSI standard, although both stated to be 1.0×10^{-2} molar according to the original titrations. Hence, there was a 30% difference between the titration methods used by IFU and PSI, even though both from dilution and titration they were expected to agree within a few percent.

The difference of 30% between the IFU standard and the calibration standards of other groups was obtained repeatedly. It could explain the found disagreement between IFU instruments and the BUW instrument, IFU2 and IFU3 values being 23% higher than BUW data. About 6% of the discrepancy between PSI and BUW can be explained by the different standards. The remaining 10-15% difference is undetermined. The IFU1 instrument deviates significantly from the results of the majority of the Hantzsch instruments. A new, larger internal zero trap was installed in this instrument after the first week of the intercomparison following an instrument malfunction (flooding of the zero trap). The quality of the zero baseline is critical in this technique and the differences of this instrument when compared to the other ones are most probably due to zero baseline problems.

Another process carried out differently by the three groups was the preparation of the Hantzsch solution. The used recipes differ in the concentrations of the chemicals (see overview in Table 5.5) and minor differences exist in the production technique of the solution, i.e. if the solution was degassed, whether acetylacetone was distilled, etc.

Table 5.5: Recipes for the ingredients of the Hantzsch solution as used by the three groups.

Ingredients	Kelly and Fortune	IFU (Aero-Laser)	PSI
Ammonium acetate	462 g l^{-1}	154 g l^{-1}	154 g l^{-1}
Acetic acid	10 ml l^{-1}	5 ml l^{-1}	5 ml l^{-1}
Acetylacetone	1 ml l^{-1}	4 ml l^{-1}	4 ml l^{-1}

PSI and IFU used a modified recipe for the Hantzsch solution, compared to the original recipe from *Kelly and Fortune* [1994] used by BUW (less ammonium acetate but more acetylacetone). Aero-Laser now recommends the new recipe for the measurement of formaldehyde mixing ratios up to 30 ppbv.

5.2.4 Summary and Conclusions

An intercomparison of most in-situ measurement techniques currently used for the detection of atmospheric formaldehyde, including the Hantzsch technique, FTIR, DOAS and a DNPH-sampler, was presented. Five Hantzsch instruments of nearly identical design, operated by three laboratories, sampled from a common inlet line. The use of White-type multi-reflection systems for the spectroscopic DOAS and FTIR techniques ensured probing of nearly the same air volume by all eight instruments. The measurement conditions and equipment used during this and previous comparison studies are summarised in Table 5.1.

CH_2O mixing ratios varied between 1 and 13 ppbv. The Hantzsch results showed a rather large variation. After elimination of some apparently unreliable measurement sequences of two instruments, the results varied within ± 11% among each other, except for one instrument, which systematically gave much higher values. The agreement of the two optical methods was within 5%, which is within the uncertainties of the UV and IR absorption cross-sections (both 5%). Hantzsch and spectroscopic techniques agreed within 15%. DNPH measurements were generally lower than those from the continuous techniques by up to 25%. The observed

discrepancies among the Hantzsch instruments can partly be attributed to the different calibration standards used by the different groups. The apparent differences in the titration methods for the 10^{-2} molar standard solution could not be solved finally within this project and could account for absolute differences of about 30%. The Hantzsch instruments BUW and PSI show an excellent correlation but an offset of 20% in the results. The reason for this could not be ascertained. Such an effect could occur when the zeroing is insufficient due to a malfunctioning formaldehyde scrubber or too short a zeroing time. The found differences in magnitude of the compared UV absorption cross-sections (see *Sec. 3.1.1.8.1*) imply possible differences of up to 11% in the concentrations determined by DOAS, depending on the employed cross-section. However, later studies confirm that the used CH_2O cross-section by *Meller and Moortgat* [2000] is the most accurate highly resolved UV cross-section available today. The deviation between IR spectra is within only a few percent and a comparison of UV and IR spectra by *Gratien et al.* [2006] showed very good agreement between the *Meller and Moortgat* [2000] UV spectrum and the IR cross-sections.

It is usually difficult to compare DOAS or FTIR long path measurements with point measurements since the probed air masses often differ from one another. In urban areas, differences in the CH_2O contents of air masses are mainly caused by primary emissions on a local scale and fast secondary formation as a consequence of the oxidation of anthropogenically emitted VOCs. In rural areas, especially close to forests, secondary formation, due to the oxidation of biogenically emitted VOCs, plays an important role. The measurement setup used during this intercomparison, sampling a uniform air mass by the folding of the light beams in the White systems, was therefore most favourable to measure under homogeneous conditions with the employed techniques.

The Hantzsch results agree generally well with the results of the spectroscopic techniques. With three independent techniques (DOAS, FTIR and Hantzsch) applying completely different ways of determining the formaldehyde concentration, results within 15% were obtained. Significant differences in mixing ratios obtained by Hantzsch monitors and the DOAS technique, as observed previously (e.g. BERLIOZ campaign, see *Grossmann et al.* [2003]), could not be detected in this study. No systematic difference between DOAS and Hantzsch was found under the conditions present during the intercomparison measurements. It is assumed that the improvement is due to the employment of multi-reflection setups in the spectroscopic techniques which ensured that all instruments sampled essentially the same air volume.

Previously reported differences between DOAS and Hantzsch techniques seem to be larger than the actual uncertainties in CH_2O measurements as characterised in this study and thus may have been caused by spatial (vertical) gradients of CH_2O concentrations. The differences in the formaldehyde concentrations by probing different air volumes are examined in the following section (see *Sec. 5.3*).

5.3 Comparison of Long Path and in-situ Measurements

Since path-integrated measurements smooth out possible influences from local sources near the sampling site, they are generally considered representative for the average trace gas concentrations in a larger patch and therefore as better suited, e.g. for comparison with model results, than in-situ measurements, which might be strongly influenced by nearby local sources. During several field campaigns in the past, significant differences were found between formaldehyde results by in-situ techniques and spatially averaged concentrations by long path DOAS [e.g. *Cárdenas et al.*, 2000; *Grossmann et al.*, 2003, see *Sec. 5.1*]. During periods of high photochemical activity, the concentrations measured by long path DOAS were often considerably larger than concentrations obtained from in-situ instruments (e.g. BERLIOZ 1998 [*Grossmann*

et al., 2003]). Up to now, no final explanation has been presented for the discrepancies. As it was one of the main objectives of the FORMAT project to gain a better understanding of the disagreement between different formaldehyde measurement techniques, the differences between long path averaged and Hantzsch in-situ measurements are further investigated here.

Potential systematic differences between DOAS and Hantzsch techniques, considering the measurement of formaldehyde, have been addressed in the previous section. As it was a prerequisite of the intercomparison study in *Sec. 5.2* to sample identical air volumes, the comparability of the measurements was ensured and the differences were reduced to the actual uncertainties between both methods, which amounted to ± 15%. Larger concentration differences as found at Alzate (see *Sec. 5.3.1*) are therefore not explained by the use of different measurement techniques but must be a consequence of the different measurement setups probing different air volumes. These possible spatial differences in CH_2O concentrations are studied in *Sec. 5.3.3* for daytime and in *Sec. 5.3.4* for nighttime conditions. Before, the existence of a spatial gradient at night is shown in *Sec. 5.3.2* for ozone.

5.3.1 Long Path DOAS Versus in-situ Results

At Alzate, measurements of formaldehyde, ozone and nitrogen dioxide were made in parallel by the path-integrating LP DOAS and by in-situ monitors (see *Sec. 4.2.2*). The long path DOAS and in-situ instruments probed different average height levels. The inlets of the in-situ monitors were installed at two metres above ground level. In contrast, the DOAS light beam traversed a layer between 1 and 40 m above local ground and passed on average 30 m above the surface (see also *Fig. 6.5*). Thus, the long path DOAS measured the average concentration in an altitude range of several tens metres above ground whereas the in-situ instruments sample close to the ground, where processes like deposition become important under stable conditions. To assess the stability conditions in the surface layer, also radon activity was measured. The inlet of the radon monitor was mounted about 1.5 m above ground level (see *Sec. 4.2.2.1*).

Half hour averages of formaldehyde, ozone and nitrogen dioxide mixing ratios measured by long path DOAS are plotted in *Fig. 5.5* versus the in-situ measurement results. Since the dynamical and chemical processes that influence the trace gas distributions are governed by solar radiation, two time periods are distinguished. The daylight time between sunrise and sunset (middle row of *Fig. 5.5*) is characterised by southerly flow, a usually well-mixed boundary layer and a multitude of photochemical reactions. During nighttime (lower row of *Fig. 5.5*), a smaller number of chemical reactions takes place. In clear nights, inversion layers form, which reduce mixing and dry deposition becomes important. Separating daytime and nighttime measurements reveals differences in formaldehyde concentrations both during day and during night and in ozone concentrations during night.

Comparable to previous measurements, the long path DOAS measured higher formaldehyde concentrations than the Hantzsch monitor during FORMAT I, both during daytime and during nighttime (left column of *Fig. 5.5*). One important point of uncertainty of the DOAS results (see *Sec. 3.1.1.8.1*) can be excluded from the start, since for all DOAS measurements presented in this thesis and the measurements mentioned above (i.e. BERLIOZ [*Alicke*, 2000], LOOP [*Alicke*, 2000]), the same CH_2O absorption cross-section (by *Meller and Moortgat* [2000]) was used. Under daylight conditions, the differences are largest for high formaldehyde concentrations, as apparent from the slightly non-linear relationship. Distinct differences are also found during the night with a near-linear deviation of long path results from in-situ results. Ozone concentrations (middle column of *Fig. 5.5*) measured along the light path agree very well with the in-situ results during the day. The daytime scatter plot in *Fig. 5.5* features a strong correlation with $r = 0.97$. The orthogonal regression yields a slope of 0.99 and intercept of 5.2 ppbv. The nighttime DOAS measurements, however, show a distinct offset compared to the in-situ results,

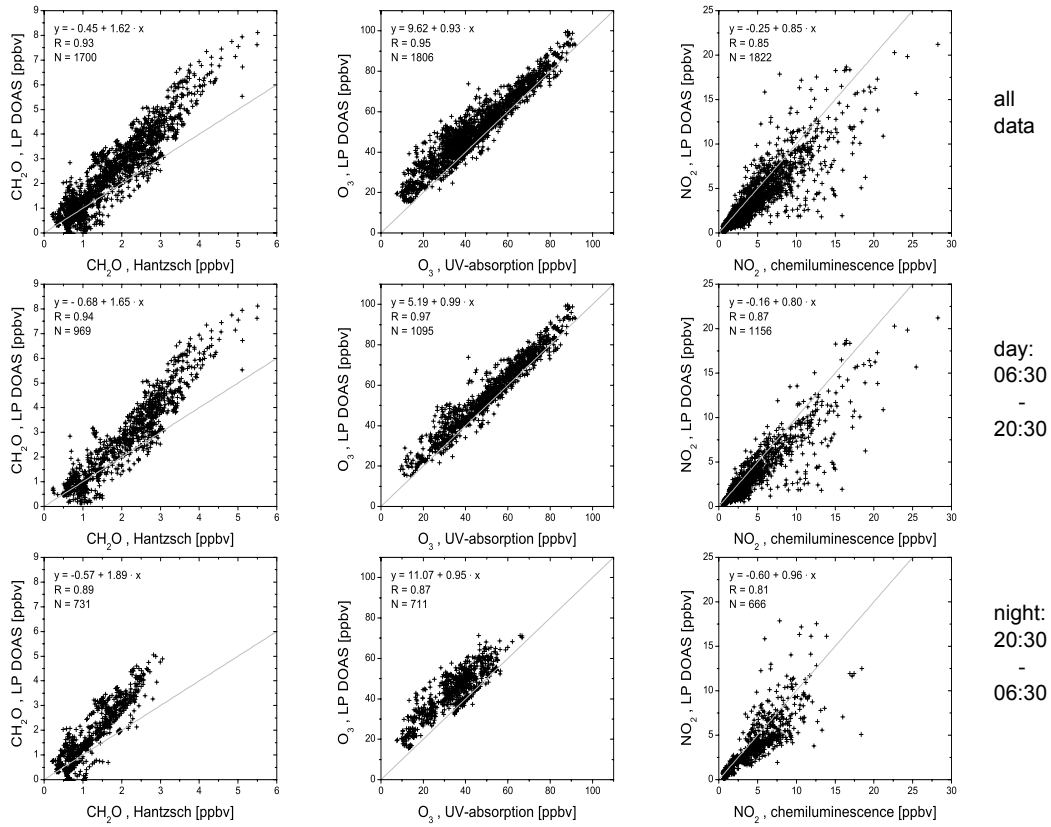

Figure 5.5: Scatter plots of path-integrated DOAS measurements versus in-situ measurements for formaldehyde, ozone and nitrogen dioxide (shown in the columns from left to right). The rows (upper to lower row) display the complete data set, daytime data between 6:30 and 20:30 h and night time data between 20:30 and 6:30 h. Orthogonal regression results are included in the plots.

with higher concentrations measured along the light beam than by the in-situ instrument. The NO_2 measurements with the long path DOAS and the chemiluminescence monitor are in reasonably good agreement (right column of *Fig. 5.5*). The in-situ instrument generally measured higher concentrations, especially at night. These observations are suggestive that at night the vertical structure in the boundary layer plays a significant role so that nitrogen dioxide accumulates in a layer close to the ground. It must also be considered that local direct sources might be present. The NO_2 difference is weakly linked to the direction of the windflow. The largest discrepancies were found for easterly flow, the lowest for westerly flow.

To interpret the observations, the uncertainties between the measurement methods and possible interferences have to be known. The ozone measurement of the DOAS and of the in-situ instrument is based on the absorption of ozone molecules in the UV wavelength range. In consideration of the good agreement of the results of both techniques during the day, interferences regarding the ozone measurements, which are only effective at night, are not assumed likely.

In the intercomparison of in-situ formaldehyde measurements in *Sec. 5.2* no systematic differences between DOAS and Hantzsch measurements were found. The study revealed uncertainties in the range of 10-15% between both methods. These uncertainties do not explain the differences of up to a factor of two which were found in Alzate at night. Since instrumental differences have been addressed and no systematic differences between DOAS and in-situ methods were found, the concentration differences found can be circumscribed to the different air volumes probed.

A considerable fraction of the difference between long path and in-situ measurements is attributed to spatial inhomogeneities. The comparison of these measurements thus provides insight into the local meteorological dynamics and chemistry. In the following sections we explain the differences in formaldehyde and ozone concentration results that can occur on small spatial scales due to the utilisation of different measurement setups. The focus of this work is on formaldehyde, however, since the ozone data help determining the mixing conditions, first an explanation is given for the ozone differences at night (*Sec. 5.3.2*). For the differences between path-integrated and in-situ CH_2O measurements two different mechanisms are assumed to be responsible. The daytime mechanism (*Sec. 5.3.3*) is attributed to be of chemical origin, whereas the nighttime mechanism (*Sec. 5.3.4*) is a result of suppressed mixing and deposition.

5.3.2 Nighttime Vertical Ozone Gradient

As shown in *Fig. 5.5*, path-integrated and point measurements of ozone at Alzate are very similar during daytime. This also arises from *Fig. 5.6* which includes both ozone concentration time series, measured during a fair weather week with stable weather conditions at the end of the FORMAT I campaign. The difference in the measurement geometries, observing different air volumes, does not seem to have an effect on the concentrations measured during the day. This argues for a sufficiently well-mixed boundary layer and a homogeneous distribution of ozone in the observed air volume. Such a smooth distribution is expected for a secondary pollutant of relatively long photochemical lifetime like ozone. The good agreement of in-situ and long path measurements with only a low offset further argues for a high level of accuracy of both methods. Both measurements agree well within the 1 σ uncertainties of ± 2 ppbv for the in-situ instrument and ± 3 ppbv for the DOAS.

There are discrepancies at nighttime when the DOAS measures significantly higher * ozone concentrations than the ozone monitor, which probes an air volume closer to the ground (see *Fig. 5.6a*). These differences are assumed to be of dynamical origin. In this section, we shortly describe the processes at night that are supposed to lead to vertically different ozone levels.

A drop in ozone concentrations is observed in both height levels between 19 and 20 h and can be ascribed to the titration reaction with NO (R 2.13), which has an evening traffic peak at 19 h and very low concentrations during the rest of the night (*Fig. 5.6b*). After 20 h, the ozone concentration close to the ground continues dropping until 20:30 h, whereas the drop in path-integrated ozone ends. This coincides with the sunset which occurs around 20:30 h, but in the hilly terrain actually some minutes earlier, and comes along with the shift of wind direction from southerly to northerly wind, which takes place between 20:15 h and 20:30 h. With the setting of the sun, vertical mixing ceases and, especially close to the ground, ozone concentrations diminish. A gradient of the order of 10 ppbv between surface (2 m) and 30 m above ground arises in stable layered nights and is maintained until mixing starts in the next morning (see *Fig. 5.6*). Due to the strongly reduced vertical mixing at night, only a shallow layer of a few metres is affected by efficient ozone loss. This explains the difference between the ozone concentrations at 2 and 30 m above the ground.

In both data sets, a decreasing tendency of ozone concentrations is discernible throughout the night (see *Fig. 5.6*). With the exception of the night 18-19 August, a nearly linear decrease of 1.6 ppbv h^{-1} could be approximated from the DOAS measurements. Generally, this rate of decrease also applies for the concentrations measured close to the ground, resulting in a loss of

*. In the night of 13-14 August, both systems measure the same ozone levels. This is attributed to the strong mixing due to enhanced wind speeds under the influence of the north foehn. There is also a distinct collapse in relative humidity during that night.

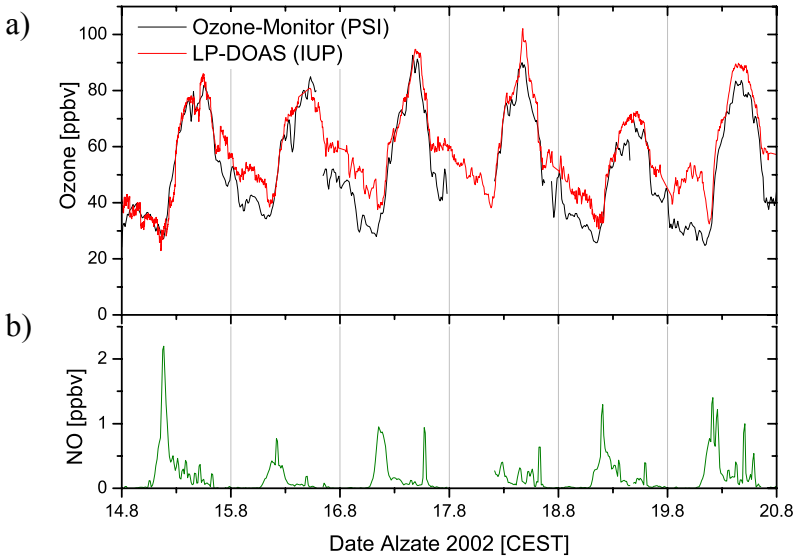

Figure 5.6: ***(a)*** *Daily variation of ozone concentrations in a stable fair weather week during FORMAT I measured by long path DOAS (red) and a UV-absorption ozone monitor (black) at Alzate. Turbulent mixing leads to a homogeneous vertical ozone distribution during daytime. At night, distinct differences are discernible.* ***(b)*** *The NO concentrations show a morning emission peak between 8 and 10 h. Nighttime NO values are below 10 pptv.*

20 ppbv ozone between 20 h and 8 h. Minimum ozone concentrations of ~ 30 ppbv remain at the end of the night. The nighttime ozone sinks are predominantly close to the ground. The processes responsible for the nocturnal ozone decrease can be dry deposition and nocturnal air chemistry, i.e. reaction with NO (R 2.13), reaction with NO_2 (R 2.6) or reaction with unsaturated VOCs (e.g. ozonolysis of alkenes). The lifetime of ozone towards these processes is estimated with equations analogous to eq. 2.13.

Ozonolysis of VOCs (see *Sec. 2.3.3.2*) is not expected to be an important pathway for the degradation of ozone at the site since the reactions are slow and the nighttime alkene concentrations, measured by PSI at Alzate, were low. The reaction of ozone with alkenes (propene, butene, isoprene) accounts for 0.1-0.2 ppbv h^{-1} ozone loss during the night. This corresponds to an ozone lifetime of ~10 d (see *Fig. 5.7*) with respect to the reaction with alkenes which might be of biogenic or anthropogenic origin. Propene accounts for 60-70% of this reaction. The nighttime emission rates of VOCs from vegetation are uncertain [*Kesselmeier and Staudt*, 1999].

While at urban sites like Bresso, existent NO amounts would react with ozone until the ozone or the NO is consumed, due to the large rate coefficient of the reaction with NO, Alzate is not exposed to strong emissions. At the semi-rural site, the measured nighttime NO levels are below 10 pptv. The lifetime of ozone regarding the reaction with NO is of the order of 4.3 d (see *Fig. 5.7*). Between the night hours 22 h until 6 h not more than 0.3-0.4 ppbv h^{-1} ozone close to the ground are lost due to reaction with NO. The reaction of ozone with NO is not considered to be the primary loss process at Alzate during the night.

The reaction between ozone and NO_2 can occur during the night to form nitrate radicals (NO_3) which further react to N_2O_5 (see *Sec. 2.2.1*). Considering NO_2 concentrations around 4-5 ppbv measured at Alzate, an ozone lifetime of 3.7 d (see *Fig. 5.7*) towards the nitrate forming reaction is expected.

Dry deposition occurs by contact of the trace gas with surfaces (see *Sec. 2.4.4*). Assuming a deposition velocity of 0.2-0.4 cm s^{-1} at night (see Table 2.7) and involving an inversion layer of 200 m, the estimated lifetime of ozone towards deposition is between 14 h (see *Fig. 5.7*) and

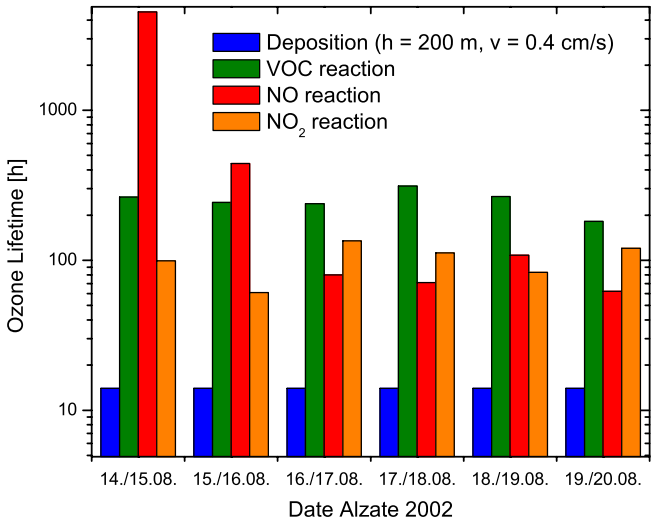

Figure 5.7: Estimation of the average lifetime of ozone towards its chemical and physical loss processes during the examined nights at Alzate.

1 d. Deposition turns out to be the most efficient nighttime loss process of ozone at Alzate. The described processes can explain the ozone loss at night to a great extent.

It can be concluded from this section that the path-integrated DOAS ozone measurements are appropriate to supplement daytime in-situ measurements of other trace gases for studying daytime chemistry, but at night measurements occur in different air masses and cannot be combined. Due to the nocturnal stable layering, loss processes which are most efficient close to the ground result in a vertical gradient of ozone concentrations. The most effective loss mechanism is deposition. Also the distribution of formaldehyde can be affected by the atmospheric layering at night as shown in *Sec. 5.3.4*.

5.3.3 Daytime Spatial Gradient of Formaldehyde

It is a different situation for formaldehyde, since there are also differences between both data sets during daytime (see *Fig. 5.5*). This section shows that the spatial inhomogeneity of the formaldehyde distribution due to reactive biogenic VOC emissions can lead to the large differences found between the long path DOAS results and the in-situ results. Under these conditions, the combination of both data sets is questionable.

To further investigate the reason for the formaldehyde daytime deviations at Alzate, the last week of the FORMAT I campaign was selected, when stable fair weather conditions were met. The daytime differences between CH_2O measured above the forest by the long path DOAS and CH_2O measured by the Hantzsch monitor close to the ground increased with increasing temperature. This is shown in *Fig. 5.8a*, where red colour represents high ambient afternoon temperatures. For temperatures higher than ~ 25°C, significantly higher CH_2O concentrations were measured by DOAS above the forest than at the container by the in-situ instrument. The increasing deviation with increasing temperature is also illustrated by *Fig. 5.9a*. Since isoprene production and emission by vegetation are a function of temperature (see *Sec. 2.1.3*) and since formaldehyde is a high-yield product of the rapid isoprene oxidation by OH radicals (see Table 2.4), this is an indication for intensified formaldehyde formation above the deciduous forest, which might explain the higher formaldehyde concentrations measured along the light path.

As pointed out in *Sec. 2.3.3.3*, formaldehyde, methyl vinyl ketone (MVK) and methacrolein (MACR) are the main degradation products of isoprene. Isoprene and the sum of its products MVK and MACR have been measured at the site by PSI [*Steinbacher et al.*, 2005], applying proton transfer reaction mass spectroscopy (PTRMS). The highest deviations of formaldehyde

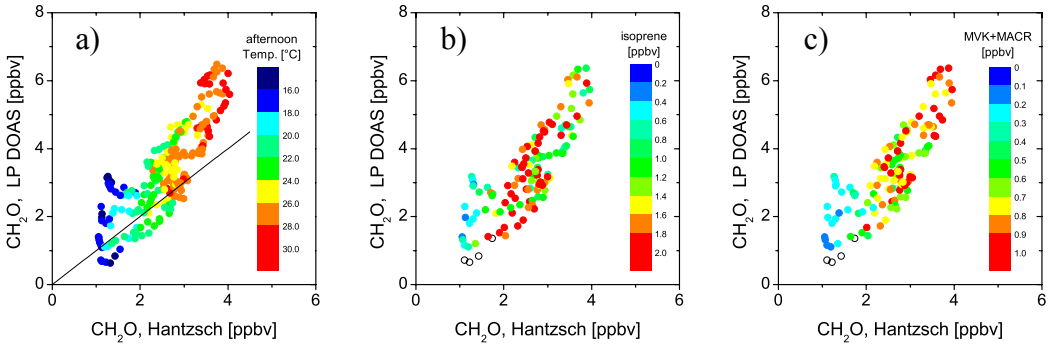

Figure 5.8: Afternoon formaldehyde concentrations measured by DOAS versus Hantzsch results during the last week of the FORMAT I campaign at Alzate. The colours label ***(a)*** *ambient temperature (afternoon),* ***(b)*** *isoprene concentrations at the container and* ***(c)*** *MVK + MACR concentrations at the container. The line in (a) represents the 1:1-line.*

concentrations measured by DOAS from the point measurement coincide with the highest MVK + MACR concentrations measured at the container (see *Fig. 5.8c*). This supports the assumption that higher local isoprene concentrations above the forest are responsible for the higher formaldehyde concentrations along the light path. Above the forest, which is the far most important isoprene source, rapid photochemical processing takes place. The forest has a distance of about 300-400 m from the container in southerly and westerly direction. The lifetime of isoprene regarding the reaction with OH is short during the day, e.g. ~ 30 min at noon for [OH] = 5×10^6 molec cm^{-3} ([OH] estimated with eq. 2.12 using photolysis frequencies measured simultaneously at Bresso). This is shorter than the time needed to transport the air mass from the forest to the container site with the weak wind speeds given here (see *Sec. 4.2.1*). Isoprene emitted from the forest is oxidised during the transport and might thus reach the container site only in trace amounts, explaining the worse correlation of the formaldehyde deviation with isoprene itself (see *Fig. 5.8b*). Also other biogenic HCs can contribute to the formation of formaldehyde over the forest, for example, reactive monoterpenes are emitted as well as mentioned in *Sec. 4.2.2*. By the rapid photochemistry over the forest, oxidising the BVOCs, a higher equilibrium concentration of formaldehyde is reached there, which explains the significantly higher

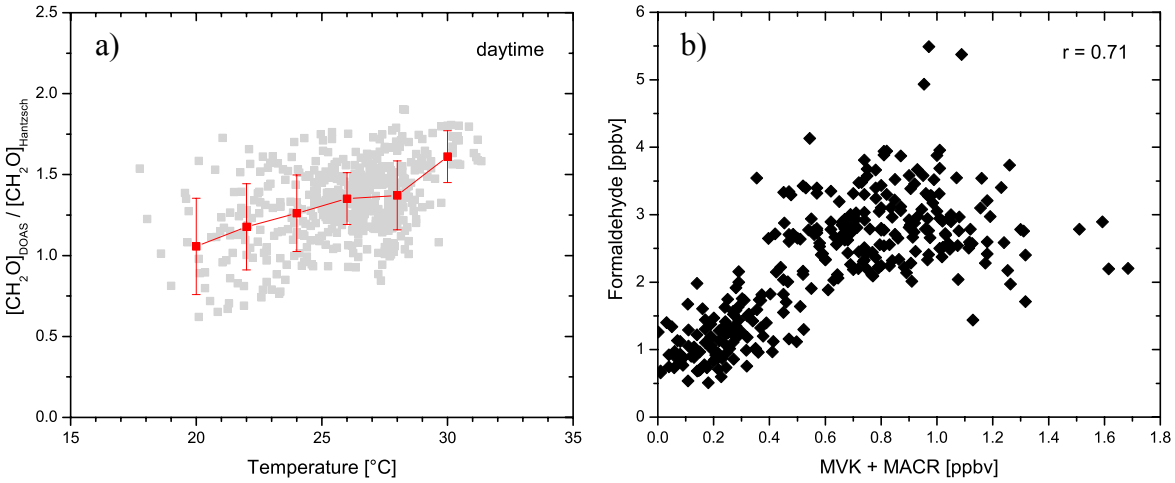

Figure 5.9: ***(a)*** *A distinct increase of the CH_2O_{DOAS} /$CH_2O_{in\text{-}situ}$ ratio with the ambient temperature can be observed during the day. The averages of 2 K bins and the standard deviation are included in red.* ***(b)*** *Scatter plot of formaldehyde versus MVK + MACR, both measured in-situ at the container.*

formaldehyde concentrations measured by the DOAS. The formaldehyde measured at the container correlates well with the sum of MACR and MVK (*Fig. 5.9b*). Those compounds are degradation products of isoprene, but with longer lifetimes than isoprene (see *Sec. 2.3.3.3*), so that larger amounts can be transported to the site.

To obtain a measurement representative for the rural area north of Milano, averaging over a long absorption path is usually favourable for a spatially variable compound. But in the case shown here, the DOAS result is strongly influenced by a local source since the light beam passes very close to the tree tops. The formaldehyde rapidly formed from isoprene oxidation has a significantly higher concentration than found outside of the forest. In this case of long path DOAS formaldehyde measurements at Alzate, the data are not assumed to be representative for a larger patch. This is also supported by the better agreement of in-situ measured formaldehyde and the modelled (RCTM) formaldehyde concentrations [*Liu et al.*, 2006]. This comparison demonstrates the importance of the choice of the experimental configuration since different instrumental setups can, depending on the surroundings, lead to highly different measurement results.

5.3.4 Nighttime Vertical Formaldehyde Variation

Here, the nighttime differences of formaldehyde levels (see *Fig. 5.5*) measured at Alzate at 2 and 30 m above ground are considered. During clear, calm nights when a stable nocturnal boundary layer has formed (see *Sec. 2.4.1*), large differences between the ground-based in-situ and long path measurements were observed for formaldehyde, where higher concentrations were measured along the light path than close to the ground. The intercomparison of measurement techniques (*Sec. 5.2*) revealed that instrumental uncertainties account for up to 15% of the differences between DOAS and Hantzsch methods. However, at night in the absence of CH_2O sources, differences between DOAS and in-situ measurements were found that were far beyond this value, indicating different influence of CH_2O sinks for both air volumes.

In the absence of photochemical processes (photolysis, photooxidation), there are no sources of formaldehyde and its sinks can be confined to a few (see *Sec. 2.3.2.2*). Deposition is an important sink close to the ground. The reaction with the nitrate radical (R 2.32) is the only chemical reaction of formaldehyde that can be important during the night. The lifetime of formaldehyde regarding the reaction with NO_3 is comparatively long. For maximum nighttime concentrations of 0.4 ppbv, measured at the site by PSI, a lifetime of > 2 days is derived for this reaction. Generally, nitrate concentrations between 0.2 and 0.3 ppbv were measured, according

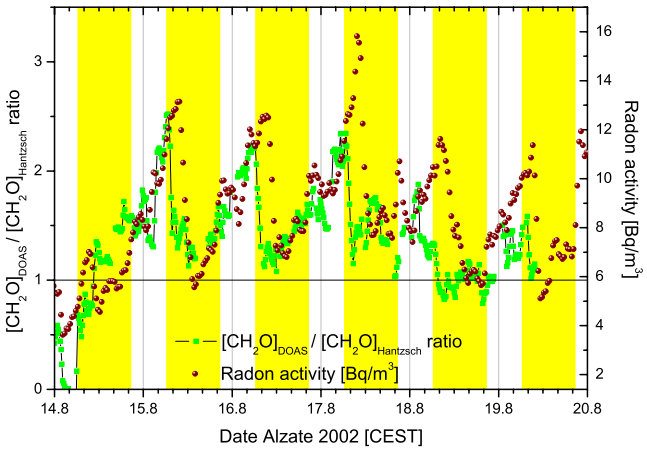

Figure 5.10: Consecutive days of a fair weather period in FORMAT I were characterised by high static stability during the night and therefore by accumulation of radon. Simultaneously, the concentration difference between elevated levels and close to the ground increased, indicating the effect of dry deposition close to the ground.

to an even longer formaldehyde lifetime. Deposition remains as the most important nighttime sink of formaldehyde.

Different temporal tendencies of the formaldehyde concentration could be found in both air volumes observed. The concentration difference between both height levels increased during the course of the night. To explain the formaldehyde differences at night, radon was used as an inert tracer for the stability of the nocturnal boundary layer (see *Sec. 2.4.3*). The temporal evolution of the (vertical) formaldehyde difference and the radon concentration is shown in *Fig. 5.10* for a couple of days (IOP during FORMAT I). The difference, represented by the ratio $[CH_2O]_{DOAS}/[CH_2O]_{in\text{-}situ}$, increases during the course of the night, reaching a maximum shortly before sunrise. By the end of the night, the DOAS frequently measures up to 2.5 times higher concentrations than the Hantzsch close to the ground. These differences cannot be explained by instrumental uncertainties. The Rn activity (measured 2 metres above ground, see *Sec. 4.2.2.1*) rises likewise during the night and reaches its maximum between 9:15 and 9:30 h. At a continental site like Milano such short-term variations of the ^{222}Rn activity can only be due to changes in vertical mixing within the boundary layer (see *Sec. 2.4.3*). The steep drop in Rn activity afterwards indicates the onset of efficient convective mixing at 9:45 h. However, the difference in CH_2O concentrations already drops shortly after sunrise and the ratio reaches its minimum value close to one around 7:45 h. The lower layers are fairly well mixed by that time. The nightly minimum formaldehyde concentration close to the ground is observed by the Hantzsch at 6:45 h in the morning. Afterwards the CH_2O concentration close to the ground rises strongly because of the beginning convective mixing and probably already photochemical formation.

The development described above may be explained by the stable stratification at night, where the vertical exchange is strongly limited. Under conditions of a strong nocturnal stability, radon, exhaling from the soil with constant flux (see *Sec. 2.4.3*), accumulates in the surface layer to high concentrations. The deposition flux of formaldehyde into the opposite direction leads to a decrease of CH_2O concentrations, especially close to the ground, since, due to the limited vertical exchange, air in lower levels, sampled by the in-situ instruments, is rather subject to effective deposition. The deposition flux to the ground surface is a function of the concentration of the trace gas and of the deposition velocity, which depends on the type of surface, the type of the trace gas and the altitude (see *Sec. 2.4.4*). As the air probed by the DOAS is more elevated above the ground and is thus less exposed to the deposition than the air sampled by the in-situ instruments, a vertical gradient of formaldehyde concentrations develops. Thus, the ratio of formaldehyde concentrations, shown in *Fig. 5.10*, is a function of the vertical CH_2O gradient arising from the deposition. At night, dew at the ground surfaces (e.g. grass) intensifies formaldehyde deposition close to the ground, since CH_2O is highly water soluble. Formaldehyde has a higher deposition velocity than ozone (see *Fig. 2.10*), leading to a more efficient removal of formaldehyde close to the ground.

The correlation of the formaldehyde ratio and radon activity observed in *Fig. 5.10* offers the chance to estimate the difference of deposition fluxes of both height levels from parallel records of the trace gas and ^{222}Rn concentration variations and calibration by the known ^{222}Rn flux, using a modification of the radon tracer method (see *Sec. 2.4.3*). The most important assumption for the application of the Rn tracer method is that the radon exhalation from the ground is constant in time and spatially homogeneous. This is confirmed in stable situations and for limited periods of time. For several stable nights with rather similar weather conditions, the CH_2O concentration deviations (CH_2O gradient) are plotted versus the radon activity in *Fig. 5.11*, where a distinct linear correlation is noticeable ($r = 0.81$). The concentration increase attributed to atmospheric inversion pile-up of radon released from ground and the increase of the formaldehyde concentration difference due to deposition occurs in the same proportion as do their

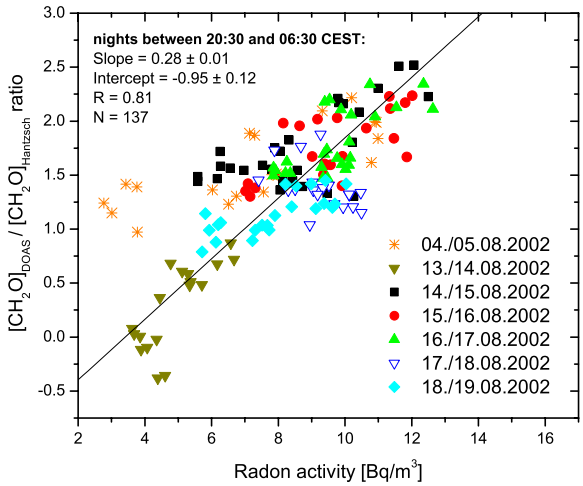

Figure 5.11: Scatter plot of the ratio of CH_2O concentrations measured by LP DOAS and Hantzsch in-situ monitor versus the Rn activity during the nights of the FORMAT I IOP. For the time between sunset (20:30 h) and sunrise (06:30 h), when the nocturnal stable layer exists, a linear regression was calculated.

respective flux densities. We define an equation equivalent to eq. 2.19 which represents the temporal change of the ratio of formaldehyde concentrations to infer the ratio of deposition fluxes ($J = j_h / j_l$) at higher (j_h) and lower (j_l) levels above the surface (eq. 5.2). With eq. 2.20, eq. 5.2 leads to the modified radon tracer method eq. 5.3.

$$\frac{\Delta[c_h / c_l](t)}{\Delta t} = \frac{j_h}{j_l} \cdot \frac{1}{\overline{H}} \qquad \text{(eq. 5.2)}$$

$$J = j_{Rn} \cdot \frac{\Delta(c_{DOAS} / c_{Hantzsch})}{\Delta c_{Rn}} \cdot \left(1 - \frac{\lambda_{Rn} \cdot c_{Rn}}{\Delta c_{Rn} / \Delta t}\right) \qquad \text{(eq. 5.3)}$$

The regression between the CH_2O ratio and ^{222}Rn during the night (21-6 h) was calculated. The slopes were determined using an error-weighted fit algorithm as described by *Press et al.* [1992b]. The slope of the regression line in *Fig. 5.11* represents the fraction term of eq. 5.3. A regression slope of 0.28 (in *Fig. 5.11*) then means that the loss of CH_2O by deposition is 5 times more efficient close to the ground than in the average height of the DOAS beam.

The ^{222}Rn tracer method used to estimate CH_2O deposition has two major sources of uncertainties, namely, ^{222}Rn flux and (CH_2O-ratio)/^{222}Rn regression. The radon flow rate from the soil was stated as 72 Bq m^{-2} h^{-1} by *Facchini et al.* [1981]. The uncertainty of the ^{222}Rn exhalation rate is estimated as ~ 25% [*Schmidt et al.*, 2001].

5.3.5 Conclusions

Spatial concentration differences were studied, which can arise from chemical or physical processes. The differences can become apparent when measuring with different measurement geometries. For the interpretation of measured DOAS data, the results from other methods often are used in addition, since not all compounds can be measured by the DOAS method. However, here one must take into consideration that the results of the different methods, which probe different air volumes, are not implicitly compatible. On the one hand, in-situ concentrations might be locally enhanced by emissions or diminished by sinks, on the other hand long path measurements above an extended area source can be strongly influenced as shown in *Sec. 5.3.3*. It is obvious that the long path integrated and in-situ trace gas data can not generally be used complementing one another. When measuring with a long path instrument one should keep in mind that different air masses are probed and the site and course of the beam should be chosen

carefully. Especially for the measurement of horizontally and vertically varying compounds, the setup should be checked thoroughly.

6 Variability of Formaldehyde in the Po Basin

The formaldehyde concentration is variable with time, horizontal location and altitude. This chapter deals with the temporal and spatial variability of formaldehyde in the Po Basin. In the planetary boundary layer in summer, the temporal variation mainly features a diurnal variation, which differs in urban and rural atmospheres, due to the nature of CH_2O as primary and secondary pollutant. The diurnal formaldehyde variability at different sites is outlined in *Sec. 6.1*. The vertical variability of formaldehyde in the lowest 100 m above ground is studied in *Sec. 6.2*, using ground-based and airborne data. An approach to explain the horizontal and temporal variability of formaldehyde is presented in *Sec. 6.3*, using data from two campaigns in the Po Basin. The last part of this chapter (*Sec. 6.4*) deals with the quantification of formaldehyde emissions from biomass burning, which is a primary CH_2O source, leading to a substantial variability of CH_2O in the Po Basin.

6.1 Temporal Variability of Formaldehyde

6.1.1 Average Diurnal Trace Gas Cycles

The diurnal variability of formaldehyde is studied for two urban and two rural ground sites using data from Mexico and from the three FORMAT sites. Concentrations of formaldehyde, ozone and nitrogen dioxide over the entire Mexico campaign were merged into hourly bins to yield average diurnal cycles. The composite diurnal cycles at Mexico City are shown in *Fig. 6.1a*. To compare diurnal cycles of the different FORMAT sites, data from a week of the FORMAT II campaign, characterised by relatively uniform trace gas variations and stable meteorological conditions (16-22 September 2003), were used and hourly averages were determined. To ensure consistent data sets, the formaldehyde data from the Hantzsch monitors were used for the three FORMAT sites which sampled 2 m above the ground in all three cases. The composite cycles for the FORMAT sites are shown in *Fig. 6.1b-d*. The temporal patterns of trace gas concentrations can be qualitatively explained in terms of the diurnal dependence of emissions, chemistry and vertical mixing (see *Sec. 2.4.2*). At the urban sites, Mexico and Bresso, there is a certain contribution of primary CH_2O which has been determined by statistical means. *García et al.* [2005] estimated 42% primary sources to ambient formaldehyde concentrations at Mexico City. For Bresso 2003, *Samuelsson et al.* [2006] estimate a primary contribution of ~10%.

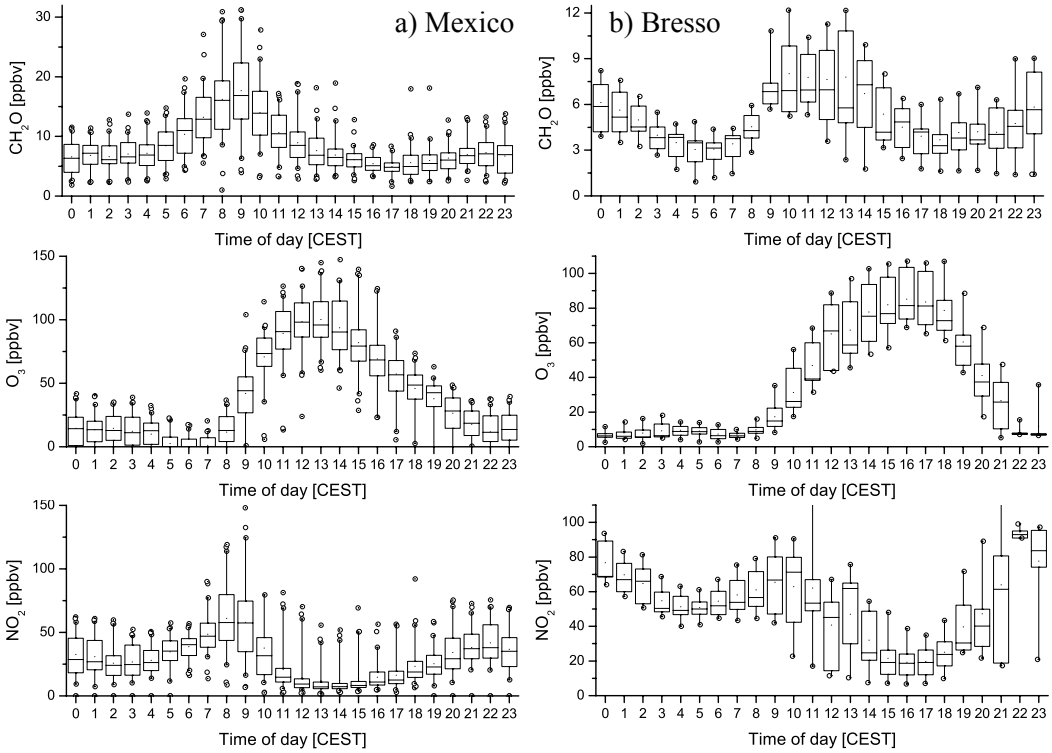

*Figure 6.1: Composite diurnal cycle for CH_2O (top), O_3 (middle) and NO_2 (bottom) at **(a)** Mexico City and **(b)** Bresso 2003. Box plots show the percentile distribution of trace gases for 1 hour time intervals. The box covers the interquartile range, between 25 and 75 percentiles. Whiskers show 10 and 90 percentile values. Circles show 5 and 95 percentile values. The line in the box represents the median.*

At Mexico City, the pollutant levels are generally high. The diurnal variations of NO_2, CH_2O and SO_2 (not shown) show a distinct maximum in the morning between 7 and 10 h CST. Since this is a period of high emission rates due to morning rush hour traffic, it is likely that the observations are capturing fresh emissions. In addition, vertical mixing is limited during this period, resulting in the high pollutant concentrations. There is no pronounced formaldehyde maximum in the afternoon. A negative correlation is found between formaldehyde and ozone. As shown in *Sec. 4.5.4*, formaldehyde is a very important radical source in Mexico City, supporting the ozone formation. Ozone has a broad maximum occurring in the early afternoon. A similar CH_2O variation is observed at Bresso, located close to the centre of Milano. An increase of formaldehyde concentrations by primary sources is generally observed in the morning. A plateau is reached over noon, further increase by secondary formation may occur in the early afternoon. The ozone maximum occurs in the late afternoon. The NO_2 average diurnal profile shows peaks associated to road traffic at 8, 13 and 20 h. High NO_2 prevails during the entire night.

The typical diurnal patterns observed at the semi-rural site Alzate downwind of Milano and the rural site Spessa upwind of Milano are shown in *Fig. 6.1c* and *d*. There was a gradual increase of trace gas concentrations at Alzate during the observed week (see *Fig. 4.12*), leading to an elevated formaldehyde background. Since the reaction of many biogenic VOCs with ozone proceeds also at night and forms CH_2O, the elevated formaldehyde background may be attributed to formation from additional temperature-driven biogenic emissions. The formaldehyde increase over the day is attributed to secondary formation from precursors emitted locally and in the metropolitan area north of Milano. Pronounced isoprene peaks, found by *Steinbacher et al.* [2005] at Alzate before noon and in the early evening are reflected in the formaldehyde concentrations. Another formaldehyde peak in the early evening, coincident with the alkenes

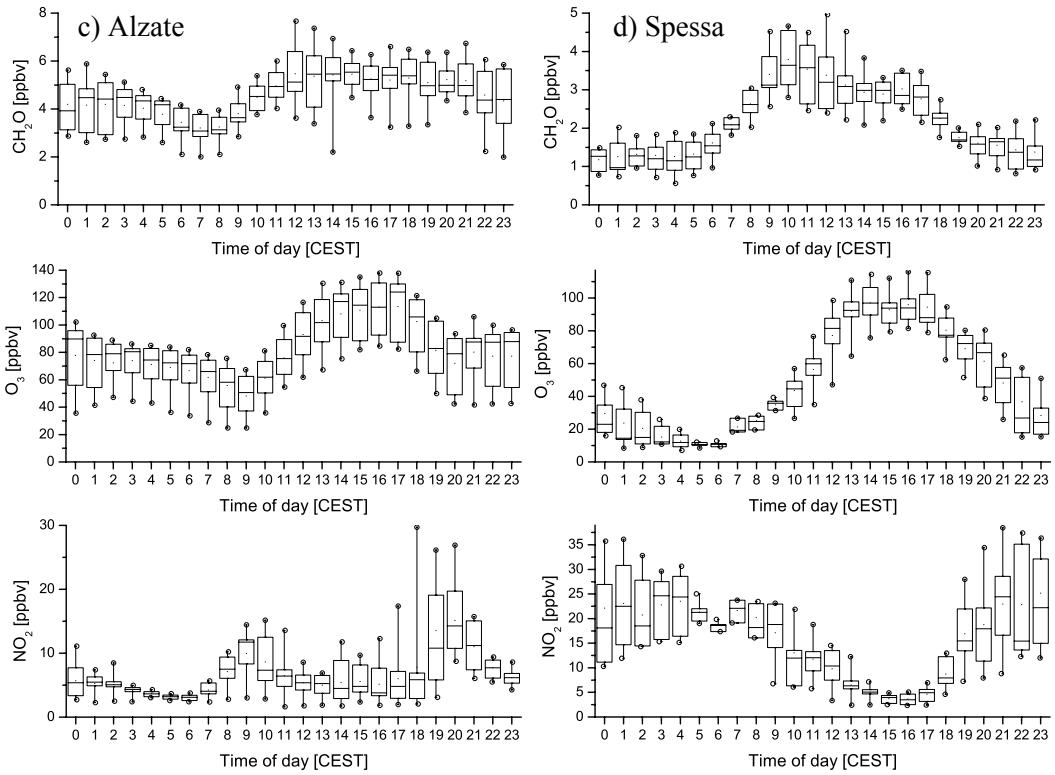

Figure 6.1 (continued): Composite diurnal cycles for the rural sites ***(c)*** *Alzate 2003 and* ***(d)*** *Spessa 2003.*

(ethene, propene) evening peak, but after the isoprene peak [*Steinbacher et al.*, 2005], was often observed and became more pronounced from day to day (see e.g. *Fig. 6.18*). It appeared around 20 h, i.e. shortly after sunset (photochemical formation can be ruled out), suggesting a dynamic influence on formaldehyde concentration. The change of the air mass due to the abrupt switch in wind direction from SSW to N between 18 and 19 h, advecting more polluted air from the vicinity north of the sampling site (a nearby street), is assumed to be the reason for the alkenes peak after sunset. A nearly linear decrease of CH_2O concentrations (~ 0.3 ppbv h^{-1}, FORMAT II) can be observed at Alzate between midnight and the formaldehyde minimum around 7-8 h, mainly attributed to dry deposition. Also the reverse flow in the evening after sunset (see *Sec. 4.1*) leads to dropping CH_2O and O_3 concentrations by dilution with cleaner air from the Alpine foothills. As opposed to the observations in Mexico City and Bresso (see above), at Alzate the CH_2O diurnal variation does not resemble the NO_2 variation. The increase of ozone concentrations in the morning is associated with the breakup of the boundary layer, which could be determined with radon data to 09:45 h. The increase of formaldehyde concentrations starts earlier than the ozone increase, which points to a strong production from local precursors (e.g. biogenic VOCs at Alzate).

At Spessa, formaldehyde concentrations are relatively constant overnight at background values of ~1 ppbv. Compared to the situation in Alzate, at Spessa no increase of the minimum concentrations during that week is observed. Here, formaldehyde concentrations start to increase from 7 h, reaching a peak before noon. There is a second, smaller buildup in concentration during the afternoon hours. A contribution by biomass burning is assumed to explain this in addition to secondary formaldehyde. The ozone concentration peak coincides with the second formaldehyde maximum. Downwind of the pollution source Milano, CH_2O peaks near noon and declines in the afternoon. Obviously, the idea of formaldehyde as a indicator of VOC oxidation is useful within the plume of a metropolis, but it is not applicable to urban air.

6.2 Spatial Variability of Formaldehyde

6.2.1 Horizontal and Vertical Variability in the Po Basin

The spatial variability of formaldehyde can be analysed in horizontal and vertical direction. It can well be captured by airborne measurements. They reveal a horizontal variability in the FORMAT experimental region which is reflected in basically higher CH_2O concentrations north of Milano than south of Milano. This is illustrated exemplarily by AMAXDOAS measurements on 18 September 2003, shown in *Fig. 6.2a*. The formaldehyde distribution is in agreement with the distribution of trace gas sources and the southerly daytime wind direction in the northern Po Basin (see *Sec. 4.1*) and represents the additional formaldehyde generated from photooxidation of organic compounds in the Milano metropolitan area. The horizontal formaldehyde variability is further discussed in *Sec. 6.3*.

Vertical profiles of CH_2O obtained from two aircraft campaigns in the Po Basin showed decreasing concentrations with increasing altitude. An average vertical formaldehyde profile derived from all flights of the Dimona aircraft during the FORMAT II campaign is shown in *Fig. 6.2*. There is a sharp concentration change at the top of the boundary layer which is located at ~1500 m. A low formaldehyde variability with concentrations between 0.5 and 1 ppbv was found in the free troposphere. Within the planetary boundary layer, the formaldehyde concentrations are higher and there is a stronger vertical formaldehyde variability. Since the sources of formaldehyde and its precursors are situated at ground level and because of the rapid vertical exchange within the mixing layer in the afternoon (see *Sec. 2.4.1*), a dependence of the concentrations on the horizontal location (i.e. the underlying surface) is observed throughout the planetary boundary layer. A strong variability is thus observed in each altitude level. The vertical variability of formaldehyde in a layer close to the ground (lowest 100 m over ground) is studied in the following section.

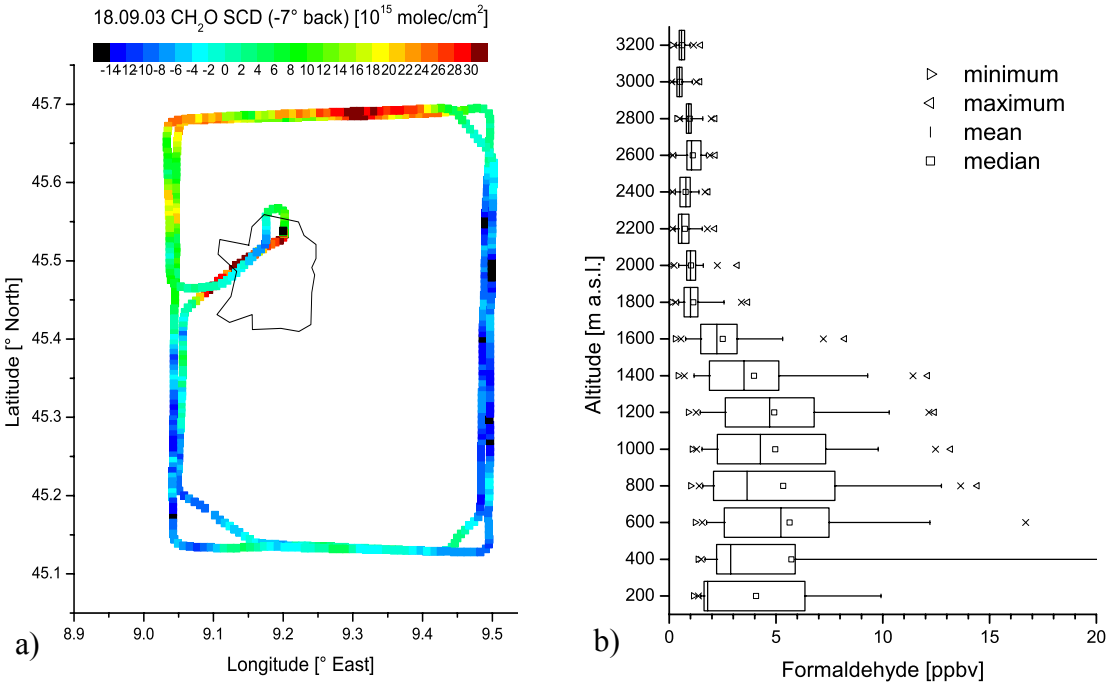

Figure 6.2: ***(a)*** *Horizontal CH_2O distribution around Milano on 18 September 2003, measured by AMAXDOAS (Klaus-Peter Heue, pers. comm., 2005).* ***(b)*** *Average vertical formaldehyde profile in the Po Basin from data obtained by the MetAir Dimona motorglider during the FORMAT II campaign. The box is determined by the 25th and 75th percentiles, the whiskers by the 5th and 95th percentiles.*

6.2.2 Airborne Measurements Along the DOAS Light Beam

Different formaldehyde measurement methods have been applied in the FORMAT campaigns and a good agreement among them was found in the intercomparison study presented in *Sec. 5.2*. Spatial differences of formaldehyde were revealed in *Sec. 5.3* applying different measurement setups of these techniques. Here, the small-scale spatial variability of the formaldehyde concentration at Alzate is examined with the aid of additional airborne data. Airborne measurement obtained by flying nearly along the DOAS beam provided the opportunity to study the vertical formaldehyde distribution.

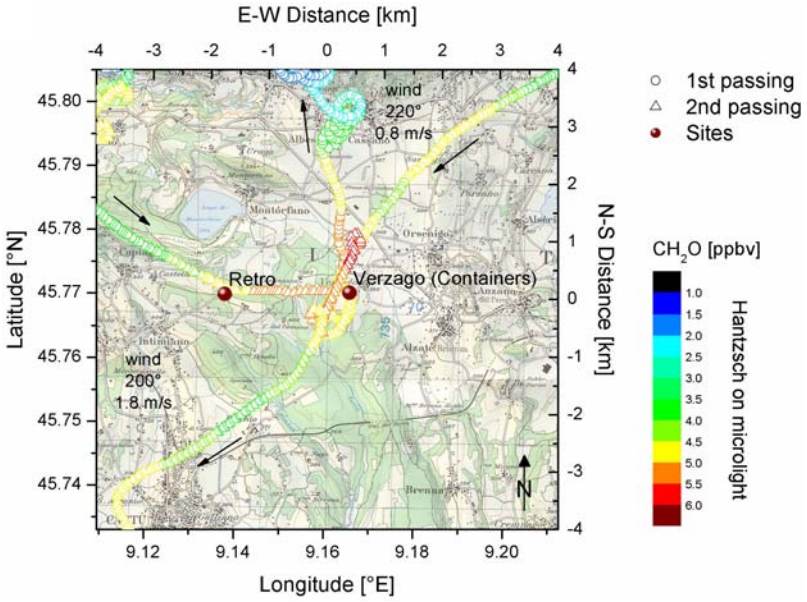

Figure 6.3: Flight routes of the IFU microlight aeroplane in the surroundings of the Alzate measurement site on 29 July 2002. The first passing of the site (12:04-12:06 h) is indicated by circles, the second one (12:34-12:40 h) by triangles. The spatial formaldehyde variability is represented by colours.

Airborne measurements aboard a microlight research aircraft, operated by IFU, were performed in the vicinity of the measurement site and nearly along the DOAS light beam. These measurements occurred on 29 July 2002 around noontime. The microlight carried a Hantzsch monitor [*Junkermann and Burger*, 2006], an ozone monitor and several sensors for radiation and particles. As pointed out in *Sec. 3.1.3*, the Hantzsch signal is subject to a temporal shift according to the time needed to pass through the instrument and, due to the time resolution of 90 sec, the signal is smeared. The shift is corrected in the data. However, it should be noted that the spatial smearing leads to an averaging along the flight track. Similarly, the DOAS results are averaged spatially along the light beam and temporally over the exposure time needed for a spectrum. Two flight approaches towards the Alzate measurement site were conducted on that day, descending to very low altitude. An overview of the vicinity of Alzate, including the flight tracks and measured CH_2O concentrations is shown in *Fig. 6.3*. The first approach is marked by circles in *Fig. 6.3* and included one pass above the measurement containers with a minimum altitude of few metres above the site level. The microlight then left the area in northward direction, ascending rapidly. The second passing was 30 minutes later after an excursion to high altitude levels above the hills north of Alzate and is marked by triangles. The microlight approached Alzate, coming from the west and directly above the DOAS light beam. It descended along this leg, but was on average 60 m above the light beam. An illustration of the flight track above the light path and a relief of the terrain is given in *Fig. 6.5* and this section is discussed in more detail below. Three passes above the container site followed before the microlight left the area heading southwest. The colours in *Fig. 6.3* reflect the spatial formaldehyde variability in the sense of horizontal and vertical variability. The highest concentrations were observed north of the measurement site. It might be considered as an effect of varying flight altitude, however as shown in the next paragraph (*Fig. 6.4b*), the highest concentration does not

coincide with the lowest altitude level. Since the wind came from 200-220° during the entire period of aircraft operation in the area, the distribution in *Fig. 6.3* points to formaldehyde formed from photooxidation of reactive HCs emitted from the forest and advected northward.

Vertical profiles of the two flight legs approaching Alzate are shown in *Fig. 6.4a,b*. Also the concentrations measured by the ground-based instruments are included there. The profiles of the first approach (*Fig. 6.4a*) show that the vertical CH_2O distribution was nearly homogeneous north of the measurement site. The formaldehyde concentrations were lower on the leg towards the container site coming from NE than they were when leaving the site into northerly direction. On a small spatial scale of 0.5 km and a temporal range of 2 min, the differences can amount to ~1 ppbv between descent and ascent in the same altitude. This horizontal difference has been observed close to the container in ~100 m above ground and is marked by a red arrow in *Fig. 6.4a*. Closer to the ground, i.e. closer to the sources, even stronger horizontal gradients might be probable. The formaldehyde concentrations found at low altitude levels by the airborne instrument are close to the concentrations measured by the ground-based Hantzsch within a temporal range of 5 min. The DOAS measured higher values, due to the processes discussed in *Sec. 5.3.3*.

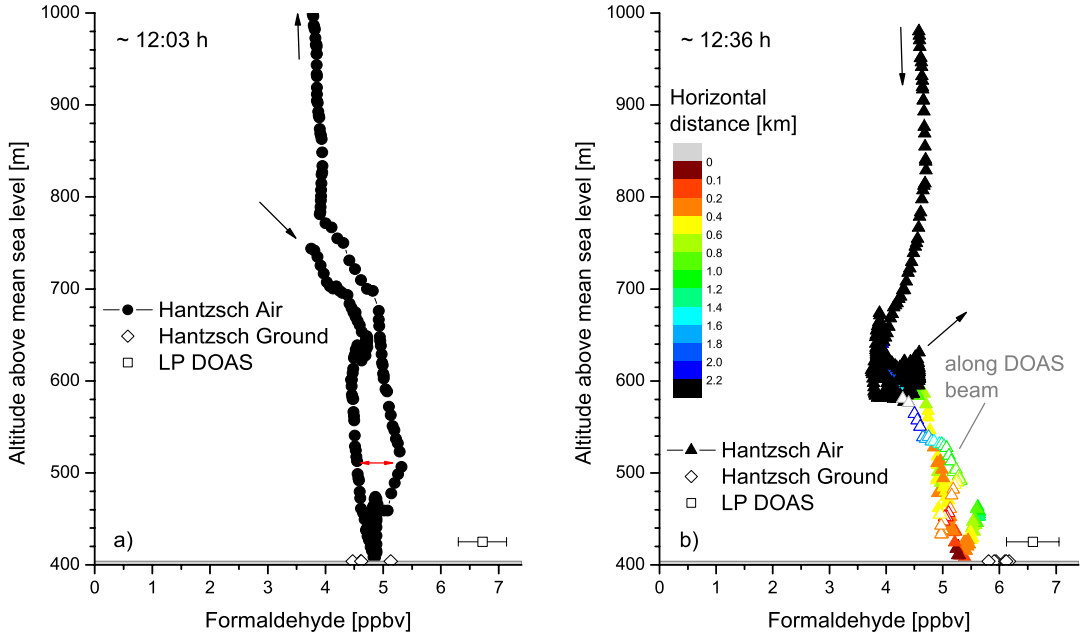

Figure 6.4: Vertical formaldehyde profiles close to Alzate on 29 July measured by the Hantzsch monitor on board of the microlight (filled markers) and ground-based measurements at Alzate (open rhombs, squares); ***(a)*** *first approach to container,* ***(b)*** *second approach including flight along DOAS beam (highlighted by open symbols).*

There is a larger vertical variability on the second flight leg to Alzate than on the first one. When the aeroplane approached the site the second time, a strong increase of formaldehyde concentrations is observed while the microlight descended above the forest (*Fig. 6.4b*), indicating intensified CH_2O production there. This flight leg above the light beam is shown with open symbols and in colours representing the horizontal distance from the container site. Concentrations as high as measured by the DOAS are not observed. On the one hand, this could be explained by the altitude of the plane which was on average eighty metres above the canopy. On the other hand, the real concentration there might be higher but, due to the time resolution of the Hantzsch, the actual concentration was not fully reached. The highest CH_2O concentrations

were not measured close to surface but ~1 km from the ground measurement site in 460 m (~100 m above local ground) and might be advected from the forest. The formaldehyde concentrations of the flight track section along the DOAS beam are compared to the ground measurements in the following.

A west-east section of the terrain along the light beam is shown in *Fig. 6.5*. The light path of the LP DOAS (grey line) directly passed over woodland as indicated by the trees in *Fig. 6.5*. The forest has a tree population typical for Northern Italy consisting of oaks (*Quercus pubescens*) and sweet chestnut (*Castanea sativa*). Both tree species emit large quantities of BVOCs. The oak is a strong isoprene emitter (70 µg g^{-1} h^{-1} at 30°C and PAR * = 1000 µmol m^{-2} s^{-1}). In contrast, *Castanea* emits monoterpenes and releases, apart from α-pinene and β-pinene, also the highly reactive † trans-β-ocimene and limonene (Guenther Seufert, pers. comm., 2005). The two latter species represent nearly 50% in the emission spectrum which was assessed to be 10 µg g^{-1} h^{-1} for standard conditions. Similar to the isoprene emission by *Quercus*, the monoterpene emission by *Castanea* is controlled by temperature and light [*Lenz et al.*, 2001]. *Lenz et al.* [2001] give a foliar biomass density of 320 and 380 g m^{-2} for *Quercus* and *Castanea* in Italy, respectively. The DOAS light beam was on average 30 m above the ground. Assuming a tree height of 20 m, the light beam traversed in 10 m above the treetops. Between the retro-reflector mast and the ground measurement site, the microlight followed the terrain and flew about 100 m above the ground. Along the descending part of the flight track between the retro-reflectors and the containers, the Hantzsch monitor on board of the microlight measured an average concentration of 5.13 ppbv (*Fig. 6.5*). The corresponding altitude was between 531 and 433 m a.s.l. (487 m on average). Over the forested area, slightly enhanced CH_2O concentrations were found (up to 5.3 ppbv in 80 m above ground). A weak negative correlation between the altitude of the microlight above wood and the measured formaldehyde concentration is discernible. Higher formaldehyde concentrations were measured at the same time (12:36 h) closer to the ground by the Hantzsch (6.1 ppbv) and closely above the forest by the long path DOAS (6.6 ppbv).

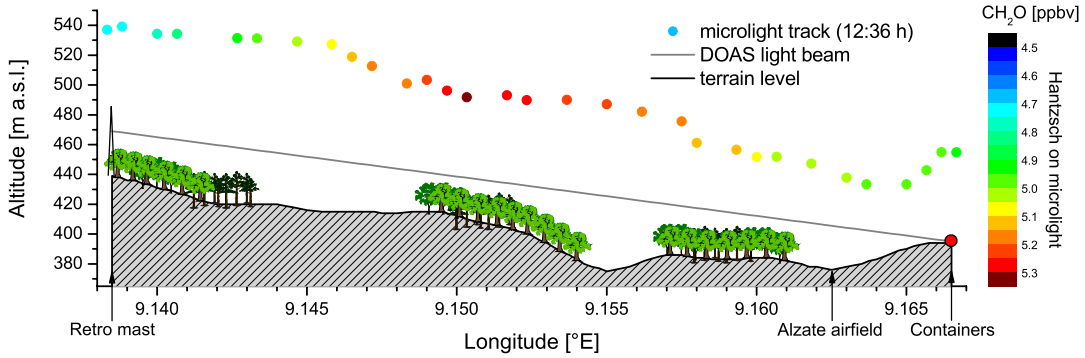

Figure 6.5: W-E section along the DOAS light path (drawn in grey), showing the terrain underneath the beam. On 29 July, the microlight flew above the light beam, on average 90 m over local ground. The container site is marked by a red circle.

It is difficult to associate the variation of formaldehyde concentrations observed from the plane unambiguously to horizontal or vertical gradients, since the landuse has a strong influence on the distribution of local CH_2O sources. The use of the ground is largely heterogeneous and not known in detail. However, the surface underneath the light beam is well known to be covered with deciduous trees. There were several more opportunities during the FORMAT I

*. PAR (Photosynthetically Active Radiation): the radiation that contributes to the photosynthesis

†. ocimene: $k_{OH} = 2.52 \times 10^{-10}$ cm^3 $molec^{-1}$ s^{-1}, $k_{O3} = 5.40 \times 10^{-16}$ cm^3 $molec^{-1}$ s^{-1}
limonene: $k_{OH} = 1.71 \times 10^{-10}$ cm^3 $molec^{-1}$ s^{-1}, $k_{O3} = 2.00 \times 10^{-16}$ cm^3 $molec^{-1}$ s^{-1}

Table 6.1: Formaldehyde concentrations at Alzate measured aboard the microlight, along the DOAS light beam and at the in-situ container site during seven overflight events (section above the forest).

Date, Time	Microlight (avg. height a.g.l.)	In-situ (2 m a.g.l.)	LP DOAS (30 m a.g.l.)
29/07/2002, 12:36	5.13 (87 m)	6.10	6.58
31/07/2002, 12:05	4.05 (79 m)	5.23	--
31/07/2002, 12:58	2.80 (87 m)	3.94	5.87
04/08/2002, 13:00	1.38 (79 m)	2.08	2.82
05/08/2002, 12:21	2.86 (122 m)	3.33	4.69
08/08/2002, 14:22	2.11 (139 m)	2.90	3.55
08/08/2002, 14:25	2.40 (123 m)	2.81	3.62

campaign to compare airborne Hantzsch results over the forest with the ground-based measurements. However, in contrast to the flight on 29 July described above, in the other cases the microlight did not fly exactly parallel to the DOAS light path. An overview of the formaldehyde concentrations measured during the individual overflights is given in Table 6.1. The general outcome is that the ground-based Hantzsch monitor measured higher formaldehyde concentrations than the airborne Hantzsch which sampled air in 100 m or more above ground. The DOAS, probing air at short distance from the source of biogenic hydrocarbons, measured the highest concentrations. Due to safety reasons, the microlight never flew at levels as low as the DOAS beam. The lower concentrations measured on the microlight is attributed to the higher sampling altitude. In an altitude of 100 m above ground, the formaldehyde concentration is already 30% decreased compared to the concentration close to the canopy. The microlight flights occurred only in the daytime and mostly at noon (see Table 6.1), when photochemical formaldehyde production from VOCs is at its maximum. No measurements during evening, night or other periods of low photochemical activity are available from the microlight.

The observations listed in Table 6.1 point to a strong vertical formaldehyde gradient within the lowest ~100 m above ground. The highest concentrations are present close above the treetops which form a strong source of reactive biogenic VOCs (see also *Sec. 5.3.3*). Under sunlit conditions, the terpenoids are rapidly processed in the presence of radicals to yield formaldehyde (see *Sec. 2.3.3.3*) underneath the light beam, thereby strongly influencing the DOAS results. An attempt to understand the differences between DOAS and aeroplane results measured above the forest was done by means of a CT model operated by IFU. The model has an isoprene source at the lower border of the model domain and involves vertical exchange processes. The vertical resolution of the model is 20 m. It is thus capable of resolving a spatial gradient between the levels of observation. Unfortunately, the model was only available to perform some test runs and could not be exactly adapted to the particular cases mentioned above. However, the model was able to describe the observed situation if the vertical exchange in the model was strongly reduced (Wolfgang Junkermann, pers. comm., 2006). Assuming low vertical mixing, the observations are consistent with model results and the concentration measured on the microlight 100 m over ground can be explained by the model. Vertical CH_2O concentration differences of 30% between the DOAS height level and the flight level could be reproduced by the model. Moreover, aerosol particles present in the air offer a surface for absorption processes (deposition) and result in a decrease of the formaldehyde concentration in higher levels, where formaldehyde is not continuously supplied. In this process, organic aerosol is formed. A significant amount of formaldehyde can exist in the form of particles (< 2.5 µm). *Grutter et al.* [2005]

measured formaldehyde in the gas phase and in particles in Mexico City and found that the fraction of formaldehyde detected in particles corresponds to 20% of the formaldehyde in the gas phase, on average, which is in agreement with other measurements [e.g. *Grosjean*, 1982].

As presented in the following, observations in the Po Basin support the above explanations. The vertical exchange is indeed weak in the Po Basin, as has regularly been observed during airborne measurements in that region (Wolfgang Junkermann, pers. comm., 2006). That means that the formaldehyde produced above the forest is not effectively mixed into high altitude levels, leading to higher concentrations in low levels. Also the horizontal mixing in the Po Basin was weak, since the wind speeds were very low (see e.g. *Sec. 4.2.1*), giving rise to an inhomogeneous horizontal distribution of formaldehyde close to its sources. Moreover, in the lower boundary layer of the Po Basin air, high aerosol concentrations were found in airborne measurements (10 000-20 000 cm^{-3} for particles < 2.5 µm). If we assume up to 20% of gaseous formaldehyde to be taken up by aerosol particles, the deposition occurring on aerosol surfaces is responsible for a significant fraction of loss of gaseous formaldehyde in the atmosphere. In all altitudes, the aerosol particles provide a sink for the formaldehyde, however in the low levels there is a continuous source due to the permanent isoprene emission and oxidation, explaining the observed rapid decrease of formaldehyde with height.

6.3 Analysis of Spatial and Temporal Variability of Formaldehyde

As indicated in the previous sections, the formaldehyde concentration in the boundary layer is subject to temporal and spatial variations. This is reflected in a pronounced diurnal pattern (see *Fig. 6.1*), which on the one hand mirrors a traffic-related pattern, on the other hand shows the contribution from secondary production by oxidation of organic compounds with OH radicals and, to a lesser extent, with O_3 molecules. In the afternoon, the main source of CH_2O is the secondary oxidation of VOCs as described in *Sec. 2.3.3*. Also a day to day variability of the formaldehyde concentration is observed. Because of its short lifetime (see *Sec. 2.3.2.3*), formaldehyde has a high spatial variability.

An approach to explain the temporal and spatial variability in afternoon CH_2O concentrations on the basis of VOC measurements is presented here. In the following sections, the trace gas data from different sites in the Po Basin are studied separately to explain the formaldehyde variability by means of secondary formation through oxidation of VOCs. An overview of the measured VOC data is given in *Sec. 6.3.1* and the concept of the statistical analysis is outlined in *Sec. 6.3.3*. The method is demonstrated exemplarily in *Sec. 6.3.4* for airborne measurements in the Milano metropolitan area and is applied to all data sets available, thereafter. The results are discussed in *Sec. 6.3.8*.

6.3.1 Measured VOC Data

Volatile organic compounds were measured during the FORMAT II campaign in autumn 2003 by colleagues from other groups participating in the project. The measurements were performed at the two ground-based sites Alzate (GC operated by EMPA) and Bresso (GC operated by JRC) and on board of the MetAir Dimona, a motorised glider, covering the Milano metropolitan area and the Po Basin. On the aeroplane, also canister samples were taken (about six per flight) to supplement the airborne VOC data by C_2 and C_3 compounds. Moreover, airborne measurements conducted in the same area during the LOOP/PIPAPO campaign in 1998, with the MetAir Dimona as well, are available for the analysis. During both campaigns, LOOP 1998 and FORMAT 2003, the Dimona aircraft was operated and equipped by MetAir and PSI. The specifications of the used gas chromatographs (GCs) are summarised in Table 6.2, the method itself is described briefly in *Sec. 3.2.2*. All GC instruments allowed drawing new samples while

analysing the previous one, leading to quasi-continuous measurements. Flame ionisation detectors (FID) were used to quantify the individual hydrocarbons. Altogether, about fifty C_2 to C_{10} VOCs were measured by gas chromatography including alkanes, alkenes, alkynes, aromatic hydrocarbons and some biogenic VOCs. An overview of the respective VOCs measured at the different ground-based sites and on board of the aeroplane is given in Table 6.3.

Table 6.2: Specifications of the gas chromatographs used on the aeroplane and the ground sites, respectively. More detailed information on the instrumental settings and performance can be found in the cited references.

Site	GC type	VOC Compounds	Enrichment time	Sample frequency	Reference
Dimona 1998	Airmotec HC-1010	C_4-C_{10}	10 min	10 min	*Konrad and Volz-Thomas* [2000]
Dimona 2003	Airmotec HC-1010	C_4-C_{10}	10 min	10 min	*Konrad and Volz-Thomas* [2000]
Alzate 2003	Varian 3400	C_2-C_7	20 min	hourly	*Steinbacher et al.* [2005]
Bresso 2003	Agilent 6890	C_2-C_9	20 min	irregularly	*Latella et al.* [2005]

Typical average afternoon (12-18 h) VOC concentrations measured at the ground-based sites and on board the aeroplane are shown in *Fig. 6.6*. Most VOCs measured had their highest concentrations at Bresso which is close to the city centre of Milano and thus most influenced by direct anthropogenic emissions like alkanes and aromatics. At Alzate, which is located in a rather forested area, the highest average isoprene concentrations were observed. The long-lived ethane and propane ($\tau > 1$ day for [OH] = 5×10^6 molec cm^{-3}) have similar concentrations at the two ground-based sites. For shorter-lived, larger alkanes the concentrations are much higher at the urban site than 4 h downwind (for average wind speeds, see *Sec. 4.2.2*) at Alzate.

The airborne and ground-based measurements should be considered separately. The lowest VOC concentrations were observed in the aircraft measurements. The most reactive VOCs have already reacted near the surface and reach the average flight level of 600-700 m a.s.l. in only small quantities. The most abundant VOCs measured were toluene, small alkanes ($< C_6$) and ethene (from canister samples). The average VOC concentrations from both aircraft campaigns were similar for most compounds except for n-butane and isopentane (see below for details). Isoprene levels observed from the Dimona are similar to those observed downtown. This might be due to two opposing effects; namely, an increase in isoprene emission rate outside of the urban area and a decrease in isoprene concentration with altitude that reflects the very short atmospheric lifetime.

The aircraft campaigns took place in different seasons but in the same area. The PIPAPO measurements were conducted in May-June, the FORMAT II measurements in September. *Figure 6.7* shows the afternoon concentrations of individual VOCs, averaged for each campaign, and suggests that the average afternoon composition of the VOC mixture in the Milano metropolitan area is largely the same in spring and autumn. The three exceptions n-butane, isopentane and propylbenzene are marked by arrows. For the aircraft measurements with the Airmotec instrument, an underestimation of the concentrations of C_4-VOCs is possible (André Prévôt, pers. comm., 2005). This might explain differences in the butane concentrations of both campaigns. For FORMAT II data, the canister samples provide another quality assurance of the airborne VOC data. The concentrations of most VOCs are similar in the canister samples and the Airmotec samples drawn simultaneously. For isopentane, however, the canister values are nearly twice the Airmotec values. This matches the observation of, on average, double

Table 6.3: VOCs measured at Alzate (Alz03), Bresso (Bre03) and on the MetAir aircraft (Can03, Air03) in 2003 and on the aircraft in 1998 (Air98). Nine compounds, printed bold, have been measured by all instruments.
'est': the reactivity of the compound was estimated (method specified in *Sec. 6.3.2*), (x): several missing values, -: compound not measured or only few data points available

VOC	Alz 03	Bre 03	Can 03	Air 03	Air 98	VOC	Alz 03	Bre 03	Can 03	Air 03	Air 98
Ethyne	x	x	x	est	est	2,2-Dimethylbutane	-	-	x	est	x
Propyne	-	x	-	-	-	**2-Methylpentane**	**sum**	**x**	**sum**	**x**	**x**
Ethene	x	x	x	est	est	**3-Methylpentane**	**sum**	**x**	**sum**	**x**	**x**
Propene	x	x	x	est	est	Methylcyclohexane	-	-	-	x	x
1-Butene	-	x	-	-	-	2-Methylhexane	-	-	-	x	x
Trans-2-Butene	-	x	-	x	(x)	3-Methylhexane	-	-	-	x	x
Cis-2-Butene	-	x	-	x	x	Isooctane	-	-	-	x	x
Isobutene	-	x	-	-	-	2-Methylheptane	-	-	-	x	x
Trans-2-Pentene	-	x	-	-	-	3-Methylheptane	-	-	-	x	x
Cis-2-Pentene	-	x	-	x	(x)	**Benzene**	**x**	**x**	**x**	**x**	**x**
1,3-Butadiene	-	x	x	-	-	**Toluene**	**x**	**x**	est	**x**	**x**
Ethane	x	x	x	est	est	Styrene	-	-	-	x	x
n-Propane	x	x	x	est	est	Ethylbenzene	est	x	-	x	x
n-Butane	**x**	**x**	**x**	**x**	**x**	m&p-Xylene	est	x	-	x	x
n-Pentane	**x**	**x**	**x**	**x**	**x**	o-Xylene	est	x	-	x	x
n-Hexane	**x**	**x**	**x**	**x**	**x**	m&p-Ethyltoluene	-	-	-	x	x
n-Heptane	x	x	est	x	x	o-Ethyltoluene	-	-	-	x	x
n-Octane	-	-	-	x	x	n-Propylbenzene	-	-	-	x	x
n-Nonane	-	-	-	x	x	Isopropylbenzene	-	-	-	x	(x)
n-Decane	-	-	-	x	x	1,3,5-Trimeth.benz.	-	x	-	x	(x)
Isobutane	**x**	**x**	**x**	**x**	**x**	1,2,4-Trimeth.benz.	-	x	-	x	x
Cyclopentane	-	-	-	-	x	1,2,3-Trimeth.benz.	-	-	-	x	x
Isopentane	**x**	**x**	**x**	**x**	**x**	**Isoprene**	**x**	**x**	**x**	**x**	**x**
Methyl-cy-pentane	-	-	-	x	x	α-Pinene	-	-	-	x	(x)
Cyclohexane	x	est	x	x	x	Acetone	-	-	-	x	x

isopentane concentrations in the LOOP GC measurements, compared to FORMAT II and suggests that there were problems identifying isopentane with the Airmotec instrument during the FORMAT II measurements. The individual, reactive and less reactive, VOCs contribute similarly to the pool of formaldehyde precursors during both campaigns.

The rate of formaldehyde formation depends on the OH reactivity of VOCs rather than solely on the VOC concentration. By weighting the VOC concentrations by their OH rate coefficients, the reactivity (see eq. 2.14 for definition) is used in the following. The selection of the reaction rate coefficients is based on recent evaluations [*Atkinson et al.*, 2005] with some exceptions where no values were available. Then the temperature-dependent rate constants, k, towards OH and O_3 were taken from the actual version v3.1 of the Master Chemical Mechanism (MCM, described by *Saunders et al.* [1997]). The complex rate constants for third-order reactions of ethene, propene and ethyne were calculated according to *Troe* [1979] using the meteorological

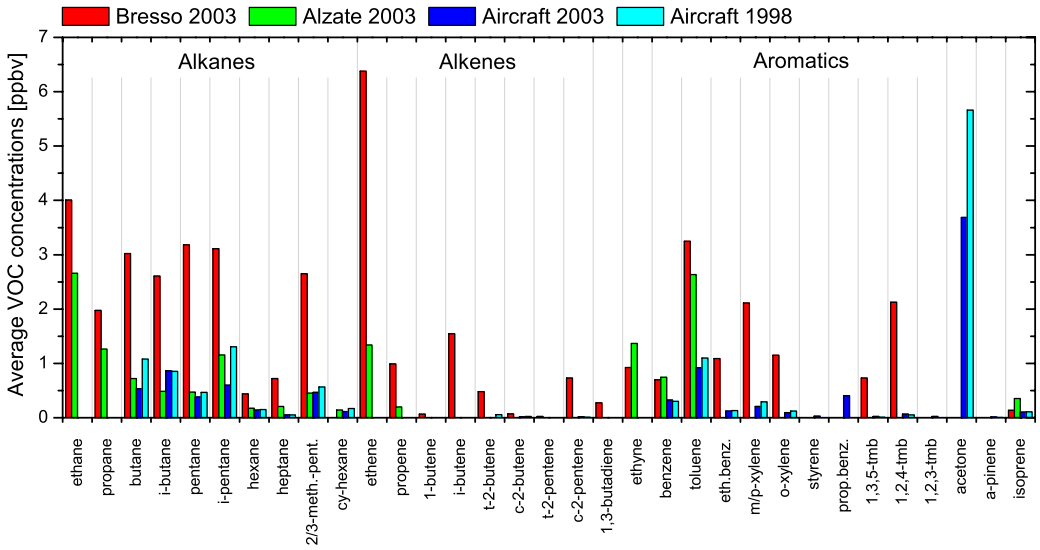

Figure 6.6: Average VOC concentrations (12-18 h) at the ground sites Bresso (red) and Alzate (green) and from airborne measurements during the FORMAT II campaign 2003 (blue) and during the LOOP campaign 1998 (light blue). The compounds are arranged by category (i.e. alkanes, alkenes, aromatics, biogenic HCs).

data measured in situ. The average afternoon VOC reactivities for ground-based and airborne measurements are summarised in *Fig. 6.8*. The highest reactivity at Alzate and in the aircraft measurements was obtained for isoprene. Isoprene exists in relatively small concentrations but it is the VOC which exhibits the fastest reaction kinetics with the OH radical (see Table 2.4). In Bresso, however, anthropogenic VOCs like alkenes and aromatics, due to their abundance, were more reactive than isoprene. Many alkanes react rather slowly, olefins and aromatics are more reactive.

Not all VOCs listed in Table 6.3 were measured by all instruments. Especially alkenes, which yield substantial amounts of formaldehyde (see Table 2.4), are not available for each site. To obtain a larger pool of formaldehyde precursors, the reactivities of several missing compounds were estimated with a method described in *Sec. 6.3.2*.

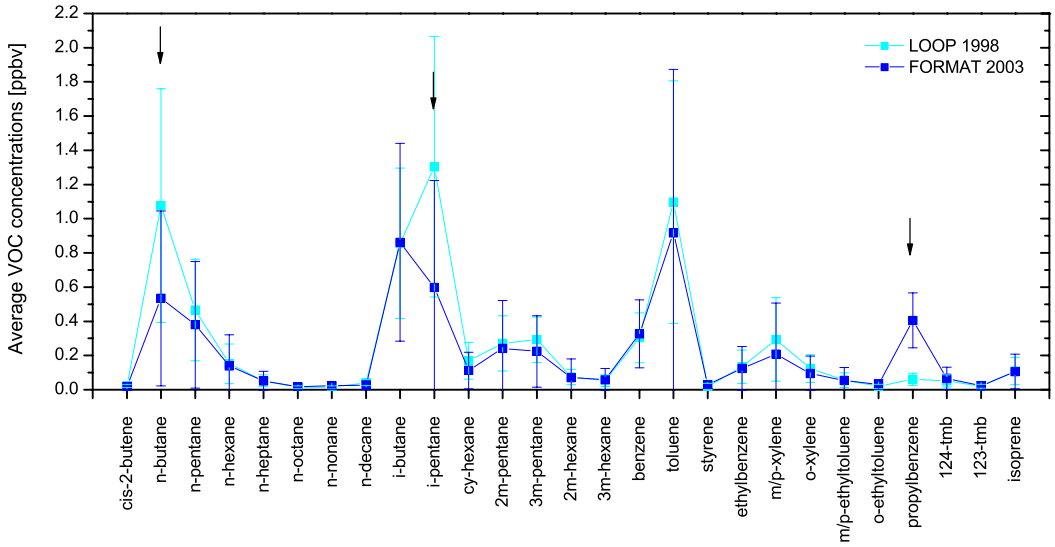

Figure 6.7: The average concentrations (12-18 h) of VOCs around Milano measured on the Dimona aeroplane were nearly identical in May/June 1998 (PIPAPO) and September 2003 (FORMAT II). The bars indicate the range of measurements in 1 standard deviation (figure from Hak et al. [2006]).

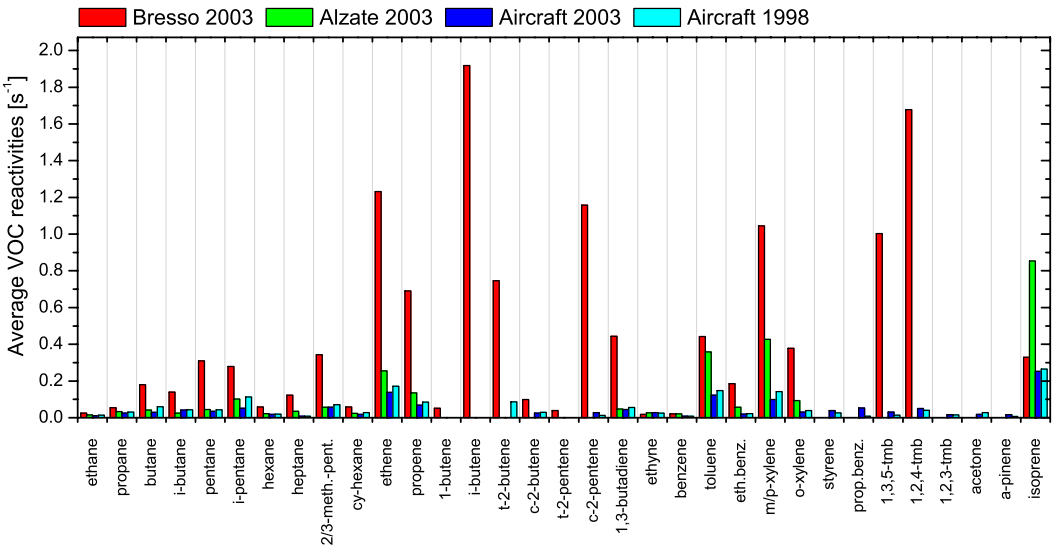

Figure 6.8: Average VOC reactivities (12-18 h). For several compounds reactivities were estimated as specified in Sec. 6.3.2.

6.3.2 Estimation of VOC Reactivities

Small VOCs were not measured by the aircraft instrument (see Table 6.2). The reactivities of C_2 and C_3 hydrocarbons for FORMAT II and LOOP airborne measurements were estimated from canister samples. During FORMAT II flights, several VOCs were measured both with canisters and with the Airmotec instrument in parallel (see Table 6.3). The results of both measurements were in good agreement for most compounds except for isopentane (see *Sec. 6.3.1*). The correlation between benzene concentration measured by the Airmotec instrument and the canister results was very good ($r^2 = 0.92$). We used the correlations of benzene reactivity to the reactivities of the species reacting slowly with OH (ethane, propane and ethyne), obtained from the canister samples, to derive continuous values of the latter for the aircraft measurements. The following relationships were obtained by least-squares regression. Although the fits were not forced through zero, the intercept equalled zero with an accuracy of two decimal places:
$R_{ethane} = 0.00 + 1.57 \cdot R_{benzene}$ ($r^2 = 0.87$); $R_{propane} = 0.00 + 3.68 \cdot R_{benzene}$ ($r^2 = 0.75$); $R_{ethyne} = 0.00 + 3.12 \cdot R_{benzene}$ ($r^2 = 0.90$).

In the case of the more reactive compounds ethene and propene, the chemical degradation after emission has to be taken into consideration. This was done using correlations of ethene and propene reactivities with compounds of similar OH rate constants, which were available both at ground (Alzate) and airborne. A linear least-squares regression yielded following relationships: $R_{ethene} = 0.00 + 5.25 \cdot R_{cy\text{-}hexane}$ ($r^2 = 0.88$); $R_{propene} = 0.00 + 2.76 \cdot R_{o\text{-}xylene}$ ($r^2 = 0.56$). By comparing the estimated reactivities with the ones derived from concentrations measured in canister samples, it was found that they could be well reproduced.

The reactivities of several aromatics (ethylbenzene, o-xylene, m/p-xylene) at Alzate were estimated from their correlation with toluene reactivities. The relationships were obtained from aircraft measurements from LOOP and FORMAT. Similar as in the rural site, the air masses sampled airborne are already processed and therefore the relationships are considered as representative also for the conditions at Alzate: $R_{m\&p\text{-}xylene} = 0.00 + 1.19 \cdot R_{toluene}$ ($r^2 = 0.87$); $R_{o\text{-}xylene} = 0.00 + 0.26 \cdot R_{toluene}$ ($r^2 = 0.87$); $R_{ethylbenzene} = 0.00 + 0.16 \cdot R_{toluene}$ ($r^2 = 0.93$).

The cyclohexane reactivity at Bresso was estimated from airborne ethene and heptane reactivities. Since cyclohexane has a rate constant between ethene and heptane, its reactivity was derived from a reaction rate weighted combination of both results.

At Alzate, only the sum of the two methylpentanes was measured. Both isomers contribute about 50% to the sum and their OH rate constants are nearly the same (see Table 2.4). Thus, an average rate coefficient of 5.35×10^{-12} cm^3 $molec^{-1}$ s^{-1} was used for methylpentanes.

The constitutional isomers of several aromatic HCs are not differentiated by most GCs. Since they have unequal rate constants towards OH (e.g. $k_{m\text{-}xylene}$ 2.31×10^{-11}, $k_{o\text{-}xylene}$ 1.36×10^{-11} and $k_{p\text{-}xylene}$ 1.43×10^{-11} cm^3 $molec^{-1}$ s^{-1}), they have to be separated. For this purpose, the fractions of the isomers meta- and para-xylene and of meta- and para-ethyltoluene have to be estimated. The reactivities of isomers measured collectively were then derived from their relative contributions to their mutual concentration, e.g. m/p-xylene. Studies have determined that p-xylene makes up approximately 20% of the total xylene fraction in urban air [*EPA*, 2003]. This is in line with the ratio of meta- to para-xylene of about 2-3 applied by *Dommen et al.* [2002]. For ethyltoluenes, the separation of the meta and para isomers is required as well, due to their unequal OH rate coefficients ($k_{m\text{-}eth.tol.} = 1.86 \times 10^{-11}$, $k_{p\text{-}eth.tol.} = 1.18 \times 10^{-11}$ cm^3 $molec^{-1}$ s^{-1}). Tunnel measurements of VOC emissions from light-duty vehicles in California revealed a ratio of meta-ethyltoluene to m/p-ethyltoluene of 0.7 [*Kirchstetter et al.*, 1996]. A similar composition is assumed for the Milano metropolitan area.

6.3.3 Statistical Analysis Method

The bulk of the CH_2O variability in the afternoon is assumed to be due to secondary formation of formaldehyde from VOC oxidation, under the condition that the NO availability is not a limiting factor (see *Sec. 2.3.3*). It is therefore expected that a large fraction of the variability of CH_2O concentrations in the afternoon can be explained by the temporal/spatial VOC variability. The idea in the following analysis is thus to explain a large amount of the formaldehyde variance by means of a quantity representing VOC oxidation by reaction with OH which initiates the major CH_2O formation pathways. The concept is realised by applying a correlation analysis to find a suitable predictor for the CH_2O variability. In return, the obtained regression model can be used to reproduce the formaldehyde variation. Since the temporal variability of formaldehyde (spatial variability in the case of aircraft measurements) might be approximated by the average VOC and OH radical content of the air mass, the predictor should be a function of VOC and OH availability.

- The ambient VOC content has a large spatial variability. Since formaldehyde is a relatively short-lived compound, the formaldehyde concentration is thus related to local VOC concentrations with a spatial smearing that increases with the VOC lifetime. Methane is the most abundant hydrocarbon in the troposphere with an average concentration of 1900 ppbv in the Po Basin [*ARPA*, 2004]. Due to its low reactivity towards oxidants, methane has a relatively long lifetime and is well-mixed in the boundary layer. Therefore, it does not contribute significantly to CH_2O variability. The variability of the formaldehyde concentrations can be associated with short-lived hydrocarbons measured at the same site. Thereby, reactive compounds (e.g. alkenes, many aromatics) contribute more to the spatial resolution of the CH_2O signal than less reactive VOCs (e.g. alkanes, benzene).
- The availability of OH is represented by a term proportional to the radicals produced. A major source for OH radicals in the afternoon is the photolysis of ozone and the subsequent reaction with water vapour (eq. 2.6). Hence, the OH production is assumed to be proportional to the product of the mixing ratios of ozone and water vapour.

To take the VOC lifetime into account, we make use of the OH reactivity (see eq. 2.15) of the VOCs. It is assumed that CH_2O is produced in the first stage of oxidation or quickly thereafter (i.e. from short-lived intermediates). The rate of formaldehyde produced from a VOC oxidation reaction depends on the local concentration of the VOC, weighted by the rate constant towards

OH (or O_3) and the respective formaldehyde yield of the reaction (see eq. 2.16). To consider the OH availability, the reactivity term is stepwise multiplied by the mixing ratios of ozone and water vapour.

The chemical variables were averaged over a time interval of 10 and 20 minutes, respectively, which corresponds to the collection time of the hydrocarbon samples (see Table 6.2). Data between 12 h and 18 h were considered for the ground sites to exclude the peak primary emissions in the morning and effects due to the formation of a shallow stable boundary layer in the evening (see *Sec. 2.4.1*), respectively. Nighttime and morning values were excluded due to missing photochemistry and fresh emissions. Both, the OH concentration and the mixing ratios of the NMHCs decrease with altitude, resulting in a much lower CH_2O production at higher altitudes. Only data below 1000 m a.s.l., i.e. within the convective boundary layer, were used in the analysis of aircraft measurements. For this data set it is assumed that formaldehyde is in equilibrium with its precursors.

6.3.4 Formaldehyde Variability over the Metropolitan Area of Milano 1998

During the LOOP/PIPAPO campaign in May/June 1998, nine measurement flights over the Milano metropolitan area have been conducted by MetAir / PSI. The Dimona aeroplane operated mostly during the afternoon hours. Formaldehyde concentrations were measured with a Hantzsch monitor [*Kelly and Fortune*, 1994] incorporated into the aircraft, ozone concentrations with a UV-photometer and concentrations of forty C_4-C_{10} VOCs by an onboard gas chromatography system (see Table 6.2), which takes integrated samples of 10 minutes each and subsequently analyses them, while drawing the next sample. The detection limit is 5-20 pptv. The further instrumentation on the aeroplane is described by *Neininger et al.* [2001]. An overview of the CH_2O concentrations along all flight tracks combined is shown in *Fig. 6.9*. The highest formaldehyde concentrations, given in yellow colour, are observed over and north of Milano. The flying altitude followed the airspace regulations. It was about 600 m a.s.l. in the plain and up to 2700 m a.s.l. above the Alpine foothills. Thus, the flights mostly took place within the planetary boundary layer. North of 45.8°N, the presence of the foothills of the Alps required higher flying altitudes.

In the following correlation analysis, the aim is to find a regression model that explains a large fraction of the formaldehyde variance and to estimate the CH_2O concentration from this regression model. Different predictor variables dealing with formaldehyde formation are used in succession to explain the CH_2O variability. The coefficient of determination (squared correlation coefficient), r^2, from the statistical analysis indicates the fraction of total variance of the formaldehyde data explained by each regression model.

The sum of OH reactivities, R_{VOC} (see eq. 2.15), of all VOCs measured on the plane, given by the respective concentrations multiplied by their OH rate constants, and including the

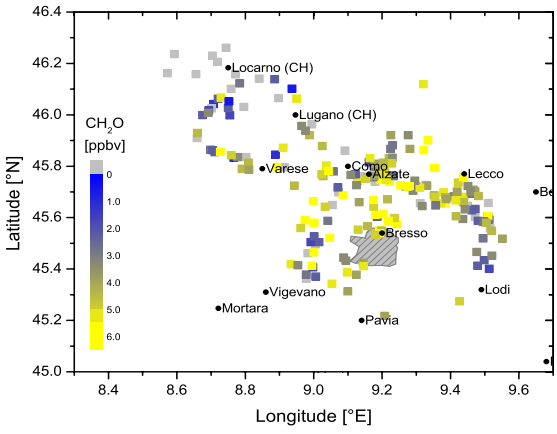

Figure 6.9: Spatial distribution of formaldehyde during the LOOP flights in early summer 1998. The highest formaldehyde concentrations (yellow) are found over and north of Milano, lower formaldehyde concentrations (blue) are found upwind, i.e. south, of the city. If no formaldehyde data were available, data points are displayed in grey. The urban area of Milano is illustrated as grey hatched area.

estimated reactivities (see *Sec. 6.3.2*), explains 42% of the CH_2O variance observed during PIPAPO 1998 (*Fig. 6.10a*). The varying availability of the OH radicals must also be considered for the oxidation of the organic compounds. Since ozone photolysis is the major source of OH radicals in the afternoon, the reactivity R_{VOC} is multiplied by the ozone concentration in a second step. The ozone-weighted term explains 58% of the variance in CH_2O concentrations (*Fig. 6.10b*). The orange markers denote data points from the flight on 13 May 1998, a day with particularly low specific humidity (average 7.0 g kg^{-1}) but high ozone concentrations. These data points are not in line with those data points from other days. Because of the high ozone concentrations a large amount of OH radicals should be produced, oxidising VOCs and yielding formaldehyde. On the other hand, the lack of water vapour on the same day lowers the expected OH production. Finally, the VOC reactivity, weighted with the respective ozone concentration and specific humidity [g kg^{-1}], gives a measure for the VOCs oxidised with the OH radicals available. The data points in *Fig. 6.10c* then fall more closely onto a line than in *Fig. 6.10a,b*. The term $R_{VOC} \cdot [O_3] \cdot [H_2O]$ seems to be an appropriate predictor for the observed CH_2O variability, explaining 73% of the spatial formaldehyde variance experienced during the LOOP flights. High altitude measurements (> 1000 m a.s.l.) are excluded from the analysis.

A linear orthogonal regression [e.g. *York*, 1966] between the measured CH_2O concentrations and the total VOC reactivity, weighted by O_3 and H_2O mixing ratios, was derived from *Fig. 6.10c*. The regression parameters obtained are used to estimate formaldehyde concentrations from the predictor variable, P (defined by eq. 6.1). The relationship, which explains around 73% of the observed CH_2O variance ($r = 0.85$), is exemplified by eq. 6.2.

$$P = R_{VOC} \cdot [O_3] \cdot [H_2O] \qquad \text{(eq. 6.1)}$$

$$CH_2O_{est} = 1.76 + 0.001679 \cdot P \qquad \text{(eq. 6.2)}$$

R_{VOC} consists of the OH-reactivities of all VOCs measured on board of the aeroplane, extended by estimated reactivities of missing VOCs. The latter were derived as outlined in *Sec. 6.3.2* and include ethane, propane, ethyne and the reactive alkenes ethene and propene.

The time series of estimated and measured CH_2O concentrations is shown in *Fig. 6.11*. Black circles denote the measured formaldehyde concentrations averaged over the same time interval as the VOC samples. The red squares show estimated formaldehyde concentrations as obtained from eq. 6.2 with the predictor P, given above. The estimated time series largely follows the measured one. There were no formaldehyde measurements on 12 May 1998, however mixing ratios estimated from VOC data for the afternoon of that day are around 4-6 ppbv. The high estimated formaldehyde concentration on 13 May 11:21 h is attributed to unusually high concentrations of several highly reactive aromatic compounds (xylenes, ethyltoluene) measured

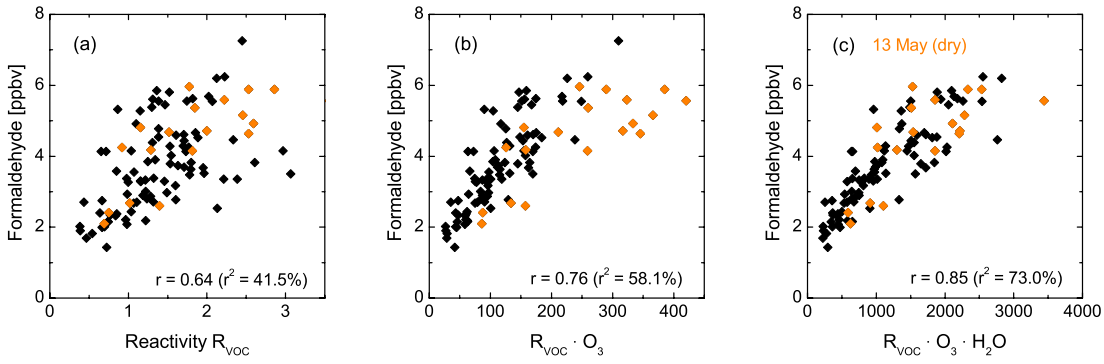

*Figure 6.10: Scatterplots of the measured CH_2O mixing ratios versus **(a)** OH-reactivity-weighted VOCs (R_{VOC}), **(b)** $R_{VOC} \cdot [O_3]$ and **(c)** $R_{VOC} \cdot [O_3] \cdot [H_2O]$. Markers in orange denote data points from 13 May 1998 (see text for details).*

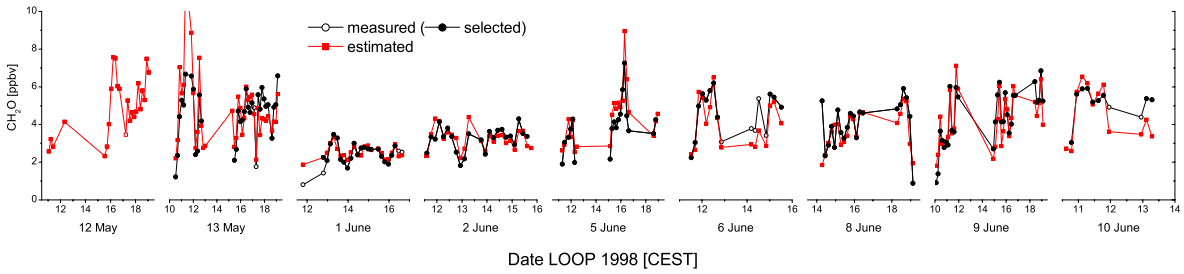

Figure 6.11: Time series of formaldehyde mixing ratios measured (black) and estimated (red) for the LOOP campaign 1998. Open circles mark data points which do not match the selected requirements, i.e. samples taken above 1000 m.

close to Como. However, formaldehyde is not formed in the first reaction steps of the oxidation of aromatic VOCs and the yields are still uncertain.

The spatial distribution of measured and estimated mixing ratios is visualised in *Fig. 6.12*. Thereby, the left hand plot denotes the measured values and the right hand plot shows values estimated from the predictor. Some samples north of 45.8°N were taken in altitudes higher than 1000 m and are displayed as empty squares. A very good overall agreement of the measured spatial CH_2O variability and the estimated values is obtained. The observation clearly shows high CH_2O concentrations north of Milano. Also west of Milano, the concentrations are higher than east of the city. This pattern is also reflected by the estimate (see *Fig. 6.12b*). The differences between measured and estimated formaldehyde concentrations can depend on the flying altitude, the time of day or the measurement region. The flying altitude in the area around Milano (south of 45.8°N) did not vary much, since the airspace allowed to operate with small aeroplanes under visual flight rules is restricted to below 2000 ft (~ 600 m) above sea level. The time of day might be relevant during the rush hour because primary formaldehyde, which is not reflected in the estimated CH_2O, could play a role then. However, the aeroplane usually operated during the afternoon hours (see *Fig. 6.11*) and the largest differences did not occur during the rush hours. The dependence on the measurement region is studied in the following paragraph.

The available data points were grouped in two classes, those located in the Milano metropolitan area and those in the pre-Alpine valleys. Average differences between estimated and measured concentrations in selected regions were quantified by calculation of the percent differences

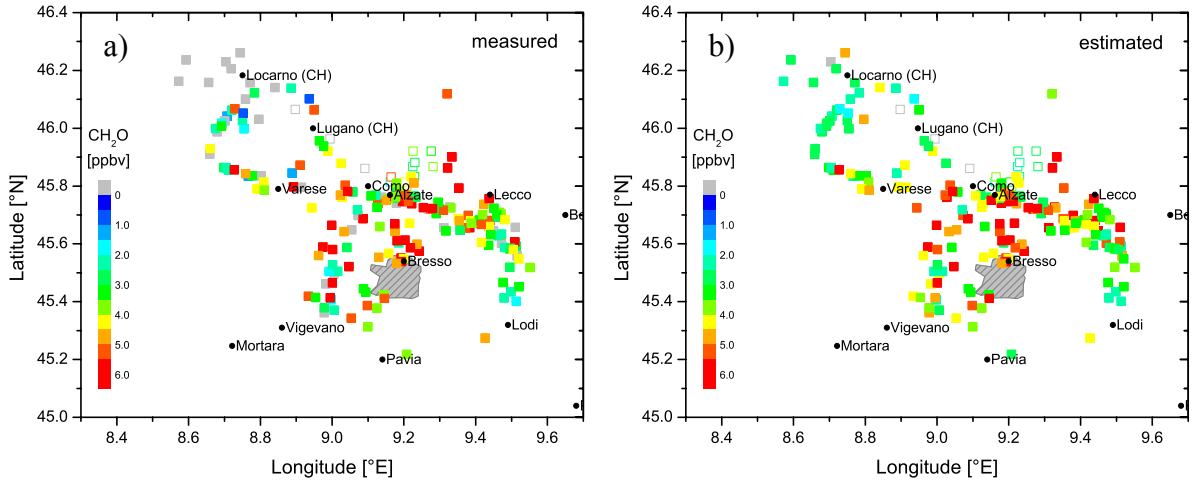

*Figure 6.12: **(a)** Measured and **(b)** estimated formaldehyde mixing ratios during LOOP flights. The colours correspond to the respective formaldehyde mixing ratios. For grey data points no concentration value is available. Open symbols denote samples taken in altitudes > 1000 m (figure from Hak et al. [2006]).*

(*Fig. 6.13*). Negative values represent overestimation of the observation and vice versa. In the region of study (around Milano) the estimated values deviated mostly around 15-20% from the measured ones, underestimating the measurements. The largest deviations were found for air samples taken around the region of Locarno (southern Switzerland), where the aeroplane was based. In the pre-Alpine valleys between Varese, Lugano and Locarno, observations were occasionally largely overestimated by the output values.

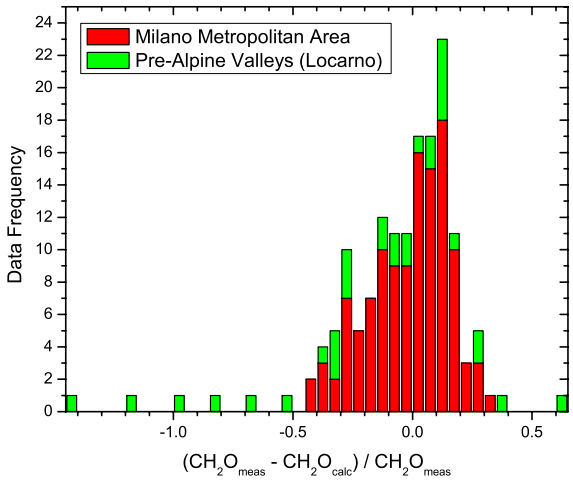

Figure 6.13: Frequency distribution of differences between measured and estimated formaldehyde concentrations in the metropolitan area of Milano (red) and the pre-Alpine valleys, i.e. close to Locarno (green).

The analysis showed that, knowing [VOC], [O_3] and [H_2O], a prognosis for the formaldehyde variability should be possible within a certain error range. With an explained variance of 73%, the variability of CH_2O can be understood to a great extent. The remaining variance might be due to unconsidered sources like primarily emitted formaldehyde, reactive VOCs not included in the analysis or possible errors in the measurements. The method solely explains the formaldehyde variability due to secondary production. However, as could be seen in the above analysis, the secondary production of formaldehyde explains a large part of its variability, i.e. the variability of CH_2O concentrations in the Milano metropolitan area reflects the production from VOC oxidation.

6.3.5 Formaldehyde Variability over the Metropolitan Area of Milano 2003

Between 15 and 27 September 2003, nine flights over the metropolitan area of Milano and along the Po Basin were performed by MetAir. The usual flying altitude in the Milano region during the FORMAT II flights was between 600 and 700 m a.s.l. as prescribed by the local flight rules. The instrumentation on board of the MetAir Dimona was basically the same as during the LOOP measurements, utilising a Hantzsch formaldehyde monitor (type described by *Junkermann and Burger* [2006]) and an ozone monitor working with UV-absorption. The concentrations of C_4-C_{10} VOCs (38 compounds) were measured continuously using a GC (see Table 6.2) with a sampling time of 10 min. Additionally, six canister samples per flight were collected (filling time 2 min) which also cover the smaller alkanes and alkenes. The hydrocarbon canister samples were later analysed by EMPA for selected C_2 to C_6 VOC compounds (see Table 6.3) using a GC-FID Varian 3400. The VOC canister samples and the subset of coincident GC measurements (of the same compounds) revealed a good agreement for most compounds measured with both methods. It is assumed that this also applies for the entire data set so that the GC measurements and the canister samples complement one another.

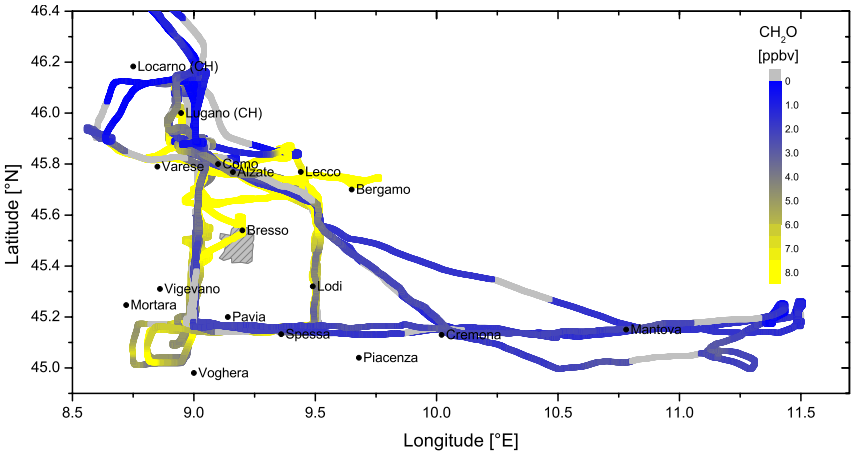

Figure 6.14: Spatial distribution of formaldehyde during the FORMAT II flights in autumn 2003 observed by the MetAir Dimona. All FORMAT II flights are merged in this overview. The urban area of Milano is illustrated as grey hatched area.

Box flights around the agglomeration of Milano were performed between 15 and 20 September in order to assess the ambient CH_2O concentration upwind (south) and downwind (north) of Milano. During the afternoon, the formaldehyde concentrations in the urban plume north of Milano are generally high compared to the concentrations south of Milano or along the Po Basin (see *Fig. 6.14*). The increased CH_2O concentrations southeast of Milano (between Voghera and Mortara) were observed on 16 and 17 September and can be related to agricultural burning taking place in this area in autumn (the formaldehyde emission from these fires is studied in *Sec. 6.4*). Low formaldehyde concentrations are observed north of 45.8°N as the aircraft had to fly at altitudes higher than 1000 m above the Alpine foothills. The last three flight days were assigned for measurements along the Po Basin where low concentrations and variability of CH_2O were found. The formaldehyde and most other measurements on the aeroplane have a higher sampling frequency than the VOC measurements (10 min), leading to the high spatial resolution shown in *Fig. 6.14*.

Again, a correlation analysis is used to obtain the strength of the statistical relationship between CH_2O and the predictor. The same approach as in *Sec. 6.3.4* is used to explain the spatial formaldehyde variability in the FORMAT II campaign. The concentrations of the VOCs weighted by their OH rate constants, i.e. the reactivity R_{VOC}, can explain 66% of the CH_2O variance during FORMAT II. More than 82% are explained by additionally weighting by the ozone concentration to take OH availability into account. However, subsequent weighting by specific humidity does not further improve this result. In contrast to the LOOP campaign, day-to-day variations of humidity were not a crucial factor for the explanation of CH_2O variance in the FORMAT II airborne measurements. The relationship between measured CH_2O and the predictor term $P = R_{VOC} \cdot [O_3] \cdot [H_2O]$, derived from linear regression, was used to estimate the formaldehyde concentrations:

$$CH_2O_{est} = 2.13 + 0.003232 \cdot P, \quad r = 0.90 \qquad \text{(eq. 6.3)}$$

Overall, the measured variability of CH_2O concentrations is reproduced very well (see *Fig. 6.15*) by the estimates. There is a clear underestimation during the first part of the flight on 18 September, while peak values are overestimated on the following day. The observations show almost no variability along the Po Basin. There, formaldehyde concentrations around 1.75 ppbv are measured most frequently. The low CH_2O concentrations and little variability during the flights on 25-27 September can be attributed to two reasons. Firstly, due to a change in the weather conditions, associated with the passage of a front resulting in a period of lower

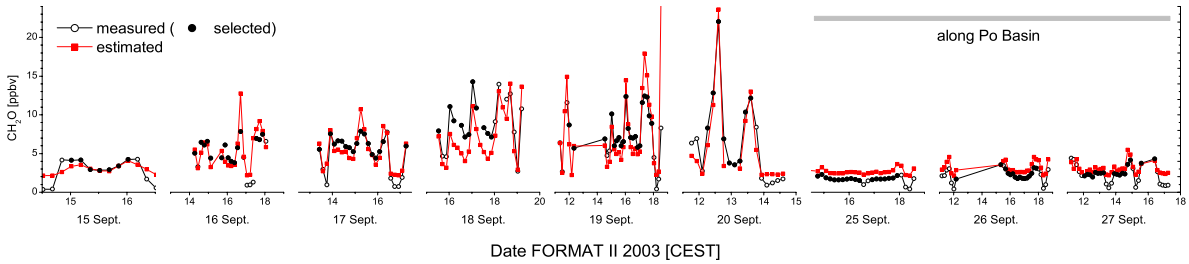

Figure 6.15: Time series of formaldehyde concentrations measured (black) and estimated (red). The first six flights took place in the metropolitan area of Milano. The last three flights extended eastward into the Po Basin. Since altitudes > 1000 m were excluded, these data points are displayed as empty circles.

temperatures, cloudy skies and occasional rain events, the formaldehyde levels observed after 22 September were generally lower than during the previous week. This also becomes obvious in the ground-based data (see e.g. *Sec. 4.3*). Comparing the measurements of the first six flights in the Milano metropolitan area with the data from the last three flights within the metropolitan area, a drop of ozone concentrations from 95 ± 18 ppbv (average ± standard deviation) to

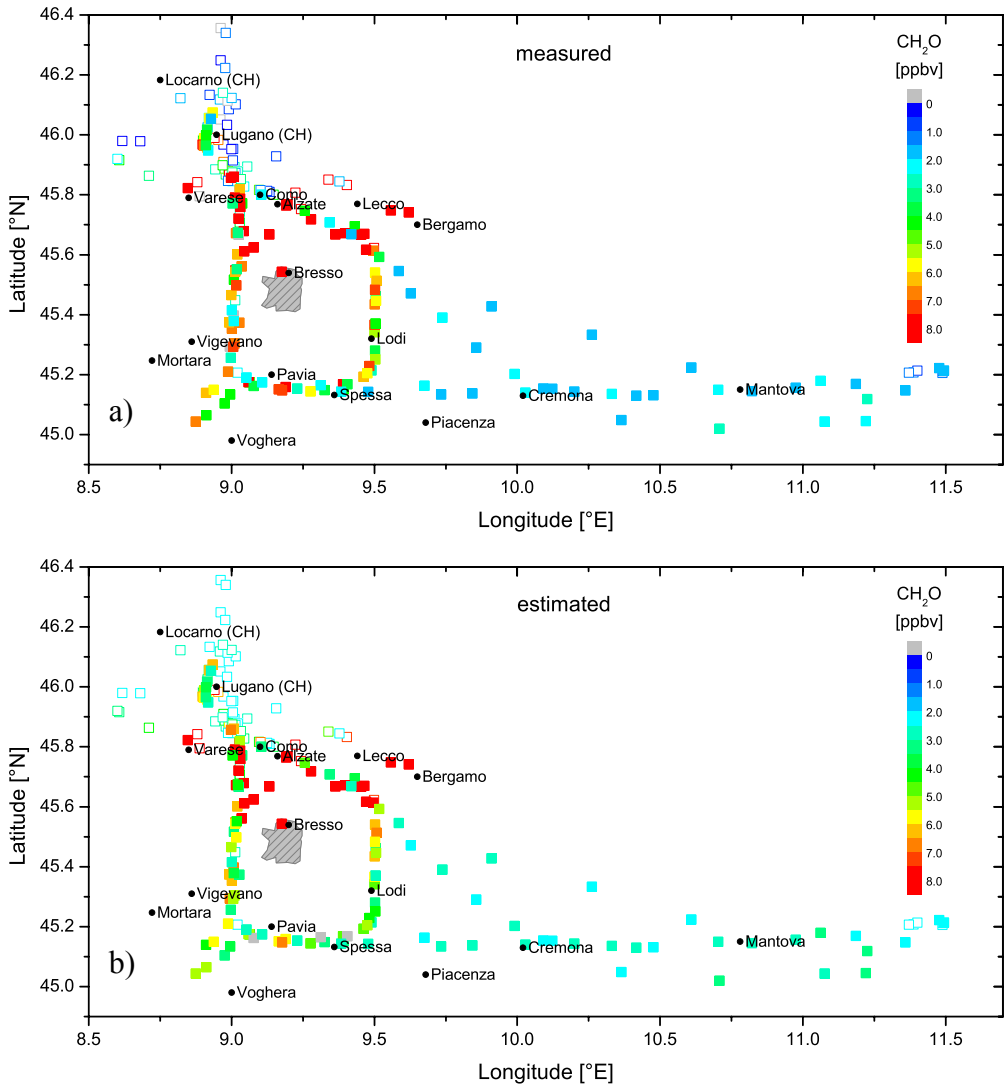

*Figure 6.16: Spatial variability of **(a)** measured and **(b)** estimated CH_2O concentration during the flights performed in the 2003 FORMAT campaign. Empty squares, predominantly north of 45.8°N, denote samples taken at altitudes > 1000 m.*

46 ± 10 ppbv becomes obvious. Similarly, the specific humidity falls from 7.8 ± 0.8 to 6.2 ± 0.5 g kg^{-1}. This means that a lower oxidant concentration was present in this final part of the campaign. The VOC reactivity, R_{VOC}, decreases from 0.80 ± 0.43 to 0.64 ± 0.38 s^{-1}. This is ascribed to both, a lower VOC concentration and to the lower temperatures, reducing the chemical reaction kinetics. The air masses probed in late September are thus less processed than those in mid-September. The O_3 and H_2O levels on 25-27 September along the Po Basin are comparable to those in the Milano area in the same time period. Secondly, additional to the reduced potential of secondary formaldehyde formation for the flights on 25-27 September due to the weather conditions, the VOC concentrations and variability are generally lower in the Po Basin than in the Milano metropolitan area. For the VOC reactivity in the Po Basin a value of 0.24 ± 0.09 s^{-1} is found (compare to above). The VOC variability is smaller in the Po Basin because there is less emission variability and this is reflected in the formaldehyde variability.

The estimated and measured spatial formaldehyde distribution is shown in *Fig. 6.16*. Estimation (lower plot) and measurement (upper plot) largely agree. In the agricultural area between Pavia, Voghera and Mortara, formaldehyde concentrations are underestimated, most probably due to primarily emitted CH_2O from agricultural fires, which were observed there on 16 and 17 September (see *Sec. 6.4*). In the Milano metropolitan area, formaldehyde concentrations are underestimated on average by 15% (see *Fig. 6.17*). During the last three flights, performed along the Po Basin, formaldehyde concentrations are overestimated on average by 30%, but up to 50%. These flights occurred late in September. Under the lower oxidant concentration due to lower radiation conditions and temperatures, the photochemistry is slowed down and the air masses stay urban-like for a longer time. the formaldehyde was probably not in equilibrium with its precursors. The actual formaldehyde production was therefore below the potential of CH_2O generation which is possible under summer conditions, considering the VOC concentrations measured.

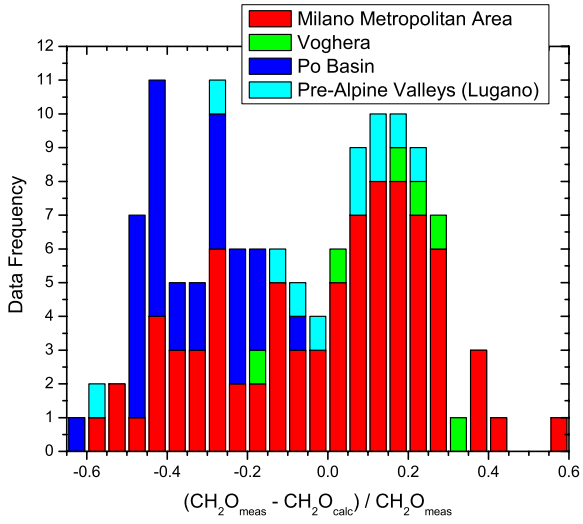

Figure 6.17: Frequency distribution of differences between measured and estimated formaldehyde concentrations in the metropolitan area of Milano (red), the Po Basin (blue) and the pre-Alpine valleys, i.e. close to Lugano (light blue).

6.3.6 Temporal Formaldehyde Variability at Alzate 2003

The principle described above is applied to ground-based measurements from the FORMAT II campaign performed at Alzate (this section) and Bresso (see *Sec. 6.3.7*). The ground-based instruments were operated day and night. However, for the analysis of secondary formaldehyde formation only daytime measurements between 12 and 18 h (afternoon) are considered. During

nighttime, other processes are responsible for the temporal variability of the formaldehyde concentrations.

Continuous measurements (hourly data) of C_2-C_7 VOCs were obtained at Alzate with a GC-FID (see Table 6.2) operated by EMPA from 16 September until 23 September and 26 September until 5 October 2003. The VOCs were enriched during 20 min as described by *Steinbacher et al.* [2005] and subsequently analysed. Ozone concentrations were measured by PSI using UV-absorption. To ensure studying identical air volumes, the data used for the present analysis were derived from instruments which sampled at the same place and provided point measurements. However, since the Hantzsch formaldehyde monitor by IFU was only operated until the evening of 3 October and was then removed from the site, it was checked whether DOAS formaldehyde data can be used for the last two days (4 and 5 October) to supplement the data set. The long path DOAS by IUP at Alzate continued measuring until 7 October. In the middle of the campaign, the data set is fragmentary due to fog and instrumental problems. Since the long path DOAS probes a different air volume than the Hantzsch monitor, differences in the measurement results can arise. This is particularly relevant in summer, when the isoprene oxidation can lead to large differences between DOAS results measured close to a forest and in-situ Hantzsch results (see *Sec. 5.3.3*). In autumn 2003, however, concurrent DOAS and Hantzsch data agree well. That is, the influence of isoprene oxidation seems to be less pronounced in this time of the year and the DOAS data can be used alternatively. The sample inlets of GC, Hantzsch and ozone monitor were mounted at a height of 2 m above the roof of the measurement container. Details on the characteristics and instrumentation of the site can be found in *Sec. 4.2.2*.

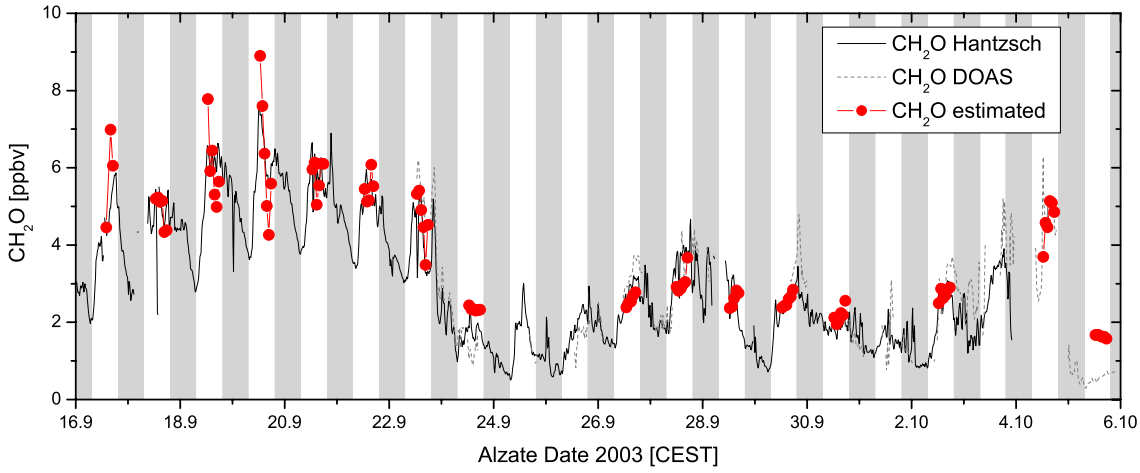

Figure 6.18: Time series of formaldehyde concentrations measured (black) at Alzate during the FORMAT II campaign in autumn 2003 and predicted (red). Ticks are located at 00:00 h. White and grey bars indicate sunlit and nighttime hours.

The temporal course of the CH_2O concentrations as measured by the Hantzsch monitor is depicted by the black line in *Fig. 6.18*. Variations of the formaldehyde concentration between 0.5 and 7.5 ppbv were observed at Alzate during the FORMAT II campaign. The meteorological parameters during the high pressure period (17-22 September) featured a regular diurnal variation and variable conditions afterwards. There was a distinct diurnal variation of formaldehyde during the stable period with concentrations rising steeply until reaching a first peak at 10-11 h. During afternoon hours, formaldehyde levels remained constant or decreased slightly. The variation described in *Sec. 6.1* is most pronounced during the fair weather periods. In the time after 22 September, the formaldehyde concentration featured a less characteristic variation.

A similar correlation analysis as shown in the previous sections was done here as well. Since the concentrations in the morning might be affected by fresh primary emissions and to avoid the

dynamical effects in the evening, the analysis was restricted to afternoon periods between 12 h and 18 h. In this range of time, the nocturnal ground inversions have dissolved and the boundary layer is well mixed. The predictor P is calculated according to eq. 6.1 from afternoon data to regard only secondary formaldehyde. The reactivities of all VOCs measured at the site and the estimated reactivities contribute to the analysis. The consideration of the water vapour variability leads to a slight improvement of the correlation. The resulting correlation coefficient $r = 0.94$ between P and the measured CH_2O concentrations indicates that more than 87% of the total variation in CH_2O at Alzate can be explained by the variation of VOCs and OH production. The relationship found between measured CH_2O and the predictor P was:
$CH_2O_{est} = 1.49 + 0.001416 \cdot P$.

The day-to-day variability of formaldehyde can be qualitatively well reproduced from the estimate $P = R_{VOC} \cdot [O_3] \cdot [H_2O]$, as the calculated CH_2O concentrations (red markers in *Fig. 6.18*) closely follow the measurements. The enhanced background values during the fair weather days in mid-September are reflected in the estimated time series as well. Also the afternoon variability can mostly be conceived from oxidation of the measured VOCs. The bimodal diurnal cycle of isoprene [*Steinbacher et al.*, 2005] reactivity strongly influences the estimated CH_2O concentrations.

The agreement between measured CH_2O and formaldehyde concentrations estimated from VOC oxidation within the selected time interval is quite good. Most of the data between 12 h and 18 h could be approximated within ± 15%. After the high pressure period in mid-September, observed and estimated concentrations hardly differ on 26, 29 and 30 September and on 2 October. Even the short-term variability of measured CH_2O could mostly be captured by VOC oxidation. Concentrations are overestimated on 23 September and underestimated on 27 September. After 3 October, no Hantzsch measurements are available to compare with, but the long path DOAS was still in operation and on 4 October there was good agreement between estimated formaldehyde concentrations and measurements by DOAS. On 5 October was a strong foehn day with very low formaldehyde concentrations (below 1 ppbv) and little diurnal variability. The estimated concentrations show no diurnal variation as well but largely overestimate the observed values. The strong northerly wind (up to 7 m s^{-1}) diluted the air to low concentration levels. During the north foehn conditions, the formaldehyde concentrations are < 1 ppbv and correspond to the background values. The VOCs emitted locally have not been converted to CH_2O yet. The formaldehyde is not in equilibrium with its precursors and too high concentrations are estimated. Since the applied method is bound to the formation of OH in the presence of sunlight, it is only valid during the photoactive periods, i.e. during daytime.

6.3.7 Temporal Formaldehyde Variability at Bresso 2003

Semi-continuous measurements of thirty ozone precursor VOCs in ambient air were performed during FORMAT II at Bresso day and night with a GC-FID analyser operated by JRC (see Table 6.2). The 163 C_2-C_9 VOC samples of 20 min each were collected at irregular points of time between 12 September to 1 October 2003 and subsequently analysed in the field. Formaldehyde was measured by IFU with a Hantzsch monitor and by IUP with an LP DOAS. The two techniques probed different air volumes, which is reflected in the formaldehyde results. Along the DOAS beams, which passed above the motorway (see *Sec. 4.3.3*), 20% higher concentrations were measured. Since the VOC measurements are point measurements, the Hantzsch in-situ data are used in the analysis. The ozone concentrations, which are assumed to be distributed more homogeneously in the boundary layer (see also *Sec. 5.3.2*), were taken from the long path DOAS. In urban areas, the most important contributor to ozone precursors is road traffic. This urban site is described in detail in *Sec. 4.2.3*.

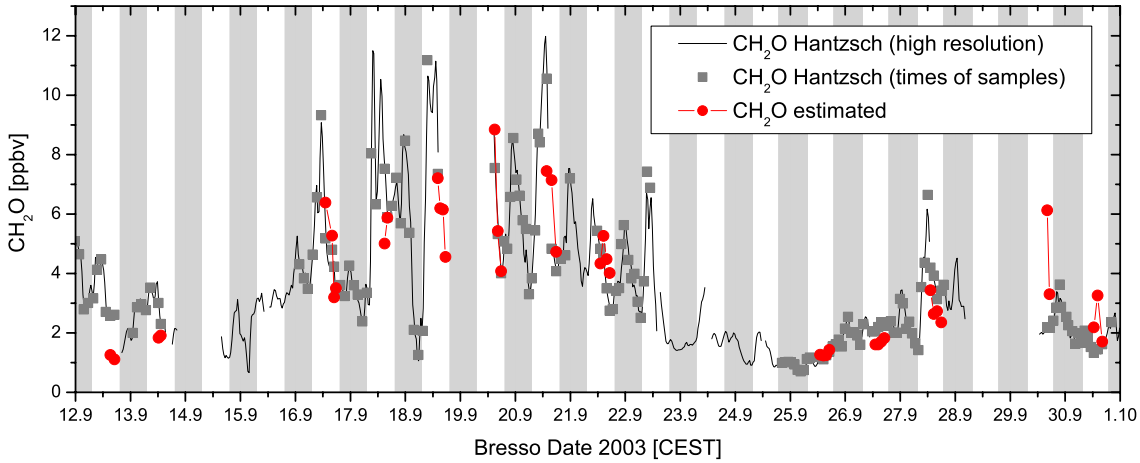

Figure 6.19: Time series of formaldehyde measured at Bresso (black trace) during the FORMAT II campaign in autumn 2003. Grey markers denote Hantzsch results averaged over the duration of each coincident VOC sample. Estimated concentrations are shown in red. Ticks are located at 00:00 h. Light grey bars mark nighttime.

At Bresso, a different diurnal formaldehyde variation than in Alzate was observed. It often featured two maxima, one around midnight and one around noon (see *Fig. 6.19*). Many peaks are not during sunlit time and therefore must originate from direct emissions. The secondary formation by reaction of alkenes with O_3 is regarded as much less important due to the more rapid titration reaction of ozone with NO. The morning formaldehyde peak coincides with NO_2 and thus seems clearly to directly originate from emissions.

First, a correlation-regression analysis as above was applied, i.e. the sum of the reactivities of all VOCs measured in Bresso was weighted by the ozone concentration and the specific humidity and an orthogonal regression of the formaldehyde concentration versus this term was calculated. Since the morning hours are assumed to be most strongly affected by emissions, only data between 12 and 18 h was considered in the analysis. Between 12 September and 1 October, 41 samples fall into this timeframe. The relationship between measured CH_2O and the term P (cp. eq. 6.1) was found to be: $CH_2O_{est} = 0.85 + 0.00077 \cdot P$ (with $r = 0.81$), where the consideration of the water vapour variation brought a slight improvement of the correlation. The red markers in *Fig. 6.19* represent CH_2O concentrations estimated from the secondary production term. On a rough temporal scale, i.e. the day-to-day variability, the variations of CH_2O concentrations are adapted well. The agreement with the measurement is in many cases quite good although this is not expected for a site like Bresso where fresh direct emissions are present. Substantial differences between the measured and calculated CH_2O were observed for some situations at Bresso. There are a few peaks in the measurements that the method does not capture and vice versa. The selection of the approach does not always appear sufficient to reproduce the measured CH_2O concentrations at an urban site. This can mean that primary CH_2O sources are important there during the entire day or that other VOCs are important producing formaldehyde. The high level of formaldehyde variance explained of 66% could be partly ascribed to the co-emission of formaldehyde and VOCs from vehicle traffic which is a very important source of pollutants at Bresso. This primarily released formaldehyde fraction might contribute to the afternoon concentrations, although these are considered as purely secondary. The secondary contribution to formaldehyde was found to make up ~ 90% at Bresso (Johan Mellqvist, pers. comm., 2006). Due to the fast reaction of NO with O_3, the distribution of ozone is not homogeneous in urban areas. Besides the VOCs which have not yet been converted to CH_2O, the possibly locally underestimated O_3 is relevant for the uncertainties in the estimation of formaldehyde at Bresso. Air masses sampled in Bresso might be influenced by very 'fresh'

emissions. Formaldehyde from direct anthropogenic emission would not be in photochemical steady state with the hydrocarbons measured at Bresso. Moreover, fresh VOC emissions are not in photochemical equilibrium with the present formaldehyde.

6.3.8 Discussion

A bulk of the CH_2O variance can be explained by the VOC-oxidation approach presented in this section. Especially in photochemically aged‡ air, the spatial CH_2O variability could be well reproduced from the term including VOC reactivity, ozone and water vapour content of the air. In the air masses observed on the aeroplane and possibly in Alzate, the formaldehyde concentrations are rather assumed to be in photochemical equilibrium with its precursors than in Bresso. This is an important requirement for the applied method. The good reproducibility of CH_2O concentrations suggests that CH_2O was mainly photochemically produced. Between 73% and 88% of the formaldehyde variance in aged air masses and 66% in the city are understood by considering the oxidation of the VOCs measured in two field campaigns. The remaining variance is most probably due to primary fractions of formaldehyde and uncertainties of the measured data. The rate constants of aromatic compounds with OH are among the largest of the VOCs measured (see Table 2.4). Since aromatics do not directly generate formaldehyde after reaction with OH and the CH_2O yields are still uncertain, the consideration of the aromatic compounds also might contribute as part of the unexplained variance.

The distribution of CH_2O is spatially dependent and reflects the relationship to major NMHC precursors and OH concentrations. Ozone and water vapour have no large spatial gradients. But for the day-to-day variability of formaldehyde, O_3 and H_2O play an important role besides the spatially strongly variable VOCs.

In the presented analysis, the OH production is assumed to be proportional to the product of the mixing ratios of ozone and water vapour; eq. 2.6 requires the diurnally varying $J_{O(1D)}$ as well in the approximation of OH production. However, the solar radiation accounts for both, formation and destruction of formaldehyde. For solar zenith angles < 70°, which are given in the afternoon before 18 h, $J_{O(1D)}$ is more or less proportional to J_{CH2O}, which is an important sink of CH_2O. This might be the reason why the solar radiation does not need to be taken into account for the approximation of formaldehyde.

In the analysis shown in *Sec. 6.3.4-6.3.7*, the extended sets of all VOCs measured at the respective sites, including estimated reactivities, were used. Since different VOC species and different amounts of species were measured at the different sites, it is not appropriate to compare the slopes of the formaldehyde-to-VOC-reactivity relationships derived from the different sites. To compare the analysis results of the two aircraft campaigns (*Hak et al.*, 2006, in prep.) and the two ground-based sites, respectively, the VOC data set has to be confined to the same selection of precursor species for all sites. Ten compounds, consisting of butane, pentane, hexane, isobutane, isopentane, 2-methylpentane, 3-methylpentane, benzene, toluene and isoprene (printed in bold in Table 6.3), have been measured at all sites. If the same correlation regression analysis as in previous sections is applied, using the reactivities of the limited set of VOCs as R_{VOC}, we obtain regression results as presented in Table 6.4. At most sites, the explained formaldehyde variance is slightly lower than before. No significant differences between formaldehyde concentrations estimated by the different predictors were found. Linear relationships are found between different predictors, using the subset of VOCs, the full data set or formaldehyde production efficiencies. This may be due to the fact that many VOC compounds are co-emitted

‡. Aged air is air which had been subject to photochemical processing so that reactive VOCs have been converted and generated formaldehyde and other products.

Table 6.4: Regression parameters (a: intercept, b: slope of regression line, r: correlation coefficient) and explained variance for an analysis using reactivities of the same 10 VOC species measured at all sites (see Table 6.3).

Site	a	b	r	Variance [%]
Bresso	1.342805	0.003247	0.806662	65.1
Alzate	1.512565	0.002330	0.934740	87.4
LOOP	1.933540	0.003040	0.837342	70.1
FORMAT II	2.109744	0.006843	0.907711	82.4

by the same sources. The proportion of explained variance is mostly well above 70% and up to 90%, reflecting that the VOC · O_3 · H_2O tracer generally replicates well the observations.
If the same limited set of VOCs is used for all sites in the above analyses, a direct comparison of the regression parameters reveals similar slopes for most sites (*Fig. 6.20a*), except the FORMAT II flights, where the slope is about twice of what was derived for the LOOP flights.

The measurements performed within the scope of the field experiment PIPAPO and during the FORMAT II campaign revealed a high degree of explained formaldehyde variance. But the slope of the regression line (0.006843) is very steep for the FORMAT II flights compared to the other three data sets (e.g. LOOP: 0.00304). This is probably due to the high formaldehyde concentrations that were measured on the plane in 2003 while the VOC concentrations were generally of the same level as those during the LOOP flights which took place in the same area (see *Sec. 6.3.1*).

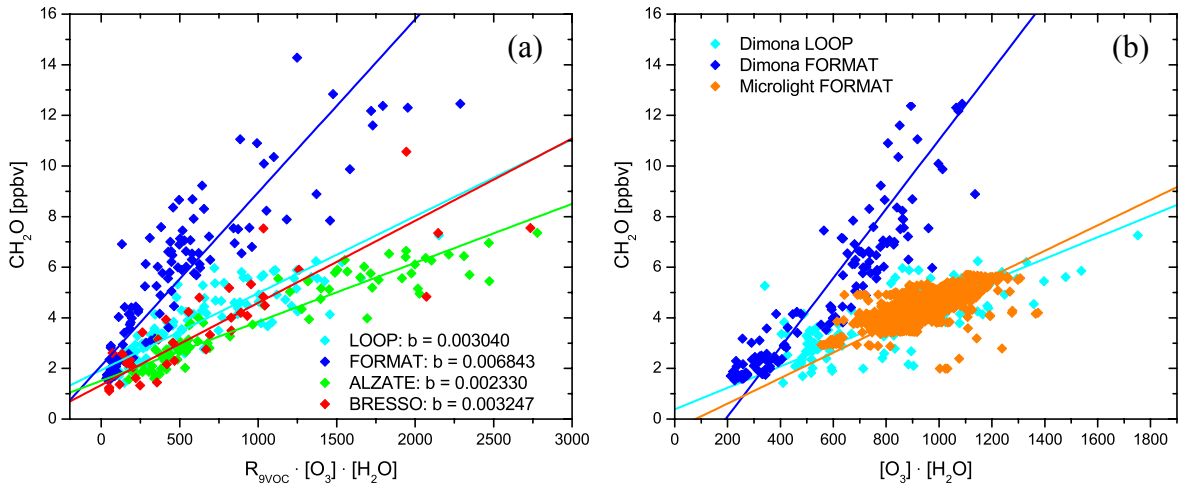

*Figure 6.20: **(a)** Formaldehyde relationships towards $R_{9VOC} \cdot O_3 \cdot H_2O$. For all data sets, except the FORMAT II airborne measurements, similar slopes are obtained if the same subset of VOCs is considered. **(b)** Formaldehyde relationships towards $O_3 \cdot H_2O$ for three aircraft data sets indicate that Dimona Hantzsch data during FORMAT were systematically high.*

Comparisons to concurrent ground-based measurements and to other airborne measurements performed in the same regions (temporally close) indicate probably too high concentrations measured by the Dimona Hantzsch monitor on some days. On 20 September, the aeroplane flew at low altitude over the Bresso runway (12:27-12:33 h) and measured concentrations between > 25 and 28 ppbv, whereas on the ground site 15 ppbv were measured by the LP DOAS, 11-13 ppbv by the FTIR White system and 11 ppbv by the Hantzsch monitor. Data from the microlight, operated by IFU, is included as another aircraft data set for FORMAT. No VOCs

were measured on board of the microlight. The air masses can nevertheless be compared regarding the term $O_3 \cdot H_2O$, because the general levels of VOCs were very similar in both campaigns (*Fig. 6.7*). The right hand plot of *Fig. 6.20* shows that the relation between formaldehyde and $O_3 \cdot H_2O$ is similar for the LOOP data set and the FORMAT data from the microlight, but the FORMAT data from Dimona deviate, though the Dimona and the microlight sampled the same air masses during FORMAT. These hints indicate that the formaldehyde concentrations measured in 2003 were too high. In fact, problems with a drifting zero baseline were encountered for the Hantzsch on board of the Dimona during FORMAT II (Josef Dommen, pers. comm., 2004).

Although it is not a homogeneous data set, regarding the different measurement instruments used at different measurement sites, a relatively consistent result is obtained by merging the different measurements. Considering that the uncertainties in the individual data sets can amount to 30%, the resulting estimated formaldehyde variability can be regarded as very good.

6.4 Direct Formaldehyde Emission by Biomass Burning

Biomass burning can be a major primary source of enhanced formaldehyde and a large number of other trace gases (see *Sec. 2.1.4*). The gases emitted by the fires influence the local to regional air chemistry by altering the oxidation capacity of the air mass. In Northern Italy, burning down of harvested fields constitutes a significant seasonal emission source in the autumn months. During the FORMAT II campaign in autumn 2003 several instances of agricultural fires were observed south of Milano and trace gases were measured, both ground-based and airborne. In this section, an emission factor of formaldehyde for the combustion of rice stubble is determined from ground-based data, in agreement with an objective of the FORMAT project to quantify the formaldehyde emissions from biomass burning. The combustion efficiency (see *Sec. 2.1.4* for definition) of agricultural fires observed in the Po Basin is derived from airborne data. CH_2O/CO emission ratios are calculated and compared to those from African savanna fires published in the literature. Further, an estimation of the influence of agricultural burning on the local radical budget is given. In the following section, a compilation of emission quantities presented in the literature is given.

6.4.1 Published Emission Factors

Physical and chemical properties of the biomass fuel have a significant effect on the emissions of a biomass fire (see *Sec. 2.1.4*). For various types of biomass burning, emission factors and ratios have been published, determined both in the laboratory and in the field. Here, we concentrate on the emissions of formaldehyde and sulphur dioxide from the fires. Some emission factors and emission ratios for CH_2O and SO_2 from savanna, rice straw and general vegetation fires are shown in Table 6.5.

Emissions from African savanna [§] fires have been intensively studied using aircraft measurements [e.g. *Yokelson et al.*, 2003; *Sinha et al.*, 2003], but there is a lack of information on 'Indonesian' fuels [*Christian et al.*, 2003]. These include rice straw burning, which is a substantial source of trace gases in Southeastern Asia. No field measurements of the CH_2O emission factors from burning of rice straw are available. *Christian et al.* [2003] performed laboratory studies, both on African and Indonesian fuels, including rice straw burning and derived a CH_2O emission factor of 3.17 g kg^{-1}. However, the setup for burning the rice straw simulated the East Asian practice to pile up the straw before burning. This results in a larger relative amount of smouldering combustion towards flaming combustion than it is the case in the open burning of

§. Savanna: seasonally dry grassland with scattered trees. Savannas are sometimes transitional zones, occurring between forest or woodland regions and grassland regions.

Table 6.5: Summary of emission factors, EF, (dry mass) of CH_2O and SO_2 and emission ratios, ER, (with respect to CO or CO_2) for the combustion of several biomass fuel types published in the literature.

EF_{CH2O} [g kg^{-1}]	EF_{SO2} [g kg^{-1}]	EF_{CO} [g kg^{-1}]	$ER_{CH2O/CO}$	$ER_{SO2/CO}$	Fuel type	Reference
-	0.62	57.4	-	-	rice straw	*Jenkins et al.* [1996] [a]
-	-	-	0.0208 0.0181	-	rice straw	*Holzinger et al.* [1999] [a]
1.1 ± 0.38	0.43 ± 0.30	68 ± 30	0.015 ± 0.004	0.85 ± 0.2 [b]	savanna	*Sinha et al.* [2003]
0.26-0.44	0.35 ± 0.16	65 ± 20	-	-	savanna and grassland	*Andreae and Merlet* [2001]
1.4	0.40 ('best guess')	92 ± 84	-	-	agricultural residues	*Andreae and Merlet* [2001]
1.12	-	71.4	0.97 [b]	-	savanna	*Yokelson et al.* [2003]
1.06 ± 0.39	-	-	0.0145 ± 0.0043	-	vegetation	*Yokelson et al.* [2003]
3.17 ± 0.88	-	179 ± 39.8	0.0166 ± 0.0034	-	rice straw	*Christian et al.* [2003] [a]
1.90	-	137	1.85 [b]	-	Indonesian fuels (avg)	*Christian et al.* [2003] [a]
-	-	-	0.021	-	savanna [c]	*Jost et al.* [2003]

a. laboratory study
b. ER with respect to CO_2 [mmol mol^{-1}]
c. used in model simulation

a stubble field. The authors indicate a modified combustion efficiency (MCE, defined in *Sec. 2.1.4*) of 0.811, which means that the combustion was almost 100% smouldering. Emission factors for SO_2 range between 0.35 and 0.62 g kg^{-1} for various fuel types. For rice straw, the value EF_{SO2} = 0.62 g kg^{-1} is given from wind tunnel experiments by *Jenkins et al.* [1996]. No study including both, formaldehyde and sulphur dioxide, was found for rice straw combustion.

Andreae and Merlet [2001] give an overview of emission factors from several types of biomass burning (Table 6.5), however rice straw burning is not specified separately. For the burning of agricultural residues, the EF_{CH2O} = 1.4 g kg^{-1} was obtained from CH_2O/CO molar emission ratios [*Andreae and Merlet*, 2001]. The CH_2O emission factor for savanna and grassland, EF_{CH2O} = 0.26-0.44 g kg^{-1}, is significantly different from other values published for savanna which average about 1.1 g kg^{-1} (Table 6.5).

Most ERs and EFs reported in the literature and included in Table 6.5 are from aged smoke, measured downwind of the fire. *Sinha et al.* [2003] define plumes that are not older than five minutes as *initial plumes*. The emission factors and average molar emission ratios (with respect to CO or CO_2) given by these authors from savanna fires in Southern Africa are explicitly stated to apply for initial smoke. However, the values do not differ significantly from most other values given for savanna fires (see Table 6.5).

6.4.2 Characterisation of the Combustion Efficiency

In the rural areas southwest of Milano, burning rice fields were observed during aircraft measurements of the FORMAT II campaign. Airborne trace gas data obtained from the MetAir Dimona aeroplane within and outside of smoke plumes were used to calculate the modified combustion efficiency (MCE, see eq. 2.4) in order to find out the combustion type of these agricultural fires. The measurement instruments on board of the aircraft are described by *Neininger et al.* [2001]. The excess mixing ratios $\Delta[CO]$ and $\Delta[CO_2]$ were derived from CO and CO_2 measurements taken in the plumes aloft on board of the aeroplane using eq. 2.1. Both, CO and CO_2, monitors work with fast-responding techniques which means that concentration changes affect their signals immediately. For airborne measurements, the background concentrations are obtained easily using data from air masses uninfluenced by the emissions, preferably upwind of the fire. In the cases shown here, the background values were taken from regions before reaching the burning areas.

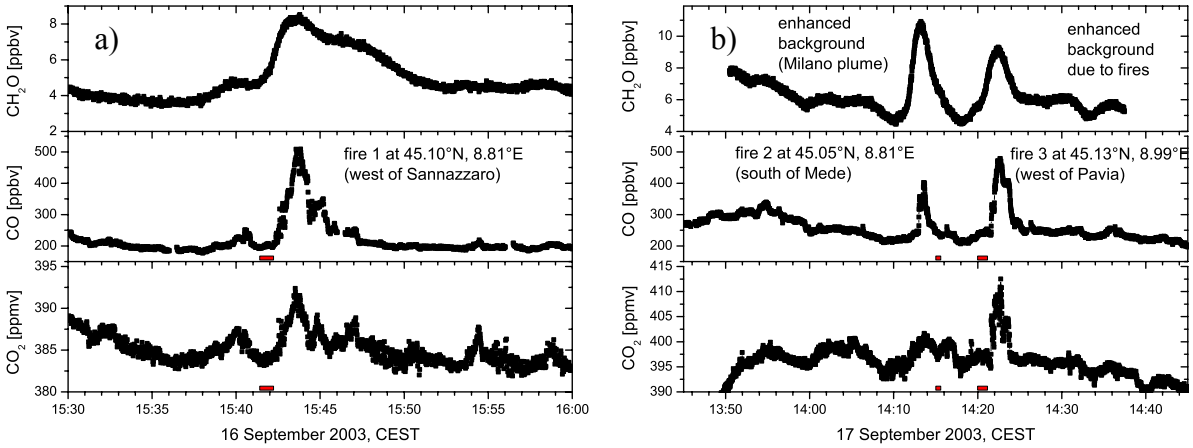

Figure 6.21: Time series of CH_2O, CO and CO_2 concentrations, including the biomass burning plumes observed by airborne instruments on board of the MetAir Dimona ***(a)*** *on 16 September,* ***(b)*** *on 17 September 2003. The red bars mark the background situations used for the calculation of the MCE.*

Three fires, one on 16 and two on 17 September, were identified from the data and studied to derive the MCE. During these days, the flight path included the respective agricultural areas of the province of Pavia. Extracts from the CO and CO_2 time series (also including CH_2O) are shown in *Fig. 6.21*. According to the local flight rules, the aeroplane was flying in an altitude of 600 m above sea level, which corresponds to 500 m above ground in the observed area. The average background concentration needed in the calculation of the excess mixing ratios of CO and CO_2 was derived over the time spans which are indicated by red horizontal bars in the plots of *Fig. 6.21*. The fire detected on 16 September (fire 1) was observed west of the refinery of Sannazzaro, whereby no influence of the refinery itself was found. From the CO and CO_2 concentrations shown in *Fig. 6.21a*, an MCE = 0.97 was derived using eq. 2.4. Following the definition of the MCE by *Yokelson et al.* [1996], given in *Sec. 2.1.4*, this high value signalises a fire with almost completely flaming combustion. On the following day, 17 September, two fire plumes were observed in succession in the same region (first south of Mede, second west of Pavia). The measured data provided an MCE = 0.94 for the plume close to Mede (fire 2). The lower MCE indicates a combustion state of this fire which tends to become smouldering. The composition of the plume near Pavia (fire 3) featured a high MCE = 0.98 which, similar to fire 1, signifies a fire with almost exclusively flaming combustion. In two of the three cases observed in the Dimona data, fire 1 and fire 3, the combustion of the agricultural fires was characterised as predominantly flaming with an average MCE = 0.98. The flaming combustion in

the open burning of a field is due to the large amount of oxygen available. The fire 2, however, had a lower MCE. The CO_2 concentration was hardly enhanced compared to the background and also the chemical composition within this plume strongly differed from the two other biomass burning plumes as discussed below.

Emission ratios of CH_2O with respect to CO within the described smoke plumes were also derived from the aircraft measurements. There are large areas southwest of Milano that featured enhanced formaldehyde concentrations. This is due to both, primary formaldehyde emitted directly by the fires and secondary CH_2O generated by oxidation of the numerous VOCs that are produced by the biomass fires. Other CH_2O sources are not likely to create large amounts of formaldehyde in this region. The CH_2O peaks of the plumes 1-3 in *Fig. 6.21* are broader than the CO peaks. This is a consequence of the measurement technique and does not necessarily indicate the width of the plumes. Formaldehyde concentrations are measured on board of the Dimona by applying the Hantzsch technique (*Sec. 3.1.3*). The method is subject to a smearing of the measured concentrations over the range of ~1 min, which is due to the response time of the instrument of 90 sec. For the emission ratio calculation, this requires the integration of the excess formaldehyde signal over the extension of the peak, instead of using the difference between peak and background as suggested by eq. 2.2. The modified approach to calculate CH_2O/CO emission ratios from fires is by eq. 6.4, where t_1 and t_2 mark the extension of elevated formaldehyde signals as signified in *Fig. 6.22*. The time step, $t_{n+1} - t_n$, between the data points is 1 second.

$$ER_{CH2O/CO} = \frac{\sum_{t=t_1}^{t_2} \Delta[CH_2O](t)}{\sum_{t=t_1}^{t_2} \Delta[CO](t)} \qquad \text{(eq. 6.4)}$$

The CO monitor, based on fast-response resonance fluorescence [*Gerbig et al.*, 1999], has a time resolution of 1 s. The CO measurements thus indicate the actual extent of the smoke plumes. The plumes 1 to 3 had approximate extensions of 5.6, 3.6 and 6.6 km, respectively.

On 16 September, several overlapping formaldehyde peaks of more than one fire plume have been sampled. Integrating over all plumes measured between t_1 and t_2, as indicated in *Fig. 6.22a*, an enhancement ratio $\Delta CH_2O/\Delta CO$ of ER = 0.034 is obtained. If compared to the ERs given in Table 6.5, this value appears high, but as explained in the following, we assume a considerable fraction of secondary CH_2O to be responsible for that. The measured CH_2O concentration starts dropping after the first plume but then stays enhanced for a while, before reaching the background level again. Moreover, the first plume is marked by steep rise and drop of the CO concentration and might be a fresh biomass burning plume. Further plumes with lower CO levels follow subsequently (see *Fig. 6.22a*). These are probably more aged than the major plume. In plumes which have been subject to aging, excess ozone is generated rapidly from the VOCs and NO_x emitted by the fires. An intermediate compound in this process is formaldehyde. Aged air masses thus contain considerable amounts of secondary formaldehyde. The $\Delta O_3/\Delta CO$ ratio has often been used as an indicator of the degree of photochemical aging of smoke samples [e.g. *Jost et al.*, 2003; *Yokelson et al.*, 2003], since a change in the ratio gives evidence for photochemical processing. The ratio $\Delta O_3/\Delta CO$ is shown as green trace in *Fig. 6.22a* for the time span of non-zero excess ozone mixing ratios. During the major CH_2O peak, the $\Delta O_3/\Delta CO$ ratio is low and relatively constant. It strongly increases afterwards (between 15:44 h and 15:48 h), which is a sign of more aged smoke plumes than the initial plume at 15:43 h. Most excess formaldehyde after the major peak is thus ascribed to secondary formation. The aged plumes exhibit a higher enhancement ratio $ER_{CH2O/CO}$ than the initial plume and thereby increase the enhancement ratio calculated between t_1 and t_2, compared to the ER of merely the initial plume. Due to

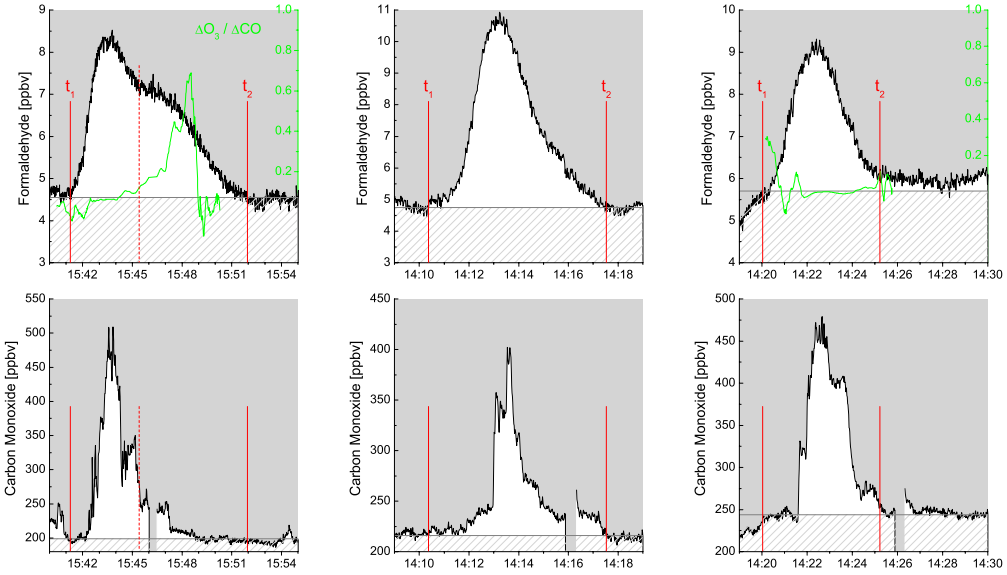

Figure 6.22: Enhanced formaldehyde and carbon monoxide concentrations in emissions plumes of the three agricultural fires. The grey hatched areas indicate the background concentrations outside the plumes used for the calculation of excess mixing ratios. The green trace in the upper panels represents the ratio $\Delta O_3/\Delta CO$ to reveal the aging of the sampled air masses.

the smearing in the formaldehyde data, the ER for the first plume cannot be separated from the following plumes.

The smoke plume of fire 2, observed on 17 September, has lower CO concentrations than both other plumes and the CO_2 concentration is hardly enhanced towards the background, which is mirrored in a lower MCE (see above). The formaldehyde enhancement ratio in the plume, derived from eq. 6.4, has a high value of 0.061. This is due to comparatively large excess CH_2O concentrations within the plume (*Fig. 6.22b*) which most probably has a large secondary contribution. Unfortunately, no ozone measurements are available for this plume, due to a temporary interruption of the O_3 monitor. Hence, the aging of the plume cannot be estimated with the above method. However, many other primary and secondary compounds have been continuously measured on board of the Dimona and there are several evidences in this data set which indicate that the fire was not active any more. Secondary compounds like HNO_3 and PAN show increased concentrations within this smoke plume. These compounds are not increased in the fresh plumes. Moreover, NO_x concentrations are not increased in plume 2, but excess mixing ratios of NO_x have been found for the plume 1 and the plume 3. The presence of typical secondary pollutants and the lack of several primary pollutants suggest that a large fraction of the formaldehyde measured in this smoke plume is of secondary origin and gives rise to the high ER.

The enhancements measured within the plume of fire 3 (on 17 September) are assumed to be due to a single emission plume. The excess CO concentrations are limited to a well defined time span with steep rise and drop of CO concentrations (*Fig. 6.22c*). The CH_2O/CO emission ratio for this plume was calculated to be 0.023 using eq. 6.4. The background CO concentrations before and after the plume are equal. The average formaldehyde background level is 0.3 ppbv higher after the plume than before. The variation of the formaldehyde background value is reflected in an ER between 0.020 and 0.024. The result is in very good agreement with the ER from rice straw combustion in the laboratory by *Holzinger et al.* [1999]. Very low excess ozone mixing ratios are found in the second plume on 17 September and the $\Delta O_3/\Delta CO$ ratio is close

to zero. Also other secondary compounds like PAN and HNO_3 do not show enhanced mixing ratios. The smoke plume is considered as a fresh emission plume.

Also the major plume of fire 1 is expected to be a fresh biomass burning plume, however, due to the smearing in the Hantzsch formaldehyde measurements, it was not possible to derive separate ERs for the primary and secondary plumes of fire 1. Since the smoke plumes of fire 1 and fire 3 had comparable spatial extensions, as derived from the width of the CO peaks, the formaldehyde signal has a similar relative increase in both plumes according to the instrumental rise time of 90 s. Since, moreover, the ground speed of the aeroplane was relatively constant (~ 46 m s^{-1}) and was similar over both fires, it should be possible to use the formula eq. 2.2 to compare the relative composition of the two smoke plumes. The ratio of differences between the peak and background values of CH_2O and CO (eq. 2.2) yields a value of 0.0167 for fire 1. Only the signal from the major peak is decisive here. The result for fire 3 was 0.0186. The very similar values suggest a similar composition of both plumes. The major plume of fire 1 therefore has a similar ER as fire 3. The high enhancement ratio calculated for overlapping plumes on 16 September is increased due to the succeeding aged plumes. The aged emission plumes contain predominantly secondarily formed CH_2O. Note that these numbers determined in this paragraph just serve comparative purposes and are no emission ratios due to reasons given above. Only eq. 6.4 serves to determine absolute emission ratios. For fire 2, a comparatively high ratio of 0.0407 was derived with eq. 2.2. This value cannot be compared to those of fire 1 and 3 since the fire 2 plume had a smaller extension.

Restricting to the primary plumes, the emission ratios obtained from fire 1 and fire 3 are in good agreement with ERs published by *Holzinger et al.* [1999] for rice straw in the laboratory, *Sinha et al.* [2003] for savanna fires and *Yokelson et al.* [2003] for vegetation fires (see Table 6.5). Finally, a formaldehyde emission factor from rice straw burning is calculated for the plume 3, applying eq. 2.3 with $ER_{CH2O/CO} = 0.020$ and $EF_{CO} = 57.4$ g kg^{-1} stated by *Jenkins et al.* [1996]. The resulting $EF_{CH2O} = 1.23$ g kg^{-1} agrees well with most values given in Table 6.5 for savanna fires. This suggests that CH_2O emissions from savanna fires and rice field fires are similar for dry conditions. The emission factor derived by *Christian et al.* [2003] in the laboratory is well larger than the other values obtained for various similar vegetation types (Table 6.5). A possible reason for this difference is given in the next section.

6.4.3 Estimation of a CH_2O Emission Factor

Ground-based DOAS measurements at Spessa (*Sec. 4.3.4*) during the FORMAT II field campaign were also influenced by occasional biomass burning plumes. The measurement site is located in an agricultural area with intensive rice cultivation as shown in *Fig. 4.13*. Several times throughout the campaign, the emissions from nearby burning rice fields could be observed at the site. Time series of the concentrations of formaldehyde and sulphur dioxide measured at Spessa are shown in *Fig. 6.23*. It is obvious that the smoke plume from burning rice straw comes along with enhanced CH_2O and also increased SO_2 concentrations. Since no significant emission sources like a city or industry are close-by, this suggests that both gases were emitted by the same source and the enhancement is due to the direct emission from biomass burning.

On four days with similar ambient conditions, the smoke plumes from nearby fires were transported to the measurement site. The fires were observed within a radius of 2 km from the farmstead. During the measurements, the wind directions were stable and the plume age was estimated from the transport time in horizontal direction. With measured wind speeds between 1 m s^{-1} and 2.5 m s^{-1}, a plume age of 10-30 min is derived. The plumes observed in the DOAS measurements are mostly older than five minutes and thus no initial plumes. But since the air masses were not older than 30 min, the shown data do not represent significantly aged air

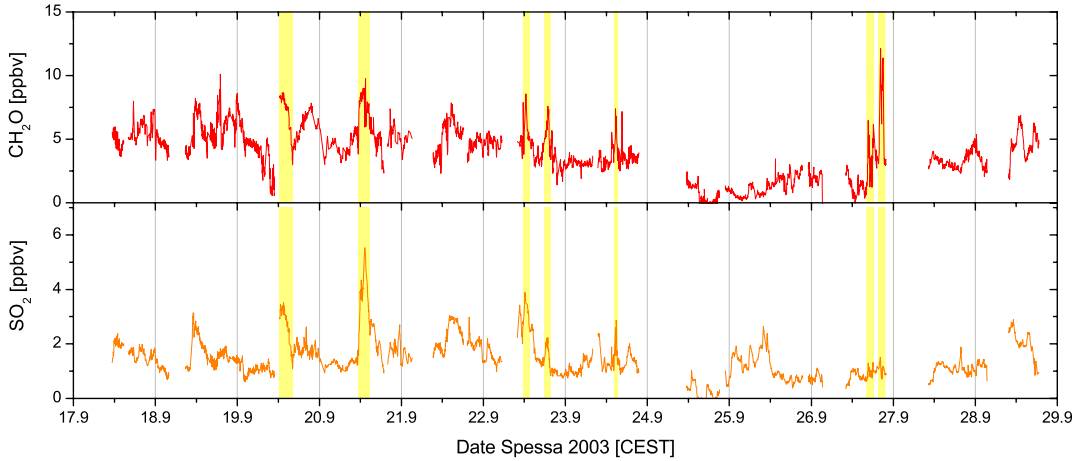

Figure 6.23: At several times during the FORMAT II campaign, which are marked by yellow bars, agricultural fires were observed in the vicinity of the measurement site at Spessa. During these episodes, enhanced concentrations of CH_2O and SO_2 were measured by long path DOAS.

masses. The observation of enhanced concentrations of CH_2O and SO_2 offered the chance to estimate the formaldehyde emissions from the combustion of rice stubble.

From the DOAS ground-based measurements at Spessa, no CO or CO_2 concentrations are available. Hence, SO_2 is used as reference tracer to determine an emission ratio (cf. eq. 2.2). Here, a molar enhancement ratio of CH_2O with respect to SO_2 is defined as

$$ER_{CH2O/SO2} = \frac{\Delta[CH_2O]}{\Delta[SO_2]}. \qquad \text{(eq. 6.5)}$$

The difficulty is to obtain an appropriate background value for the particular situation to acquire the excess mixing ratios. Since no direct sources of CH_2O and SO_2 are expected at the site, except from the biomass fires, the background concentrations were derived from the average diurnal variation of the concentrations during the high pressure period (17-23 September), omitting the burning periods. The stable meteorological conditions between 17 and 23 September led to a recurrent daily pattern of meteorological parameters. These boundary conditions for the examined time period promise a similar variation of secondary formaldehyde during the same time span. Considering that Spessa was the background site, upwind of major pollution sources, it is assumed to be justified to use an average background variation for this time period. Little day to day variation of the concentrations of both trace gas is expected at the background site.

Excess mixing ratios $\Delta[CH_2O]$ and $\Delta[SO_2]$ were calculated according to eq. 2.1 for the burning events observed at Spessa in mid-September 2003. *Figure 6.24* shows $\Delta[CH_2O]$ as a function of $\Delta[SO_2]$ inside the smoke plume. The data from the four smoke plumes observed during the afternoons of 19, 20, 22 and 23 September contributed to the shown data set. Different marker types are used in *Fig. 6.24* for the individual fires. The straight red line on this figure is the average linear least-squares regression with the intercept forced into zero. Its slope indicates the average CH_2O to SO_2 emission ratio for the four smoke plumes observed at Spessa. The trace gas enhancement ratios found within the smoke plumes were very similar for the four observed fire events that occurred in the surrounding of the measurement site. They are listed in Table 6.6. The results indicate a weak variability of the ratio of CH_2O and SO_2 in the plumes. The average value for the ratio of CH_2O to SO_2 is 2.08 ± 0.05. Also during each fire event the ratio between $\Delta[CH_2O]$ and $\Delta[SO_2]$ in the plume was almost constant. This points to similar

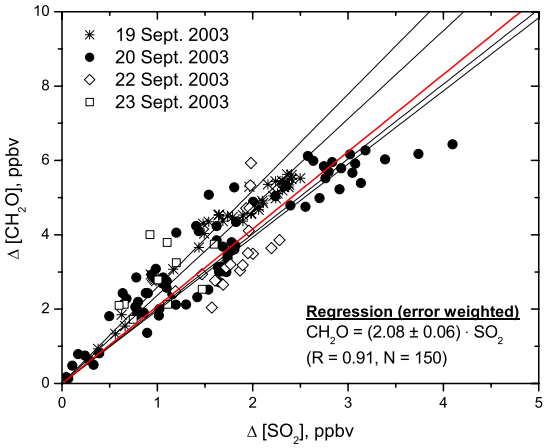

Figure 6.24: Linear relation between CH_2O and SO_2 excess mixing ratios found in four smoke plumes observed during the high-pressure period (17-23 September) at the ground site Spessa.

combustion conditions on the consecutive days and a good estimation of the background concentrations.

On the basis of the SO_2 emission factor $EF_{SO2} = 0.62$ g kg^{-1}, published by *Jenkins et al.* [1996] for burning rice straw (see Table 6.5), the molecular weights¶ of CH_2O and SO_2 and using the emission ratio $ER_{CH2O/SO2} = 2.08 \pm 0.06$ derived from the regression presented in *Fig. 6.24*, the formaldehyde emission factor results from eq. 6.6 [*Andreae and Merlet*, 2001]. The uncertainty of the emission factor is calculated from considering the 1 σ errors of $[SO_2]$ and $[CH_2O]$ in the regression.

$$EF_{CH2O} = EF_{SO2} \cdot \frac{M_{CH2O}}{M_{SO2}} \cdot ER_{CH2O/SO2} \qquad \text{(eq. 6.6)}$$

The average formaldehyde emission factor $EF_{CH2O} = 0.60 \pm 0.02$ g kg^{-1} for the combustion of rice straw was derived for the conditions given during the fair weather part of the FORMAT II campaign. This emission factor, obtained from the ambient smoke plumes at Spessa, is far below the emission factor reported by *Christian et al.* [2003] from laboratory measurements (see Table 6.5). However, the laboratory measurements obeyed the special rice straw burning habits which are common in East Asia. There, the rice straw is burned in small to large piles that burn by smouldering for up to several days [*Christian et al.*, 2003]. By piling the straw, they simulated these conditions which lead to dominating smouldering combustion (MCE = 0.81, see above). Therefore, larger amounts of formaldehyde are released than in the predominantly flaming combustion (see *Sec. 6.4.2*) observed in Italy. Also in savanna fires flaming combustion dominates [e.g. *Sinha et al.*, 2003]. The formaldehyde emission factor found for rice straw fires

Table 6.6: Summary of the emission ratios in the emission plumes of the fire events between 17 and 24 September 2003 at Spessa.

Fire No.	Date, Time	$\Delta[CH_2O]/\Delta[SO_2]$	r	N
1	19/09/2003, 15:15-16:00	2.37 ± 0.13	0.97	44
2	20/09/2003, 11:30-14:30	2.01 ± 0.07	0.94	78
3	22/09/2003, 11:50-13:30	1.97 ± 0.10	0.60	18
4	23/09/2003, 14:30-15:15	2.59 ± 0.24	0.51	10
error-weighted average:		2.08 ± 0.05		

¶. $M_{CH2O} = 30.0262$ g mol^{-1}, $M_{SO2} = 64.0648$ g mol^{-1}

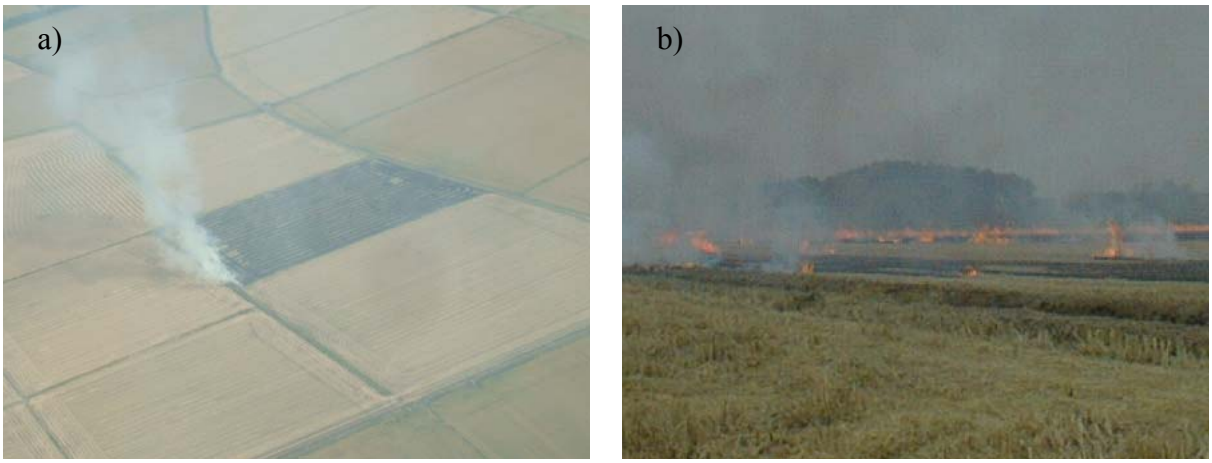

*Figure 6.25: Burning rice field **(a)** in the area between Voghera and Mortara (photo taken on 17 September by Klaus-Peter Heue), **(b)** in Spessa.*

is similar to the values reported by *Andreae and Merlet* [2001] for savanna fires and grassland and similar to several individual values reported by *Sinha et al.* [2003] for savanna fires, but significantly lower than the average reported by *Sinha et al.* [2003]. The emission factor derived from the ground-based measurements differs form the value obtained from the airborne measurements (see *Sec. 6.4.2*). This may be attributed to differences in the composition of the ascending plume aloft and the plume transported to the ground site in horizontal direction. The convection rapidly transports the fire emissions upwards where the air is probed by the airborne instruments. The results from FORMAT II airborne measurements are consistent with the literature results presented in Table 6.5 which, apart from the laboratory studies, also derive from airborne measurements. Further, the plumes measured by the DOAS might not cover the entire light beam, so that air from inside and outside the plume, with different trace gas composition, is probed at the same time.

Agricultural fires, as well as savanna and forest fires, are dynamic events where a moving flame front passes over the fuel source, such as a field or forest. Consequently, both smouldering and flaming combustion zones are present at any given time and their combined emissions are released into the smoke plume which is transported to the measurement site. Their proportions at a given point vary over time, typically dominated by flaming in the earlier part of the fire and smouldering during the later part. The typical extent for an agricultural fire in the Po Basin is illustrated in *Fig. 6.25*. The left hand photo was taken on 17 September (at 13:59 h) close to Mede (encircled in *Fig. 6.26*). One can clearly find that the fire activity is restricted to individual fields. The right hand photo of *Fig. 6.25* shows one of the fires that occurred at the ground-based site Spessa. Using the MCE as indicator for the combustion conditions and considering the observation of the flaming fires in the area, the above result appears plausible and the presented EF is representative for rice field burning in Italy. As in many other field measurements, the ER value derived in this section is most likely not a pure emission ratio (rather an enhancement ratio as distinguished in *Sec. 2.1.4*), since a certain amount of secondary CH_2O is included in the smoke plumes measured at Spessa. For formaldehyde, which is a rapid and high-yield oxidation product of organic compounds, it is difficult to assess a pure emission ratio in the field. Primary formaldehyde emission could be inferred from combustion events during the night, however agricultural fires have only been observed during daytime, usually in the afternoon.

The fires included in this analysis occurred between 16 and 23 September 2003 which was a period of uniform external conditions. The burning conditions during the regarded time period were thus similar for all fires observed at Spessa and the calculated emission estimation applies

for the given conditions, offering very low moisture levels of the vegetation. There was another fire on 26 September which shows different emission characteristics with high formaldehyde contributions (see *Fig. 6.23*), which are most probably due to changed external conditions. After 23 September, several rain events lead to moister conditions and larger emissions of CH_2O can be expected. Enhanced formaldehyde concentrations are observed on that day until the evening hours. Most probably the fire had a larger relative amount of smouldering combustion compared to the examined period in mid-September. The fire on 26 September is not considered in above calculations because of the changed conditions. Further, it was not possible to estimate reliable background concentrations for that part of the campaign.

6.4.4 Remote Sensing of CH_2O and SO_2 Distributions

Passive airborne DOAS measurements (AMAXDOAS) were performed in both FORMAT campaigns by IUP Heidelberg and Bremen. During the FORMAT II flights in September 2003, several biomass burning events were observed also in the AMAXDOAS data set. The instrument on board of the Partenavia aeroplane and the measurements are described in detail by *Heue* [2005]. The Partenavia had a flight altitude of 570 m a.s.l. in the Po Basin and a cruise speed of ~ 200 km h^{-1}. The AMAXDOAS comprises nine telescopes, three pointing upward and six looking downward. For the flight on 17 September, differential slant column densities (dSCD) of formaldehyde and sulphur dioxide from one telescope are shown in *Fig. 6.26*. The received scattered light was detected by a telescope oriented backward with an angle of –7° relative to the horizontal. The light mainly originates from the air mass below the aeroplane. Above the area where agricultural fires occurred, enhancements of SO_2 and CH_2O were detected in the AMAXDOAS measurements (*Fig. 6.26a,b*) but no ratios could be quantified, since the background is very noisy, especially for SO_2. The concentration maxima of both compounds are collocated and can be clearly attributed to the same source, a burning rice field close to Mede, which is also shown in *Fig. 6.25a*. The fire was overflown two times (at 13:56 h and 14:09 h) and the same column amounts were measured in both cases. As can be seen in *Fig. 6.26*, the highest differential slant column densities (dSCD) of formaldehyde and sulphur dioxide observed during the flight on 17 September were due to biomass burning. The formaldehyde dSCD values were even higher than in the urban plume north of Milano, although 17 September was a day with high photochemical activity. Since no comparable point sources of these trace gases are present in the surroundings, the fires constitute a strong local source for both,

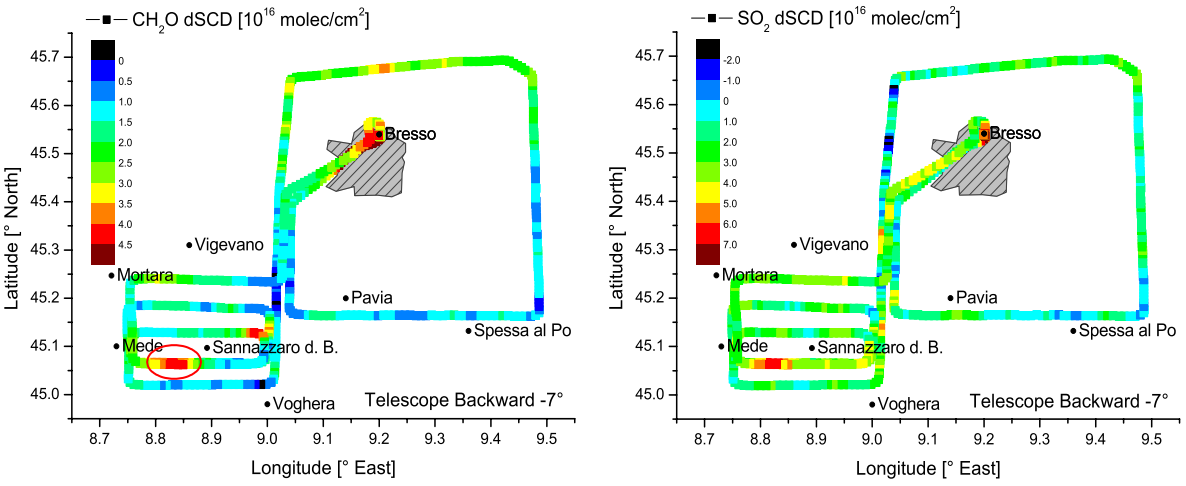

Figure 6.26: AMAXDOAS measurements of ***(a)*** *formaldehyde and* ***(b)*** *sulphur dioxide on 17 September 2003. The agricultural fires were observed close to Mede (Klaus-Peter Heue, pers. comm., 2005).*

formaldehyde and sulphur dioxide. From the FORMAT aircraft in-situ measurements on the Dimona and the microlight, unfortunately no SO_2 data is available. However, from the CO and CO_2 data, the combustion efficiency and formaldehyde emission ratios towards CO could be derived (see *Sec. 6.4.2*).

A similar correlation between CH_2O and SO_2 distributions in biomass burning plumes is also observed in satellite measurements by the GOME (Global Ozone Monitoring Experiment) instrument on board of the ERS-2 satellite [*Marbach et al.*, 2005; *Khokhar*, 2006]. Large areas in low-latitude regions are affected by wide-stretching fires. In Indonesia, the fires take place in the rain forest. The spatial agreement of surface areas affected by fires and the distribution of CH_2O and SO_2 enhancements, shown in *Fig. 6.27*, emphasises that both trace gases are produced from these fires. The excess formaldehyde and sulphur dioxide levels have not yet been quantified. On a global scale, biomass burning is known to be a major direct source of formaldehyde. The large fires in tropical regions can be of global relevance, whereas forest fires or agricultural fires are of regional or local importance.

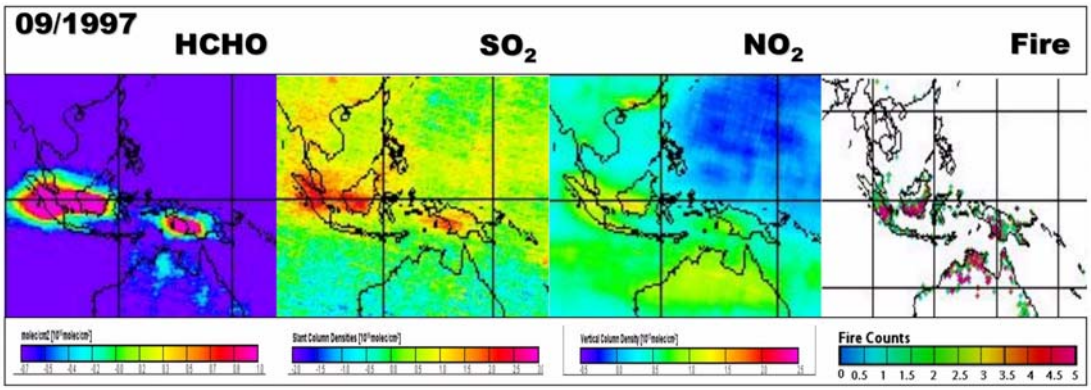

Figure 6.27: Biomass burning in Indonesia is correlated with enhanced CH_2O and SO_2 concentrations (figure from Marbach et al. [2005]).

6.4.5 Radical Budget

The most important sources of tropospheric HO_x radicals, promoting ozone formation (see *Sec. 2.2.4*), are the photodissociations of O_3, CH_2O and HONO (see *Sec. 2.2.1*). Their relative contributions to HO_x formation vary during the course of a day. In the early morning, HONO is the main OH source. Formaldehyde, similar to ozone, is an important HO_x source during noon and afternoon. This is also the time when agricultural fires lead to enhanced formaldehyde concentrations. From the data measured at Spessa, the additional formation of HO_x radicals because of the fire emissions is estimated here.

The HO_x radical production rates of ozone, formaldehyde and nitrous acid are calculated from eq. 2.6-2.8 using trace gas and meteorological data measured at Spessa and photolysis frequencies measured at Bresso (40 km north of Spessa) with a spectroradiometer. Bresso and Spessa are located on nearly the same altitude level (Bresso 146 m a.s.l., Spessa 64 m a.s.l.). An error due to the altitude variation of photolysis frequencies can therefore be neglected. At both sites, the amount of cloud coverage was usually zero during the period of interest, as could be verified from the measurements of global radiation at Bresso and Spessa.

The relative fractions of the most important HO_x radical sources were calculated for the average background concentrations, that is, excluding fire events, during the period 17-23 September. The fraction of HO_x production due to CH_2O photolysis as well as the contributions from photolysis of O_3 and HONO derived from the ground-based measurements at Spessa are shown in *Fig. 6.28*. In the background case of no biomass burning, the radical formation during the

afternoon is dominated by the ozone photolysis, yielding excited O(^{1}D) atoms, and subsequent reaction with H_2O, which constitutes ~ 45% (blue columns), whereas formaldehyde photolysis (red columns) contributes ~ 40% to the HO_x production. The bars indicate the range of the percental contributions within 1 standard deviation. Note that due to the rapid photolysis of nitrous acid, its concentrations measured during daytime are close to or below the detection limit (see Table 4.4). Therefore, the HO_x contribution derived from the HONO measurements is subject to large uncertainties and the value of 15% represents an upper limit of the HO_x fraction due to nitrous acid.

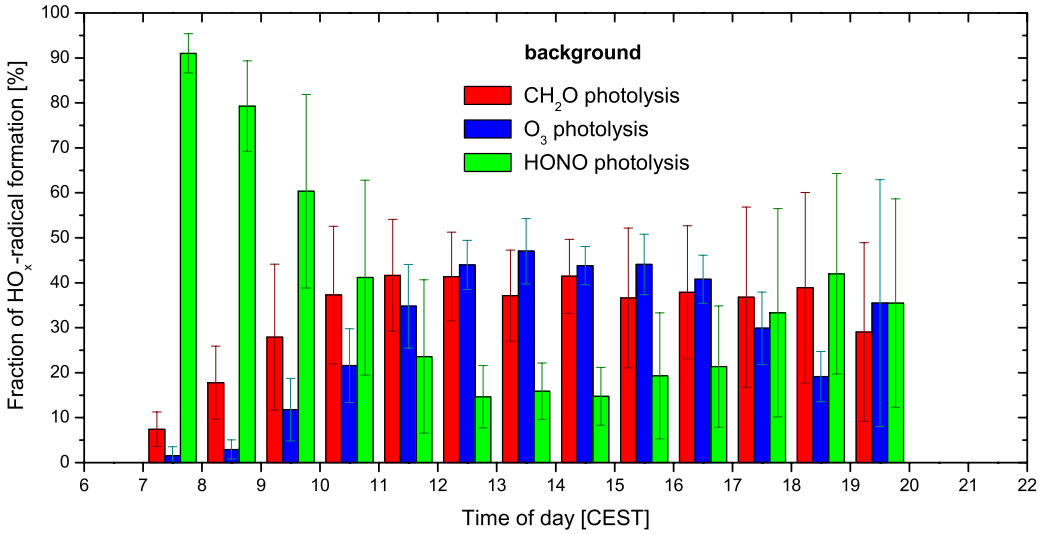

Figure 6.28: Average fractions of HO_x radical sources as a function of the time of day. Radical formation rates for background conditions were determined from hourly averaged data of the time period 17-23 September at Spessa.

The enhancement of CH_2O concentrations due to emissions from the biomass fires shifts the relative portions. The relative HO_x radical contributions from formaldehyde, ozone and nitrous acid were determined as averages over the duration of the fires for each of the fire plumes separately. The deviation from the background case, which is shown in *Fig. 6.28*, is depicted in *Fig. 6.29*. There is a 10-15% enhancement of the HO_x fraction by CH_2O due to higher formaldehyde concentrations in the plumes. The highest excess local HO_x production fractions by CH_2O are observed for fires around noon (fires 2 and 3) when the actinic flux is at its maximum and the radical channel of photolysis constitutes ~ 25% of the formaldehyde loss (see *Sec. 2.3.2.1*). In the young (~ 30 min) biomass burning plumes, processing has not yet occurred to a great extent so that O_3 concentrations are not significantly enhanced and the relative portion of HO_x formation due to ozone photolysis is decreased by 5-10%. The decrease of the relative significance of ozone as HO_x source is due to the increase of the relative importance of formaldehyde by higher formaldehyde concentrations. Also the relative contribution by HONO is decreased compared to the background case, but, as stated above, the contribution from nitrous acid is subject to uncertainty, because its concentrations are below the detection limit. In the smoke plumes, formaldehyde is responsible for 50-55% of the radicals formed. With increasing aging of the plume downwind, also enhanced O_3 concentrations are expected. The average absolute radical production rate at 12 h in background conditions at Spessa is 8.5×10^6 molec cm^{-3} s^{-1}. In the presence of biomass burning plumes, the radical production rate is increased towards the background case by a factor of 1.2-1.5, mostly due to the increased CH_2O concentration since the absolute radical formation rates for ozone and nitrous acid are not significantly enhanced. The absolute quantitative statements given here are subject to uncertainties due to the effect of aerosols. Whether the presence of aerosol enhances or reduces the

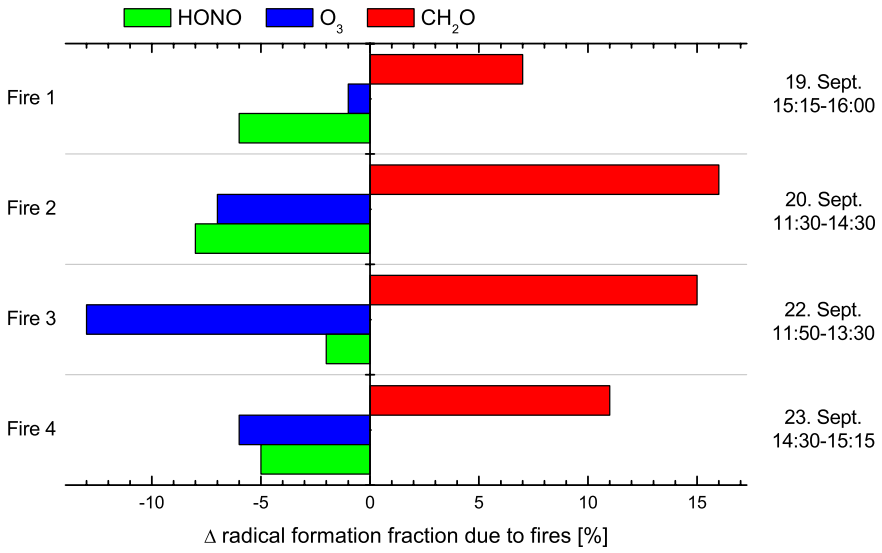

Figure 6.29: Deviation of relative radical contributions by CH_2O, O_3 and HONO within the fire plumes observed at Spessa, compared to corresponding background situation (shown in Fig. 6.28) at the same time of day.

available actinic flux and therefore the photolysis frequencies, depends on the aerosol optical depth and the absorbing properties of the aerosol.

The local and regional boundary layer chemistry is distinctly affected by the compounds emitted from agricultural fires. A substantial increase of HO_x formation rates owing to fires has been found and the associated rate of production of ozone and other secondary compounds could be estimated by means of CTMs. However, emissions from biomass burning are not included in the emission inventories of several regional models (Li Liu, pers. comm., 2006). This might lead to a seasonal local underestimation of the oxidation capacity in the boundary layer and thus of the ozone levels. Local effects are expected in the grain cultivation regions in Piemonte and Lombardia.

6.4.6 Regional Impact

Italy is the most important rice growing country in Europe with 220 000 ha (about half of the total rice acreage in the European Union). The main areas for the cultivation of rice in Italy are located in the regions Piemonte and Lombardia (western Po Basin), covering an area of 202 000 ha [*Ente Nazionale Risi*, 2005]. Another 18 000 ha is grown in the rest of Italy. In the areas indicated in green colour in *Fig. 6.30b*, rice is the most important crop, cultivated both in irrigated paddy and dry field culture. Most fires detected by MODIS (MODerate resolution Imaging Spectrometer aboard the TERRA and AQUA satellites) in the Po Basin in the time between 1 September and 10 October 2003 were located southwest of Milano in the area between Pavia, Novara and Alessandria (*Fig. 6.30a*). The observation period of FORMAT II (September-October) coincided with the harvest time. It is interesting to note that the regions with the highest fire activity observed coincide with the areas in Piemonte, Lombardia and at the estuary of Po where predominantly rice is grown (*Fig. 6.30b*). This gives a strong indication that most of these fires reflect the agricultural burning of rice stubble fields. In northern Italy, the fire activity is very high in autumn, compared to the rest of the year.

The emission results obtained above for fires observed in the Pavia region (see *Sec. 6.4.2* and *Sec. 6.4.3*) are considered to be representative for the fires that occur seasonally in the Po Basin region. It should thus be possible to estimate the emissions of prescribed agricultural fires in Northern Italy from the area burned per season. The agricultural fires should be taken into

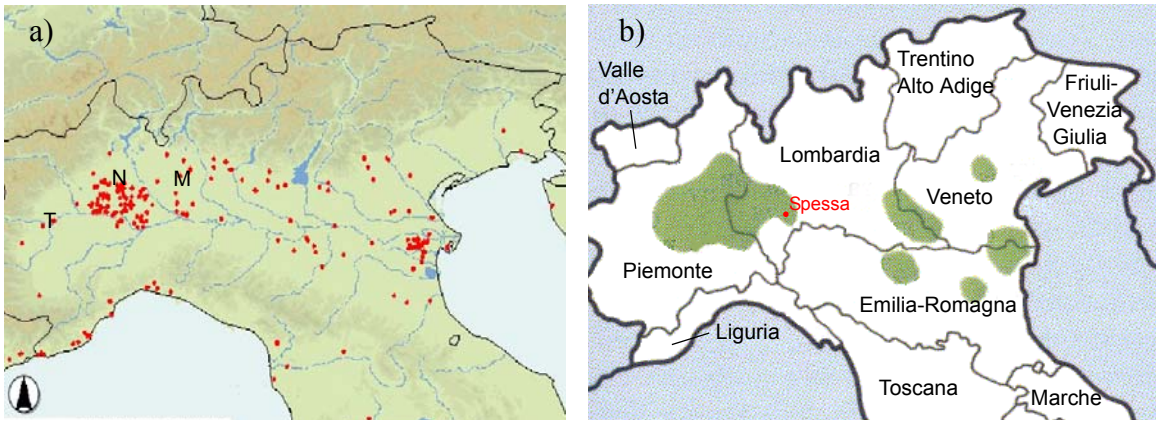

Figure 6.30: ***(a)*** *Fires detected by MODIS (MODerate resolution Imaging Spectroradiometer) in the Po Basin during its overpasses in the time period between 1 September and 10 October 2003. Most fires were located southwest of Milano in the area between Pavia, Novara and Alessandria [MODIS, 2004].* ***(b)*** *Green areas label regions of intensive rice cultivation [Ente Nazionale Risi, 2005].*

account as seasonal area source of pollutants in emission inventories. Using the formaldehyde emission factor derived from aircraft measurements (*Sec. 6.4.2*), the emission from the 202 000 ha rice acreage in the western Po Basin can be estimated. The California Environmental Protection Agency assumes a fuel loading of 3.0 tons/acre for rice fields [*U.S. EPA*, 2005]. Converted to metric units, this corresponds to 6.72 tons ha^{-1}. The amount of rice straw burned in the western Po Basin thus can be extrapolated to 1 357 440 tons. With the derived emission factors the emissions of CH_2O and SO_2 per unit area are estimated to be 8.2 kg ha^{-1} and 4.2 kg ha^{-1}, respectively. The total emissions per harvest time in the western Po Basin (202 000 ha) can be calculated as 55.5 Mmol CH_2O or 0.6 Gg C and 13.1 Mmol SO_2. These are minimum emission estimations for dry conditions, assuming that the entire cropped rice area is burnt and that each rice field is burnt down once per year.

The California Rice Commission specifies annual emissions of the primary pollutants of value from rice field burning in California per unit area. On an annual basis, the burning of an average rice field emits approximately 14.1 pounds of VOC per burned acre (15.8 kg ha^{-1}) and 3.3 pounds of SO_2 per burned acre (3.7 kg ha^{-1}) [*Buttner*, 2001].

The region of Lombardia operates an observational network of 264 stations distributed over all provinces to measure a large number of trace gases, including SO_2. No significantly enhanced SO_2 concentrations or SO_2/CO ratios have been found for autumn months for the time span 1987-2004. This is attributed to the fact that the stations are not located in background sites but within the centres of the villages and towns with high traffic density and therefore are strongly influenced by traffic emissions.

Average emissions of CH_2O and SO_2 from the city of Milano are derived from the high-resolution emission inventory for the region of Lombardia by *Dommen et al.* [2003]. The major source of formaldehyde in the region of Lombardia concentrates on Milano, for sulphur dioxide, additional strong sources are located in the metropolitan area of Milano. The average emissions of the urban area of Milano (φ = [45°26', 45°35'], λ = [9°08', 9°15']) are specified for morning hours 8-12 h and the afternoon 13-17 h. Formaldehyde emissions are stated as 7 300 mol h^{-1} $(3km)^{-2}$ between 8 and 12 h and 5 800 mol h^{-1} $(3km)^{-2}$ between 13 and 17 h. For sulphur dioxide, the emissions vary between 70 200 mol h^{-1} $(3km)^{-2}$ in the morning and 68 400 mol h^{-1} $(3km)^{-2}$ during the afternoon hours. On an hourly basis, the urban emissions account for 0.2 kg ha^{-1} CH_2O and 5 kg ha^{-1} SO_2. The primary fraction of formaldehyde in ambient air is low (~10% in Bresso (Johan Mellqvist, pers. comm., 2006)). The emission per

hour is thus comparatively low. The CH_2O emission from agricultural fires per unit area which was derived above (8.2 kg ha^{-1}) is significantly higher than the urban CH_2O emissions per hour. However, most formaldehyde present in the urban air mass is of secondary origin. The amount of formaldehyde included in the Milano plume which is transported downwind from the city is therefore probably closer to the fire emissions. For SO_2 emissions the mass emitted per unit area by agricultural fires is similar to the mass SO_2 emitted per unit area by the city during one hour. The fires constitute locally important point sources for formaldehyde, increasing the oxidising capacity of the air mass. Formaldehyde is an especially important constituent during midday time.

7 Conclusions and Outlook

Within this thesis, long path DOAS (Differential Optical Absorption Spectroscopy) measurements of photochemically relevant trace gases were performed with the emphasis on the measurement of formaldehyde (CH_2O). For this purpose, three field measurement campaigns were carried out in polluted urban areas. Two campaigns took place in the Milano area (northern Italy) in the frame of the European FORMAT project. Another campaign, referred to as the MCMA-2003, was conducted in Mexico City. Additionally, data from a previous campaign in the Milano area (PIPAPO 1998, see e.g. *Neftel et al.* [2002]) were frequently used to extend the data set. Further, it was made use of a wide range of additional data, measured during the campaigns by other groups, to analyse the data set. The results of this thesis, which had two main subject areas – the comparison of different formaldehyde measurement methods and the variability of formaldehyde – are subsumed in the following.

Measurement of Formaldehyde

For the accuracy of a DOAS result, the exact knowledge of the UV absorption cross-section is of utmost importance. Since for formaldehyde, a number of highly resolved cross-sections are available, these were compared with one another and differences in magnitude of up to 17% were found in the range 300-360 nm. Two different cross-sections were recommended by IUPAC and JPL. They differ by 11%, translating into uncertainties in the determination of CH_2O concentrations by DOAS and in the evaluation of photolysis frequencies by the same amount. The agreement among the most recent spectra was better than 5%, which is conform to the stated uncertainties and strongly supporting the assumption that they are most suitable, representing the reality. The results indicate that the employed cross-section by *Meller and Moortgat* [2000] is the most accurate available at present.

A structure was found in the DOAS spectra, influencing the retrieved CH_2O concentration. The examination of the spectra suggested that it originated from the lamp used in the active DOAS system. The structure occurred for both types of xenon lamp used. Depending on its magnitude, the structure caused an offset in the obtained formaldehyde mixing ratios of up to 1 ppbv. By simultaneous measurements with four DOAS light beams along identical absorption paths, it was shown that the offset can be remedied by fitting a correction spectrum to the measured one, thus leading to an improvement in the formaldehyde retrieval.

Previously found discrepancies between the results of different formaldehyde measurement methods demanded an intercomparison study of the most widely used in-situ formaldehyde

measurement techniques. The intercomparison experiment was carried out at ambient urban air and included the spectroscopic techniques DOAS and FTIR, the wet chemical Hantzsch fluorescence technique as well as the time-integrating chromatographic DNPH technique. In contrast to most previous studies, great importance was attached to sampling the same air volume with all instruments. White systems were applied for the spectroscopic techniques to ensure this. The intercomparison yielded an overall good agreement of Hantzsch and spectroscopic techniques within 15%, where DOAS and FTIR results agreed within 5%. However, discrepancies up to 20% were found among the results of five Hantzsch monitors identical in construction. A large part of this deviation could be attributed to the calibration standards used which had been prepared independently by each group.

Although usually, long path integrated measurements are considered representative for the comparison with model data, this was not the case for the formaldehyde measurements during FORMAT. The large deviations from in-situ measurements found were attributed to chemical and physical processes influencing the measurements differently. Since the light beam traversed an air volume more elevated above the ground than the inlet of the in-situ instrument, the DOAS measurements were less exposed to loss by deposition, resulting in higher concentrations measured by DOAS at night. The emission of reactive biogenic hydrocarbons from a deciduous forest during the day and subsequent generation of formaldehyde there was found to strongly influence CH_2O concentrations measured by DOAS directly above the canopy, resulting in higher concentrations than measured by the point instrument.

Importance and Variability of Formaldehyde in the PBL

By including the data from a previous campaign (PIPAPO 1998), the results from three measurement campaigns at the same site in Milano offered the possibility to estimate radical formation rates by the most important odd hydrogen radical sources and to compare these. Formaldehyde was found to represent the second most important HO_x source of the entire day at Bresso, being responsible for at least 20-40% of the radicals produced in Milano during 24 hours. Its importance was usually close to the importance of ozone. At Mexico City, however, formaldehyde was found to be the most important HO_x radical source, accounting for 40%. The relative importance of CH_2O as radical source particularly varies with location and water vapour content of the air.

Distinct vertical formaldehyde gradients up to a height of ~100 m above a deciduous forest have been observed using airborne and ground-based measurements. The slow vertical mixing typically observed in the Po Basin and the loss of CH_2O by adsorption of gaseous formaldehyde to particles were suggested to be responsible for the inhomogeneous distribution of formaldehyde which is continuously produced above the canopy.

The temporal and spatial variability of formaldehyde was studied using ground-based and airborne data of formaldehyde and its precursors. A simple model, involving VOC reactivities and a quantity proportional to OH production, is sufficient to understand a large part of the afternoon formaldehyde variability. In a statistical analysis with an approach based on the OH-reactivity of VOCs and the variability of the OH production, a large amount (70-82%) of the spatial formaldehyde variance in the Milano metropolitan area could be explained. The temporal variability of formaldehyde at a semi-rural site in the afternoon could be understood very well from the local measurements. The formaldehyde variability could be qualitatively and quantitatively well reproduced in all cases which are not immediately subject to fresh emissions.

During the second FORMAT campaign in autumn 2003, the emissions from agricultural fires were measured regularly, both by ground-based and by airborne instruments. Enhanced concentrations of formaldehyde, sulphur dioxide, carbon monoxide and carbon dioxide were found

within the emission plumes and it was possible to derive emission ratios (*ERs*) from the data. Formaldehyde emission ratios with respect to CO were calculated from airborne measurements. From three smoke plumes measured, one was considered a single fresh plume with $ER_{CH2O/CO} = 0.020$. The formaldehyde emissions from the observed rice field fires were found to be comparable to the emissions from African savanna fires, reported by other authors.

From CH_2O/SO_2 emission ratios obtained from ground-based DOAS measurements of agricultural fire plumes, a formaldehyde emission factor was calculated. With $EF = 0.60$ g kg^{-1} it was similar to values reported for African savanna fires. Four biomass burning plumes have been observed at the Spessa site. The enhanced formaldehyde concentration in the vicinity of the biomass fires was found to provide a significant increase of local HO_x radical concentrations. A 10-15% increase of the importance of CH_2O as a radical source was found during noon. The agricultural fires were found to represent major sources of formaldehyde and sulphur dioxide, far exceeding the emissions from the urban area of Milano.

Outlook

A field which gains in importance is the formation of secondary organic aerosol, also by aldehydes [e.g. *Tong et al.*, 2006], which should be studied. More intensive studies on the vertical distribution of formaldehyde will thus be interesting, both in the respect of the formation of secondary organic aerosol and regarding formaldehyde loss by deposition to the ground surface. In the investigation of the vertical formaldehyde distribution within the lowest 100 m above ground, a CTM could help understanding the formaldehyde loss processes better.

The discrepancies in Hantzsch formaldehyde results still give reason to concern. Different titration methods for the standard solutions in the very low concentration range are available and are commonly used among the different laboratories. Unfortunately, they do not totally agree with one another. To date it was impossible to solve the apparent differences of up to 30%. A standardised method for the preparation of calibration standards should be found and used.

Measurements in different heights above ground, together with micrometeorological measurements, provide the data necessary to determine the deposition flux of formaldehyde and thus the deposition velocity. In this respect, it is also interesting to study the differences of the deposition velocity above different surfaces. However, in view of the uncertainties between the results of individual instruments, due to the different calibration standards, it is advisable to use one single instrument, which is moved upward and downward. Further, to obtain a significant result, this experiment should extend over an altitude range of more than 10 m with altitude steps of several metres each.

Abbreviations

ARPA	Agenzia Regionale per la Protezione dell'Ambiente
BUW	Bergische Universität Wuppertal, Germany
CEST	Central European Summer Time (UTC + 2)
CRI	Croce Rossa Italiana (Italian Red Cross)
CST	Central Standard Time (UTC – 6)
CTH	Chalmers University of Technology (Chalmers Tekniska Högskola), Göteborg, Sweden
DNPH	Dinitrophenylhydrazine
DOAS	Differential Optical Absorption Spectroscopy
EMEP	European Monitoring and Evaluation Program
EMPA	Swiss Federal Institute for Material Testing and Research, Dübendorf, Switzerland
EF	Emission Factor
ER	Emission Ratio
FID	Flame Ionisation Detector
FORMAT	FORMAldehyde as a Tracer of photooxidation in the troposphere
FTIR	Fourier Transform InfraRed
GC	Gaschromatograph
IFU	Institute for Atmospheric Environmental Research (Institut für Atmosphärische Umweltforschung), Research Centre Karlsruhe, Garmisch-Partenkirchen, Germany
IUP	Institut für Umweltphysik, University of Heidelberg, Germany
IUP-HB	Institut für Umweltphysik, University of Bremen, Germany
IUPAC	International Union of Pure and Applied Chemistry
JPL	Jet Propulsion Laboratory
JRC	Joint Research Centre, Ispra, Italy
LIF	Laser Induced Fluorescence
LOOP	Limitation Of Oxidant Production
MACR	Methacrolein
MCMA	Mexico City Metropolitan Area
MIT	Massachusetts Institute of Technology, Boston, USA
MVK	Methyl Vinyl Ketone
NIHC	Non-Isoprene Hydrocarbon

NILU	Norsk Institutt for Luftforskning, Kjeller, Norway
NMHC	Non-Methane Hydrocarbon
PIPAPO	Pianura Padana Produzione di Ozono
PSI	Paul Scherrer Institut, Villigen, Switzerland
SZA	Solar Zenith Angle
UIO	University of Oslo, Norway
UTC	Coordinated Universal Time (= Greenwich Mean Time)
VOC	Volatile Organic Compound

Literature

Albritton, D. L., A. L. Schmeltekopf and R. N. Zare (1976) An introduction to the least-squares fitting of spectroscopic data, *In:* R. K. Narahari and M. W. Weldong, eds. *Molecular Spectroscopy: Modern Research*, Orlando, FL: Academic.

Alicke, B. (2000) *The role of nitrous acid in the boundary layer*, Ph.D. thesis, University of Heidelberg.

Alicke, B., J. Stutz and U. Platt (2002) Impact of nitrous acid photolysis on the total hydroxyl radical budget during the Limitation of Oxidant Production/Pianura Padana Produzione di Ozono study in Milan, *J. Geophys. Res.*, 107 (D22), 8196.

Altshuller, A. P. (1991a) Chemical reactions and transport of alkanes and their products in the troposphere, *J. Atmos. Chem.*, 12, 19-61.

Altshuller, A. P. (1991b) Estimating product yields of carbon-containing products from the atmospheric photooxidation of ambient air alkenes, *J. Atmos. Chem.*, 13, 131-154.

Altshuller, A. P. (1993) Production of aldehydes as primary emissions and from secondary atmospheric reactions of alkenes and alkanes during the night and early morning hours, *Atmos. Environ.*, 27A, 21-32.

Anderson, L. G., J. A. Lanning, R. Barrell, J. Miyagishima, R. H. Jones and P. Wolfe (1996) Sources and sinks of formaldehyde and acetaldehyde: An analysis of Denver's ambient concentration data, *Atmos. Environ.*, 30, 2113-2123.

Andreae, M. O. (1991) Biomass burning: Its history, use and distribution and its impact on environmental quality and global climate, *In:* J. S. Levine, ed. *Global biomass burning: Atmospheric, climatic and biospheric implications*, Cambridge, MA: MIT Press, pp. 3-21.

Andreae, M. O. and P. Merlet (2001) Emission of trace gases and aerosols from biomass burning, *Global Biogeochem. Cycles*, 15, 955-966.

ARPA - Agenzia Regionale per la Protezione dell'Ambiente, Regione Lombardia (2004) *Richiesta dati archivio aria* [online], Data downloaded from: http://www.ambiente.regione.lombardia.it/webqa/webqasrvs/download/NewDataRequest.jsp [Accessed 10 February 2004].

Atkinson, R. (1994) Gas-phase tropospheric chemistry of organic compounds, *J. Phys. Chem. Ref. Data*, Monograph 2, 1-216.

Atkinson, R., E. C. Tuazon and S. M. Aschmann (1995) Products of the gas-phase reactions of O_3 with alkenes, *Environ. Sci. Technol.*, 29, 1860-1866.

Atkinson, R. (1997) Gas-phase tropospheric chemistry of volatile organic compounds: 1. Alkanes and alkenes, *J. Phys. Chem. Ref. Data*, 26, 215-290.

Atkinson, R., D. L. Baulch, R. A. Cox et al. (2002) *IUPAC Subcommittee on Gas Kinetic Data Evaluation - Data Sheet P1* [online], 16 May 2002, Available from: http://www.iupac-kinetic.ch.cam.ac.uk/datasheets/photol/P1_HCHO+hv.pdf [Accessed 2 September 2005].

Atkinson, R., D. L. Baulch, R. A. Cox, J. N. Crowley, R. F. Hampson, R. G. Hynes, M. E. Jenkin, J. A. Kerr, M. J. Rossi and J. Troe (2005) *Summary of evaluated kinetic and photochemical data for atmospheric chemistry, IUPAC Subcommittee for gas kinetic data evaluation for atmospheric chemistry*, Web Version March 2005 [online], Available from: http://www.iupac-kinetic.ch.cam.ac.uk/, University of Cambridge [Accessed 19 October 2005].

Axelsson, H., B. Galle, K. Gustavsson, P. Ragnarsson and M. Rudin (1990) A transmitting/receiving telescope for DOAS-measurements using retro-reflector technique, *In: Optical Remote Sensing of the Atmosphere*, Vol. 4, OSA Technical Digest Series, 641-644.

Ayers, G. P., R. W. Gillet, H. Granek, C. de Serves and R. A. Cox (1997) Formaldehyde production in clean maritime air, *Geophys. Res. Lett.*, 24 (4), 401-404.

Bass, A. M., L. C. Glasgow, C. Miller, J. P. Jesson and D. L. Filkin (1980) Temperature dependent absorption cross-sections for formaldehyde (CH_2O): The effect of formaldehyde on stratospheric chlorine chemistry, *Planet. Space Sci.*, 28, 675-679.

Benning, L. and A. Wahner (1998) Measurement of atmospheric formaldehyde (HCHO) and acetaldehyde (CH_3CHO) during POPCORN 1994 using 2,4-DNPH coated silica cartridges, *J. Atmos. Chem.*, 31, 105-117.

Bevington, P. R. (1969) *Data reduction and error analysis for the physical sciences*, New York: McGraw Hill.

Bobrowski, N., G. Hönninger, B. Galle and U. Platt (2003) Detection of bromine monoxide in a volcanic plume, *Nature*, 423, 273-276.

Bogumil, K., J. Orphal, T. Homann, S. Voigt, P. Spietz, O. C. Fleischmann, A. Vogel, M. Hartmann, H. Bovensmann, J. Frerick and J. P. Burrows (2003) Measurements of molecular absorption spectra with the SCIAMACHY pre-flight model: Instrument characterization and reference data for atmospheric remote sensing in the 230-2380 nm region, *J. Photochem. Photobiol. A: Chem.*, 157, 167-184.

Bohn, B., H. Berresheim, W. J. Bloss, L. Clapp, K. C. Clemitshaw, G. Corlett, M. Gillmann, D. E. Heard, I. A. Mbakwe, F. Meixner, N. Mihalopoulos, P. S. Monks, C. Plass-Dülmer, A. S. H. Prévôt, S. Sanghavi, R. Schmitt, G. Stange, E. Tensing, M. Vrekoussis (2005) *Actinic Flux / Photolysis Frequency Measurement Intercomparison, A contribution to WP 11: Quality assurance*, poster presented at 1st ACCENT Symposium, 12-16 September 2005, Urbino, Italy.

Buttner, P. (2001) *Emission reduction credits for unburned rice straw acreage: Information growers should know* [online], California Rice Commission, Available from: http://www.calrice.org/downloads/ERC_Summary.pdf [Accessed 26 October 2005].

Cantrell, C. A., J. A. Davidson, A. H. McDaniel, R. E. Shetter and J. G. Calvert (1990) Temperature-dependent formaldehyde cross sections in the near-ultraviolet spectral region, *J. Phys. Chem.*, 94, 3902-3908.

Cárdenas, L. M., D. J. Brassington, B. J. Allan, H. Coe, B. Alicke, U. Platt, K. M. Wilson, J. M. C. Plane and S. A. Penkett (2000) Intercomparison of formaldehyde measurements in clean and polluted atmospheres, *J. Atmos. Chem.*, 37, 53-80.

Carlier, P., H. Hannachi and G. Mouvier (1986) The chemistry of carbonyl compounds in the atmosphere - a review, *Atmos. Environ.*, 20 (11), 2079-2099.

Carslaw, N., N. Bell, A. C. Lewis, J. B. McQuaid and M. J. Pilling (2000) A detailed case study of isoprene chemistry during the EASE96 Mace Head campaign, *Atmos. Environ.*, 34, 2827-2836.

Chameides, W. L. (1987) Acid dew and the role of chemistry in the dry deposition of reactive gases to wetted surfaces, *J. Geophys. Res.*, 92, 11 895-11 908.

Chameides, W. L., F. Fehsenfeld, M. O. Rodgers et al. (1992) Ozone precursor relationships in the ambient atmosphere, *J. Geophys. Res.*, 97, 6037-6055.

Chance, K., P. I. Palmer, R. J. D. Spurr, R. V. Martin, T. P. Kurosu and D. J. Jacob (2000) Satellite observations of formaldehyde over North America from GOME, *Geophys. Res. Lett.*, 27 (21), 3461-3464.

Christian, T. J., B. Kleiss, R. J. Yokelson, R. Holzinger, P. J. Crutzen, W. M. Hao, B. H. Saharjo and D. E. Ward (2003) Comprehensive laboratory measurements of biomass-burning emissions: 1. Emission from Indonesian, African, and other fuels, *J. Geophys. Res.*, 108 (D23), 4719, doi: 10.1029/2003JD003704.

Crutzen, P. J. and M. O. Andreae (1990) Biomass burning in the tropics: Impact on atmospheric chemistry and biogeochemical cycles, *Science*, 250, 1669-1678.

Czerny, M. and A. F. Turner (1930) Über den Astigmatismus bei Spiegelspektrometern, *Z. Phys.*, 61, 792-797.

de Foy, B., E. Caetano, V. Magaña, A. Zitácuaro, B. Cárdenas, A. Retama, R. Ramos, L. T. Molina, M. J. Molina (2005) Mexico City basin wind circulation during the MCMA-2003 field campaign, *Atmos. Chem. Phys.*, 5, 2267-2288.

de Serves, C. (1994) Gas phase formaldehyde and peroxide measurements in the Arctic atmosphere, *J. Geophys. Res.*, 99 (D12), 25391-25398.

Dommen, J., A. S. H. Prévôt, B. Neininger and M. Bäumle (2002) Characterization of the photooxidant formation in the metropolitan area of Milan from aircraft measurements, *J. Geophys. Res.*, 107 (D22), 8197.

Dommen, J., A. S. H. Prévôt, N. Baertsch-Ritter, G. Maffeis, M. G. Longoni, F. C. Grüebler and A. Thielmann (2003) High-resolution emission inventory of the Lombardy region: Development and comparison with measurements, *Atmos. Environ.*, 37, 4149-4161.

Dosio, A., S. Galmarini and G. Graziani (2002) Simulation of the circulation and related photochemical ozone dispersion in the Po plains (northern Italy): Comparison with the observations of a measuring campaign, *J. Geophys. Res.*, 107 (D18), 8189.

Duane, M., B. Poma, D. Rembges, C. Astorga and B. R. Larsen (2002) Isoprene and its degradation products as strong ozone precursors in Insubria, Northern Italy, *Atmos. Environ.*, 36, 3867-3879.

ECMWF - European Centre for Medium-Range Weather Forecasts (2004) The exceptional warm anomalies of summer 2003, *ECMWF Newsletter*, 99, 2-8.

Edlen, B. (1966) The refraction index of air, *Metrologia*, 2, 71-80.

Ehhalt, D. H. and F. Rohrer (2000) Dependence of the OH concentration on solar UV, *J. Geophys. Res.*, 105 (D3), 3565-3571.

Ente Nazionale Risi - National Rice Agency (2005) *Vent'anni di risicoltura, analisi grafica di superfici, varietà, dimensioni e numero delle aziende risicole in Italia dal 1982 al 2001* [online], Available from: http://www.enterisi.it/index.jsp [Accessed 31 October 2005].

EPA (2003), *State of the Environment Queensland 2003*, Report of the Environmental Protection Agency Brisbane, Australia.

EU, Council Directive 2002/3/EC of 9 March 2002 on *Relating to ozone in ambient air*, Official Journal of the European Communities, L 67, 14-30.

Facchini, U., M. Martini, E. Morniroli, G. Procopio, G. Tamborini, A. Canuti and G. Capelli (1981) Concentration of radon progeny in the open air and interiors of Milan and other Italian sites, *Health Phys.*, 41, 23-28.

Faloona, I. C., D. Tan, R. L. Lesher, N. L. Hazen, C. L. Frame, J. B. Simpas, H. Harder, et al. (2004) A laser-induced fluorescence instrument for detecting tropospheric OH and HO_2: Characteristics and calibration, *J. Atmos. Chem.*, 47, 139-167.

Fayt, C. and M. van Roozendael (2001) *WinDOAS 2.1 Software User Manual*, Institut d'Aéronomie Spatiale de Belgique (IASB), Bruxelles.

Fehsenfeld, F., J. Calvert, R. Fall, P. Goldan, A. B. Guenther, et al. (1992) Emissions of volatile organic compounds from vegetation and the implications for atmospheric chemistry, *Global Biogeochem. Cycles*, 6, 389-430.

Finlayson-Pitts, B. J. and J. N. Pitts (2000) *Chemistry of the upper and lower atmosphere: Theory, experiments and applications*, San Diego: Academic Press.

Fischer, H. and H. Oelhaf (1996) Remote sensing of vertical profiles of atmospheric trace constituents with MIPAS limb-emission spectrometers, *Appl. Opt.*, 35 (16), 2787-2796.

Flatøy, F., Ø. Hov and H. Smit (1995) Three-dimensional model studies of exchange processes of ozone in the troposphere over Europe, *J. Geophys. Res.*, 100 (D6), 11 465-11 481.

Forrer, J., R. Rüttimann, D. Schneiter, A. Fischer, B. Buchmann and P. Hofer (2000) Variability of trace gases at the high-Alpine site Jungfraujoch caused by meteorological transport processes, *J. Geophys. Res.*, 105 (D10), 12 241-12 251.

Fried, A., S. McKeen, S. Sewell, J. Harder, B. Henry, P. Goldan, W. Kuster, E. Williams, K. Baumann, R. Shetter and C. Cantrell (1997) Photochemistry of formaldehyde during the 1993 Tropospheric OH Photochemistry Experiment, *J. Geophys. Res.*, 102 (D5), 6283-6296.

Galbally, I. E. and C. R. Roy (1980) Destruction of ozone at the earth's surface, *Quart. J. Roy. Meteor. Soc.*, 106, 599-620.

García, A. R., R. Volkamer, L. T. Molina, M. J. Molina, J. Samuelsson, J. Mellqvist, B. Galle, S. C. Herndon and C. E. Kolb (2005) Separation of emitted and photochemical formaldehyde in Mexico City using a statistical analysis and a new pair of gas-phase tracers, *Atmos. Chem. Phys. Discuss.*, 5, 11 583-11 615.

Gerbig, C., S. Schmitgen, D. Kley, A. Volz-Thomas, K. Dewey and D. Haaks (1999) An improved fast-response vacuum-UV resonance fluorescence CO instrument, *J. Geophys. Res.*, 104 (D1), 1699-1704.

Gilpin, T., E. Apel, A. Fried, B. Wert, J. Calvert, Z. Genfa, P. Dasgupta, J. W. Harder, B. Heikes, B. Hopkins, H. Westberg, T. Kleindienst, Y. N. Lee, X. Zhou, W. Lonnemann and S. Sewell (1997), Intercomparison of six ambient [CH_2O] measurement techniques, *J. Geophys. Res.*, 102 (D17), 21 161-21 188.

Gomer, T., T. Brauers, F. Heintz, J. Stutz and U. Platt (1996) *MFC User Manual Vers. 1.99*, University of Heidelberg.

Graedel, T. E. and P. J. Crutzen (1994) *Chemie der Atmosphäre: Bedeutung für Klima und Umwelt*, Heidelberg: Spektrum Akademischer Verlag.

Gratien, A., B. Picquet-Varrault, J. Orphal, E. Perraudin, J.-F. Doussin and J.-M. Flaud (2006) Laboratory intercomparison of the formaldehyde absorption coefficients in the infrared (1660-1820 cm^{-1}) and ultraviolet (300-360 nm) spectral regions, submitted to *J. Geophys. Res.*

Griffith, D. W. T. (1996) Synthetic calibration and quantitative analysis of gas-phase infrared spectra, *Appl. Spectrosc.*, 50, 59-70.

Griffiths, P. R. and J. A. de Haseth (1986) *Fourier Transform Infrared Spectroscopy*, New York: John Wiley & Sons Inc.

Grosjean, D. (1982) Formaldehyde and other carbonyls in Los Angeles ambient air, *Environ. Sci. Technol.*, 16, 254-262.

Grosjean, D., R. D. Swanson and C. Ellis (1983) Carbonyls in Los Angeles air: Contribution of direct emissions and photochemistry, *Sci. Total Environ.*, 29, 65-85.

Grosjean, D. (1991) Ambient levels of formaldehyde, acetaldehyde and formic acid in Southern California: Results of a one-year base-line study, *Environ. Sci. Technol.*, 25, 710-715.

Grosjean. E., H. Williams, D. Grosjean (1993) Ambient levels of formaldehyde and acetaldehyde in Atlanta, Georgia, *Journal of the Air Waste Management Association*, 43, 467-474.

Grosjean, E., J. B. de Andrade and D. Grosjean (1996) Carbonyl products of the gas-phase reaction of ozone with simple alkenes, *Environ. Sci. Technol.*, 30, 975-983.

Grossmann, D., G. K. Moortgat, M. Kibler, S. Schlomski, K. Bächmann, B. Alicke, A. Geyer, U. Platt, M.-U. Hammer, B. Vogel, D. Mihelcic, A. Hofzumahaus, F. Holland, A. Volz-Thomas (2003) Hydrogen peroxide, organic peroxides, carbonyl compounds, and organic acids measured at Pabstthum during BERLIOZ, *J. Geophys. Res.*, 108 (D4), 8250.

Grüebler, F. C. (1999) *Reactive hydrocarbons in the Milan area: Results from the PIPAPO campaign*, Ph.D. thesis, Swiss Federal Institute of Technology (ETH), Zürich.

Grutter, M., E. Flores, G. Andraca-Ayala and A. Báez (2005) Formaldehyde levels in downtown Mexico City during 2003, *Atmos. Environ.*, 39, 1027-1034.

Guenther, A. B., C. N. Hewitt, D. Erickson, R. Fall, C. Geron, T. Graedel, P. Harley, L. Klinger, M. Lerdau. W. A. McKay, T. Pierce, B. Scholes, R. Steinbrecher, R. Tallamraju, J. Taylor and P. Zimmerman (1995) A global model of natural volatile organic compound emissions, *J. Geophys. Res.*, 100 (D5), 8873-8892.

Hak, C., I. Pundt, S. Trick, C. Kern, U. Platt, J. Dommen, C. Ordóñez, A. S. H. Prévôt, W. Junkermann, C. Astorga-Lloréns, B. R. Larsen, J. Mellqvist, A. Strandberg, Y. Yu, B. Galle, J. Kleffmann, J. C. Lörzer, G. O. Braathen and R. Volkamer (2005) Intercomparison of four different in-situ techniques for ambient formaldehyde measurements in urban air, *Atmos. Chem. Phys.*, 5, 2881-2900.

Hak, C., J. Dommen, A. S. H. Prévôt et al. (2006) On the spatial variability of formaldehyde in the Po Basin: An approach based on VOC reactivities, in preparation.

Hammer, M.-U., B. Vogel and H. Vogel (2002) Findings on H_2O_2/HNO_3 as an indicator of ozone sensitivity in Baden-Württemberg, Berlin-Brandenburg and the Po Valley based on numerical simulations, *J. Geophys. Res.*, 107 (D18), 8190.

Harder, J. W., A. Fried, S. Sewell and B. Henry (1997) Comparison of tunable diode laser and long-path ultraviolet/visible spectroscopic measurements of ambient formaldehyde concentrations during the 1993 OH Photochemistry Experiment, *J. Geophys. Res.*, 102 (D5), 6267-6282.

Harley, P. C., R. K. Monson and M. T. Lerdau (1999) Ecological and evolutionary aspects of isoprene emission from plants, *Oecologia*, 118, 109-123.

Harris, G. W., G. I. Mackay, T. Iguchi, L. K. Mayne and H. I. Schiff (1989) Measurements of formaldehyde in the troposphere by Tuneable Diode Laser Absorption Spectroscopy, *J. Atmos. Chem.*, 8, 119-137.

Hartl, A., B.-C. Song and I. Pundt (2006) 2-D reconstruction of atmospheric concentration peaks from horizontal long path DOAS tomographic measurements: Parametrisation and geometry within a discrete approach, *Atmos. Chem. Phys.*, 6, 847-861.

Haszpra, L., I. Szilágyi, A. Demeter, T. Turányi and T. Bérces (1991) Non-methane hydrocarbon and aldehyde measurements in Budapest, Hungary, *Atmos. Environ.*, 25A, 2103-2110.

Hatakeyama, S., K. Izumi, T. Fukuyama, et al. (1991) Reactions of OH with α-pinene and β-pinene in air: Estimate of global CO production from the atmospheric oxidation of terpenes, *J. Geophys. Res.*, 96, 947-958.

Heckel, A., A. Richter, T. Tarsu, F. Wittrock, C. Hak, I. Pundt, W. Junkermann and J. P. Burrows (2005), MAX-DOAS measurements of formaldehyde in the Po-Valley, *Atmos. Chem. Phys.*, 5, 909-918.

Hermans, C., A. C. Vandaele, M. Carleer, S. Fally, R. Colin, A. Jenouvrier, B. Coquart and M.-F. Mérienne (1999), Absorption cross-sections of atmospheric constituents: NO_2, O_2, and H_2O, *Environ. Sci. & Pollut. Res.*, 6 (3), 151-158.

Hermes, T. (1999) *Lichtquellen und Optik für die Differentielle Optische Absorptionsspektroskopie*, Diplomarbeit, Universität Heidelberg.

Heue, K.-P., A. Richter, M. Bruns, J. P. Burrows, C. v. Friedeburg, U. Platt, I. Pundt, P. Wang and T. Wagner (2005) Validation of SCIAMACHY tropospheric NO_2-columns with AMAXDOAS measurements, *Atmos. Chem. Phys.*, 5, 1039-1051.

Heue, K.-P. (2005) *Airborne Multi AXis DOAS instrument and measurements of two-dimensional tropospheric trace gas distributions*, Ph.D. thesis, University of Heidelberg.

Holzinger, R., C. Warneke, A. Hansel, A. Jordan and W. Lindinger (1999) Biomass burning as a source of formaldehyde, acetaldehyde, methanol, acetone, acetonitrile, and hydrogen cyanide, *Geophys. Res. Lett.*, 26 (8), 1161-1164.

Houweling, S., F. Dentener and J. Lelieveld (1998) The impact of non-methane hydrocarbon compounds on tropospheric photochemistry, *J. Geophys. Res.*, 103 (D9), 10 673-10 696.

IPCC - Intergovernmental Panel on Climate Change (2001) *Climate change 2001: The scientific basis*, J. T. Houghton, ed. New York: Cambridge University Press, pp. 105.

Jacob, D. J., B. G. Heikes, S.-M. Fan, J. A. Logan, D. L. Mauzerall, J. D. Bradshaw, H. B. Singh, G. L. Gregory, R. W. Talbot, D. R. Blake and G. W. Sachse (1996) Origin of ozone and NO_x in the tropical troposphere: A photochemical analysis of aircraft observations over the South Atlantic Basin, *J. Geophys. Res.*, 101 (D19), 24 235-24 250.

Jacobi, W. and K. André (1963) The vertical distribution of radon 222, thoron 220 and their decay products in the atmosphere, *J. Geophys. Res.*, 68, 3799-3814.

Jenkin, M. E., S. M. Saunders and M. J. Pilling (1997) The tropospheric degradation of volatile organic compounds: A protocol for mechanism development, *Atmos. Environ.*, 31, 81-104.

Jenkins, B. M., S. Q. Turn, R. B. Williams, M. Goronea et al. (1996) *Atmospheric pollutant emission factors from open burning of agricultural and forest biomass by wind tunnel simulations: Final Report*, Volume 1, California Environmental Protection Agency.

Jiménez, R., A. Martilli, I. Balin, H. v. d. Bergh, B. Calpini, B. R. Larsen, G. Favaro and D. Kita (2000) Measurement of formaldehyde (HCHO) by DOAS: Intercomparison to DNPH measurements and interpretation from Eulerian model calculations, *In: Proceedings of the 93rd Annual Conference & Exhibition*, *Air & Waste Management Association*, Paper #829, 18-22 June 2000, Salt Lake City, Utah.

Jost, C., J. Trentmann, D. Sprung, M. O. Andreae, J. B. McQuaid and H. Barjat (2003) Trace gas chemistry in a young biomass burning plume over Namibia: Observations and model simulations, *J. Geophys. Res.*, 108 (D13), 8482, doi:10.1029/2002JD002431.

Junkermann, W. and J. M. Burger (2006) A new portable instrument for continuous measurement of formaldehyde in ambient air, *J. Atmos. Ocean. Tech.*, 23, 38-45.

Kelly, T. J. and C. R. Fortune (1994) Continuous monitoring of gaseous formaldehyde using an improved fluorescence approach, *Int. J. Environ. Anal. Chem.*, 54, 249-263.

Kesselmeier, J., K. Bode, U. Hofmann, H. Müller, L. Schäfer, A. Wolf, P. Ciccioli, E. Brancaleoni, A. Cecinato, M. Frattoni, P. Foster, C. Ferrari, V. Jacob, J. L. Fugit, L. Dutaur, V. Simun and L. Torres (1997) Emission of short chained organic acids, aldehydes and monoterpenes from *Quercus ilex* L. and *Pinus pinea* L. in relation to physiological activities, carbon budget and emission algorithms, *Atmos. Environ.*, 31 (S1), 119-133.

Kesselmeier, J. and M. Staudt (1999) Biogenic volatile organic compounds (VOC): An overview on emission, physiology and ecology, *J. Atmos. Chem.*, 33, 23-88.

Khokhar, M. F. (2006) *Retrieval and interpretation of tropospheric SO_2 from UV/VIS satellite instruments*, Ph.D. thesis, University of Leipzig.

Kirchstetter, T., B. C. Singer, R. A. Harley, G. R. Kendall and W. Chan (1996) Impacts of oxygenated gasoline use on California light-duty vehicle emissions, *Environ. Sci. Technol.*, 30, 661-670.

Kleindienst, T. E., P. B. Shepson, C. M. Nero, R. R. Arnts, S. B. Tejada, G. I. Mackay, L. K. Mayne, H. I. Schiff, J. A. Lind, G. L. Kok, A. L. Lazrus, P. K. Dasgupta, S. Dong (1988) An intercomparison of formaldehyde measurement techniques at ambient concentration, *Atmos. Environ.*, 22, 1931-1939.

Kleinman, L. I., P. H. Daum, J. H. Lee, Y. N. Lee, L. H. Nunnermacker, S. R. Springston, L. Newman, J. Weinstein-Lloyd and S. Sillman (1997) Dependence of ozone production on NO and hydrocarbons in the troposphere, *Geophys. Res. Lett.*, 24 (18), 2299-2302.

Klemp, D., D. Kley, F. Kramp, H. J. Buers, G. Pilwat, F. Flocke, H. W. Pätz and A. Volz-Thomas (1997), Long-term measurements of light hydrocarbons (C_2-C_5) at Schauinsland (Black Forest), *J. Atmos. Chem.*, 28, 135-171.

Klemp, D., K. Mannschreck and B. Mittermaier (2003) Comparison of two different HCHO measurement techniques: TDLAS and a commercial Hantzsch monitor – Results from long term measurements in a city plume during the EVA experiment, *In:* R. Friedrich and S. Reis, eds. *Emissions of air pollutants – Measurements, calculations and uncertainties*, Berlin: Springer Verlag, pp. 228-235.

Konrad, S. and A. Volz-Thomas (2000) Characterization of a commercial gas chromatography-flame ionization detection system for the in situ determination of C_5-C_{10} hydrocarbons in ambient air, *J. Chromatography* (A), 878, 215-234.

Kraus, A., F. Rohrer and A. Hofzumahaus (2000) Intercomparison of NO_2 photolysis frequency measurements by actinic flux spectroradiometry and chemical actinometry during JCOM97, *Geophys. Res. Lett.*, 27 (8), 1115-1118.

Krinke, S. M. W. (1999) *Experimentelle Bestimmung der Depositionsgeschwindigkeit von Formaldehyd und Ozon über einem Laubwaldbestand*, Ph.D. thesis, University of Stuttgart.

Larsen, B. R., D. Di Bella, M. Glasius, R. Winterhalter, N. R. Jensen and J. Hjorth (2001) Gas-phase OH oxidation of monoterpenes: Gaseous and particulate products, *J. Atmos. Chem.*, 38, 231-276.

Latella, A., G. Stani, L. Cobelli, M. Duane, H. Junninen, C. Astorga and B. R. Larsen (2005) Semicontinuous GC analysis and receptor modelling for source apportionment of ozone precursor hydrocarbons in Bresso, Milan, 2003, *J. Chromatogr.* A, 1071, 29-39.

Lawson, D. R., H. W. Biermann, E. C. Tuazon, A. M. Winer, G. I. Mackay, H. I. Schiff, G. L. Kok, P. K. Dasgupta and K. Fung (1990) Formaldehyde measurement methods evaluation and ambient concentrations during the Carbonaceous Species Methods Comparison Study, *Aerosol Sci. Technol.*, 12, 64-76.

Lee, Y.-N., X. Zhou, L. I. Kleinman, L. J. Nunnermacker, S. R. Springston, P. H. Daum, L. Newman, W. G. Keigley, M. W. Holdren, C. W. Spicer, V. Young, B. Fu, D. D. Parrish, J. Holloway, J. Williams, J. M. Roberts, T. B. Ryerson and F. C. Fehsenfeld (1998) Atmospheric chemistry and distribution of formaldehyde and several multioxygenated carbonyl compounds during the 1995 Nashville/Middle Tennessee ozone study, *J. Geophys. Res.*, 103 (D17), 22 449-22 462.

Lemieux, P. M., C. C. Lutes, D. A. Santoianni (2004) Emissions of organic air toxics from open burning: a comprehensive review, *Progress in Energy and Combustion Science*, 30, 1-32.

Lenz, R., R. Köble, G. Seufert (2001) Species-based mapping of biogenic emissions in Europe – case study Italy, *In: Proceedings of the 8th European symposium on the physico-chemical behaviour of atmospheric pollutants: "A changing atmosphere"*, 17-20 September 2001, Torino, Italy.

Levin, I. (2000) *Manual for the radon monitor*, developed at the Institut für Umweltphysik, University of Heidelberg.

Levin, I., M. Born, M. Cuntz, et al. (2002) Observations of atmospheric variability and soil exhalation rate of radon-222 at a Russian forest site. Technical approach and deployment for boundary layer studies, *Tellus*, 54 (5), 462-475.

Li, S., B. Lin and W. Zhou (2005) Crop response to sulfur fertilizers and soil sulfur status in some provinces of China. *In:* L. J. De Kok and E. Schnug, eds. *Proceedings of the 1st Sino-German Workshop on Aspects of Sulfur Nutrition of Plants, Shenyang, China*, 23-27 May 2004, Braunschweig: Bundesforschungsanstalt für Landwirtschaft (FAL), pp. 81-84.

Liu, L., F. Flatøy, C. Ordóñez, G. O. Braathen, C. Hak, W. Junkermann, S. Andreani-Aksoyoglu, J. Mellqvist, B. Galle, A. S. H. Prévôt and I. S. A. Isaksen (2006) Photochemical modelling in the Po Basin with focus on formaldehyde and ozone, *Atmos. Chem. Phys. Discuss.*, 6, 5057-5094.

Logan, J. A., M. J. Prather, S. C. Wofsy and M. B. McElroy (1981), Tropospheric chemistry: A global perspective, *J. Geophys. Res.*, 86 (C8), 7210-7254.

Logan, J. A. (1985) Tropospheric ozone: Seasonal behaviour, trends and anthropogenic influence, *J. Geophys. Res.*, 90, 10 463-10482.

Lohberger, F., G. Hönninger and U. Platt (2004) Ground-based imaging differential optical absorption spectroscopy of atmospheric gases, *Appl. Opt.*, 43 (24), 4711-4717.

Louban, I. (2005) *Zweidimensionale spektroskopische Aufnahmen von Spurenstoff-Verteilungen*, Diploma thesis, University of Heidelberg.

Lowe, D. C. and U. Schmidt (1983) Formaldehyde (HCHO) measurements in the nonurban atmosphere, *J. Geophys. Res.*, 88 (C15), 10 844-10 858.

Maps of Mexico (2003) *Distrito Federal Mexico map* [online], Map available from: http://www.maps-of-mexico.com/distrito-federal-df-mexico/mexico-df-distrito-federal-mexico-map-main.shtml [Accessed 14 May 2003].

Marbach, T., S. Beirle, F. Khokhar, U. Platt and T. Wagner (2005) *Identification of tropospheric emissions sources from satellite observations: Synergistic use of HCHO, NO_2, and SO_2 trace gas measurements*, paper presented at 1st ACCENT Symposium, 12-16 September 2005, Urbino, Italy.

Martilli, A., A. Neftel, G. Favaro, F. Kirchner, S. Sillman and A. Clappier (2002) Simulation of the ozone formation in the northern part of the Po Valley, *J. Geophys. Res.*, 107 (D22), 8195.

Martin, R. S., H. Westberg, E. Allwine, L. Ashman, J. C. Farmer and B. Lamb (1991) Measurement of isoprene and its atmospheric oxidation products in a central Pennsylvania deciduous forest, *J. Atmos. Chem.*, 13, 1-32.

Martin, V. R. M. A. Fiore, and A. van Donkelaar (2004) Space-based diagnostics of surface ozone sensitivity to anthropogenic emissions, *Geophys. Res. Lett.*, 31 (6), L06120.

Meller, R. (1992) personal communication to Max-Planck-Institut für Chemie, Mainz, Germany, Data from the CD-ROM of Nölle et al. (Nölle, A., F. Pätzold, S. Pätzold, R. Meller, G. K. Moortgat, E. P. Röth, R. Ruhnke and H. Keller-Rudek, UV/VIS Spectra of Atmospheric Constituents, Version 1, ATMOS User Centre at Deutsches Fernerkundungsdatenzentrum (DFD), 1998).

Meller, R. and G. K. Moortgat (2000) Temperature dependence of the absorption cross sections of formaldehyde between 223 and 323 K in the wavelength range 225-375 nm, *J. Geophys. Res.*, 105 (D6), 7089-7101.

Mettendorf, K. U. (2005) *Aufbau und Einsatz eines Multibeam Instrumentes zur DOAS-tomographischen Messung zweidimensionaler Konzentrationsverteilungen*, Ph.D. thesis, University of Heidelberg.

Milford, J., A. G. Russell and G. J. McRae (1989) A new approach to photochemical pollution control: Implications of spatial patterns in pollutant responses to reductions in nitrogen oxides and reactive organic gas emissions, *Environ. Sci. Technol.*, 23, 1290-1301.

MODIS - Moderate Resolution Imaging Spectroradiometer (2004) *Web Fire Mapper* [online], Available from: http://maps.geog.umd.edu/ [Accessed 4 November 2004].

Moortgat, G. K., W. Klippel, K. H. Möbus, W. Seiler and P. Warneck (1980) *Laboratory measurements of photolytic parameters for HCHO*, FAA Report FAA-EE-80-47, US Department of Transportation, Office of Environment and Energy, Washington D.C.

Nash, T. (1953) The colorimetric estimation of formaldehyde by means of the Hantzsch reaction, *Biochem. J.*, 55, 416-421.

Navas, M. J., A. M. Jiménez and G. Galán (1997) Air analysis: Determination of nitrogen compounds by chemiluminescence, *Atmos. Environ.*, 31, 3603-3608.

Neftel, A., C. Spirig, A. S. H. Prévôt, M. Furger, J. Stutz, B. Vogel and J. Hjorth (2002) Sensitivity of photooxidant production in the Milan Basin: An overview of results from a EUROTRAC-2 Limitation of Oxidant Production field experiment, *J. Geophys. Res.*, 107 (D22), 8188, doi: 10.1029/2001JD001263.

Neininger, B., W. Fuchs, M. Baeumle, A. Volz-Thomas, A. S. H. Prévôt and J. Dommen (2001) A small aircraft for more than just ozone: Metair's 'Dimona' after ten years of evolving development, *In: Proceedings of the 11th Symposium on Meteorological Observations and Instrumentation*, *81st AMS Annual Meeting*, 14-19 January 2001, Albuquerque, NM, USA.

Nondek, L., D. R. Rodler and J. W. Birks (1992) Measurement of sub-ppbv concentrations of aldehydes in a forest atmosphere using a new HPLC technique, *Environ. Sci. Technol.*, 26, 1174-1178.

NPI - National Pollutant Inventory (2003) *NPI definition for volatile organic compounds* [online], Australian Government, Department of the Environment and Heritage, Available from: http://www.npi.gov.au/handbooks/pubs/voc.pdf [Accessed 3 June 2005].

Palmer, P. I., D. J. Jacob, A. M. Fiore, R. V. Martin, K. Chance and T. P. Kurosu (2003) Mapping isoprene emissions over North America using formaldehyde column observations from space, *J. Geophys. Res.*, 108 (D6), 4180, doi: 10.1029/2002JD002153.

Parco Nord Milano (2004) *Mappa di dettaglio* [online], Map available from: http://www.parks.it/parco.nord.milano/mapl.html [Accessed 15 March 2004].

Pätz, H.-W., U. Corsmeier, K. Glaser, U. Vogt, N. Kalthoff, D. Klemp, B. Kolahgar, A. Lerner, B. Neininger, T. Schmitz, M. G. Schultz, J. Slemr and A. Volz-Thomas (2000) Measurements of trace gases and photolysis frequencies during SLOPE96 and a coarse estimate of the local OH concentration from HNO_3 formation, *J. Geophys. Res.*, 105 (D1), 1563-1583.

Paulson, S. E., M. Y. Chung and A. S. Hasson (1999) OH radical formation from the gas-phase reaction of ozone with terminal alkenes and the relationship between structure and mechanism, *J. Phys. Chem. A*, 103 (41), 8125-8138.

Pfeilsticker, K. and U. Platt (1994) Airborne measurements during the Arctic stratospheric experiment: Observation of O_3 and NO_2, *Geophys. Res. Lett.*, 21 (13), 1375-1378.

Plass-Dülmer, C., T. Brauers and J. Rudolph (1998) POPCORN: A field study of photochemistry in north-eastern Germany, *J. Atmos. Chem.*, 31, 5-31.

Platt, U., D. Perner and H. W. Pätz (1979) Simultaneous measurement of atmospheric CH_2O, O_3 and NO_2 by differential optical absorption, *J. Geophys. Res.*, 84 (C10), 6329-6335.

Platt, U. (1994) Differential Optical Absorption Spectroscopy (DOAS), *In:* M. W. Sigrist, ed. *Monitoring by Spectroscopic Techniques*, New York: John Wiley & Sons, pp. 27-84.

Pope, F. D., C. A. Smitz, M. N. R. Ashfold and A. J. Orr-Ewing (2005) High-resolution absorption cross sections of formaldehyde at wavelengths from 313 to 320 nm, *Phys. Chem. Chem. Phys.*, 7, 79-84.

Possanzini, M., V. Di Palo and A. Cecinato (2002) Sources and photodecomposition of formaldehyde and acetaldehyde in Rome ambient air, *Atmos. Environ.*, 36, 3195-3201.

Press, W. H., S. A. Teukolsky, W. T. Vetterling and B. P. Flannery (1992a) Levenberg-Marquardt method, *In: Numerical recipes in C, The art of scientific computing*, Cambridge: Cambridge University Press, pp. 678-682.

Press, W. H., S. A. Teukolsky, W. T. Vetterling and B. P. Flannery (1992b) Straight-line data with errors in both coordinates, *In: Numerical recipes in C, The art of scientific computing*, Cambridge: Cambridge University Press, pp. 660-664.

Prévôt, A. S. H., J. Staehelin, G. L. Kok, R. D. Schillawski, B. Neininger, T. Staffelbach, A. Neftel, H. Wernli and J. Dommen (1997) The Milan photooxidant plume, *J. Geophys. Res.*, 102 (D19), 23 375-23 388.

Pundt, I. and K. U. Mettendorf (2005) The Multibeam long path differential optical absorption spectroscopy instrument: A device for simultaneous measurements along multiple light paths, *Appl. Opt.*, 44 (23), 4985-4994.

Pundt, I., K. U. Mettendorf, T. Laepple, V. Knab, P. Xie, J. Lösch, C. v. Friedeburg, U. Platt and T. Wagner (2005) Measurements of trace gas distributions using long-path DOAS-tomography during the motorway campaign BAB II, *Atmos. Environ.*, 39, 967-975.

Rappenglück, B. and P. Fabian (1999) An analysis of simultaneous online GC measurements of BTEX aromatics at three selected sites in the Greater Munich Area, *J. Appl. Meteorol.*, 38, 1448-1462.

Rembges, D., G. Fantecchi, L. Dutaur and C. Brun (1999) *AIRMON annual report*, European Commission, EUR 19665 EN.

Ren, X., H. Harder, M. Martinez, R. L. Lesher, A. Oliger, J. B. Simpas, W. H. Brune, J. J. Schwab, K. L. Demerjian, Y. He, X. Zhou and H. Gao (2003), OH and HO_2 chemistry in the urban atmosphere of New York City, *Atmos. Environ.*, 37, 3639-3651.

Riedel, K., R. Weller and O. Schrems (1999) Variability of formaldehyde in the Antarctic troposphere, *Phys. Chem. Chem. Phys.*, 1, 5523-5527.

Riggs, D. S., J. A. Guarnieri and S. Addelman (1978) Fitting straight lines when both variables are subject to error, *Life Sciences*, 22, 1305-1360.

Ritz, D., M. Hausmann and U. Platt (1993) An improved open-path multireflection cell for the measurement of NO_2 and NO_3, *In:* H. I. Schiff and U. Platt, eds. *Optical methods in atmospheric chemistry*, SPIE Proceedings, Vol. 1715, pp. 200-211.

Rodenas García, M., M. Martín Reviejo, M. Pons, T. Vera Espallardo, R. Volkamer, K. Wirtz (2003) EUPHORE Data Sheet 200310053.

Rogers, J. D. (1990) Ultraviolet absorption cross sections and atmospheric photodissociation rate constants of formaldehyde, *J. Phys. Chem.*, 94, 4011-4015.

Rothman, L. S., R. R. Gamache, A. Goldman, L. R. Brown, R. A. Toth, H. M. Pickett, R. L. Poynter, J. M. Flaud, C. Camy-Peyret, A. Barbe, N. Husson, C. P. Rinsland and M. A. H. Smith (1987), The HITRAN database: 1986, *Appl. Opt.*, 26 (19), 4058-4097.

Samuelsson, J., B. Galle, J. Mellqvist, C. Ordóñez, A. S. H. Prévôt, C. Astorga, B. R. Larsen, W. Junkermann, C. Hak and B. Neininger (2006) Primary and secondary formaldehyde and fuel based emission factors in Milan obtained by long path FTIR, on-road and flight measurements 2002-2003, in preparation for *Atmos. Chem. Phys*.

Sander, S. P., R. R. Friedl, D. M. Golden, M. J. Kurylo, R. E. Huie, V. L. Orkin, G. K. Moortgat, A. R. Ravishankara, C. E. Kolb, M. J. Molina, B. J. Finlayson-Pitts (2003), *Chemical kinetics and photochemical data for use in atmospheric studies* [online], Evaluation Number 14, Pasadena, CA, JPL Publication 02-25, Available from: http://jpldataeval.jpl.nasa.gov/ [Accessed 22 November 2004].

Saunders, S. M., M. E. Jenkin, R. G. Derwent and M. J. Pilling (1997) World Wide Web Site of a Master Chemical Mechanism (MCM) for use in tropospheric chemistry models, *Atmos. Environ.*, 31, 1249-1249.

Savage, N. H., R. M. Harrison, P. S. Monks and G. Salisbury (2001) Steady-state modelling of hydroxyl radical concentrations at Mace Head during the EASE'97 campaign, May 1997, *Atmos. Environ.*, 35, 515-524.

Schmidt, M., H. Glatzel-Mattheier, H. Sartorius, D. E. Worthy and I. Levin (2001) Western European N_2O emissions: A top-down approach based on atmospheric observations, *J. Geophys. Res.*, 106 (D6), 5507-5516.

Seinfeld, J. H. and S. N. Pandis (1998) *Atmospheric chemistry and physics: From air pollution to climate change*, New York: John Wiley & Sons Inc.

Shaw, R. W. (1984) The atmosphere as delivery vehicle and reaction chamber for acid deposition, *In:* C. M. Bhumrather, ed. *Meteorological aspects of acid rain*, Acid precipitation series, Vol. 1, Stoneham, MA: Butterworth Publishers, pp. 33-55.

Sillman, S., J. A. Logan and S. C. Wofsy (1990) The sensitivity of ozone to nitrogen oxides and hydrocarbons in regional ozone episodes, *J. Geophys. Res.*, 95 (D2), 1837-1851.

Sinha, P., P. V. Hobbs, R. J. Yokelson, I. T. Bertschi, D. R. Blake, I. J. Simpson, S. Gao, T. W. Kirchstetter and T. Novakov (2003) Emissions of trace gases and particles from savanna fires in southern Africa, *J. Geophys. Res.*, 108 (D13), 8487, doi: 10.1029/2002JD002325.

Spirig, C., A. Neftel, L. I. Kleinman and J. Hjorth (2002) NO_x versus VOC limitation of O_3 production in the Po Valley: Local and integrated view based on observations, *J. Geophys. Res.*, 107 (D22), 8191, doi: 10.1029/2001JD000561.

Staehelin, J., A. S. H. Prévôt and I. Barnes (2000) Photochemie der Troposphäre, *In:* R. Guderian, ed. *Handbuch der Umweltveränderungen und Ökotoxikologie, Band 1A: Atmosphäre*, Berlin: Springer Verlag, pp. 207-324.

Staffelbach, T., A. Neftel, A. Blatter, A. Gut, M. Fahrni, J. Staehelin, A. Prévôt, A. Hering, M. Lehning, et al. (1997) Photochemical oxidant formation over southern Switzerland, 1. Results from summer 1994, *J. Geophys. Res.*, 102 (D19), 23345-23362.

Stahl, Q. R. (1969) *Air pollution aspects of aldehydes, Scott Research Laboratories*, NTIS Report PB 188081.

Steinbacher, M., J. Dommen, C. Ordóñez, S. Reimann, F. C. Grüebler, J. Staehelin, S. Andreani-Aksoyoglu, A. S. H. Prévôt (2005) Volatile organic compounds in the Po Basin. Part B: Biogenic VOCs, *J. Atmos. Chem.*, 51, 293-315.

Stull, R. B. (1988) *An introduction to boundary layer meteorology*, Dordrecht: Kluwer Academic Publishers.

Stutz, J. (1996) *Messung der Konzentration troposphärischer Spurenstoffe mittels Differentieller Optischer Absorptionsspektroskopie: Eine neue Generation von Geräten und Algorithmen*, Ph.D. thesis, University of Heidelberg.

Stutz, J. and U. Platt (1996) Numerical analysis and estimation of the statistical error of differential optical absorption spectroscopy measurements with least-squares methods, *Appl. Opt.*, 35 (30), 6041-6053.

Stutz, J. and U. Platt (1997) Improving long-path differential optical absorption spectroscopy with a quartz-fibre mode mixer, *Appl. Opt.*, 36 (6), 1105-1115.

Stutz, J., E. S. Kim, U. Platt, P. Bruno, C. Perrino and A. Febo (2000) UV-visible absorption cross sections of nitrous acid, *J. Geophys. Res.*, 105 (D11), 14 585-14 592.

Thielmann, A., A. S. H. Prévôt, F. C. Grüebler and J. Staehelin (2001) Empirical ozone isopleths as a tool to identify ozone production regimes, *Geophys. Res. Lett.*, 28 (12), 2369-2372.

Thielmann, A., A. S. H. Prévôt and J. Staehelin (2002) Sensitivity of ozone production derived from field measurements in the Italian Po Basin, *J. Geophys. Res.*, 107 (D22), 8194.

Tong, C., M. Blanco, W. A. Goddard III and J. H. Seinfeld (2006) Secondary organic aerosol formation by heterogeneous reactions of aldehydes and ketones: A quantum mechanical study, *Environ. Sci. Technol.*, 40, 2333-2338.

Trapp, D. and C. de Serves (1995) Intercomparison of formaldehyde measurements in the tropical atmosphere, *Atmos. Environ.*, 29, 3239-3243.

Trick, S. (2004) *Formation of nitrous acid on urban surfaces - a physical-chemical perspective*, Ph.D. thesis, University of Heidelberg.

Troe, J. (1979) Predictive possibilities of unimolecular rate theory, *J. Phys. Chem.*, 83, 114-126.

Tuazon, E. C., R. A. Graham, A. M. Winer, R. R. Easton, J. N. Pitts Jr. and P. L. Hanst (1978) A kilometer pathlength Fourier-transform infrared system for the study of trace pollutants in ambient and synthetic atmospheres, *Atmos. Environ.*, 12, 865-875.

U.S. EPA (2005), *Compilation of air pollutant emission factors* (AP-42), 5th edition, Research Triangle Park (NC), USA.

Vairavamurthy, A., J. M. Roberts and L. Newman (1992) Methods for determination of low molecular weight carbonyl compounds in the atmosphere: A review, *Atmos. Environ.*, 26A (11), 1965-1993.

Vandaele, A. C., P. C. Simon, J. M. Guilmot, M. Carleer and R. Colin (1994) SO_2 absorption cross section measurement in the UV using a Fourier transform spectrometer, *J. Geophys. Res.*, 99 (D12), 25 599-25 605.

Veitel, H. (2002) *Vertical profiles of NO_2 and HONO in the boundary layer*, Ph.D. thesis, University of Heidelberg.

Voigt, S., J. Orphal, K. Bogumil and J. P. Burrows (2001) The temperature dependence (203-293 K) of the absorption cross sections of O_3 in the 230-850 nm region measured by Fourier-transform spectroscopy, *J. Photochem. Photobiol. A*, 143, 1-9.

Voigt, S., J. Orphal and J. P. Burrows (2002) The temperature and pressure dependence of the absorption cross-sections of NO_2 in the 250-800 nm region measured by Fourier-transform spectroscopy, *J. Photochem. Photobiol. A*, 149, 1-7.

Volkamer, R. (2001) *A DOAS study on the oxidation mechanism of aromatic hydrocarbons under simulated atmospheric conditions*, Ph.D. thesis, University of Heidelberg.

Volkamer, R., W. Junkermann, K. Wirtz and U. Platt (2002) *Formation of formaldehyde, glyoxal and methylglyoxal from the toluene + OH reaction in the presence of NO_x*, poster presented at EGS XXVII General Assembly, 21-26 April 2002, Nice, France.

Volz-Thomas, A., H. Geiss, A. Hofzumahaus and K. H. Becker (2003) Introduction to special section: Photochemistry experiment in BERLIOZ, *J. Geophys. Res.*, 108 (D4), 8252, doi: 10.1029/2001JD002029.

von Friedeburg, C. (2003) *Derivation of trace gas information combining Differential Optical Absorption Spectroscopy with Radiative Transfer Modelling*, Ph.D. thesis, University of Heidelberg.

Wang, P., A. Richter, M. Bruns, J. P. Burrows, R. Scheele, W. Junkermann, K.-P. Heue, T. Wagner, U. Platt and I. Pundt (2006) Airborne multi-axis DOAS measurements of tropospheric SO_2 plumes in the Po-valley, Italy, *Atmos. Chem. Phys.*, 6, 329-338.

Wagner, T. and U. Platt (1998) Satellite mapping of enhanced BrO concentrations in the troposphere, *Nature*, 395, 486-490.

Wayne, R. P., I. Barnes, P. Biggs, J. P. Burrows et al. (1991) The nitrate radical: Physics, chemistry and the atmosphere, *Atmos. Environ.*, 25A, 1-203.

Weber, R. O and A. S. H. Prévôt (2002) Climatology of ozone transport from the free troposphere into the boundary layer south of the Alps during North Foehn, *J. Geophys. Res.*, 107 (D3), 4030.

Wesely, M. L. and B. B. Hicks (2000) A review of the current status of knowledge on dry deposition, *Atmos. Environ.*, 34, 2261-2282.

White, J. U. (1976) Very long optical paths in air, *J. Opt. Soc. Am.*, 66, 411-416.

WHO - World Health Organisation (2000) *Air quality guidelines for Europe - Second edition*, WHO Regional Publications, European Series, No. 91, WHO Copenhagen.

Wilkening, M. H. and W. E. Clements (1975) Radon 222 from the ocean surface, *J. Geophys. Res.*, 80, 3828-3830.

Williams, I. D., D. M. Revitt and R. S. Hamilton (1996) A comparison of carbonyl compound concentrations at urban roadside and indoor sites, *Sci. Total Environ.*, 189-190, 475-483.

Yokelson, R. J., D. W. T. Griffith and D. E. Ward (1996) Open-path Fourier transform infrared studies of large-scale laboratory biomass fires, *J. Geophys. Res.*, 101 (D15), 21 067-21 080.

Yokelson, R. J., I. T. Bertschi, T. J. Christian, P. V. Hobbs, D. E. Ward and W. M. Hao (2003) Trace gas measurements in nascent, aged and cloud-processed smoke from African savanna fires by airborne Fourier transform infrared spectroscopy (AFTIR), *J. Geophys. Res.*, 108 (D13), 8478, doi: 10.1029/2002JD002322.

York, D. (1966) Least-square fitting of a straight line, *Can. J. Phys.*, 44, 1079-1086.

Zhou, X. and K. Mopper (1993) Carbonyl compounds in the lower marine troposphere over the Caribbean Sea and Bahamas, *J. Geophys. Res.*, 98 (C2), 2385-2392.

Zhou, X., Y.-N. Lee, L. Newman, X. Chen and K. Mopper (1996) Tropospheric formaldehyde concentration at the Mauna Loa Observatory during the Mauna Loa Observatory Photochemistry Experiment 2, *J. Geophys. Res.*, 101 (D9), 14 711-14 719.

Acknowledgements

Finally, I would like to thank all these people who made it possible for me to realise this thesis and who contributed to the success of this work.

I want to thank my examiner Prof. Dr. H. Fischer for accepting me as an external Ph.D. student and for the interest he took in having a look down on tropospheric chemistry.
I also thank Prof. Dr. U. Platt (Institute of Environmental Physics at the University of Heidelberg) for being my co-examiner for this thesis and for providing me the possibility to do my Ph.D. at the IUP.

Thanks to Dr. Irene Pundt for employing me to work on this interesting subject.

I am especially grateful to Dr. André Prévôt and Dr. Josef Dommen from Paul Scherrer Institut for the productive and successful cooperation during the past years and for inviting me to spend some weeks at PSI. I learned a lot about the VOC chemistry during this time.

For helpful discussions on several topics I would like to thank Dr. Wolfgang Junkermann, Dr. Roland von Glasow and Dr. Rainer Volkamer.

The intensive field campaigns required a large number of people to install and operate the instruments. I would like to thank the colleagues and helpers involved in the campaigns, namely Kai Uwe Mettendorf, Christian Kunz and Achim Bäuerle for operating the multibeam DOAS instruments at two of the three sites during the FORMAT II campaign.
Particular thanks to Werner Maneschg, whose help as Italian interpreter was indispensable for campaign planning and during the second FORMAT campaign.
Thanks also to ’i vikinghi’ Aasmund Vik and Harald Willoch and ’lo spagnolito’ Carlos Ordóñez for funny times and interesting discussions during the campaigns at Alzate.

I want to thank Dr. Susanne Pechtl, Dr. Thierry Marbach, Denis Poehler for proof-reading parts of the manuscript and especially Klaus-Peter Heue, who ’had to’ read nearly every part of this thesis, and Dr. Thomas Wagner for suggestions on the text and motivating conversations.
Thank to Klaus-Peter Heue, Andreas Hartl and Denis Poehler for the distraction during our 15:00 h (s.t.) tea break.

Special thanks to Helga Hak and Dr. Hermann Haug who supported me during my studies and in whatever I did.

Curriculum Vitae

Claudia Hak
born on 27 April 1976 in Bobingen

1982 - 1986	Grundschule Taufkirchen
1986 - 1995	Gymnasium Unterhaching degree: Abitur
1995 - 2001	Meteorology studies at the Ludwig-Maximilians-Universität of Munich
December 2001	Diploma in Meteorology Diploma thesis: „Zusammenhang zwischen atmosphärischen Telekonnektionen und stratosphärischer Ozonverteilung“ (Correlation between atmospheric teleconnections and stratospheric ozone distribution) Supervisors: Dr. Peter von der Gathen (Alfred Wegener Institute for Polar and Marine Research, Potsdam) and Dr. Peter Köpke (University of Munich)
2002 - 2006	Ph.D. studies at the Institute of Environmental Physics (IUP) of the University of Heidelberg Supervisors: Prof. Dr. Herbert Fischer (University of Karlsruhe) and Prof. Dr. Ulrich Platt (University of Heidelberg)

Heidelberg, July 2006